BREATH FIGURES ASSISTED FABRICATION OF POLYMER FILMS WITH CONTROLLABLE MICROSTRUCTURES FOR ENERGY HARVESTING

GONG JIANLIANG

Ph.D

The Hong Kong Polytechnic University

2017

The Hong Kong Polytechnic University
Institute of Textiles & Clothing

Breath Figures Assisted Fabrication of Polymer Films with Controllable Microstructures for Energy Harvesting

GONG Jianliang
A thesis submitted in partial fulfillment of the requirements
for the Degree of Doctor of Philosophy

September 2016

CERTIFICATE OF ORIGINALITY

I hereby declare that this thesis is my own work and that, to the best of my knowledge and belief, it reproduces no material previous published or written, nor material that has been accepted for the award of any other degree or diploma, except where due to acknowledgement has been made in the text.

___________________(signed)

GONG Jianliang (Name of student)

ABSTRACT

The breath figure (BF) technique is a unique one-step strategy of using easily-available and nontoxic water droplet arrays as soft dynamic templates to produce porous films with the size ranging from 200 nm to 20 μm for a wide range of applications in micro/nanofabrication, superhydrophobic/responsive coating, sensing, catalysis, separation, and various biological, optical and electronic devices. It possesses simple, low-cost, time-saving, easily-scalable and non-destructive advantages, and requires no trivial work on the preparation and removal of templates because the condensation, assembly and removal of BFs are all spontaneous.

However, considerable challenges and problems still exist in the BF field. Firstly, the reported BFs are usually single-component, which often results in the formation of monotonous porous or spherical structures. And there are still no systematic studies on controllable fabrication and formation mechanism of polymer microstructures *via* different BFs. Then the optimal experimental conditions for dissimilar materials to obtain ordered pore arrays are usually different, narrow and specific. Currently it is difficult to find a general and scalable fabrication approach for highly ordered porous films with commercial polymeric and non-polymeric materials on different substrates. Thirdly, there are few studies on construction of three-dimensionally (3D) ordered porous film conformably formed on nonplanar substrates (particularly for flexible fabrics with

complex surface textures), although uneven and curved surfaces are usually encountered in most real applications. Finally, BFs generated pore arrays (BFAs) and their derived materials have demonstrated promising and valuable applications in various fields, but to our best knowledge, their applications in energy-related fields are significantly less developed.

In this thesis, firstly, the BF principle of water was successfully extended to methanol (MeOH) and binary liquids of different water/MeOH ratios for assisted fabrication of various film microstructures under different experimental conditions based on a series of well-defined polystyrene (PS) homopolymers ($1600 <$ number molecular weight (M_n)<19500, and molecular weight distribution (M_n/M_w) < 1.1). Three kinds of solvents with different affinity to water, i.e. completely immiscible carbon disulfide (CS_2), partial immiscible chloroform ($CHCl_3$) and highly miscible tetrahydrofuran (THF), were used to prepare solutions with the concentration of 5 mg mL^{-1} to 640 mg mL^{-1}, respectively. It was found that aqueous BFs led to the fabrication of porous microstructures regardless of molecular weight, solvent type and solution concentration, while MeOH BFs generally resulted in the production of microspherical particles. A surprising phenomenon was that microspherical caps were obtained from the casting solutions with better water affinity by combining use of water and MeOH as binary BFs. The formation of microspherical caps was independent on the molecular weight and solution concentration, while adjusting the methanol ratio of binary BFs, asymmetrical particles ranging from large-portion to small-portion microspherical caps were prepared quickly and directly. Through the comparative and systematic analysis, the whole BF processes starting from the initial spreading of solution film on substrate, the formation and spreading of nonsolvent BFs on solution film, the physical gelation of polymer-rich phase to the final formation of polymer microstructures by complete removal of liquids were thoroughly elucidated based on the different physicochemical properties of nonsolvent, solvent and polymer.

Then after unambiguous clarification on formation mechanism behind the BF processes, an additive-assisted strategy was developed for a robust and universal modified BF technique for a range of commercially available polymers which are not good candidates for conventional BF technique, such as PS, PS-*b*-polybutadiene-*b*-PS (SBS), poly(ethylene oxide) (PEO), and polycarbonate (PC). Through adjusting the addition of asphalt, all of them were successfully employed to prepare highly ordered BFA films without any cracks in more accessible BF conditions on different substrates with either a planar or nonplanar surface. This asphalt-assisted BF technique was also feasible for incorporating different nanoparticles, such as titanium dioxides nanoparticles (TiO_2 NPs), silver nanowires and copper nanowires, into the porous films for tailorable functionality with little change of the regularity of pore arrays. The TiO_2 NPs incorporated BFA films were exemplified and demonstrated to harvest luminous energy more efficiently for photocatalytic degradation of pollutants in both air and water.

Thirdly, the formation of 3D conformal BFAs (3C-BFAs) was systematically investigated on different nonplanar substrates, particular on flexible fabrics. A novel silicon-containing graft copolymer poly(dimethylsiloxane)-*graft*-polyacrylates (PDMS-*g*-PAs) that can form non-cracking and ordered BFAs was first explored and demonstrated on a planar substrate by the BF technique in a wide solution concentration. Then based on a special metal fabric, copper/nickel coated conductive polyester fabric, the influence of solution concentration was systematically studied to find an optimal concentration range for the formation of 3C-BFAs. Such modified fabrics may pave the way to a brand-new class of textile composites featured with the porous microstructures of film-forming materials conformably formed on the uneven surface of textile substrates, which possesses customized multifunctional properties of introduced materials, inherent properties (such as breathability and flexibility) and unique texture features of fabrics. Moreover, taking advantages of the silicon-containing characters, PDMS-*g*-PAs BFA films were used as single-source precursor for in situ formation of honeycomb microstuctured ceramics.

Finally, the BFA films on both planar substrates and 3C-BFAs on nonplanar substrates were used as negative micro molds to prepare positive PDMS films with different micro lens arrays (MLAs) and hierarchical MLAs (H-MLAs). They were further used as frictional materials for the assembly of vertical contact-separation mode based triboelectric nanogenerators (TENGs) to convert mechanical energy into electricity, respectively. The influence of surface microstructures on the electric performance of TENGs was systematically

investigated by applying different external forces and resistance loads. Based on the PDMS film with an optimal surface microstructure, a portable and wearable TENG device was developed to harvest the mechanical energy generated by human body motions such as finger tapping, hand clapping, and walking.

In summary, this study provided a better understanding of the complex mechanism behind the BF approaches for designing and fabricating polymer films with controllable microstructures, and developed a universal additive-assisted BF technique for general fabrication and functionalization of large-area, non-cracking and highly ordered BFA films on either planar or nonplanar substrates with customized polymers and nanoparticles for different practical uses. A brand-new kind of textile composites merging the properties of both porous materials and textiles was first developed and realized by systematically studying the formation of 3C-BFAs on flexible fabric substrates. This benefits the development of novel, flexible and wearable materials with tailorable architectures and functionalities based on traditional textile materials for higher value applications, such as TENGs.

PUBLICATIONS

Refereed Journal Papers

1. **Jianliang Gong**, Bingang Xu*, Xiaoming Tao, Lei Li. Binary Breath Figures for Straightforward and Controllable Self-Assembly of Microspherical Caps, Physical Chemistry Chemical Physics, 2016, 18: 13629-13637.

2. **Jianliang Gong**, Bingang Xu*, Xiaoming Tao. Asphalt-Assisted Assembly of Breath Figures: A Robust Templating Strategy for General Fabrication of Ordered Porous Polymer Films, RSC Advances, 2015, 5 (19): 14341-14344.

3. **Jianliang Gong**, Bingang Xu*, Xiaoming Tao. Aramid-Assisted Acid Spinning of Continuous Multi-Walled Carbon Nanotube Fibers for Twisted, Robust, and Multifunctional Yarns, Macromolecular Materials and Engineering, 2015, 300 (10): 954-959.

4. **Jianliang Gong**, Bingang Xu*, Xiaoming Tao, Lei Li. Honeycomb Microstructured Silicon Oxycarbide Sheets from Silicon-Containing Graft Copolymer Films, Plasma Processes and Polymers, 2014, 11 (11): 1001-1009.

5. **Jianliang Gong**, Bingang Xu*, Xiaoming Tao. Breath Figure Micromolding Approach for Regulating the Microstructures of Polymeric Films for Triboelectric Nanogenerators, ACS Applied Materials & Interfaces, DOI: 10.1021/acsami.6b14729.

Conference Proceedings

1. **Jianliang Gong**, Bingang Xu*, Xiaoming Tao. *In Situ* Formation of

Honeycomb Silicon-Containing Polymer-Derived Ceramics by a Hybrid Strategy Involving Plasma and Pyrolysis, 2015 International Chemical Congress of Pacific Basin Societies, Honolulu, Hawaii, USA, Dec 15-20, 2015.

2. **Jianliang Gong**, Bingang Xu*, Huayang Yu, Xiaoming Tao. Novel Honeycomb-Microstructured Asphalt Composite Coatings for Sustainable Photocatalytic Application, The 3rd International Conference on Applied Materials and Electronics Engineering (AMEE), Hong Kong, April 26 & 27, 2014.

ACKNOWLEDGEMENTS

First and foremost, I would like to express my sincerest gratitude to my chief supervisor, Dr. Bingang Xu, for his professional guidance, invaluable support and incredible patience. During the PhD period, Dr. Xu also offered me high trust and freedom that I need to move on, but he can always steer me in the right direction whenever he thought I need it. And when I ran into a trouble spot in my research, study, writing, and even life, the door to his office was always open. Without his self-giving help, I would not finish my PhD study within a normal period. I sincerely appreciate all his contributions of time, energy, ideas and suggestions to make my PhD experience productive and meaningful.

I would also like to express my sincerest thanks to my co-supervisors, Prof. Xiaoming Tao and Prof. Lei Li. It is my honor to have the opportunities to interact with Prof. Tao in the weekly group meeting, and the subgroup discussion every two weeks. I specially appreciate Prof. Tao for bringing me to the interesting research field of triboelectric nanogenerators. Besides one of my PhD co-supervisors, Prof. Li was also my MPhil supervisor. I have been so lucky to be his student since 2009. I always appreciate Prof. Li for bringing me into the research field and transferring me a hard-working spirit and rigorous academic attitude. Special thanks also go to him for kindly helping me to be an exchange student at Xiamen University for three months in 2015 by a special scheme of the PRC Ministry of Education.

I would like to acknowledge the Hong Kong Polytechnic University for providing me with a postgraduate scholarship and funding support of my PhD work. I also acknowledge the research facilities and technical support from all the departments at the Hong Kong Polytechnic University.

I would like to thank my roommate Mr. Huayang Yu of Department of Civil and Environmental Engineering for providing me with some asphalt materials, Dr. Jianzhuang Chen of East China University of Science and Technology and Mrs. Qiaoling Zhao of Shanghai Institute of Organic Chemistry (Chinese Academy of Science) for their kind help on several characterization tests.

I would like to specifically thank Dr. Shenyan Li, Dr. Fei Wang, Dr. Jie Feng, Dr. Wei Zheng, Dr. Lin Shu, Dr. Zhifeng Zhang, Dr. Bao Yang and Dr. Song Chen for their kind help and suggestions in my PhD study and life. They are just like my brothers and sisters in Hong Kong. I would like to particularly thank Dr. Fei Wang and Dr. Lingling Wang to celebrate my 29th birthday in September for me.

I would like to thank Mr. Xinkun Lu, Dr. Liang He, Mr. Wenyi Wang, Dr. Lin Tan, Dr. Lu Gan, Mr. Jianhua Li, Mr. Diandong Zhao, Dr. Huawen Hu, Dr. Guoyou Cui, Miss Jiayi, Dr. Jinping Wang and other colleagues to help and accompany me in the materials synthesis and processing laboratory located at W605.

It is helpful, wonderful and joyful to study and work in a multidisciplinary research group, such as materials, chemicals, textiles, mechanics, electronics, optics, etc.

I would like to thank Mr. Xi Wang, Dr. Qiao Li, Mr. Zehua Peng, Miss Shuping Lin, Miss Ying Li, Miss Yuheng Zhang, Mr. Ke Chen, Mr. Rong Yin, Dr. Xingxing Huang, Dr. Yangyong Wang, Dr. Zeguang Pei, Dr. Wei Zeng, Mr. Ziheng Zhang, Mr. Shirui Liu and other colleagues.

I would also like to thank my friends Mr. Daoxing Zou, Mr. Xiaogang Peng, Mr. Jinping Chen, Mr. Zhaoyang Hu, Mr. Shuyou Wu, Mr. Yonggang Chen, Mr. Changliang Liu, Mr. Qin Zhang, Mr. Deyuan Zhong and other friends who gave me selfless and great help during those years.

Lastly, but most importantly, I would like to give my most particular thanks to my wife Bingyu Liu for her love, support and encouragement, to my parents, mother-in-law and sisters for their continuous understanding, encouragement and support. My gratitude to them is always beyond words.

TABLE OF CONTENTS

LIST OF FIGURES

CHAPTER 1

CHAPTER 2

CHAPTER 3

CHAPTER 4

CHAPTER 5

CHAPTER 6

LIST OF TABLES

CHAPTER 3

ABBREVIATIONS

^{1}H NMR	**Proton nuclear magnetic resonance**
2D	Two-dimensionally
3C-BFAs	Three-dimensionally conformal breath figure arrays
3D	Three-dimensionally
AFM	Atomic force microscope
Ag NWs	**Silver nanowires**
Al	Aluminum
aPS	Polystyrene synthesized by atom transfer radical polymerization
ATRP	Atom transfer radical polymerization
BCPs	Block copolymers
BFA-no.	Polymer films with breath figure arrays prepared from the casting solution with different concentration, e.g. BFA-15 indicates that the BFA film was prepared from 15 mg mL^{-1} solution
BFAs	Breath figure arrays
BFs	Breath figures
$CHCl_3$	Chloroform
Cu/Ni-coated fabric	Copper/Nickel coated conductive polyester fabric
CNTs	Carbon nanotubes
cPS	Commercial polystyrene
CS_2	Carbon disulfide
Cu NWs	Copper nanowires
CuBr	Copper(I) bromide
EDX	Energy dispersive X-ray spectrometer

F3C-BFA-no.	Fabric based three-dimensionally conformal breath figure arrays prepared from the casting solution with different concentration, e.g. F3C-BFA-15 indicates that the F3C-BFA was prepared from 15 mg mL^{-1} solution
F3C-BFAs	Fabric based three-dimensionally conformal breath figure arrays
GO	Graphene oxide
GPC	Gel permeation chromatography
HMLA-no.	Polymer film with hierarchical micro lens arrays prepared by using different fabric based three-dimensionally conformal breath figure arrays as templates, e.g. HMLA-15 indicates that the HMLA film was prepared by using F3C-BFA-15 as template
HMLAs	Hierarchical micro lens arrays
HSPs	Hansen solubility parameters
MBP	Methyl-2-bromopropionate
MeOH	Methanol
MLA-no.	Polymer films with micro lens arrays prepared by using polymer film with different breath figure array as templates, e.g. MLA-15 indicates that the polymer film with micro lens arrays was prepared by using BFA-15 as template
MLAs	Micro lens arrays
M_n	Number-average molecular weight
MO1	Mordant orange 1
M_w	Weight-average molecular weight
M_w/M_n	Molecular weight distribution
NO_x	Nitrogen oxides
OM	Optical microscope
P3HT	Poly-3-hexythiophene
PC	Polycarbonate
PDMS	polydimethylsiloxane

PDMS-*g*-PAs	Poly(dimethylsiloxane)-*graft*-polyacrylates ()
PEO	Poly(ethylene oxide)
PET	Polyethylene glycol terephthalate
PMDETA	N’, N’, N, N’’, N’’-pentamethyldiethylenetriamine
PS	Polystyrene
PSA	Polystyrene/Asphalt blends
PS-*b*-PPP	Polystyrene-*b*-polyparaphenylene
PTFE	Polytetrafluoroethylene
RhB	Rhodamine B
SBS	Polystyrene-*block*-polybutadiene-*block*-polystyrene
SD	Standard deviation
SEM	Scanning electron microscope
TEM	Transmission electron microscope
TENGs	Triboelectric nanogenerators
T_g	Glass transition temperature
THF	Tetrahydrofuran
TiO_2 NPs	Titanium dioxides nanoparticles
Tol	Toluene
UV	Ultraviolet radiation
XPS	X-ray photoelectron spectroscopy

CHAPTER 1 Introduction

1.1 Research Background

The complex interplay between the structures and physicochemical properties of different polymers (macromolecules) leads to a wonderful world. Nature and biology provide inexhaustible inspiration for people to design and construct materials with desired components and structures ranging from nanoscale, microscale to macroscale for different promising applications. Typical examples involve the development of superhydrophobic surface with self-cleaning characteristic based on the so-called lotus effect,[1] the study of gecko footpad to prepare hierarchical structures for achieving high adhesion property,[2,3] the mimic of nacre for tough hybrid composites,[4] and the fabrication of similar microstructure of butterfly wings for structurally colored fabrics without the use of any dyes or pigments.[5] The booming development of fabricating and applying microstructured materials by mimicking nature or biology constitutes an emerging field of biomimetics.[6]

The use of breath figures (BFs) for fabricating the porous microstructures of materials is a novel nature-inspired example developed recently.[7] BFs are named according to the mode of their generation, which means the figures of liquid droplets with a size range from dozens of nanometers to several millimeters that can be generated upon exhaling aqueous vapor onto a cold surface, such as fog and dew phenomenon in nature. They are facilely available, green and dynamic templates in nature for the porous microstructure of polymers and beyond. In comparison with the conventional lithography approaches, this BF technique possesses simple, low-cost, time-saving, easily-scalable, and non-destructive advantages. And because the condensation, assembly and evaporation of water droplet arrays are all spontaneous, it can also effectively avoid the tedious preparation and post-treatment procedures that are commonly required in non-lithography approaches of using self-assembled block copolymers, colloidal particles, and emulsions as sacrificial templates.

Over the past two decades, the BF technique has been boomingly developed as one of the most promising strategy for rapid fabrication of porous films with adjustable pore size (typically ranging from 200 nm to 20 μm), shape, layer, array and regularity based on different film-forming materials (mainly polymers, also involving carbon nanomaterials, inorganic nanoparticles and small molecules) by varying experimental conditions, such as solvent, solution concentration, humidity, airflow velocity, temperature, and substrate. These films can meet the requirements of different uses directly or after modification and have demonstrated in a wide range of applications in micro/nanofabrication, superhydrophobic/responsive coating, sensing, catalysis, separation, and various biological, optical and electronic devices.[7-15]

The BF technique is simple and straightforward, but it actually involves complicated transfers of heat and mass at the interfaces among water, solvent and polymer, which has many thermodynamic and kinetic underpinnings that need to be further fully understood, such as the spreading behaviors of casting solution on substrate and condensed water droplets on solution surface, the role of water and its interaction with polymer solution, and the influence of solution concentration variation on the precipitation and gelation process. And for the practical applications, there are also several challenging issues that need to be addressed, such as the circumvention of film defects and cracks. It is still difficult to find a general approach for scalable fabrication of highly ordered porous films with commercial polymeric and non-polymeric materials on either planar or nonplanar substrates. Moreover, uneven and curved surfaces are usually encountered in most real applications, but three-dimensionally (3D) ordered porous films conformably formed on nonplanar substrates is significantly less developed, particularly for flexible fabrics with complex surface textures.

Moreover, the BFs generated porous films on planar substrates, 3D conformal porous microstructures on nonplanar fabric substrates and their derived materials are believed to possess great economical cost and structural advantages used in energy storage or conversion devices, such as triboelectric nanogenerators (TENGs). However, to our best knowledge, there are still no systematic study on the fabrication, application and evaluation of TENGs based on such kind of BFs generated materials and structures. TENG is an innovative kind of energy harvester developed recently for converting mechanical energy into electricity based on the conjunction of triboelectrification and electrostatic induction.[16] It is also named organic nanogenerator because its most used materials are polymers.[17] Polymeric materials and their microstructures are found to play key roles in the generation, accumulation, and retainment of triboelectric charges, which decisively determines the final electric performance of TENGs.[16-19]

1.2 Research Objectives

This research study aims to design and fabricate polymeric films with adjustable microstructures and components based on commercially available materials and textiles by the very promising BF technique for harvesting energy that ubiquitously exists in nature, such as luminous energy and mechanical energy. The detailed objectives of this study include:

(1) to study and develop the BF approach and principle in non-aqueous liquid and more complex binary aqueous/non-aqueous liquids for systematically investigating the influence of different experimental parameters on the formation of polymeric microstructures based on well-defined polymers;

(2) to develop an additive-assisted universal BF strategy for general fabrication of highly ordered and non-cracking porous films with commercially available polymers, and to functionalize the polymer films with the incorporation of desired nanoparticles into the porous microstructures for harvesting luminous energy for photocatalytic degradation of pollutants;

(3) to design and study 3D conformal porous microstructures developed by the BF technique on nonplanar substrates, particular on flexible fabrics with complex surface textures, and to develop a new class of textile materials that possess

both the multifunctional properties of film-forming materials and the good inherent properties of fabric substrates;

(4) to design and develop positive micro lens arrays (MLAs) and hierarchical MLAs (HMLAs) by using BFA films on both planar substrates and nonplanar substrates;

(5) to design and assemble vertical contact-separation mode based TENGs with the MLA and HMLA polymer films developed above for converting mechanical energy into electricity, and to investigate the influence of film microstructures on the electric performance of TENGs for finding the optimal microstructure to assemble a portable and wearable TENG for harvesting the mechanical energy generated by human body motion.

1.3 Research Methodology

The following research methodology will be adopted in this research study.

(1) Formation mechanism study of film microstructures by the BF technique in different nonsolvent vapors

A series of well-defined polystyrene (PS) homopolymers synthesized by atom transfer radical polymerization (ATRP) will be used for the formation mechanism study of polymeric microstructures by the BF technique through adjusting the experimental variables. High-surface-tension liquid water, low-surface-tension liquid methanol (MeOH) and their binary mixtures with different ratios will be used to form nonsolvent vapors in a sealed vessel, respectively. Besides nonsolvent type and MeOH/water ratio, other influencing factors involving the molecular weight, solution concentration and solvent type will be also studied for controlling the self-assembly of polymeric microstructures. Through systematic comparison and analysis, the complex mechanism behind the relevant BF technique will be thoroughly elucidated in terms of physicochemical properties of polymer, vapor pressure, surface tension and miscibility of solvents and nonsolvents.

(2) Additive-assisted BF fabrication of highly ordered porous films with commercial polymers

Commercial polymers such as PS, PS-*b*-polybutadiene-*b*-PS (SBS), poly(ethylene oxide) (PEO), and polycarbonate (PC) are easily available materials that are widely used in different fields, but they are not very good candidates for the fabrication of ordered porous films by conventional BF technique. To develop a robust and universal BF technique applicable for most polymers, an oligomer such as polydimethylsiloxane (PDMS) and asphalt will be explored as an additive to assist fabrication of ordered porous microstructures in more accessible experimental conditions. The influence of additive amount, solution concentration and planar substrate types will be investigated on the film microstructures. Different 3D objects such as copper grids, inorganic particles, and cotton and polyester fabrics will be used as nonplanar surfaces to demonstrate the feasibility of additive-assisted BF technique. Nanoparticles such as titanium dioxides nanoparticles (TiO_2 NPs), silver nanowires (Ag NWs) and copper nanowires (Cu NWs) will also be incorporated into the porous films for more advanced functionalization. One of their applications in harvesting luminous energy will be exemplified for photocatalytic degradation of pollutants.

(3) Study of 3D conformal porous films with controllable dimensional architectures on fabrics

3D conformal film with the porous microstructures well contouring to the uneven surface of fabric substrate possesses the potential of merging the properties of porous microstructures, introduced materials and textile fabrics. Starting with the chemical structure and properties of film-forming material, a novel silicon-containing graft copolymer poly(dimethylsiloxane)-*graft*-polyacrylates (PDMS-*g*-PAs) that can form non-cracking and ordered BFAs in a wide solution concentration will be first explored on a planar substrate by the BF technique. Then based on a special metal fabric, copper/nickel coated conductive polyester fabric (Cu/Ni-coated fabric), 3D conformal BFA films will be developed and systematically studied to find an optimal concentration range of casting solution that can both form ordered BFAs and maintain elaborate surface features of the fabric. Moreover, taking advantages of the silicon-containing characters, PDMS-*g*-PAs BFA films will also be explored as single-source precursor for in situ formation of honeycomb microstuctured ceramics.

(4) Templating synthesis of PDMS MLAs and HMLAs from different BFAs for TENGs

A series of BFA films on planar substrates will be used as negative molds for templating synthesis of PDMS films with different MLAs. And fabric-based

BFA films will also be employed for the fabrication of HMLAs. Then these PDMS films with different surface patterns will be used as frictional materials for the assembly of TENGs to generate electricity by harvesting the mechanical energy. And the influence of surface microstructures on the electric performance of TENGs will be systematically investigated and evaluated based on a vertical contact-separation TENG mode. Different pure resistors will be used as external load to determine the output voltage for the calculation of output current, average/instantaneous power (density), and electric energy. Finally, PDMS films with optimal surface microstructures will be used for wearable TENG devices to harvest the mechanical energy generated by different human body motions, such as finger tapping, hand clapping and walking.

(5) Characterization of materials and microstructures

The basic physicochemical properties of materials, liquids and substrates, such as molecular weight, solubility parameter, surface tension and vapor pressure, will be collected from related literatures or determined by corresponding experimental apparatus involving gel permeation chromatography (GPC), proton nuclear magnetic resonance (^{1}H NMR), contact angle apparatus, etc. Surface microstructures of different materials are the most concerned research topics. The characterization of surface microstructures will be systematically performed by scanning electron microscope (SEM), optical microscope (OM), atomic force microscope (AFM), etc. To monitor the element variation, energy dispersive X-ray spectrometer (EDX) and X-ray photoelectron spectroscopy (XPS) will be employed. The electric performance of TENGs under different triggering conditions will be monitored by an oscilloscope connected with a high sensitive probe.

1.4 Research Significance

Design and fabrication of porous materials with desired components and microstructures have long been an important science subject and a thriving research area because of their potential capacities of merging structural and material properties for numerous applications.[20-25] The BF technique is a unique one-step strategy of using easily-available and nontoxic water droplet arrays as dynamic templates for producing the porous microstructures of diverse materials with simple, low-cost, time-saving, easily-scalable and non-destructive advantages. However, it has to be noted that the promising BF technique is a nonisothermal and nonequilibrium process in nature.[7,8,11] Subtle changes in the casting conditions may result in a different outcome of the film porous microstructures. Therefore, it is of great significance and necessity to systematically study the complex mechanism behind the BF technique for the microstructure of polymers. Besides the BFAs by BF in aqueous vapor and microspheres by BF in MeOH vapor, this study will extend the BF principle to binary aqueous/nonaqueous liquids for the formation of novel micropsherical caps with adjustable shapes that can meet the specific requirements of some special applications. Most importantly, based on the thorough and comparative elucidation of formation mechanism of different polymer microstructures, this study will provide a novel and explicit understanding on controllable fabrication of asymmetrical microparticles by the BF technique directly, which will benefit further improvement of new BF means and the exploitation of more polymeric and nonpolymeric materials for one-step creation of more complex microstructures.

Different film-forming materials often require different elaborate casting conditions for ordered BFAs because the BF process is sensitive to experimental variables.[7] Moreover, for some commercial polymers without polar groups and special architecture, further chemical modification or functionalization is usually required. It is very difficult to find a universal BF strategy to prepare ordered porous films based on commercial polymers that are abundant and facilely available. The additive assisted BF technique developed in this study will not only provide an effective solution for direct and general fabrication of ordered BFA films with commercial polymers but also enable their optimal BF conditions to be more easily accessible. Moreover, the additive BF principle can be extended to direct incorporation of different nanoparticles for customized functionalization of BFA films. These studies are believed to accelerate the development of BF techniques and BFA films for more commercial applications.

3D conformal porous films are of great interest in many areas because uneven and curved surfaces are usually encountered in most real applications. However, it is quite challenging for the direct formation of 3D conformal porous microstructures with the film-forming materials well contouring to the nonplanar surface of substrate by the use of lithographic and other non-lithographic techniques. This study first develops the BF technique for fabricating 3D conformal ordered BFAs on nonplanar and flexible fabrics with complex surface textures, which will pave the way to a brand-new class of textile composites featured with the porous microstructures of film-forming materials conformably formed on the uneven surface of textile substrates. Such modified fabrics can meanwhile possess customized multifunctional properties of introduced materials (such as TiO_2 NPs, Ag NWs and Cu NWs), inherent properties (such as breathability and flexibility) and unique texture features of fabrics, which are believed to be promising materials for a wide spectrum of flexible and wearable applications. The applications of these porous microstructured fabrics in TENGs can harvest various waste mechanical energy generated by human body motions for producing electricity, which can potentially drive vast types of portable electronics and sensors for different purposes, such as health monitoring and medical care.

1.5 Thesis Structure

This thesis comprises the following seven chapters.

Chapter 1 firstly makes a brief introduction on the background of this study. Then the specific objectives of this thesis are put forward according to the existing challenges and problems. Finally, the adopted methodology and research significance are summarized respectively.

Chapter 2 provides a comprehensive literature review of this study including porous materials and polymers, BFs and their templating applications in porous polymers, and applications of porous polymers in energy harvesting. The research gaps in general fabrication of BFAs, conformal porous microstructures on nonplanar fabric substrates and applications in harvesting energy are pointed out.

Chapter 3 presents a systematical and detailed investigation of polymer microstructures prepared by the BF technique under different nonsolvent vapors and experimental conditions based on the synthesized polymers with well-defined chemical structures. A comprehensive understanding of formation mechanisms of the resultant polymeric microstructures is thoroughly elucidated.

Chapter 4 develops an asphalt-assisted universal BF technique for general fabrication of highly ordered and non-cracking BFA films with commercially available polymers. This technique is also further applied for the functionalization of BFA films by incorporating desired nanoparticles into the porous microstructures to meet more advanced applications.

Chapter 5 develops and studies 3D conformal BFAs formed on nonplanar and flexible fabrics by exploring a novel silicon-containing graft copolymer as film-forming material. Taking advantage of the high silicon-containing characteristic of used materials, a hybrid strategy combining plasma modification and pyrolysis techniques is also developed for the in situ formation of honeycomb patterned ceramics.

Chapter 6 explores and demonstrates the applications of PDMS films with MLAs and HMLAs templated from BFAs on both planar substrate and fabric substrate in TENGs. The influence of surface microstructures on the electric performance of TENGs is then systematically evaluated under different external loads and triggering conditions. The promising use of PDMS film-based TENGs in converting mechanical energy generated by body motion into electricity is also studied.

Chapter 7 makes general conclusions on the primary finding of this study, discusses the limitations and offers recommendations for future work.

The structure of this thesis is outlined in Fig. 1.1.

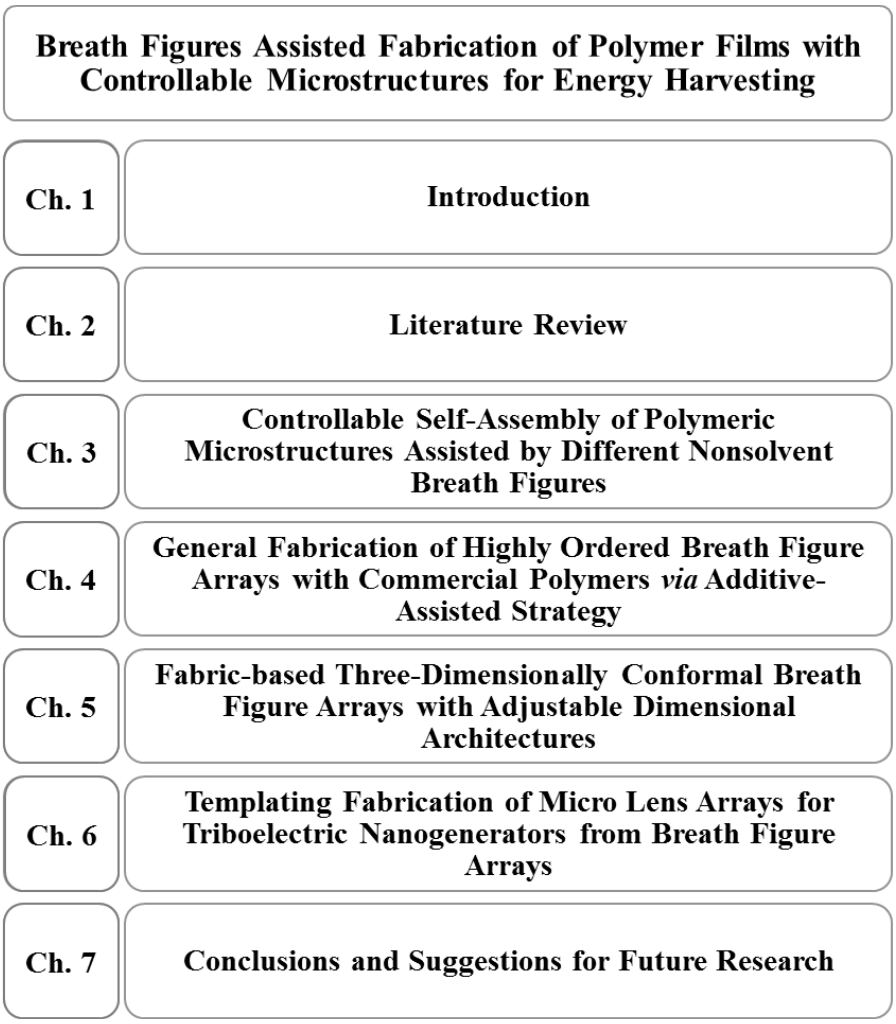

Breath Figures Assisted Fabrication of Polymer Films with Controllable Microstructures for Energy Harvesting

Ch. 1	**Introduction**
Ch. 2	**Literature Review**
Ch. 3	**Controllable Self-Assembly of Polymeric Microstructures Assisted by Different Nonsolvent Breath Figures**
Ch. 4	**General Fabrication of Highly Ordered Breath Figure Arrays with Commercial Polymers *via* Additive-Assisted Strategy**
Ch. 5	**Fabric-based Three-Dimensionally Conformal Breath Figure Arrays with Adjustable Dimensional Architectures**
Ch. 6	**Templating Fabrication of Micro Lens Arrays for Triboelectric Nanogenerators from Breath Figure Arrays**
Ch. 7	**Conclusions and Suggestions for Future Research**

Figure 1. 1 Structure of the thesis

CHAPTER 2 Literature Review

This chapter presents an overall literature review regarding the related topics covered in the thesis, including porous materials and polymers, BFs and their templating applications in porous polymers, and applications of porous polymers in energy harvesting. The purpose of this review is to identify the research gaps in general fabrication of BFAs, conformal porous microstructures on nonplanar fabric substrates and applications in harvesting energy.

2.1 Porous materials and polymers

From bamboo, corallite and honeycomb in nature, synthetic charcoal, sponge, polyfoam and textiles in everyday life, to foamed metals, thermal baffle and biological scaffold in commercial production, the ubiquitous porosity plays an essentially important role in the world. For different applications, design and fabrication of porous structures with desired materials and architectures have long been an important science subject and a thriving research area.[20-25] Examples range from well-defined nano-/micro-structured films,[24,26,27] high-surface-area molecular sieves,[28] carbon nanomaterials involving carbon nanotubes[29] and graphene,[30] to novel graphene-like two-dimensional (2D) materials.[31,32]

Porous polymers especially received vast attention because of their abundant raw resources, easy processability and broad applications.[20,33,34] From vitally important natural nucleic acids, proteins, polysaccharides and enzymes to ubiquitous synthetic plastics, rubbers, fibers and adhesives, polymers are a kind of extremely abundant and facilely available materials. Moreover, with the rapid development of controlled/living radical polymerization techniques, polymers with predictable molecular weight, controllable molecular weight distribution, designed topology, composition and functionality can be well defined and synthesized as required.[35,36] In comparison to nonpolymeric materials, polymers have lightweight advantage and versatile properties, and most importantly possess a unique characteristic of easy-processability. This facilitates the design and construction of well-defined microstructures in monolith, film, fiber or other complex forms by either melting or solution strategy. Their good compatibility with other materials provides a facile access to numerous composite materials with hybrid microstructures. Moreover, the easy-removal feature of some polymers by simply dissolving or heating enables them to act as ideal sacrificial templates for inorganic, metal or other nonpolymeric materials.

Owing to the excellent processing character of polymers, numerous methodologies such as lithography,[37] plasma/laser etching,[38,39] ink printing,[40] physical/chemical deposition,[41,42] foaming,[43] sintering,[44,45] templating,[46] synthesis[47] and self-assembly[48] can be employed for the construction of porous microstructures in polymeric materials with the size ranging from nanoscale, microscale to macroscale. They can be further subdivided into top-down strategy and bottom-up strategy. The former strategy is usually to create desired porous microstructures in a bulk polymeric material by removing the redundant parts using mechanical, photic, plasma, chemical, or other form of energy; while the latter strategy is an opposite approach starting from atomic or molecular bricks for the construction of porous microstructures *via* synthesis or assembly.

Each strategy has its own advantages and disadvantages. The top-down approaches such as various lithography techniques possess good accuracy and repeatability, but they usually involve a destructive process and require high-cost facilities and multistep procedures for complex structures. Moreover, they are slow for large scale production and cannot create pores with the size down to dozens of nanometers. Foaming in bulk polymers with gas or supercritical fluid as porogenic agent also belongs to the top-down strategy, but its resultant porous microstructures are often irregular and disordered, which cannot be controlled effectively.

The bottom-up strategy can prepare porous polymers with the pore size down to 2 nm by direct synthesis of monomers with multifunctional reaction sites and rigid and contorted structures.[49-51] And based on the self-assembly of well-defined block copolymers (BCPs), ordered porous polymers with size in the range of 2-50 nm can be created by selective swelling[52-55] or etching.[56,57] The fabrication of porous polymers with the pore size larger than 50 nm often involves templating in most cases.[58,59] Both polymers and monomers can be used as raw bricks. The monomer brick usually undergoes an additional chemical reaction during the fabrication process.[60] Theoretically, any materials or objects that can be removed by post-treatment can be used as templating medium for the porous microstructures of polymers, such as patterned silicon mold,[61] anodic aluminum oxides,[59] and self-assembled colloidal particles.[60] Some solid molds can be used repeatedly, but it has to be noted that their pattern and size are fixed, which cannot be further adjusted. The size, shape and assembling behavior of colloidal particles can be adjusted, but they act as sacrificial templating role, which need to be further removed by physical or chemical post-treatment. Generally, one of the main drawbacks remained in the bottom-up approaches involving synthesis or self-assembly is that their generation of pores requires an additional post-treatment, i.e. removal of catalysts, solvent, or redundant components.

The breath figure (BF) technique is a unique one-step strategy of using easily-available and nontoxic water droplet arrays as soft dynamic templates for producing the porous microstructures of diverse materials (mainly polymers), which possesses simple, low-cost, time-saving, easily-scalable and non-destructive advantages.[7-11] This promising strategy requires no trivial work on the preparation and removal of templates because all the condensation, assembly and evaporation of BFs are spontaneous.

2.2 Breath Figures (BFs) and their templating applications in porous polymers

2.2.1 Early studies of BFs

In everyday life, the fog or dew phenomena of aqueous vapor condensing onto the surfaces of shower mirrors, eyeglasses and pot covers are familiar to all (Fig. 2.1a-c). Such phenomena are also ubiquitous in nature. Examples involve the dew produced on leaves (Fig. 2.1d), cobwebs (Fig. 2.1e) and insect wings (Fig. 2.1f).

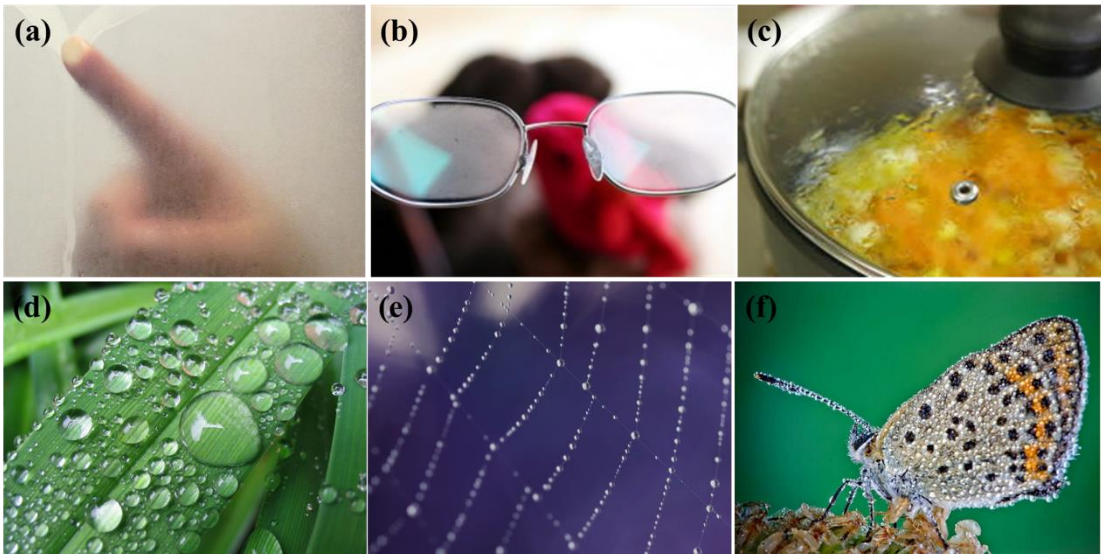

Figure 2. 1 Examples of fog and dew on (a) shower mirror, (b) eyeglass, (c) pot cover, (d) leaves, (e) cobweb and (f) insect wing, respectively. Pictures were collected from Internet

In as early as 1893, Aitken first investigated this phenomenon by directly observing the water figures on the surfaces of glasses or mirrors generated by breathing.[62] He first described the BFs by developing a simple and interesting experiment of replicating the image of a coin. The coin was first placed on one side of a piece of glass or mirror, and heated by electrification or a gas blow-pipe flame. Then the coin was removed. After the substrate became cold, breathing upon the surface region where the coin rested led to the formation of a coin image with explicit engraving features. Examination with an optical microscope (OM) showed that the black and white image was sketched by condensed water patches with different sizes at different areas. At the bright areas, the deposited water patches were small and homogeneous, and looked like a layer of numerous convex lenses with close juxtaposition; while at the darker areas, the water patches were larger and flatter. BFs were also formed by directly breathing on the mirror surface treated by the blow-pipe flame without a coin. The track of the flame, which looks quite black, was clearly marked. OM revealed that the flamed area was covered with a thin film of water. Based on these experiments, Aitken speculated that the dusts or other impurities on the surfaces of substrates play a determined role on the formation of BFs. In 1911, Rayleigh observed the similar BFs phenomena on the glass plates treated by hot sulfuric acid or diluted hydrofluoric acid.[63] The surface region treated by acid was found to be covered with a large lamina of water, which behaved similar to the flame track in Aitken's experiment. Therefore, he suggested that the formation reason of BFs was owing to the different degrees of surface cleanliness. This identical BFs phenomenon on the different cleanliness surfaces initiated an interesting and wonderful discussion among scientists from different research areas about a century ago.[62-68] In 1957, Spur and Butlin further noticed that the cloudy areas with a layer of tiny droplets were contaminated and hydrophobic, while the clear areas covered with uniform patches were hydrophilic and thought to be cleaner. They suggested that the action of flame or electrification for cleaning the organic contaminations on glass surfaces may introduce free radicals to change the wetting properties of surfaces.[69]

After the inspired work by Aitken and Rayleigh, the term "BFs" named according to the mode of generation was widely used to describe the kind of phenomena of aqueous vapor condensing onto a relatively cold surface by researchers. From late 1980s to early 1990s, the formation mechanism of BFs attracted physicists' strong interest.[70-81] They regarded the condensation of BFs as a physical process of homogeneous vapor phase transforming in a liquid phase on a substrate with a relatively low temperature, which evolves through the nucleation and growth of liquid droplets accompanied with the interaction of coalescence. Therefore, the BFs phenomenon is essentially a process of physical phase transition constrained on a two-dimensional (2D) plane that can be theoretically analyzed by temperature and wettability. These two parameters control the nucleation and growth of BFs. And the surface wettability additionally has major influences on the surface features of BFs.[72,73,75]

2.2.1.1 Nucleation of BFs

Nucleation of BFs from water vapor is the first phenomenon. As shown in Fig. 2.2a, when the temperature of substrate (T_R) is lower than that of the surrounding aqueous atmosphere (T_R), the saturation pressure of water at T_S (P_S) should be correspondingly smaller than the saturation pressure at T_R (P_R). The pressure difference will drive the vapor at T_R (state 1) to the substrate surface. This will result in the increase of vapor density near the substrate (State 2), which is larger than the density at the thermodynamically stable vapor state (State 4). Driven by the energy minimization, the unstable vapor at T_S will transform into thermodynamically stable liquid phase with a larger liquid density (State 3). This gains an energy caused by the volume difference ($\Delta E = E_1 - E_2$, as shown in Fig. 2.2b). However, to reach the final equilibrium state, an energy cost (barrier) of forming vapor-liquid interface needs to be overcame firstly. Beysens pointed out that the total energy for a droplet of radius R can be described by Eq. 2.1[75]

$$F = -\frac{4\pi R^3}{3}\Delta E + 4\pi R^3 \gamma \tag{2.1}$$

Where F is the total energy for a droplet on a substrate. R is the radius of droplet, ΔE is the energy difference caused volume variation, and γ is the interfacial tension of vapor and liquid.

For the formation of a stable droplet, its R needs to be larger than a "critical" radius (R^*)

$$R > R^* = 2\gamma/\Delta E \tag{2.2}$$

Therefore, the energy of a droplet with R^* is

$$F(R^*) = \frac{16\pi}{3}\frac{\gamma^3}{\Delta E^2} \tag{2.3}$$

Considering that the nucleation of BFs is a thermally activated process, the nucleation rate (d_n/d_t) is[75]

$$\frac{d_n}{d_n} \sim \exp(\frac{F(R^*)}{k_B T}) = \exp(\frac{16\pi}{3}\frac{\gamma^3}{k_B T \Delta E^2}) \tag{2.4}$$

Where d_n/d_t is the number (d_n) of droplets of R^* nucleated during the time (d_t). T is the temperature, and k_B is the Boltzman constant. The number of water droplets shows an exponential increase when the temperature and ΔE are varied.

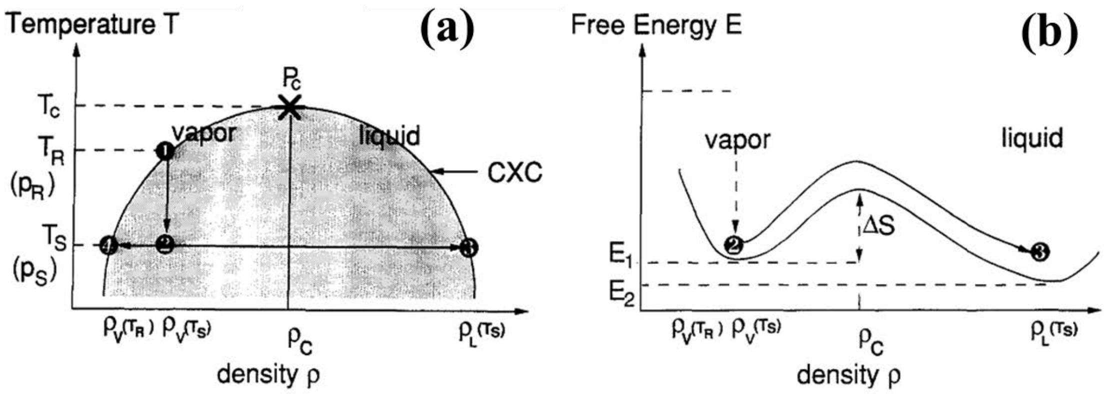

Figure 2. 2 Schematic of nucleation process of BFs on a substrate: (a) in a T-ρ diagram and (b) in an energy diagram[75]

Das Gupta et al. estimated that saturated vapor of water at 20 °C would nucleate at about 0 °C with $R^* \approx 3$ nm.[82] However, experimental observation and life experience show that BFs can form on a substrate with a much higher temperature. Beysens ascribed such phenomena to the heterogeneous nucleation of BFs caused by the wetting properties of substrate, which contributes to lowering the energy barrier of forming vapor-liquid interfaces.[75] This was also confirmed by Nepomnyashchy et al. They found that the energy barrier for heterogeneous nucleation occurring at an interface was always smaller than that for homogeneous nucleation in the bulk vapor.[83] The surface wettability is usually characterized by the contact angle (θ). For a surface with complete wetting, its θ is zero (Fig. 2.3a). And $\theta = 180^\circ$ indicates the surface is perfectly non-wetting (Fig. 2.3d). In most cases, the surface is partial wetting, where a droplet rest with a θ between 0° and 180° at equilibrium (Fig. 2.3b and c).

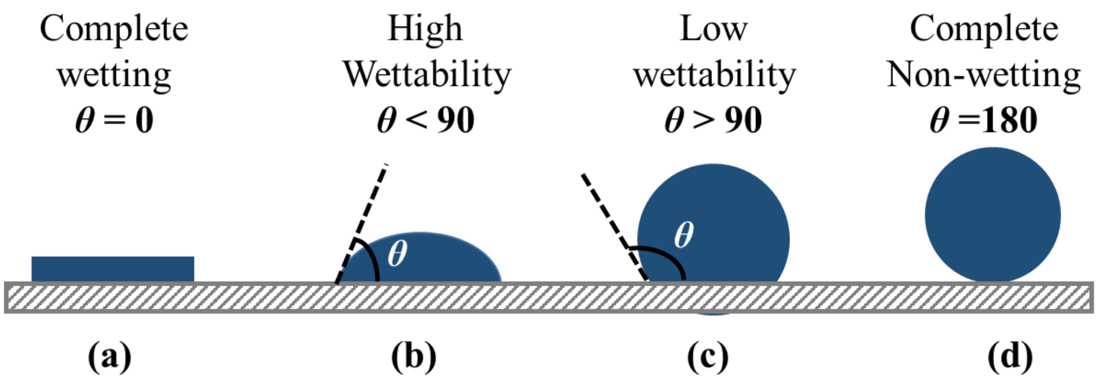

Figure 2. 3 Contact angle of a droplet on substrate with different surface wettability

Depending on the function of θ, Sigsbee further modified Eq.2.4 as following[84]

$$\frac{d_n}{d_n} \sim \exp[F(R^*)\Phi(\theta)] \tag{2.5}$$

In which

$$\Phi(\theta) = 2\frac{3-\cos\theta+\cos^3\theta}{3sin^3\theta} \tag{2.6}$$

For 0°< θ < 180°, Eqs. 2.5 and 2.6 indicate that the heterogeneous nucleation on a surface possesses a higher nucleation rate than the homogeneous nucleation occurring in the bulk (which can be described by Eq. 2.4). Therefore, in a less temperature difference, heterogeneous nucleation can lead to form more water droplets than homogeneous nucleation.

2.2.1.2 Growth of BFs

The growth of BFs occurs after the initial nucleation. Experimental observations show that BFs can grow to be either a liquid film that appears dark (Black BF), or an assembly of liquid droplets that scatters light and appears white (Gray BF). This is greatly dependent on the wetting properties of surfaces. Generally, on the surface with high hydrophilicity wettability (typically θ < 10°), quasi-films are formed by filmwise condensation, while on the surface with low hydrophilicity (typically $\theta > 70°$), dropwise condensation leads to the formation of spherical droplets.[85-88] More specifically, the basic pattern of BFs is a uniform and intact film on perfect wetting surface ($\theta = 0°$), but it consists of quasi-films on the surface with $0° < \theta < 10°$. Here quasi-films refer to several discontinuous hole-free films eventually formed from individual nuclei by filmwise condensation. The hole-free film pattern cannot be further merged into an intact film because of the pinning force of surface heterogeneity. Thin-film interference can lead to the formation of unique fringes. And the film thickness can be estimated based on the fringe distance, which basically grows with time (t).[70]

The dropwise growth of BFs on less hydrophilic surface ($\theta > 70°$) is more complex than the filmwise growth on the surface with good hydrophilicity. It evolves four different growth regimes.

The first regime occurs just after nucleation and lasts for a short period of time. It is characterized by a large population of small droplets, but with a low surface coverage (s, the ratio of surface area covered by droplets/the substrate area). The coalescence of droplets can be observed in this regime. However, due to the low surface coverage, the occurrence probability of coalescence events is still low. Therefore, the growth of BFs in the first regime can be regarded as the growth of a single droplet without significant interactions. For a water droplet nucleated on the substrate, it will grow along its periphery at the expense of water molecules from vapor atmosphere (as shown in Fig. 2.4a and b).[72,75] Assuming that the vapor atmosphere is generated by saturated humid flow with a constant velocity U parallel to the substrate surface, Beysens and Knobler calculated that the liquid droplet size (R) grows as a function of $t^{1/3}$ (Eq.2.7). They also pointed out that the radii and distance of liquid droplets in this regime are generally both smaller than 2 μm.[70]

$$< R > = R \sim (t)^{1/3} \tag{2.7}$$

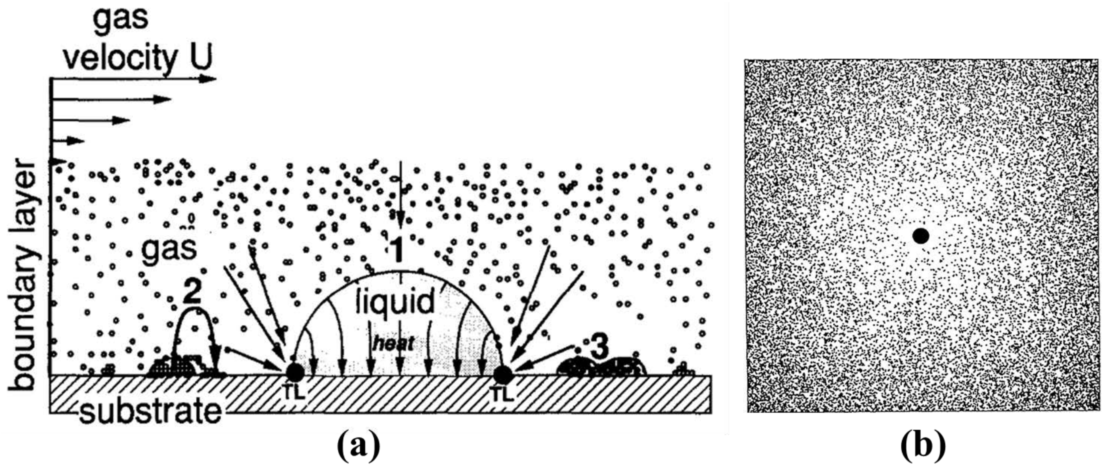

(a) (b)

Figure 2. 4 (a) Schematic of the growth of an individual droplet. The velocity (U) of a humid gas flow decreases near the substrate and equals zero close to the surface, resulting in the formation of a velocity gradient. A boundary layer of water vapor forms where the velocity goes to zero. Different processes for the growth of droplet can concur in this layer. (b) and simulation of the growth of an individual droplet. Water molecules are allowed to diffuse to and accommodate at the perimeter of a droplet placed at the center of a square[72,75]

The appearance of a well-defined order indicates that the growth of BFs goes to the intermediate regime. This stage is also called self-similar regime because of the self-similar growth of droplets and universal characteristics of BFs in time. It happens when the surface coverage typically exceeds 30% and usually stabilizes at about 50%-55% (Fig. 2.5a). The coalescence between droplets becomes frequent in this regime, which plays important interactions on the growth of BFs. As shown in Fig. 2.5b, the average size of BFs should continuously grow as a function of $t^{1/3}$, which is identical with the growth of an individual droplet. However, the coalescence speeds up the growth of BFs. The mergence of two or more droplets results in a step increase in the size of new formed droplets. Generally, the average size of BFs is proportional to time, which grows as $\langle R \rangle \sim t$.[70,72,75] Based on a polyethylene film, the evolution of BFs during the first two regimes was directly observed by Briscoe and Galvin (Fig. 2.6). The occurrence of coalescence would not alter the basic shape of water droplets but rescale the droplet sizes and distances.[78]

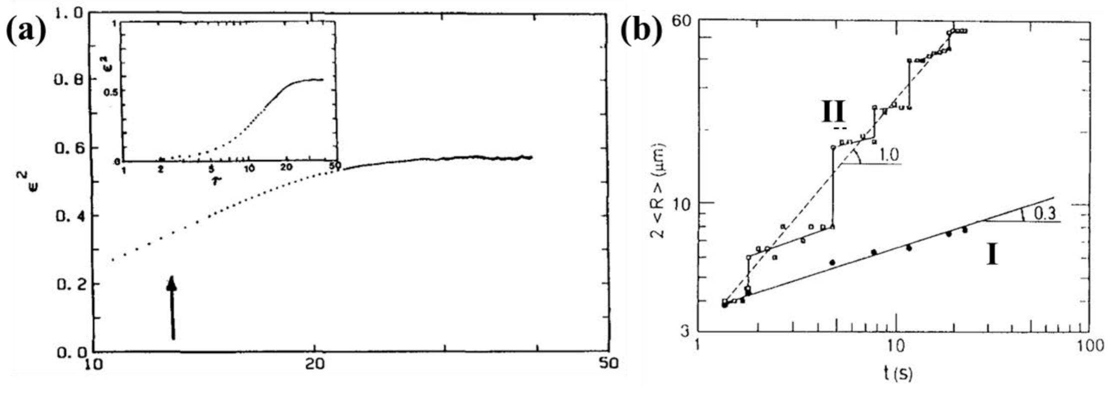

Figure 2. 5 Evolution of surface coverage (a) and average size (b) of BFs with time. Line I and Line II are the growth of BFs with and without the removal of coalescence effect, respectively[75]

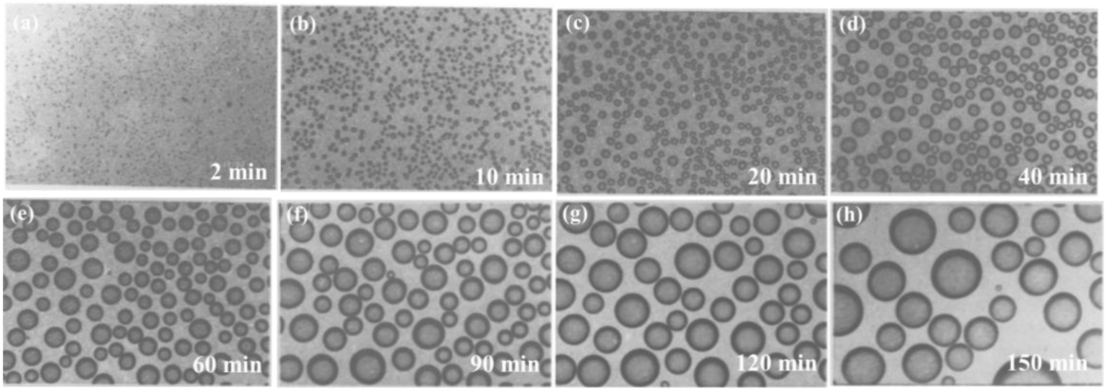

Figure 2. 6 The evolution of BFs on a PE film during the first two regimes. The width of each image is 1.5 mm[78]

Continuous condensation results in the formation of larger droplets and increases the probability of coalescence. The coalescence can free some space on the surface and allow the nucleation of new droplets among the large droplets. They possess the same growth laws and scaling properties with the first generation of BFs. The appearance of new generations of water droplets can be regarded as the third regime. During this regime, the BFs are composed of numerous droplets with different sizes, as shown in Fig. 2.7.[72] They are produced in different generations, and are smaller than the water droplets formed in the first generation, but all of them still have the self-similar properties when taken separately.

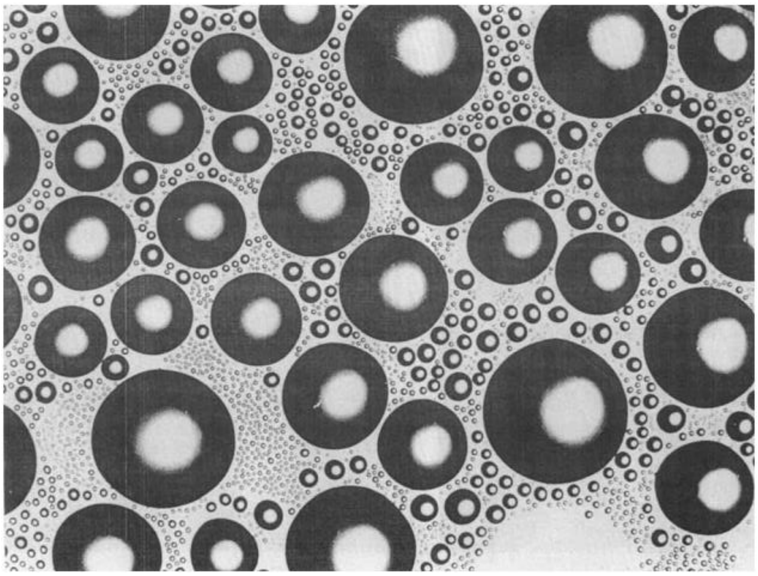

Figure 2. 7 BFs consisted of water droplets produced in different generations[72]

The basic shapes of water droplets in BFs will remain unchanged until the largest droplets begin to flatten by gravity. This indicates that the growth of BFs goes to the final regime. The shape and size of water droplets both become gravity-dependent. It is calculated that gravity can cause the water drop size up to a capillary length, about 2.5 millimeters at room temperature.[75] With the size of droplets eventually increasing to several mm, the growth of BFs would finally reach a steady state. If the substrate is vertical, the largest droplets will be driven to flow away from the substrate by gravity, leaving free space for the nucleation and growth of new droplets.

The patterns of BFs are different on the surface with an intermediate wettability, which varies with θ. Zhao et al observed that the growth of BFs on modified silicon substrates clearly evolves from dropwise condensation to filmwise condensation when θ was gradually decreased from 70° to 10°, as shown in Fig.

2.8.[89] On the less hydrophilic surface (θ = 70º), the condensed droplets grow in spherical shapes (Fig. 2.8a-c). With the decrease of θ to 40º, the formed droplets become non-spherical and irregular (Fig.2.8d-f). And more irregular and larger droplets are found on the surface of θ = 20º (Fig. 2.8g-i). When the surface becomes very hydrophilic (θ = 10º), the growth of BFs shows a filmwise condensation process, resulting in the formation of quasi-films (Fig. 2.8j-l). It is noted that the basic features of BFs at each θ remain unaltered with time and the surface coverage possesses an increase trend with the decrease of contact angle. The morphology variation of BFs with surface wettability can be ascribed to the substrate heterogeneity and the hysteresis effects in the contact angle of droplets. Because heterogeneities can fix the perimeter of droplets through the pinning force on the contact line, the growth and coalescence routes will be very different, which can result in the formation of droplets with ellipsoidal or more complicated shapes.[72,73,75,89]

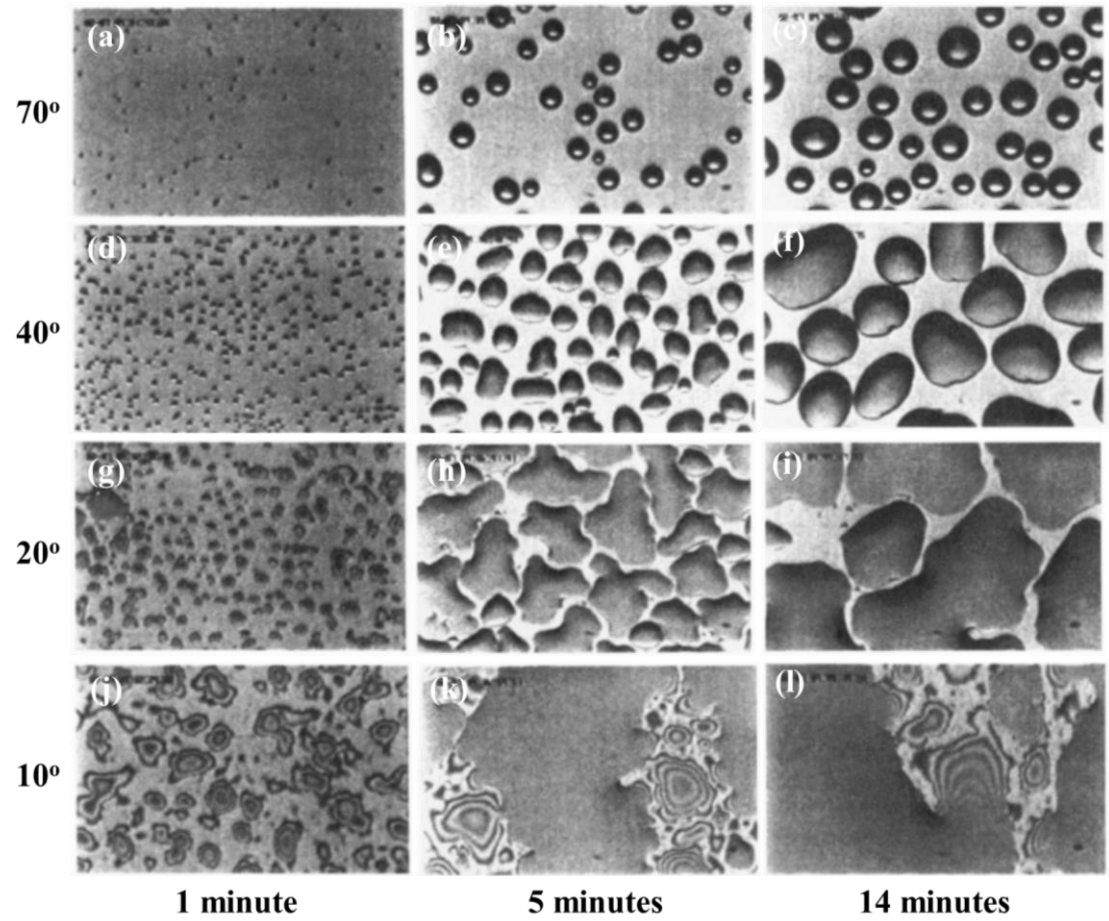

Figure 2. 8 Morphology evolution of BFs with time on modified silicon substrates with different contact angles. The width of each photo is 385 μm[89]

2.2.1.3 Formation of BFs on liquid surfaces

The formation of BFs occurs not only on solid surfaces but also on liquid surfaces.[71,90,91] Steyer et al investigated the condensation and growth of BFs on the surface of water-immiscible paraffin oil. They found that the growth of BFs on a liquid surface evolves through similar stages with those on a solid surface, which were described as initial stage (Fig. 2.9a), crossover stage (Fig. 2.9b) and coalescence-dominant stage (Fig. 2.9c), respectively. The initial and coalescence-dominant stages were equivalent to the first and second regimes of growth on solid surfaces. The evolution of BFs from small, isolated, and randomly distributed droplets to ordered and regular water droplet arrays was confirmed by their corresponding structure factors (Fig. 2.9d-f) and the decreasing entropy of configuration (Fig.2.9g_3). With the increase of growth time, BFs mainly consisted of hexagonally ordered arrays (Fig. 2.9g_2), and the surface coverage (ε, the ratio of droplet area/liquid surface) stably reached at about 0.55. The growth of BFs on liquid surfaces with time exhibits the same power laws on solid surfaces. As shown in Fig. 2.9g_1, the average droplet size <R> of BFs is $<R>\sim t^{1/3}$ during the initial stage but increases as $<R>\sim t$ in the coalescence-dominant stage.[71]

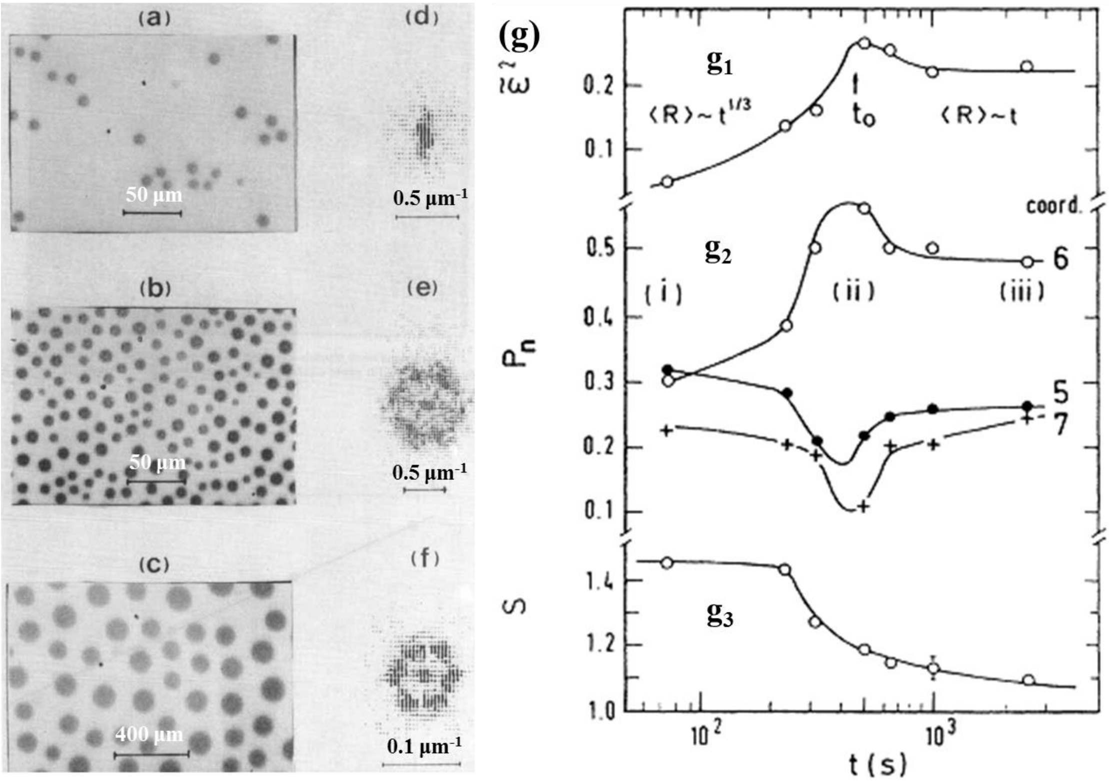

Figure 2. 9 Three typical stages of BFs on a liquid film: (a) and (d) initial stage, (b) and (e) crossover stage, (c) and (f) coalescence-dominant stage. (d)-(f) are the corresponding structure factor of (a)-(c). (g) The evolution of surface

coverage (ε^2, g_1), distribution of polygons with coordination number n=5, 6, 7 (P_n, g_2), and entropy of configuration per drop (S, g_3) with time[71]

The nucleation and growth of BFs on the surface of a liquid are similar to the formation of BFs on a solid surface but still possess some unique features.[71,92] The liquid surface is homogeneous and clean, which has much fewer impurities than the solid surface. And it can be smooth up to the scale of the thermally-induced capillary fluctuation. This indicates that the nucleation sites on liquid surfaces are less than solid surfaces. It will result in the formation of nuclei with a lower density on liquid surfaces. And due to the low-density nuclei, the dimensional space for droplet growth becomes large. Besides, it was found that a thin film of oil can be formed to play a role in preventing the water droplets from coalescence. Therefore, the initial stage of growth on liquid surfaces exhibits longer time than the first regime on solid surfaces. Moreover, in contrast to the BFs on solid surfaces, the hexatic phase is formed for BFs on liquid surfaces. This can be ascribed to the soft characteristic of liquid surface, which allows the mobility and rearrangement of water droplets. With the counterbalance of gravity and surface tensions, the condensed droplets can induce the deformation of liquid surface, producing elastic attractive forces for the rearrangement of droplets in turn. When all droplets reach an equilibrium state, BFs should exhibit an ordered hexatic phase only. Actually, through taking great care for maintaining the liquid surface clean, Steyer et al. successfully obtained larger-area BFs consisted of hexagonally arranged water droplets in a long-range order, as shown in Fig. 2.10.[72,91]

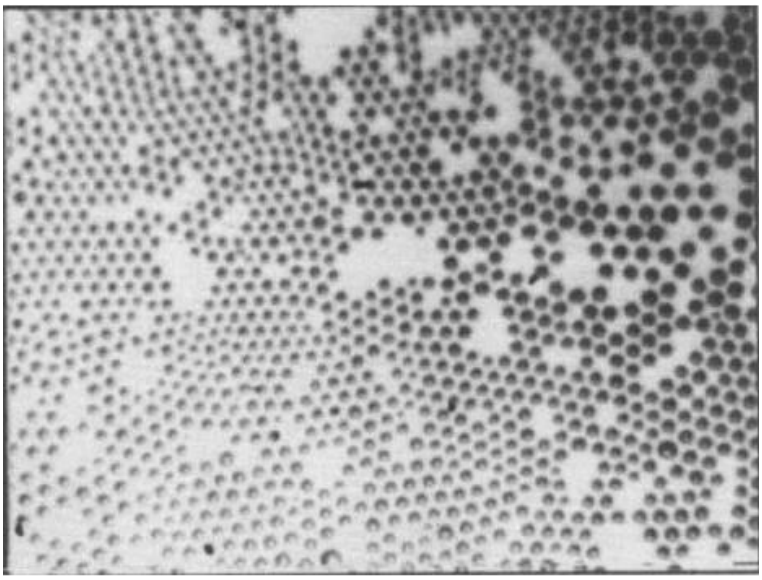

Figure 2. 10 A photograph of larger-area BFs on a liquid surface consisted of hexagonally arranged water droplets in a long-range order[72]

2.2.2 From BFs to BF arrays (BFAs)

2.2.2.1 Discovery and advantages of BFs for BFAs

Generation of BFs by directly breathing is a familiar, simple and effective method of detecting the contamination on glass surfaces. In the past, BFs were often employed by photographers to make negative pictures *via* a wet-plate processing technique. Recently, BFs were directly collected from humid atmospheres based on a kind of sponge-like cotton fabrics with a temperature-responsive characteristic.[93] In most cases, however, BFs are considered to be an annoying phenomenon, because they lower the transmission of light, enable fungus spores, limit the yield of agricultural production, and contaminate biological samples. Therefore, BFs were often studied by most researchers with the purpose of suppressing their generation through developing effective anti-fog or self-cleaning materials and methodologies.[94-99] For a considerably long time, Little attention was given to the investigation of BFs with positive applications.

A significant and valuable application of BFs for the fabrication of ordered porous films in materials science was first discovered by François and coworkers in 1994.[100] Through exposing a droplet of polystyrene-*b*-polyparaphenylene (PS-*b*-PPP, the inset of Fig. 2.11a)/carbon disulfide (CS_2) solution on a substrate to a moist air flow, they innovatively introduced BFs on the liquid surface by the evaporative cooling of solvent. The dissolved polymer was left as a thin film on the substrate after complete evaporation of solvent and water. Highly regular honeycomb morphology (or hexagonal dot patterns), similar to the water droplet arrays of BFs, were observed under optical microscopy (OM), as shown in Fig. 2.11a. They were confirmed as multiple layers of microspherical holes (like water droplet imprints) arranged in hexagonal arrays by scanning microscopy image (SEM, Fig. 2.11b and c). By adjusting the thickness or concentration of solution film, honeycomb porous films with single pore layer were also obtained, as shown in Fig. 2.11d. François et al. later found similar honeycomb surface morphologies by the same method with different polymers and polymer mixtures, including star (or star-shaped) PS, PS lithium sulfonate, PS-*b*-polythiophene, PS grafted C_{60}, PS-*b*-poly-3-hexythiophene(PS-*b*-P3HT) doped with $FeCl_3$, and star PS mixed with 33% of P3HT.[100-102] They also obtained similar results when using 1,2-dichloroethane to replace CS_2 for dissolving PS-*b*-PPP.[103]

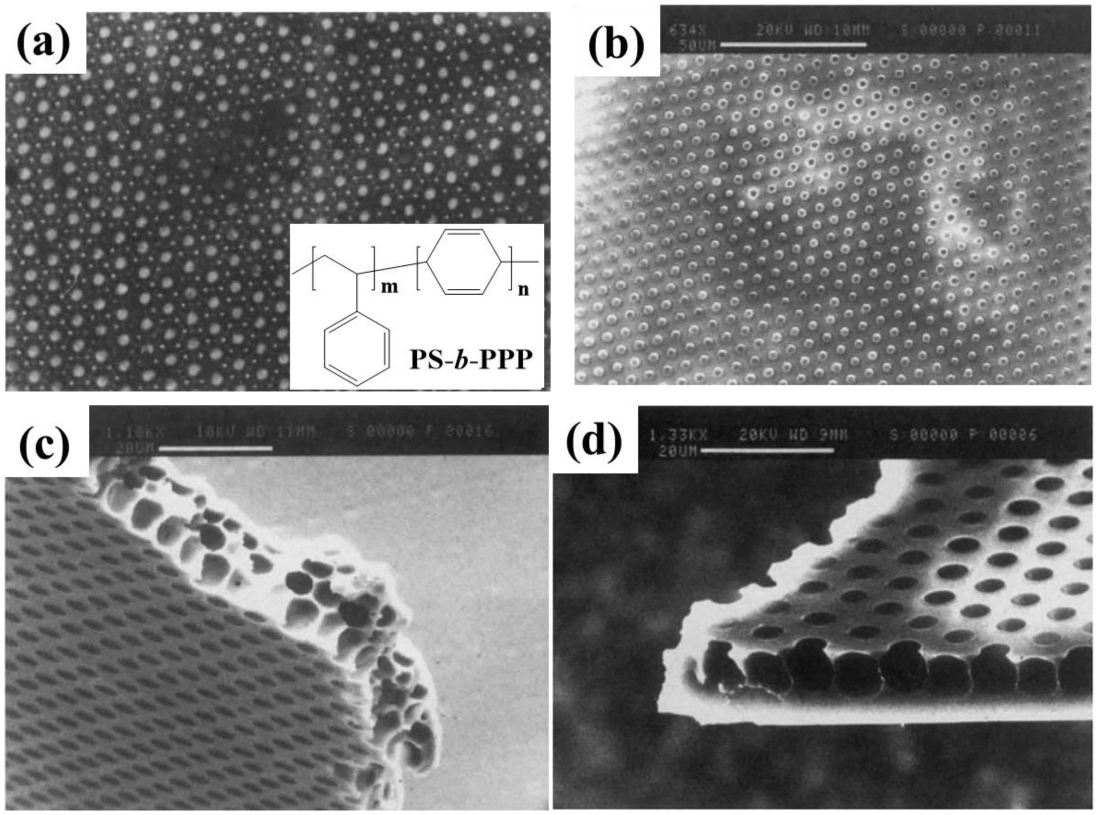

Figure 2. 11 (a) OM and (b)-(d) SEM images of honeycomb porous PS-*b*-PPP films with different pore layers: (a) and (b) top views, (c) and (d) cross-sectional views. The inset is the chemical structure of PS-*b*-PPP[100]

Soon after the inspired work of François et al, several other research groups successively reported the typical honeycomb porous films with more different polymers and solvents by the same method of casting polymer solution on substrate under humidity flow.[104,105] For example, Srinivasarao et al found that honeycomb porous films with three-dimensionally (3D), highly ordered arrays can be prepared in larger scale based on a PS with one end terminated by a carboxylic acid group (PS-COOH). The ordered microstructures were not only observed on the film surface (Fig. 2.12a) but also throughout the film thickness (Fig. 2.12b). Srinivasarao et al believed that the 3D ordered microporous arrays were the results of BFs on the surface of the polymer solution, where water droplets play a key role in templating.[106] This was confirmed by their later studies on directly observing the formation of BFs on the surface of polymer solution. Therefore, such pore arrays templated from the water droplet arrays of BFs were named breath figure arrays (BFAs) by researchers. The microstructured films were called BFA films. And the process of generating BFs for templating fabrication of porous films were defined as the BF technique.[7,8,11]

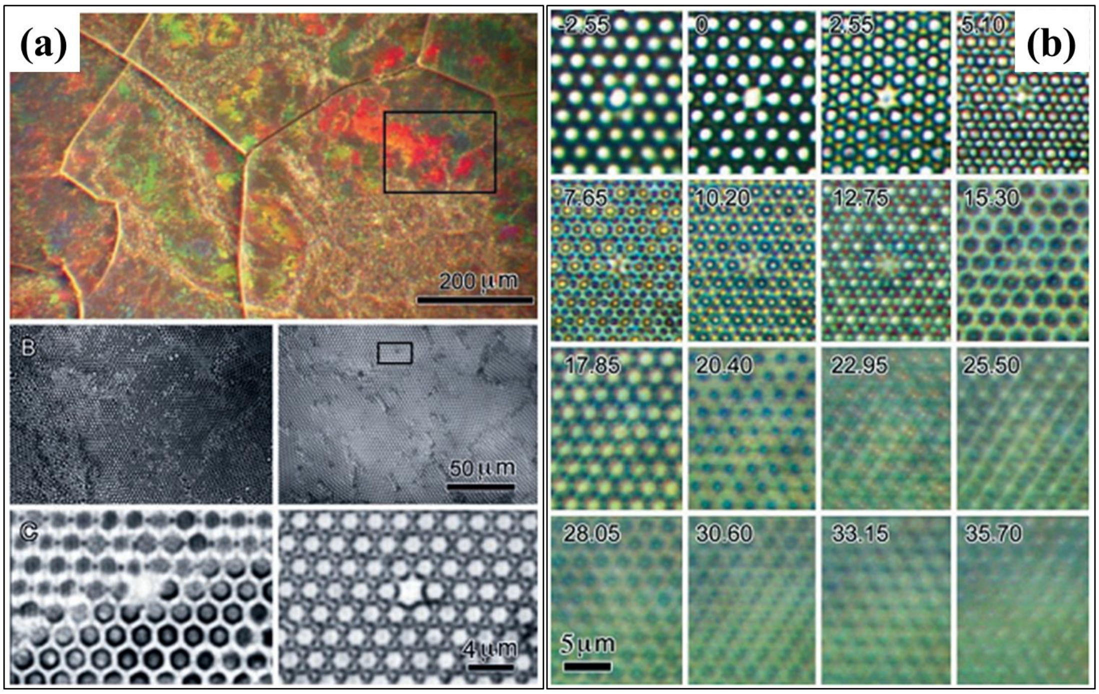

Figure 2. 12 Optical images of honeycomb films with three-dimensionally, highly ordered pore arrays at different (a) magnifications and (b) depths of focus, respectively[106]

BFs are natural and excellent templates for the porous microstructures of polymers and other materials. In comparison to conventional templates, such as patterned solid molds and sacrificial templates involving block copolymer self-assembly and polymer/silica colloidal particles, BFs templates possess following advantages and characteristics:

(a) The droplet size of BFs is adjustable. From dozens of nanometer nuclei to several millimeter droplets, BFs theoretically can act as templates for porous structures with an adjustable size ranging over six orders of magnitude.

(b) The whole formation process of BFs is spontaneous. Specifically, the nucleation, growth, rearrangement (self-organization or self-assembly) and evaporation (removal) of BFs are spontaneous. This avoids complicated work on the preparation of templates and post-treatment of removing templates.

(c) The templating medium, water, is nontoxic, abundant, recyclable, and facilely available.

A typical BF process is just simply to spread a given amount of solution containing desired film-forming materials on a target surface under a humid environment. Therefore, compared with other strategies involving both top-down techniques (e.g. direct writing, imprinting, photo/plasma lithography and chemical etching) and bottom-up strategies (such as BCP self-assembly and emulsions), the BF technique has also following advantages:

(d) Simple. The operation procedures ranging from dissolving polymers, casting solution to drying films are conventional and simple, which can be simply performed at ambient temperatures and pressures.

(e) Time-saving. The one-step BF process ranges from dozens of second to several minutes, depending on the evaporation rate of used solvent.

(f) Low-cost. The humid environment can be easily generated by saturating a sealed cell with liquid water or bubbling the water in a flask with airflow. Therefore, the required apparatuses such as vessel, tube, thermometer, hygrometer and flowmeter are commercially available and very economical. Moreover, because the BF technique is a spontaneous process, the operation cost such as electricity consumption is also very low.

(g) Easily-scalable. The area of films can be facilely tailored by the used substrates and cast volume of solution. The production rate of BFAs can be rapidly accelerated by simply increasing the BF sites in a single batch.

(h) Non-destructive. Different from most bottom-top and top-down techniques involving a destructive process to remove redundant portion for porous microstructures physically or chemically, the BF strategy is a completely non-destructive technique of using film-forming materials as molecule/nanoscale bricks for self-assembling along the BFs templates.

2.2.2.2 Formation mechanism of BFAs

General formation mechanism of BFAs

In comparison to simple condensation of BFs from water vapor on a relatively cold surface mentioned in previous section 2.1, the formation of BFAs involves two more variables: solvent and solute (mainly polymers). This results in much more complicated transfers of heat and mass at the interfaces among water, solvent and polymer. Therefore, behind the simple operation and procedures, the formation mechanism of BFAs is actually very complex. It can be regarded as the result of three mutually interactive and restrictive processes of (I) evaporation of solvent, (II) formation of BFs involving the nucleation and growth of water droplets, and (III) self-assembly of polymers with BFs as templates involving molecule aggregation, precipitation and gelation, as shown in Fig. 2.13.

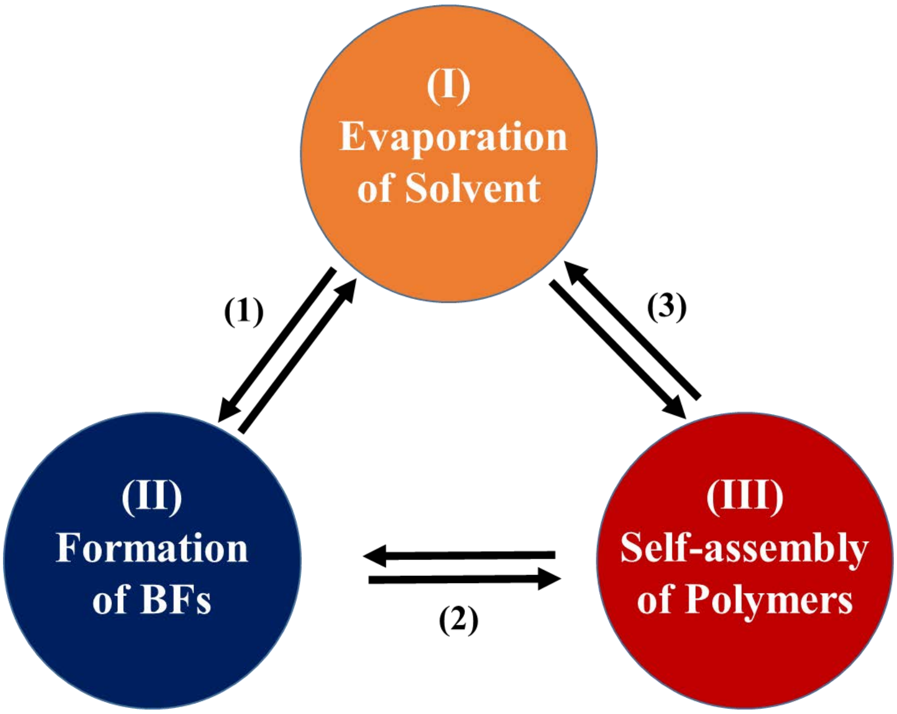

Figure 2. 13 Schematic of the relationships of (I) evaporation of solvent, (II) formation of BFs, and (III) self-assembly of polymers

Specifically, their mutual interactions and restrictions mainly include the following points with respect to Fig. 2.13:

(1) The evaporation of solvent cools down the surface of polymer solution, leading to the nucleation and growth of water droplets to form BFs; while the increasing surface coverage of BFs may decrease the evaporation rate of solvent.

(2) The condensed water is a non-solvent for polymers, which induces the collapse

and precipitation of polymer chains at the water/solution surface with BFs as templates; while the precipitation of polymers can form a polymer protective layer to prevent the water droplets from coalescence, thereby slowing the growth rate of water droplets.

(3) The dissolved polymers have an influence of reducing the evaporation rate of solvent; while the reduction of solvent will increase the solution viscosity, inhibit the movement of polymer chains and accelerate the gelation phenomenon.

Therefore, the BF technique for the formation of BFAs actually involves many complex thermodynamic and kinetic underpinnings that need to be fully understood.

Besides the three basic variables of solvent, solute (mainly polymers) and nonsolvent (typically water), many derivative variables such as solution concentration, humidity, temperature, pressure, flow velocity, and substrate types, also have important influences on the formation process of BFs on the surface of polymer solution.[7,9,10,12,14,15] Theoretically, any factors that can affect the formation of BFs have a certain effect on the final microstructures of BFAs. So far, through adjusting these variables, BFA films with different regularity and various pore shape, size, distance and layers have been reported in the past two decades. The essence of forming BFAs by the BF technique can be briefly summarized as to construct a cold solution surface for the condensation of water droplets from a humid atmosphere by the use of easily volatile solvent. However, it should be kept in mind that currently there is still no universal mechanism applicable for all reported BFAs. The exact mechanism of BFA formation is greatly dependent on the specific experimental conditions of the BF process.

To form highly ordered BFAs, there are some important empirical laws for the choice of solvents and film-forming materials based on the published data: (a) using low-boiling-point and high-vapor-pressure solvent that is completely or highly immiscible with water, such as carbon disulfide (CS_2)[107] and chloroform ($CHCl_3$),[108] and (b) Using solvent-dissolvable film-forming materials that can well precipitate in water, such as star polymers[109] and amphiphilic block copolymers.[110] When casting such solutions with an optimal concentration on a solvent-wettable surface under a high-humidity environment (generally RH > 70%) at an appropriate temperature (typically ambient temperature), continuous films with highly regular and ordered BFAs can be usually obtained after complete evaporation of solvent and water, as shown in Fig. 2.14.[9] During such an entire BF process, it is generally accepted that the following procedures and phenomena will be involved:

(1) Nucleation of BFs by evaporative cooling, producing random and small water droplets on the surface of solution film.

(2) Growth and self-assembly of BFs, leading to the formation of single or multiple layers of ordered and closely packed water droplet arrays on the entire solution film. Polymer precipitation occurs at the water /solution interface, which play a key role in preventing the coalescence of water droplets.

(3) Evaporation of solvent and water droplets, leaving a highly ordered BFA film on the substrate. This is usually carried out after the gelation of polymer solution, which indicates the termination point of effective growth and self-assembly of BFs.

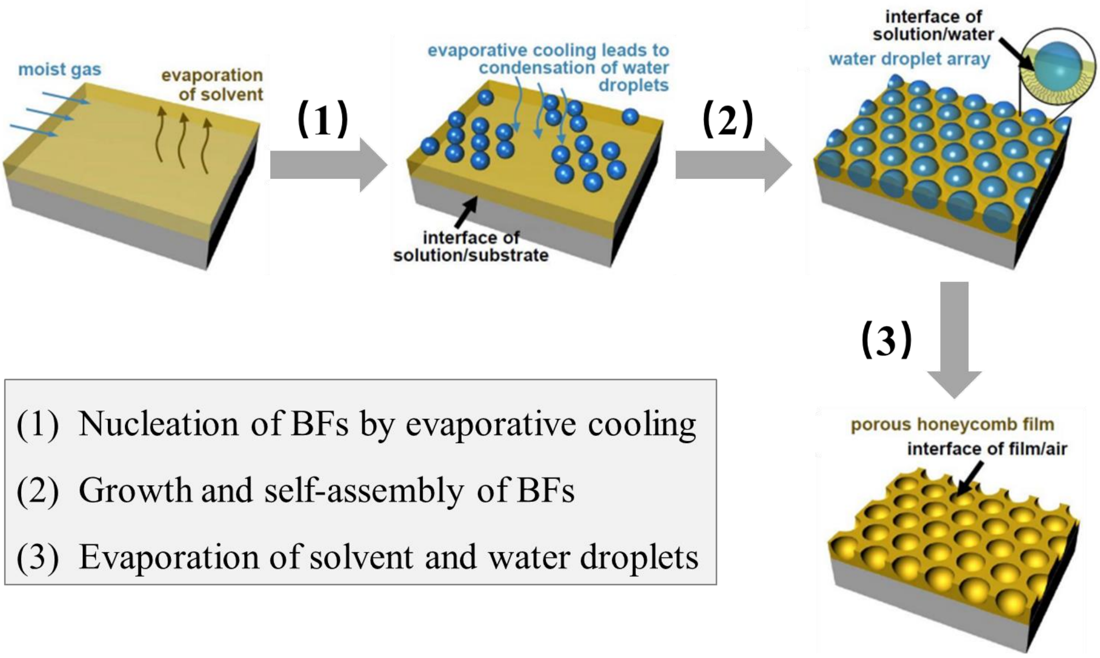

Figure 2. 14 Schematic diagram of general formation mechanism of highly ordered BFAs[9]

Nucleation of BFs by evaporation cooling

For a droplet of polymer solution cast on a solid substrate under a saturated humidity environment (Fig. 2.15), the vapor pressure of solvent close to the solution liquid surface (P_{sl}) is much higher than the vapor pressure of solvent in saturated humidity environment (P_{sv}). Therefore, the solvent would immediately evaporate to reach an equilibrium as closely as possible. Due to the enthalpy of vaporization, the temperature of solvent vapor (T_{sv}) close to the solution surface will drop, thereby playing a role of cooling down the surface of polymer solution.

During this process, the temperature and pressure variation of solvent can be described by the following Clausius–Clapeyron equation[111]

$$In\frac{P_{sl}}{P_{sv}} = -\frac{\Delta\mathrm{H}_{vap}}{R}\left(\frac{1}{T_{sl}} - \frac{1}{T_{sv}}\right) \tag{2.8}$$

Where P_{sl} and T_{sl} are the vapor pressure and temperature close to solution surface, respectively. And P_{sv} and T_{sv} are the vapor pressure and temperature of solvent in saturated vapor environment, respectively. ΔH_{vap} is the enthalpy of vaporization, and R is the universal gas constant.

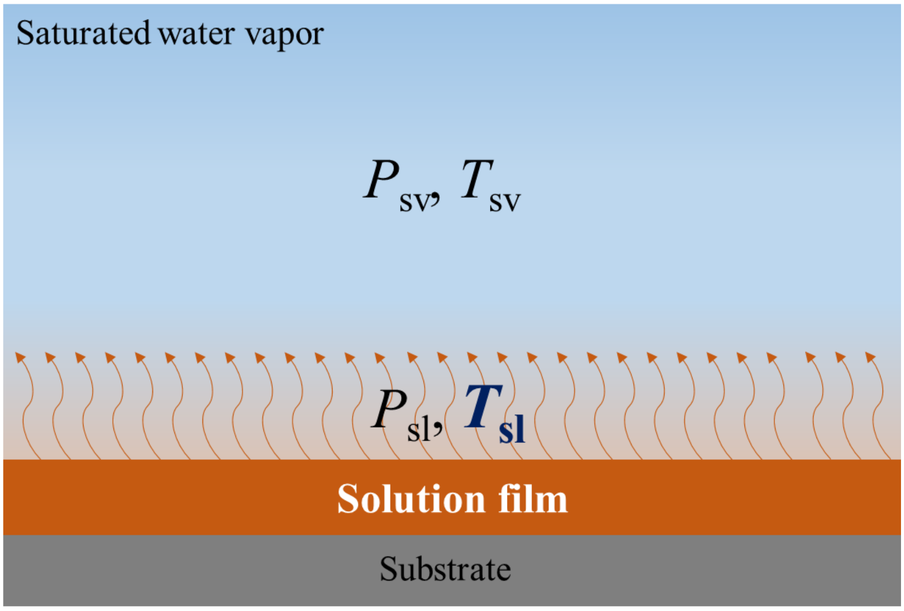

Figure 2. 15 Schematic diagram of solvent evaporated in a saturated humidity environment after casting a droplet of polymer solution on the substrate

If the saturated humidity is generated by a constant humid flow in an open environment, P_{sv} at ambient temperature can be regarded as a small constant. The vapor pressure difference will always drive the solvent to escape from its solution. Based on Eq. 2.8, the higher vapor pressure of solvent is, the colder the solution surface will be. For examples, carbon disulfide (CS_2) and chloroform ($CHCl_3$) are two of most frequently-used solvents to dissolve polymers. Through the evaporation of $CHCl_3$, it was reported that the temperature of its solution film can fall to 0 - 6°C.[108] And the temperature of CS_2 solution surface could reach at -6 °C owing to its higher vapor pressure.[112] Battenbo et al confirmed these results by directly monitoring the temperature variation during the evaporation process of pure solvent.[113] As shown in Fig. 2.16a and b, an obvious sharp decrease of temperature is observed immediately once either CS_2 or $CHCl_3$ begins to evaporate.

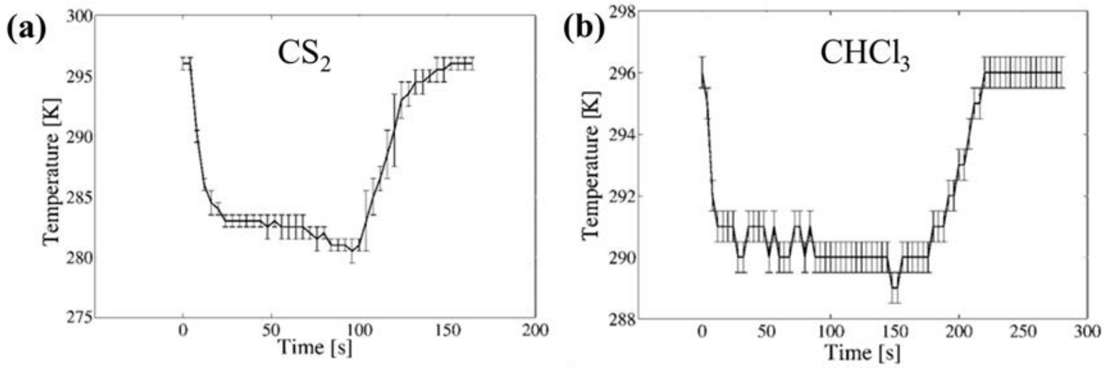

Figure 2. 16 Temperature variations during the evaporation process of 0.05 mL (a) CS_2 and (b) $CHCl_3$ in a dry environment respectively[113]

Considering that the formation process of BFAs is often performed at ambient temperature (about 25 °C) and T_{sv} can be regarded as equal to the ambient temperature, a temperature difference of up to 30 °C can be created upon the solution surface by the evaporation of solvent. This greatly exceeds the required temperature difference for heterogeneous nucleation of BFs.[75,82] Therefore, it is theoretically feasible for the nucleation and condensation of BFs by the evaporation of solvent. Newby et al experimentally observed the formation process of highly ordered BFs on a substrate through evaporating a thin film of pure ethanol under a humid flow, as shown in Fig. 2.17a-d. With the evaporation of ethanol, the condensation, accumulation and detachment of water droplets were clearly observed near the receding contact line. This left highly and hexagonally ordered BFs on the substrate (Fig. 2.17e). Through tuning the surface wettability of substrate, they also obtained BFs with water droplets arranged in square arrays.[114,115] To further describe the evaporative cooling process, some researchers have developed several theoretical modes based on the experimental data.[113,116,117] However, they are quite different, which still cannot well describe the evaporation process of solvent generally.

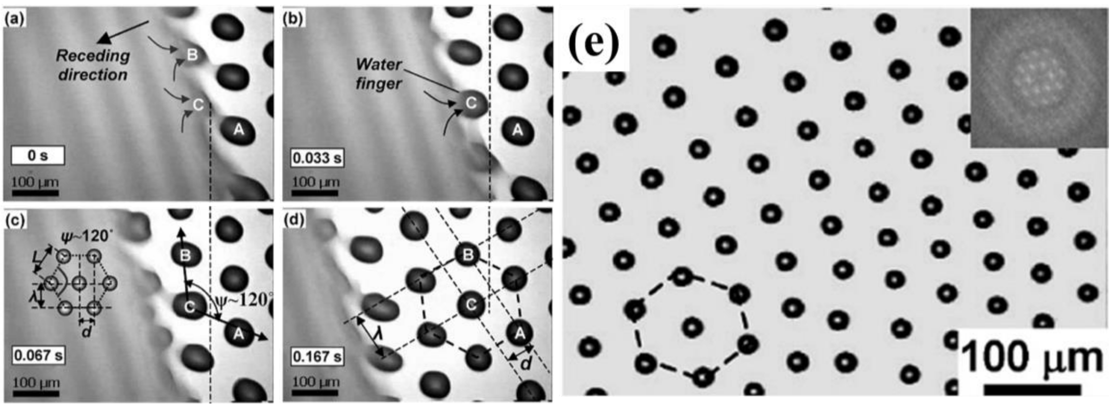

Figure 2. 17 Formation of hexagonally ordered BFs formed by the evaporation of pure ethanol under a humid airflow[115]

Growth and self-assembly of BFs

The surface of solution maintains the soft characteristic of pure liquid surface, which allows the mobility and rearrangement of water droplets. Besides the nucleation initiated by evaporative cooling, the growth of BFs is similar to the direct formation of BFs on a cold surface of oil as stated before. Srinivasarao et al. monitored the growth of BFs on the surface of monocarboxy terminated polystyrene (PS-COOH)/CS_2 solution by using a high speed micro-photographic technique. They successfully obtained the images of BFs growing at different stages, and observed the clear evolution of BFs from small isolated water droplets to ordered water droplet arrays with obviously increased size (Fig. 2.18, Frames #1-#5). However, different from the BFs directly growing on a cold oil surface reported by Beysens et al., no coalescence phenomenon was observed for these water arrays by further condensation. They finally self-organized as a monolayer of BFs with highly ordered hexagonal arrays (Fig. 2.18, Frame #6).[118] When using a solvent with a lower density than water to replace CS_2, such as benzene or toluene, the coalescence of water droplet arrays was still not observed. Instead, they sunk into the polymer solution. On their top surface, one or more layers of water droplets can be formed.[106]

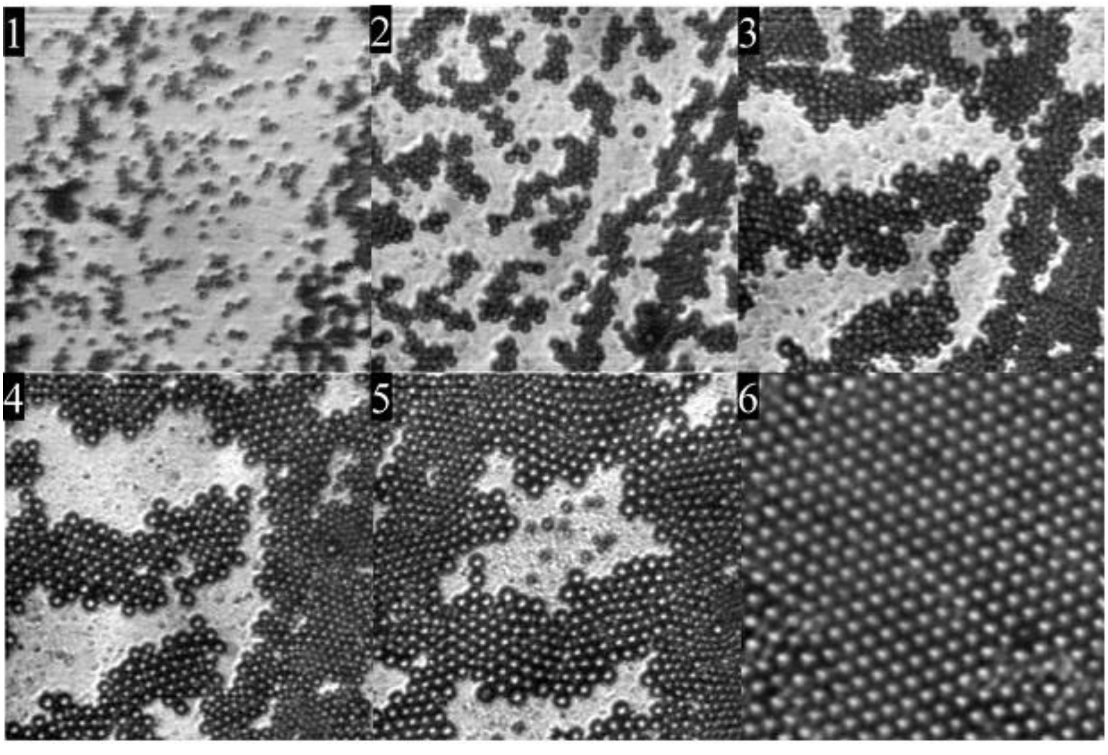

Figure 2. 18 The growth of BFs on the solution surface of carboxylate-terminated PS in CS_2 at different stages. The time interval of BFs evolved from frame #1 to frame #5 is about 50 seconds. The width of each square image is 180μm[118]

The growth of BFs on the surface of water-immiscible solution exhibits similar power laws with the direct growth of BFs on a cold liquid surface that is also immiscible with water. Pitois and François performed light-scattering experiments to monitor the growth process of BFs on the surface of PS-*b*-PPP/CS_2 solution. They found that the droplet grew slowly at the beginning, and then stably grew as $R \sim t^{0.35}$ after 3 s. This is very approachable to the power law of $R \sim t^{1/3}$ for BFs on pure oil as stated before. However, the growth law of $R \sim t$ was not identified by further condensation under the same conditions. This indicates that the water droplet arrays do not coalesce during the BF process, which well coincides with the results above. François et al. ascribed this particular behavior to the precipitation of the polymer along the interface of water and solution, which forms a layer of polymer to encapsulate the water droplets and effectively prevent their coalescence.[92] And through further designing an experiment of hanging a droplet of water in the PS-*b*-PPP/CS_2 solution with a syringe needle, they skillfully confirmed the presence of a polymer layer enveloping around the drop, as shown in Fig. 2.19a.[103] This is because water is completely immiscible with CS_2. When the condensed water comes into contact with polymer solution, based on the principle of minimum energy, polymer chains tend to aggregate at the water/solution interface to alleviate the produced interfacial tension. Besides, water is a nonsolvent for most polymers. It contributes to inducing the extended polymers in good solvent to become compact and collapsed, and finally precipitate at the interface of water and solution. Based on the use of a polymer bearing aggregation-induced-emission moieties as film-forming material, Qin et al monitored the BF process by a fluorescence microscopy, and directly observed the water droplet arrays encapsulated with a polymer film (Fig. 2.19b).[119] Therefore, the formation of polymer at the water/solution interface during the BF process does play a role in stabilizing the water droplets from coalescence.

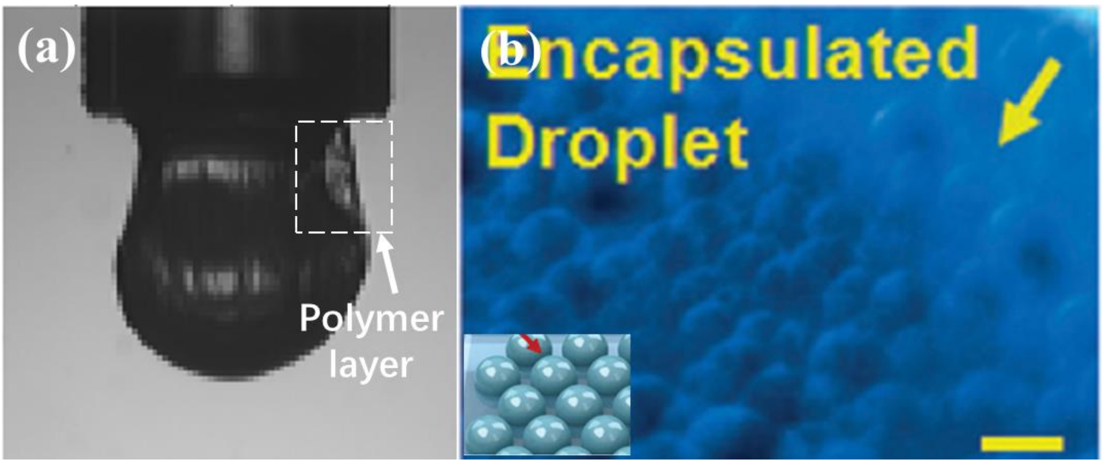

Figure 2. 19 Direct evidence of water droplets encapsulated by polymer layer. (a) Digital photograph of a water droplet in PS-*b*-PPP solution in CS_2, [103] (b) Fluorescence microscopy image of encapsulated droplets during the BF process[119]

The regularity of water droplets is not high during the growth process, which can be due to the random nucleation initially. Finally, monolayer or multilayer of water droplet arrays with highly hexagonal order can be formed regardless of the solution density. This indicates that, to form hexagonally ordered BFs, the condensed water droplets undergo a self-assembling process. But how do the water droplets move and assemble spontaneously? For water droplets condensed on a liquid surface, they would be immediately acted by buoyancy, gravity and surface tension. Beysens suggested that the rearrangement of water droplets can be ascribed to the deformation of liquid surfaces because it can produce elastic attractive forces for long-range interactions between the droplets.[75] However, this cannot fully explain the formation of three-dimensional water droplet arrays. Besides, the experiments of Qin et al also revealed that the protective layer of polymer is formed after the formation of water droplets. These indicate that there are more complicated forces generated during the BF process to drive the water droplets to keep apart and movable. Actually, they do exist, and are believed to be Marangoni convection and thermocapillary effect by most researchers.[7-10,13-15,114] In the case of a volatile solution film on a substrate, because of the evaporation on the surface, the solution surface is undoubtedly colder than any other film regions. And due to the different evaporation rates near the contact line and near the center of the drop, a temperature gradient can be created along both the perpendicular and parallel directions to the surface of liquid. Owing to the temperature-dependent characteristic of surface tension, this will lead to a surface tension gradient in the corresponding direction, thereby leading to Marangoni convection instability and thermocapillary-convection instability, respectively.[120-122] Therefore, as shown in Fig. 2.20, the water droplets condensed on the solution surface can be driven to move horizontally by thermocapillary or drawn into the solution by Marangoni convection. The horizontal motion, coupled with a thin film of air among the water droplets that act as a lubricating role, can effectively suppress the coalescence of neighboring water droplets. When the non-coalescence water droplets are close enough, they can be arranged in order by capillary interactions. Therefore, combining with the long-range interactions caused by the deformation of liquid surface, BFs consisted of larger area ordered water droplet arrays can be obtained. In addition, if the generated Marangoni convection is strong enough, the water droplet arrays floating on the surface of the solution can be drawn into the solution, leading to the formation of multilayered BFs.[8,104]

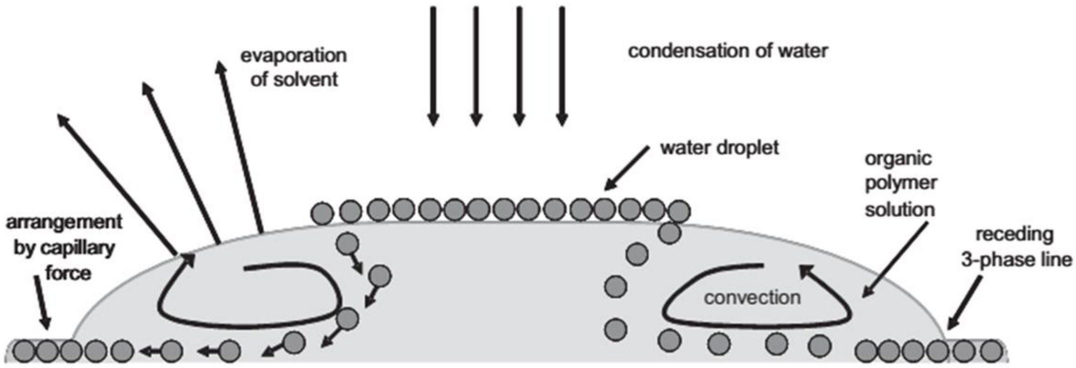

Figure 2. 20 Schematic of self-assembly mechanism of water droplets during the BF process[8]

Evaporation of solvent and water

Besides cooling down the solution surface and inducing the condensation of water droplets, the evaporation of solvent also rapidly increases the concentration of casting solution. This results in the rapid increase of solution viscosity correspondingly.[123] Some researches considered that physical gelation occurs when the solution concentration becomes high enough. The temperature decrease of film and nonsolvent-induced effect of water also have a certain influence on the gelation of polymer solution.[124,125] After gelation, it is difficult for the growth and movement of water droplets. If further condensation of water exists, it would have little influence on the final microstructures of BFAs. Unfortunately, there are few reports on detailed investigation of the physical gelation on the dimensional architectures of BFA films.

It has been confirmed that the evaporate rate of solvent shows a decreasing trend with the increase of solution concentration.[126-128] When the evaporative cooling of residual solvent cannot maintain a low temperature, the film will return to ambient temperature. Then the embedded water droplets will evaporate. This will result in bursting the top of the encapsulated polymer layers (Fig. 2.21).[119,129] After complete evaporation of solvent and water, only polymers are left on the substrate, displaying as a porous film. During the solidifying process, the positions of generated pore arrays should keep in accordance with those of water droplet arrays because of gelation. However, due to volume shrinkage, the pore size of BFAs will become larger than the droplet size of BFs.[129] And if the encapsulated polymer layer is not thick enough, burst in different directions can occur, thereby leading to the formation of interconnected pores.[119]

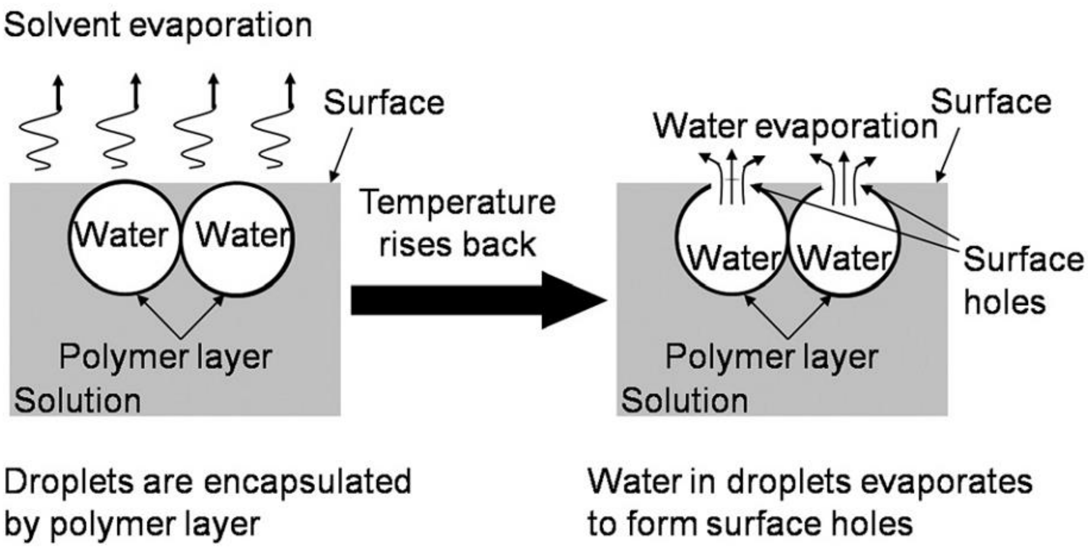

Figure 2. 21 Schematic of forming porous microstructures by the burst of encapsulated polymer layers[129]

2.2.3 Development of BF techniques and BFAs

The BF techniques have been boomingly developed recently as one of the most promising strategy for the fabrication of porous films with adjustable regularity, pore size, pore distances, pore layers and even pore shapes on desired substrates to meet different applications based on any film-forming materials that can be well dissolved/dispersed in volatile solvents. The development in BF techniques and BFAs can be further subdivided in to five aspects: (1) modification of BF techniques, (2) film-forming materials, (3) morphology control, (4) substrate types and (5) applications. This section mainly makes a brief review on the former four aspects, while the last aspect will be briefly reviewed in Section 2.3.

2.2.3.1 Modification of BF techniques

There have been various modified BF techniques for the preparation of BFA films. One of their general characters is to construct a humid environment for the evaporation of solution film on a desired substrate. Depending on the way of constructing humid atmosphere, the process can be divided into dynamic BF technique (Fig. 2.22a) and static BF technique (Fig. 2.22b), while based on the method of forming solution film, spin-coating assisted BF technique and dip-coating assisted BF technique have been developed to meet different requirements of applications.[7] For the former two BF techniques, the solution film is usually formed by spontaneous spreading on the substrate.

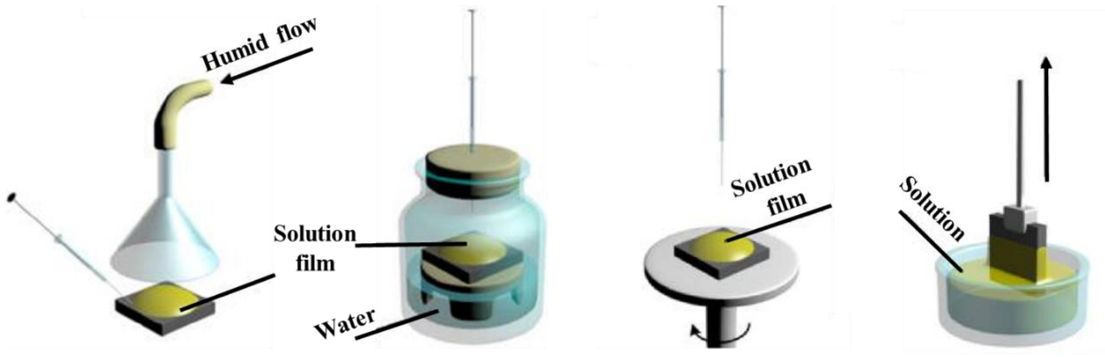

(a) Dynamic **(b)** Static **(c)** Spinning **(d)** Dip-coating

Figure 2. 22 Schematic diagram of forming BFA films by different BF techniques, (a) dynamic BF technique, (b) static BF technique), (c) spinning-coating assisted BF technique, and (d) dip-coating assisted BF technique

The dynamic BF technique is the most widely used strategy for fabrication of BFA films, which is also the first BF method reported by François et al.[100] This name originates from the character of generating a humid environment by a humid airflow. The humid airflow can be simply generated by bubbling air through a water-filled flask and introduced over a solution film on a solid substrate with a conical funnel as nozzle (Fig. 2.22a). During the dynamic process, the velocity, humidity, outlet angle and distance of airflow can be finely adjusted to control the evaporation rate of solvent, condensation of BFs, and thereby final morphology of BFAs.[130]

The static BF technique is often performed in a sealed cell filled with some water liquid (Fig. 2.22b). Obviously, the humid atmosphere is dependent on the saturation of water vapor. And its humidity can be tuned by the addition of inorganic salts in water. During the BF process, the substrate is usually placed on the sealed cell beforehand. After reaching at equilibrium, the polymer solution is then injected onto the substrate through a syringe. Because there is no disturbance caused by the airflow, the static BF technique possesses good experimental repeatability, and is very suitable for studying the mechanism of BFA formation. It also shows a better performance on the fabrication of highly ordered BFA films than the dynamic BF technique. For example, linear PS homopolymer without the polar end group is usually considered as an undesirable film-forming material by the dynamic BF technique, while it was successfully employed for the formation of highly and hexagonally ordered BFAs by the static BF technique (Fig. 2.23).[131] Moreover, the static BF technique may also contribute to the preparation of BFA films with few cracks.[132] This can be ascribed to the evaporated solvent that is constrained in the sealed cell. The solvent vapor assists the residual solvent to play a plasticization role in the polymer film to alleviate the possible internal stress generated during the drying process.[132]

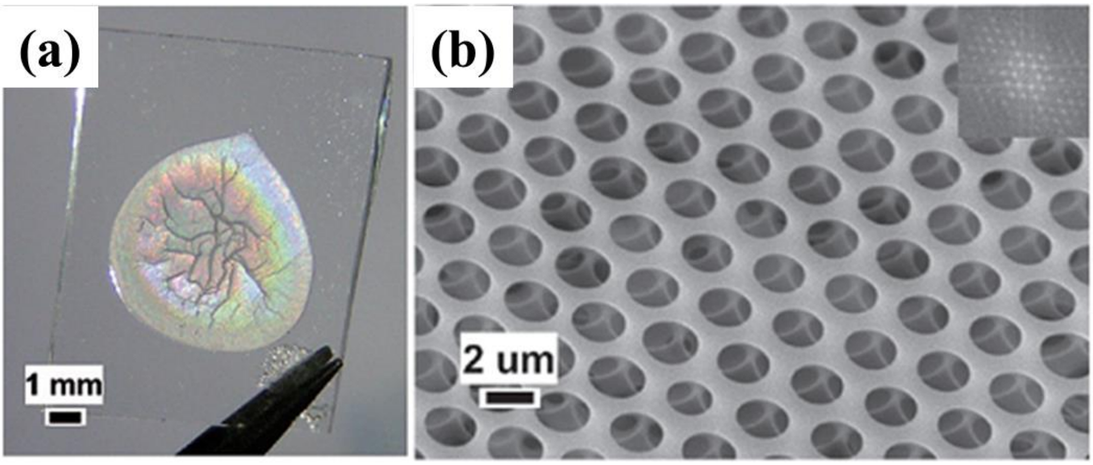

Figure 2. 23 Highly ordered BFA films prepared from a non-polar linear PS homopolymer by the static BF technique.[132] Because of the diffractive and interference effects, the film exhibits a beautiful nacre color in the sunlight

Spin-coating can quickly and easily form a uniform thin film on a planar substrate by centrifugal force (Fig. 2.22c). Through controlling the solution concentration and spinning rate, the film thickness can be controlled between a few nanometers and a few micrometers. Kim et al. firstly employed this technique for assisting cellulose acetate butyrate in mixed solvent of tetrahydrofuran (THF) and $CHCl_3$ to spread on the substrate at 1000 rpm during the BF process.[133,134] The resultant BFA films can be conveniently prepared in large area, but they were obviously less regular than those prepared by conventional BF technique. Increasing the spinning rate can effectively decrease the evaporation time of solution, which correspondingly shortens the growth time of BFs. This can lead to the preparation of BFA films with much smaller pore size. Munoz-Bonilla et al. prepared BFA films *via* spinning-coating block copolymer/homopolymer solution with different concentrations at 4000 rpm. As shown in Fig. 2.24a-d, although the resultant BFAs are irregular and disordered, and their pore sizes are obviously decreased to 100 nm ~ 300 nm. The pore size of BFA films basically shows an increasing trend with the increase of solution concentration (Fig. 2.24e).[135]

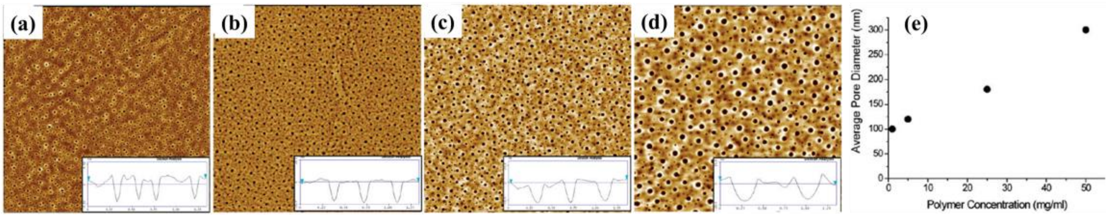

Figure 2. 24 Various BFA films of block copolymer/homopolymer blends prepared by spin-coating assisted BF technique from different solution concentrations, (a)-(d) AFM topography images and cross sections (insets) at different solution concentrations, and (e) the correspondingly plot of average pore diameter with respect to the solution concentration[135]

Dip-coating is a simple old way of introducing materials onto the surface of substrate that do not require sophisticated facilities. It can be applicable for various substrates with different materials, flexibilities and surface morphologies. The dip coating of a substrate can be simply inserted into the solution firstly and then removed (Fig. 2.22d). When the substrate is long and flexible, such as fabric, the dip-coating can also be performed as a continuous roll-to-roll process. The thickness of coating is dependent on the competition among viscosity, wettability and gravity[136], which can be controlled by adjusting the solution concentration, withdrawal speed and holding time. Mansouri et al demonstrated that dip coating can be well incorporated into the BF process for the fabrication of BFA films on the substrate with complex surfaces.[137] They firstly immersed a nylon mesh in the polysulfone/dichloromethane (CH_2Cl_2) solution and held for a given period of time. The mesh substrate was then withdrawn upward with a control speed, and finally drained under a high humidity environment. This allows the formation of BFs on the liquid coating, thereby leading to the templating formation of BFAs with open channels. This work well demonstrated the application of BF technique on the flexible fabric substrate with complex surfaces. Unfortunately, there are no more reports on further study, although it may lead to a brand-new class of textile composites that possess both the multifunctional properties of introduced materials, excellent properties (such as breathability and flexibility) and unique texture features of fabrics.

2.2.3.2 BFA Film-forming materials

With the development of BF techniques, the reported film-forming materials have been greatly expanded over the past two decades from polymeric materials involving linear homopolymers, linear copolymers, branched polymers to non-polymeric materials involving carbon nanomaterials, inorganic nanomaterials and small molecules, as shown in Fig. 2.25. Theoretically, any materials that can (1) be dissolved or dispersed in a solvent and (2) stabilize the water droplet arrays can be used for the production of BFAs.

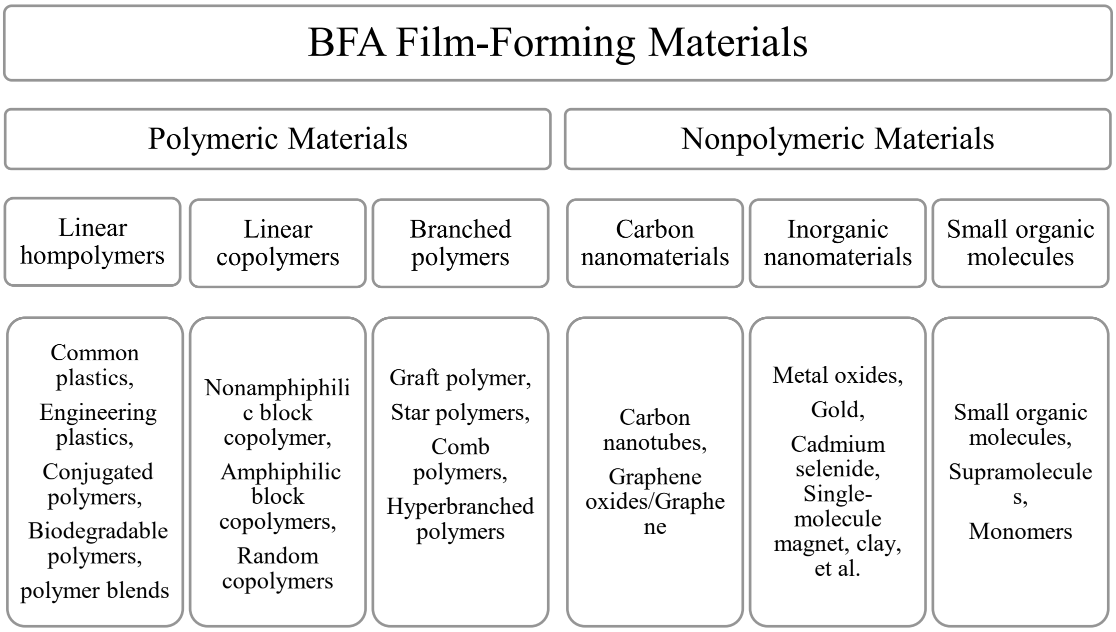

Figure 2. 25 The types of film-forming materials reported by the BF techniques for the production of BFAs

Polymeric materials

Fig. 2.26 schematically illustrates seven different main topographical morphologies of polymers reported for the fabrication of BFA films. They are linear polymers including homopolymer (Fig. 2.26a), lock copolymer (Fig. 2.26b) and random copolymer (Fig. 2.26c), and branched polymers including graft polymer (Fig. 2.26d), star polymer (Fig. 2.26e), comb polymer (Fig. 2.26f) and hyperbranched polymer (Fig. 2.26g), respectively.[35]

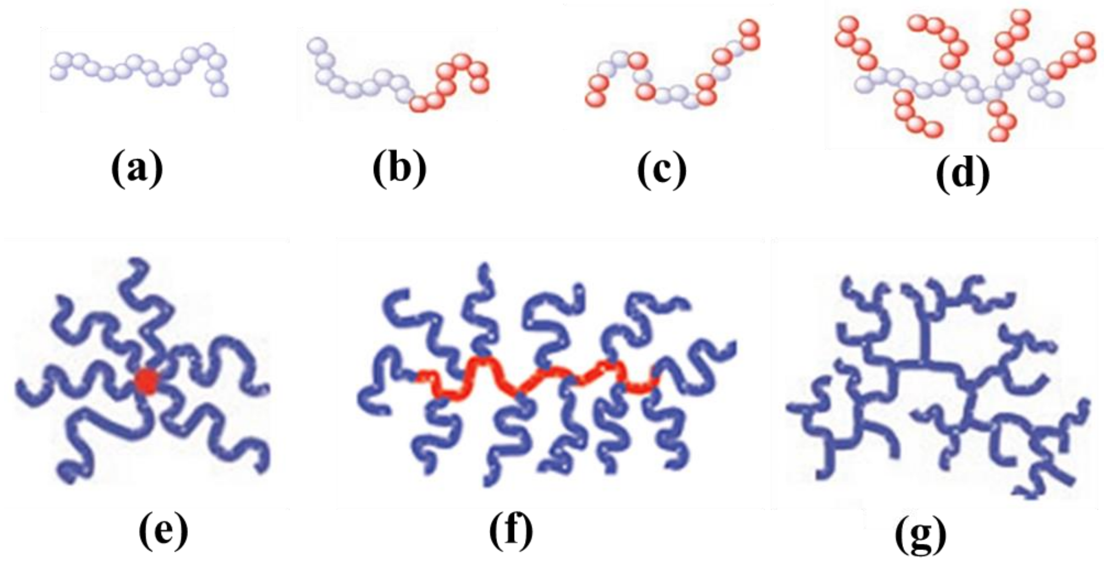

Figure 2. 26 Schematic diagram of polymers with different topographical morphologies for the fabrication of BFA films, (a) linear homopolymer, (b) linear block copolymer, (c) linear random copolymer, (d) graft polymer, (e) star polymer, (f) comb polymer and (g) hyperbranched polymer[35]

PS terminated with different functional groups and PS derivatives (such as polystyrenesulfonate) are the most widely used linear homopolymers for the preparation of BFAs owing to their easy availability in synthesis and modification.[138-141] Other common plastics including poly(methyl methacrylate),[142] polyvinyl chloride[143] and poly(1,2-butadiene)[144] and PDMS[145] have also been used to prepare BFA films. These films often require further chemical modification, such as cross-linking, to have better heat endurance, chemical resistance and/or mechanical properties. An alternative strategy is to employ engineering plastics as film-forming materials, such as polycarbonate,[146] poly(ether ether ketone),[147] polyimide,[148] poly(phenylene oxide)[149] and poly(ether sulfone).[150] Their resultant BFA films can be directly used for different applications under the rigorous conditions. The construction of BFA films with some special polymers has also been studied to meet the specific requirements in some special fields, such as conjugated polymers for optical and electrochemical devices[151-154] and biodegradable polymers for bioengineering applications. [155-158] The reported biodegradable homopolymers includes poly lactic acid,[155,156] poly(ε-caprolactone)[157] and poly(3-hydroxybutyrate).[158] In some cases, it is noted that the single use of some polymers is difficult to obtain ordered BFAs or desired performance. Therefore, polymer blends composed of two or more polymer types are reported to facilitate the formation of BFA films with tailorable properties.[155,159] The exploration of effective additives for adjusting the interfacial tension of water and solution during the BF process is also an alternative to improve the film-forming ability of brick materials for more ordered BFAs. Various homopolymers,[160] amphiphilic block copolymers,[161] dendritic amphiphiles,[162] and short chain surfactants[163] with different hydrophile-lipophile balance (HLB) values have been demonstrated to be useful additives for some specific polymers. However, there are still no universal additives found for different common polymers to prepare highly ordered BFAs by the BF technique.

Both well-defined block copolymers (BCPs) and random copolymers [164,165] have been employed to prepare BFA films by the BF techniques. Compare with linear homopolymers, linear copolymers particularly for BCPs can lead to the formation of ordered BFAs more easily. This can be ascribed to their unique self-assembling behavior in solutions and at water/ solution interface, which contributes to good stabilization of the water droplet arrays.[166,167] BCPs can be further divided into nonamphiphilic and amphiphilic BCPs. Typical nonamphiphilic BCPs used for the fabrication of BFA films include PS-*b*-PPP,[100] PS-*b*-PDMS,[168] polymethylene-*b*-PS[169] and PS-*b*-poly(methacrylates) series[170] and PS-b-poly(acrylates) series.[171,172] Amphiphilic BCPs are larger class of BFA film-forming materials because they can stabilize the water droplets more effectively than nonamphiphilic BCPs through the specific adsorption at the interfaces owing to the surface activity. Examples range from typical amphiphilic PS-*b*-poly(acrylic acid),[173] PS-*b*-poly(4-vinylpyridine),[174] PS-*b*-poly(N, N-dimethylaminoethyl methacrylate),[175] PS-*b*-poly(2-hydroxyethyl methacrylate),[176] PS-*b*-poly(2-vinylpyridine),[177] PS-*b*-poly-(N, N-dimethyl acrylamide),[178] PS-*b*-poly(ethylene oxide)[179] to thermo-responsive PS-*b*-poly(N-isopropyl acrylamide).[180] Besides PS-based BCPs, non-PS-containing BCPs can also be employed for the fabrication of BFA films, such as poly(N, N-dimethyl acrylamide)-*b*-poly(ethylene oxide).[181] Moreover, benefiting from the rapid development of controlled polymerization techniques, some BCPs containing unique blocks, such as conjugated polymers[182,183] and fluorinated polymers,[184,185] are also precisely synthesized and employed for the fabrication of BFA films with unique structures and functions.

The reported branched polymer for the fabrication of BFA films ranges from simple graft polymer,[186,187] star polymer,[188-191] comb polymer[192] to hyperbranched polymer.[193-195] Owing to the high segment density, branched polymers are usually good BFA film-forming materials because they can easily precipitate around the water droplets to play a stabilization role. Because of the easy polymerization of styrene by different means and good solubility of PS in common organic solvents, PS-based branched polymers are most commonly reported in the literature. Stenzel et al. synthesized a series of branched polymers with well-defined molecular weight and branching degrees based on living/controlled radical polymerization, and found that these branched polymers intended to form spherical micelles in solution.[196-201] All of them were successfully used for the preparation of BFA films. Moreover, they observed that increasing the arm number of star polymers can effectively decrease the pore size of BFA films. For example, 18-arm star PS can lead to form BFA film with the pore size of 250 nm, while under the same BF conditions, the resultant pore size of 5-arm star PS BFA film was approximately 800 nm.[201]

Nonpolymeric materials

The reported nonpolymeric materials for the fabrication of BFAs can be classified into three categories: carbon nanomaterials,[202-206] inorganic nanomaterials[207-215] and small organic molecules.[216-220] These kinds of materials usually possess unique catalytic, electric, thermal, photic, and/or bioactive properties. The porous microstructures of these nanomaterials can enhance their inherent properties and build a bridge to the macroscopic products.

Most small organic molecules are not suitable for the formation of BFAs because they cannot form self-supported and continuous films. A solution is to choose monomers that can be polymerized during the BF process as organic molecules, such as alkylcyanoacrylate[217] that can be polymerized by using water as initiator and acrylate/diacrylate mixtures[216] that can be initiated by UV irradiation. During the formation process of BFAs, the synthesis of polymers can occur simultaneously. Therefore, a solidified polymer BFA films can be finally produced after complete evaporation of water and solvent. Recently, a novel kind of supermolecules was also reported for the successful fabrication of BFAs without the need of chemical reaction. Such kind of small organic molecules can lead to form supermolecular polymers through the generation of reversible noncovalent interactions, such as hydrogen bonding, π-π packing and host-guest recognition.[219,220] For some special organic molecules that can directly form self-supported films after the evaporation of solvent, the crystallization phenomenon during the BF process is another challenging issue. Karthaus et al. found that this problem can be alleviated by the mixed use of metal complex with a cationic or anionic surfactant, and they successfully obtained ordered BFA films from small organic molecules.[218]

Different from the good dissolvability of polymeric materials and small organic molecules, both carbon nanomaterials and inorganic nanoparticles tend to precipitate in organic solvents rather than being dissolved. Therefore, to employ them as BFA film-forming materials, the preparation of their homogeneous dispersion in a volatile organic solvent is of critical importance.

Carbon nanotubes and graphene are two main kinds of carbon nanomaterials reported for the preparation of BFAs.[202-206] To obtain good dispersibility in an organic solvent, they usually require the assistance of organic ligands, surfactants or polymers. For examples, Takamori et al explored a lipid to assist the dispersion of shortened single-walled CNTs (SWCNTs) in $CHCl_3$, and first prepared SWCNTs/lipid conjugate BFAs by casting the resultant dispersion on substrates under high humidity environment. Then with an ion-exchange process, they successfully obtained pure CNT BFA films by the removal of lipids.[206] Lee et al. obtained graphene BFA films by developing a similar two-step strategy involving BF technique. They first improved the dispersibility of graphene oxide (GO) patelets in benzene by the graft polymerization of styrene monomer for the preparation of PS-grafted GO BFA films, and then obtained reduced GO BFAs by pyrolysis at high temperature.[205]

There have been different types of inorganic nanomaterials involving nanospheres, nanowires, nanorods and quantum dots used as nanoscale bricks for the fabrication of BFAs. The reported nanomaterials include metal oxides,[207] gold,[209,212,213,215] cadmium selenide,[208] single-molecule magnet,[214] clay,[211] and so on. Like carbon nanomaterials, most of them also require the addition of organic ligands or polymers to prepare homogeneous dispersion that can be cast by the BF techniques. Recently, Yabu et al. developed a general strategy for the creation of BFA films of organic nanoparticles based on a catechol copolymer of N-(3,4-dihydroxyphenethyl)methacrylamide and N-dodecylacrylamide.[207] They found that such copolymer can assist a variety of nanoparticles including SiO_2 (Fig. 2.27a), TiO_2 (Fig. 2.27d), Al_2O_3 (Fig. 2.27g) and ZnO (Fig. 2.27j) to homogeneously disperse in chloroform. After obtaining BFAs by the BF technique (Fig. 2.27b, e, h and k), all of them can lead to the formation of hierarchical porous microstructures composed of microscale pores and pure nanoparticles by the following sintering process, as shown in Fig. 2.27c, f, i and l, respectively.[207]

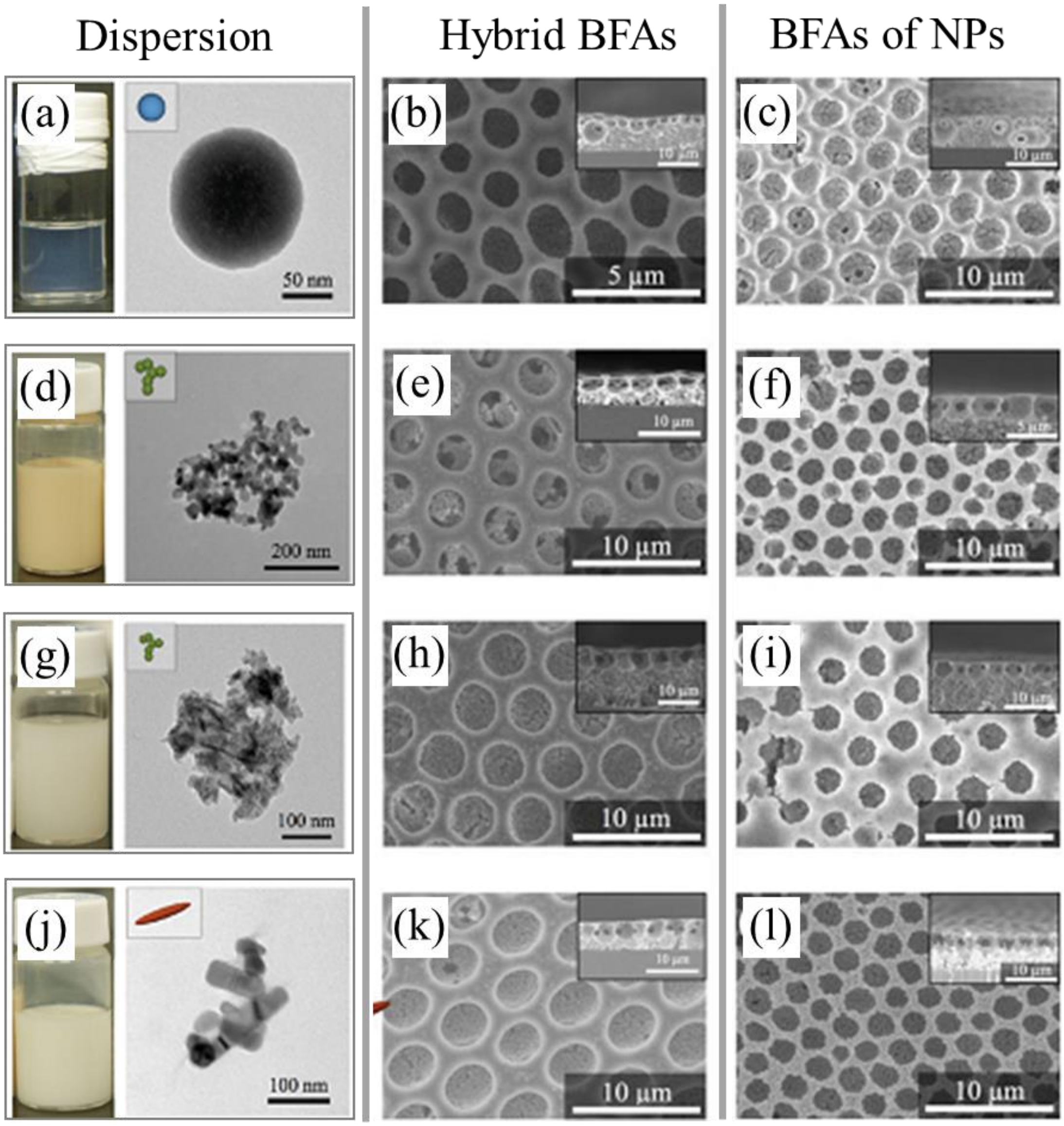

Figure 2. 27 Photographs and TEM images of different nanoparticle dispersions with the addition of a catechol-containing copolymer (a, d, g & j), and SEM images of resultant BFAs (b, e, h & k) before and (c, f, j & l) after sintering, (a)-(c) SiO_2, (d)-(f) TiO_2, (g)-(i) Al_2O_3, and (j)-(l) ZnO[207]

2.2.3.3 Morphology Control

Honeycomb porous microstructures or hexagonally ordered pore arrays are typical surface features for most BFA films. The control of their pore regularity, pore size, spacing between pores, and thickness of film has been widely studied by adjusting the experimental variables including solvents, solution concentration, humidity, gasflow velocity and temperature during the BF process. For example, the inherent properties of solvent, such as vapor pressure, boiling point, and the affinity with water, usually have an important influence on the pore regularity and shape of final films. Generally, the solvent with less water miscibility, low boiling point and high vapor pressure tends to form homogeneous and ordered BFAs.[221] The concentration of casting solution also has an obvious influence on the pore regularity. Neither too low nor too high solution concentration can lead to the formation of ordered BFAs. Besides, the pore size of BFA films is usually greatly dependent on the concentration of casting solution. Most reports showed that the pore size of BFA films generally has a decreasing trend with the increase of solution concentration.[222-225]

The distances between/among pores can also be finely adjusted. Thong et al. successfully obtained non-closely packed BFA films with different spacing distances through adjusting the temperature of solution during the process, as shown in Fig. 2.28. The spacing distance-to-pore size ratios of BFAs up to 12.44 can be prepared by this strategy.[226] This is because that the increase of solution temperature can accelerate the evaporation of both solvent and water droplets, which plays a role in controlling the in situ growth and shrinkage of the water droplet arrays during the BF process.

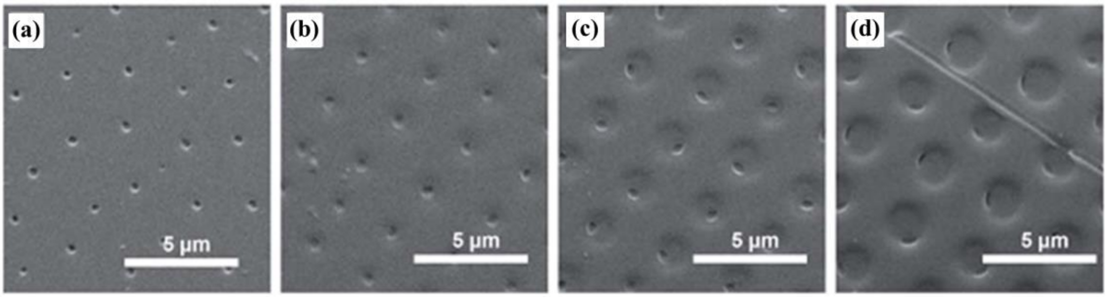

Figure 2. 28 BFA films with different spacing distances prepared *via* controlling the solution temperature during the BF process[226]

Due to the high surface tension of water, the condensed water droplets always tend to keep spherical shape during the BF process. This leads to the formation of 3D spherical pores in the films, which usually displays a honeycomb porous surface consisted of homogeneous and circular pores. However, the circular shape of pores can be transformed into different shapes by adjusting the experimental variables or post-treatment. For examples, Han et al. obtained ellipse pores with tunable aspect ratios through carefully controlling the direction and velocity of airflow during the dynamic BF process,[227] while Shimomura et al. developed a simple secondary processing method of mechanical stretching the hexagonally packed round pores and successfully obtained ordered square, rectangular, and triangular pore arrays by adjusting the stretching directions and stretching ratios.[228] Recently, Wang et al. developed a simpler and noncontact technique for directional photomanipulation of honeycomb pore arrays based on an azobenzene-containing block copolymer (Fig. 2.29a and b). The round pores can be directly converted to rectangular, rhombic, and parallelogram-shaped pores in the 30 min irradiation of linearly polarized light (Fig. 2.9c-e). They ascribed this to the anisotropic mass migration of the photo-reconfiguration of the azobenzene units. Interestingly, the pore transformation is reversible. The transformed pores can be recovered through rotating the sample by 90° for a secondary irradiation with an equal time interval.[229]

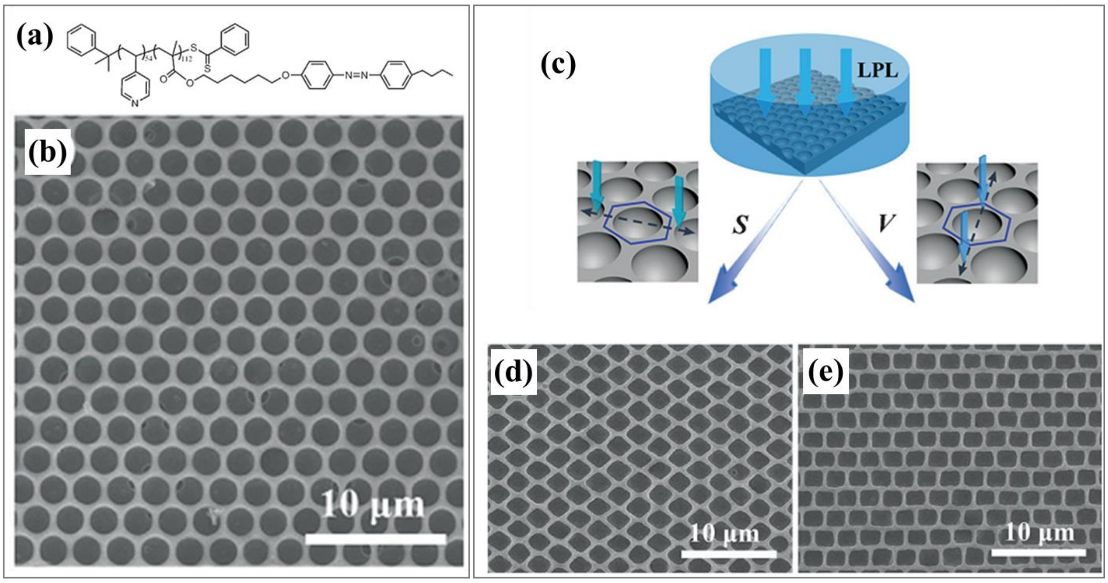

Figure 2. 29 (a) The chemical structure of the azobenzene-containing block copolymer and (b) its highly ordered round pore arrays without the light irradiation. (c) Schematic view of two types of polarization light irradiation in S and V direction, SEM images of ordered rhombic pore arrays along the S direction and rectangular pore arrays along the V direction with the polarization light irradiation for 30 min, respectively[229]

The pore shape of BFA films can also be controlled by adjusting the atmospheric solvent. Li et al. systematically investigated the pore structures of PS-*b*-PDMS films prepared by the BF technique under water, methanol and ethanol vapor respectively.[230] Aqueous BFs resulted in the formation of ordered BFAs consisted of spherical pores (Fig.2.30a and b), but honeycomb porous film with ellipsoid (Fig. 2.30c and d) and cylindrical (Fig. 2.30e and f) pores were prepared in ethanol vapor and methanol vapor, respectively. They first mainly ascribed these results to the decrease of the surface tension and evaporation enthalpy of the atmospheric solvent, which results in changing the shapes of liquid droplets and increasing their volume.[230] However, for most other film-forming materials, it is noted that microspheres with the size of hundreds of nanometers to several micrometers are usually formed by the BF technique in methanol techniques rather than ordered BFAs.[231-233] This indicates that film-forming materials also play a decisive role on the film morphology. Li et al further explained the formation of ordered BFAs in alcohol vapors by the preferential aggregation of low-surface-energy siloxane segments of PS-*b*-PDMS at the air/solution interface, which can effectively prevent the condensed alcohol BFs to spread on solution surface. And based on this more explicit formation mechanism, they successfully developed a genera modified BF process for successful preparation of similar BFAs of cylinder pores in methanol vapor with common polymers by the addition of a small amount of a surface-active agent to the casting solution, such as siloxane- and fluorine-containing BCPs.[234]

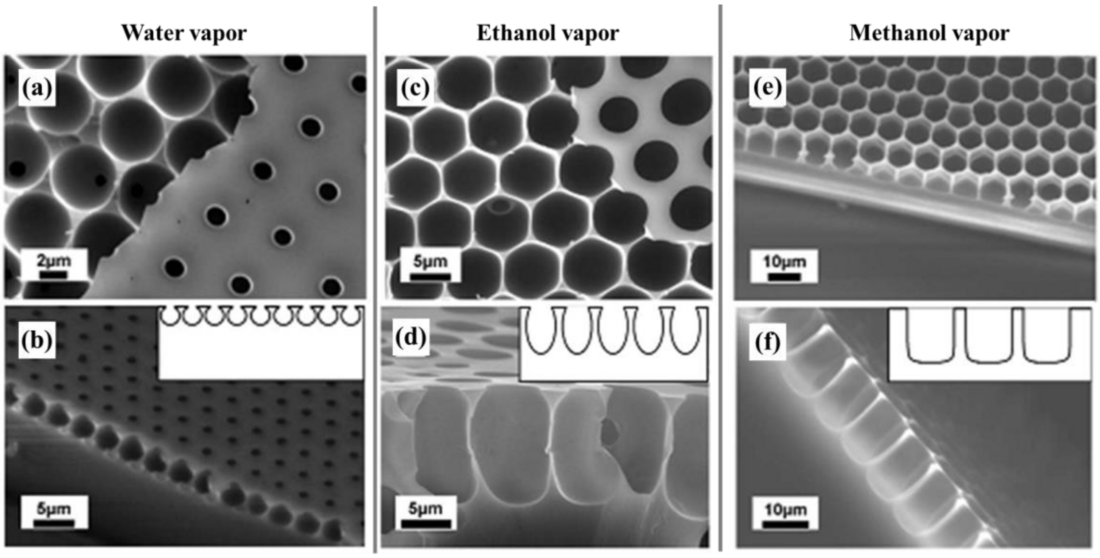

Figure 2. 30 SEM images of BFA films with different pore shapes prepared by the BF technique under (a and b) water vapor, (c and d) methanol vapor, and (e and f) ethanol vapor, respectively[230]

2.2.3.4 Types of Substrates

Substrate has a direct bearing on the final application of BFA films, which is a special and important factor of the BF process. It is speculated that the substrate does not directly contact the formation and assembly of condensed water droplets on the solution surface, but its surface morphology and properties greatly influence the spreading behavior of solution, thereby determine the final distribution density and area of films on substrates. Moreover, although it is still indistinct on how the substrate influences the formation of BFs, some research results evidently pointed out that the surface energy of planar substrate plays an important role on the formation of BFAs.[171,235-238] For example, the substrates on which solution can well spread tend to form BFA films with more ordered microstructures, while for substrates with low surface energy, ordered porous microstructures cannot be easily obtained, such as the difficult wettable fluorinated substrates.[235] In addition, because the BF process involves complex mass and heat transfer among polymer, solvent and water, the thermal conductivity of substrate actually has also an important influence on the final formation of BFAs.[239]

Most BFA films were constructed on solid substrates with a planar surface. The employed substrates can be inorganic materials, metal materials, and polymeric materials that cannot be dissolved by the solvent. Moreover, the surface of liquids can also be as substrates. For examples, through directly depositing a droplet of water-immiscible polymer solution on the water surface, the polymer solution can immediately spread as a thin liquid film for the formation of BFs. Shimomura and Parisi et al. successfully employed this strategy to obtain ordered BFA films.[240,241] Ma et al. further investigated the influence of liquid substrate types on the formation of BFAs, and found that the liquid substrate with higher surface tension and lower viscosity tended to form BFA films with smaller pores.[242] BF on the liquid substrate possesses the unique advantage of preparing freestanding BFA films. Hao and Wan et al. found that free-standing BFA films also can be prepared at an air/ice interface because the melted ice surface can lead to form a very thin film of water.[243,244] Moreover, the resultant BFAs of free-standing films were perforated (Fig. 2.31a-c). Wan et al. demonstrated that the high surface tension of water was essential for the formation of perforated BFAs. The thickness of polymer solution would become thinner than the size of water droplets with the evaporation of solvent (Fig. 2.31d). This resulted in the formation of a meniscus under the water droplet (Fig. 2.31e). During the evaporation process of water, a pressure difference across the meniscus was induced by the surface tension of water substrate. When it exceeds the critical pressure (Fig. 2.31f), perforated pores were generated by the ruptures of polymer films.[243] Recently, Li et al. developed a more versatile mean for direct fabrication of free-standing perforated BFcA films on conventional solid substrate.[245] The key of this means is to suck out the redundant polymer solution underneath the floating droplets array during the BF process. In this way, the floating droplet on the substrate was only separated by a thin layer of polymer. Therefore, the pressure between the water droplet and substrate can easily rupture the thin polymer layer during the drying process.

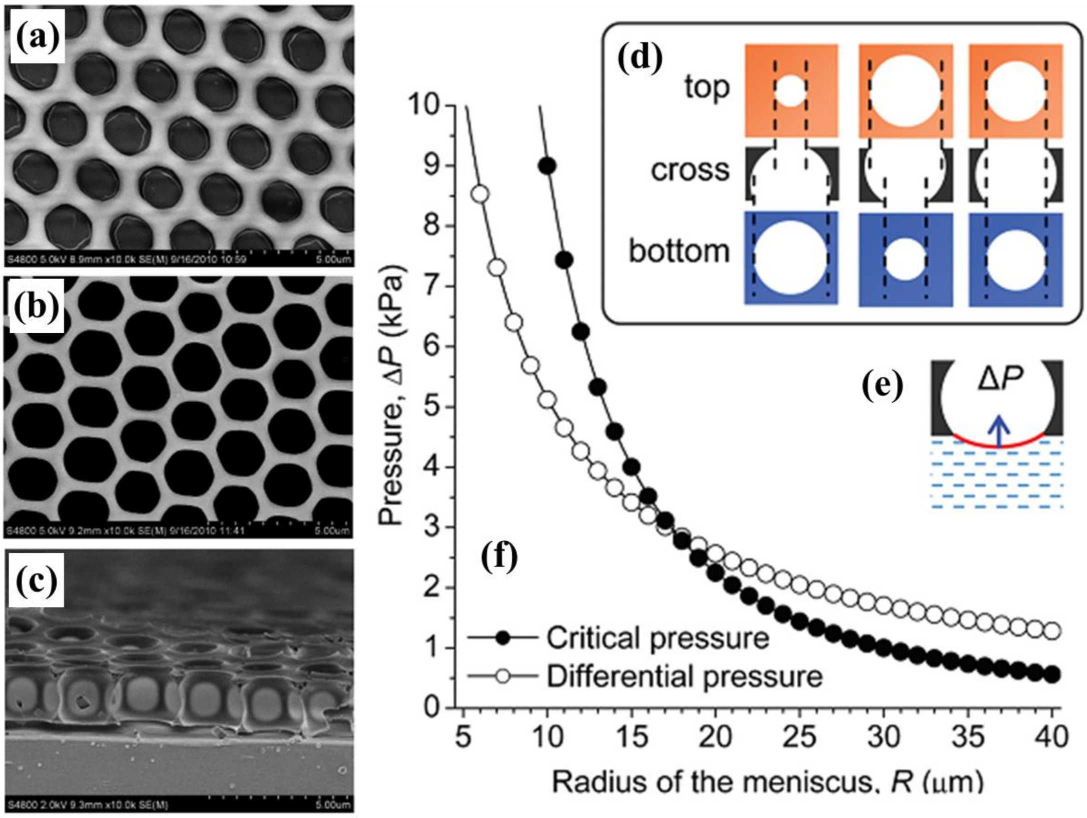

Figure 2. 31 SEM images of BFA films with perforated pores, (a) top view, (b)

bottom view, and (c) cross section. (d) Pore structures of ordered membranes prepared from solutions using benzene, chloroform, and CS_2 (from left to right) as the solvent and (e) Illustration of the formation of through-pores. (f) Calculated curves of differential pressure and critical differential pressure vs the radius[243]

Although the introduction of porous microstructures on planar substrates can be achieved by different techniques, the study of 3D conformal microstructures on nonplanar surface is significantly less developed because it is very challengeable for conventional techniques. The BF technique shows promising prospects for the formation of BFAs on nonplanar surfaces regardless of the surface profiles. Qiao et al. first successfully prepared BFAs on nonplanar substrates based on a core cross-linked star polymer with PDMS as arm.[190,191] Owing to the low T_g of PDMS, such polymer possesses unique soft-flowing nature, and allows the formed honeycomb porous microstructures well contouring to the nonplanar surfaces of different substrates without cracks, such as spherical kaolin particle, “doughnut”-shaped kaolin particle, silica chromatography particle, and copper grids with different patterns and meshes (Fig. 2.32).[190]

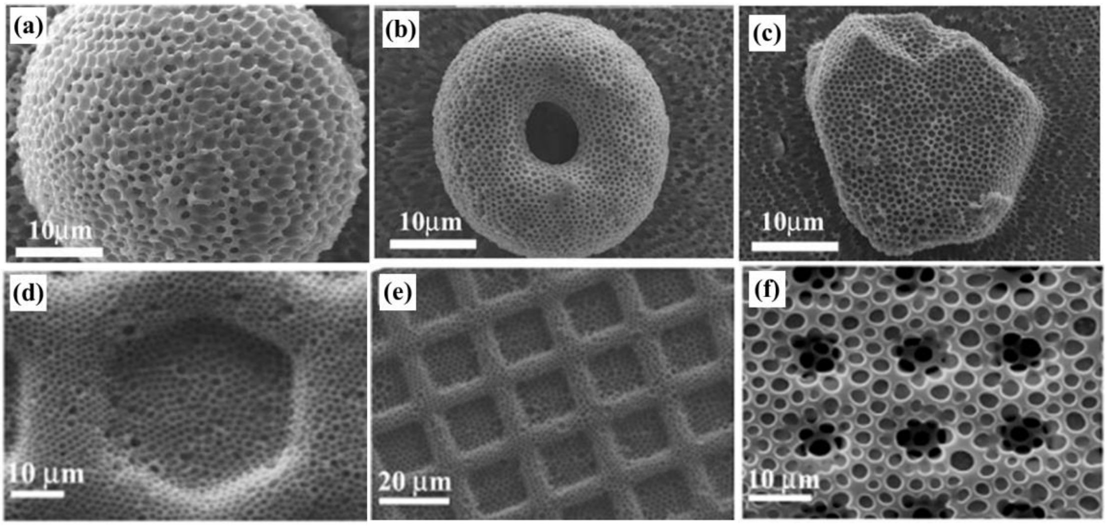

Figure 2. 32 SEM images of star PDMS BFA films on different nonplanar substrates, (a) spherical kaolin particle, (b)"Doughnut"-shaped kaolin particle, (c) Silica chromatography particle, and (d) copper grids with different patterns and meshes[190]

Qiao et al.[188 246]then systematically studied the influence of T_g and Yong's modulus of star polymers on the formation of BFA films on nonplanar substrates. They first found that star polymers with a *T*g below 48 ºC are good candidates for the fabrication of noncracking BFA films,[246] and then demonstrated that star polymers with a high T_g but suitable Young's modulus are also suitable for the formation of BFA films on nonplanar substrates without cracks.[188] Li et al. further pointed out that the plasticization effect of solvent during the BF process also plays an important role in the formation of noncracking BFA films.[132] Through performed the BF process in a sealed cell, they demonstrated that various polymers can be employed as film-forming materials for the fabrication of BFA films on nonplanar surfaces with few cracks.[132,247]

2.3 Applications of porous polymers in energy harvesting

Porous polymers well synergize the properties of porous structures and polymers, which have a broad spectrum of applications in science and engineering. They can be directly used as catalysts,[248] biosensors[249] and chemical sensors;[250] as thermal insulation,[251] dielectric,[252] photonic band gap,[253] encapsulation[254] and packing materials;[255] as antireflection,[256] (super) hydrophobic[257] and (super) hydrophilic[258] and superamphiphobic coatings;[259] as separation,[260] filtration[261] and proton exchange membranes,[262] as negative templates for positive replication;[263] as masks for printing, soft lithography and photolithography;[264-268] as scaffolds for cell culture;[269] as supports for various functional hybridization and biomolecular immobilization;[270-273] as gas storage for the adsorption of hydrogen[274] and carbon dioxide;[275] as precursors for in situ synthesis of carbon and nonpolymeric nanomaterials;[276-280] and so on.

Porous polymers are of particular importance in energy conversion and storage applications. They can either act an assistant role in packaging, encapsulating, supports, carriers and electrodes,[281,282] etc., or play a key role in harvesting ambient solar, mechanical, thermal electric energy for catalytic reaction, heating, luminance or generating electricity based on pyroelectric effect, photovoltaic effect and piezoelectric effect.[283-292] Typical examples include conducting-polymer-based supercapacitors,[293] conjugated-polymer-based organic solar cells,[294,295] and piezoelectric polymer-based nanogenerators.[296] It is obvious that all of these energy capacitors and harvesters require special kind of polymers.

Recently, based on facilely available common polymers, the Prof. Wang's group demonstrated an innovative kind of energy harvesters, namely triboelectric nanogenerator (TENG), for converting mechanical energy into electricity through the conjunction use of triboelectric effect and electrostatic induction.[297] It is the first energy harvester composed of most useful organic materials. Therefore, TENG is also called organic nanogenerator.[17] Since its invention in 2012, TENG has attracted increasing attentions owing to the wide choice of materials, simple and low-cost fabrication process, easily scale-up size, and encouraging properties. A range of TENGs with light, portable, flexible and/or transparent characteristics have been rapidly developed in less than five years, which can be simply classified into four main fundamental operation modes including vertical contact-separation mode, lateral sliding mode, single-electrode mode, and freestanding triboelectric-layer mode.[16-19,298]f

The generation of electricity by TENG can be simply regarded as a periodically physical process of contact friction and separation between two different materials under an externally applied force. Two non-contacted outside surfaces of materials are laminated with an electrode, respectively. Sometimes one of the used materials plays dual roles of contact and electrode. Physical contact enables the electrons, ions and/or molecules transfer between the inner surfaces of two materials, leading to the creation of triboelectric charges. After separation, a potential drop can be generated. If the two electrodes attached on the materials are connected, the electrostatic induced electrons can be driven to flow forth and back to balance the potential during the contacting process and separating process. Generally, two basic electrical signals, namely voltage and current, are measured to characterize the performance of TENG, which can be further employed for the calculation of electric energy, power density and conversion efficiency.[16]

The first reported TENG was a flexible Kapton/polyester (PET)-based device, which can only give an output voltage of 3.3 V at a power density of about 10.4 mW cm^{-2}.[299] When a gold-nanoparticle coated surface was used as electrode and contact surface, the PDMS-based TENG can achieve an area power density of 313 W m^{-2}.[300] The performance of TENG was improved by 5 orders of magnitude in output power density. However, the required contacting force needs to be up to 600 N. Recently, Lee et al. has developed a sponge structure-based TENG based on a porous PDMS film prepared by the direct templating technique, as shown in Fig. 2.33a.[301] PS colloidal crystals were used to template cross-linkage of PDMS precursor by heating at 90 ºC. After the removal of PS by soaking in acetone for 24 h, PDMS film with highly regular inverse opal structures were obtained (Fig. 2.33b). An aluminum plate and an aluminum attached with a Kapton films were attached on the bottom and top surfaces of porous film to assemble a TENG. The used Al plate and Kapton film have the opposite triboelectric polarity to PDMS, acting as triboelectric materials. Besides, Al plate acts both bottom and top electrodes. Under a cycled compressive force of up to 90 N, the output voltage and current of such TENG increases were measured as 130 V and 0.10 mA cm^{-2}, respectively (Fig. 2.33c and d). In comparison to solid film-based TENG, up to

10-time power enhancement can be obtained in the same conditions. It was also found that decreasing the pore size of PDMS film leads to an increase of output voltage and current density. Moreover, benefiting from the hydrophobicity of porous PDMS, this sponge structure-based TENG can maintain a stable powered performance under a wide humidity range.[301]

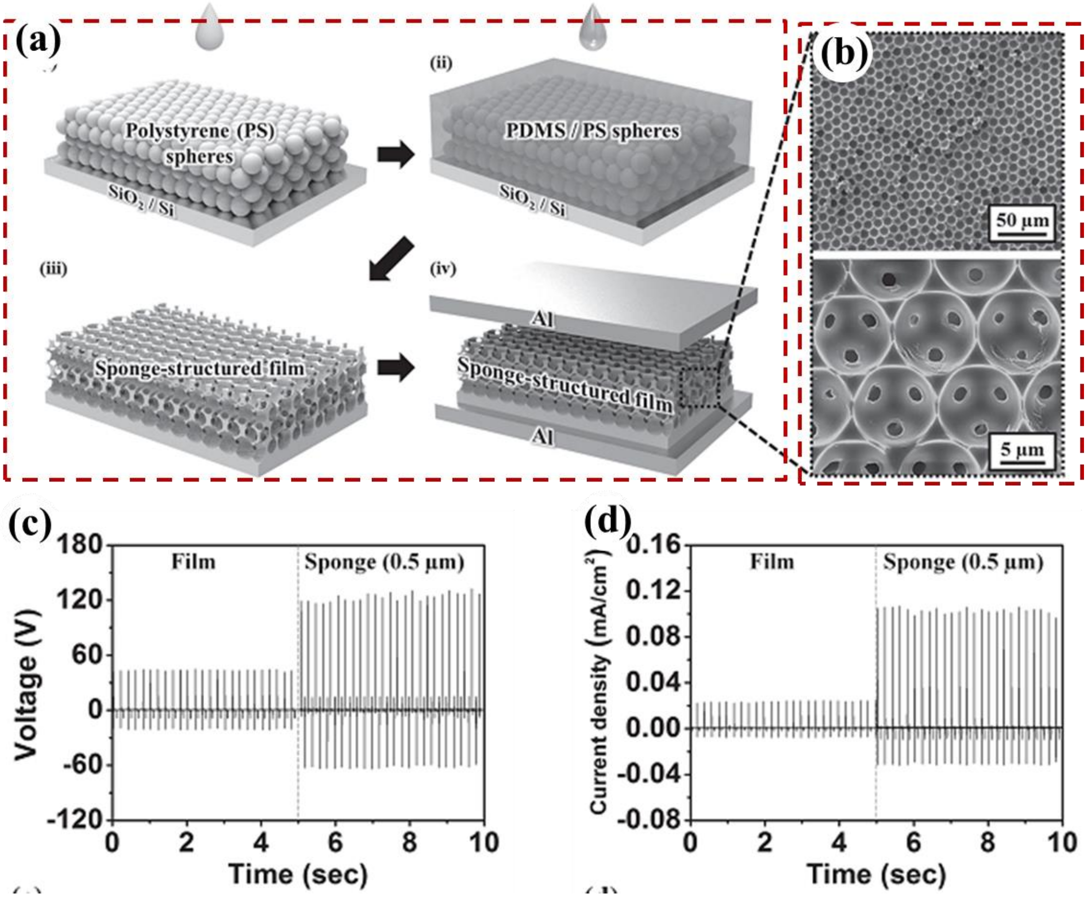

Figure 2. 33 (a) Schematic view of assembling TENG based on a PDMS film with ordered pore arrays. (b) SEM images of inverse opal structure of PDMS film. Comparison of electrical output performances of the solid film-based TENG and porous film-based TENG: (c) Output voltage, and (d) Current density[301]

Instead of using sacrificial templates, reusable Si wafers with designable patterns were used as molds for the fabrication of patterned PDMS film with line, cube, and pyramid features, as shown in Fig. 2.34a.[302] Firstly, the Si wafer molds with desired patterns were fabricated by the combination of photolithography method and etching technique. Specifically, a dry etching process was used to obtain recessed pyramids, and a wet etching process was used to fabricate recessed line and cubic features respectively. Then all the surfaces of the Si templates were modified with trimethylchlorosilane by gas phase silanization to avoid the adhesion between PDMS and Si molds. To prepare patterned PDMS, PDMS precursors and cross-linker were mixed together according to a weight ratio and then cast on the modified Si molds. After a degassed process, the mixtures were further spin-coated at 500 rpm, and then crosslinked at 85 °C for 1 h. SEM images demonstrated the successful preparation of PDMS films with line, cube, and pyramid patterns, as shown in Fig. 2.34b, c and d respectively.

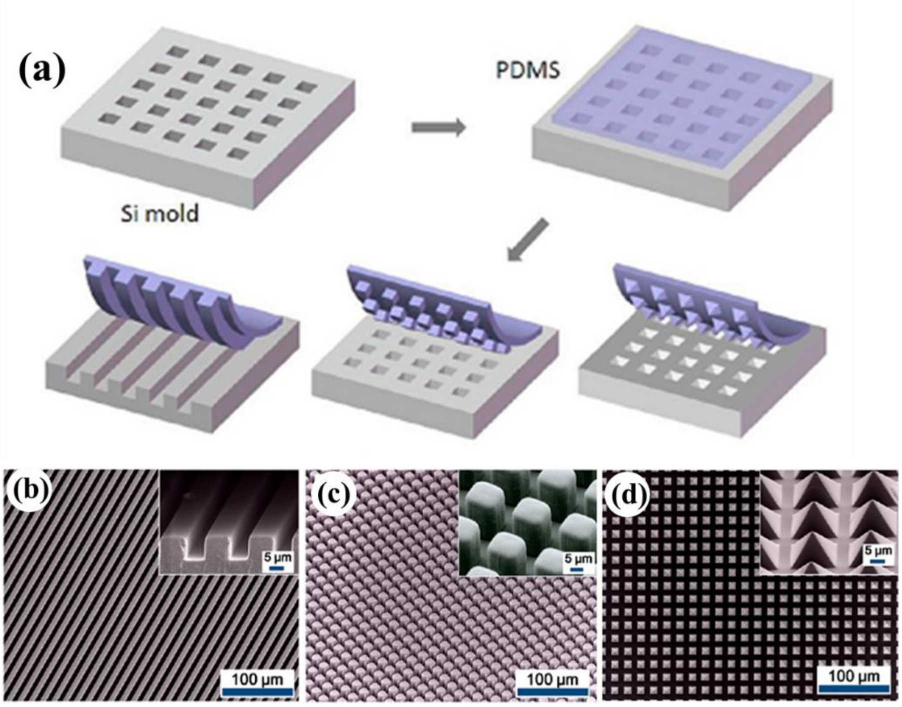

Figure 2. 34 (a) Schematic illustration of fabricating PDMS films with different features by using the patterned silicon wafer as templates. Patterned PDMS films

with (b) line, (c) cube and (d) pyramid features[302]

Based on the obtained patterned PDMS, Fan et al. studied the influence of nanopatterns on the performance of TENG with the purpose of improving the power generation density.[302] They replaced the solid metal electrodes with indium tin oxide (ITO) electrodes to enable TENG with flexible and transparent characteristics. The entire device was assembled with only two transparent polymer materials (PET and PDMS) and a transparent electrode material (ITO). The open-circuit voltage and short-circuit of such devices of using different patterned PDMS films were shown in Fig. 2.35a and b. The obtained results clearly showed that the order of the output efficiency of different patterned film-based TENGs is flat film < line < cube < pyramid. The pyramid-based TENG device generated an output voltage of over 18 V at a current density of about 0.13 $\mu A\ cm^{-2}$. The TENG device was further demonstrated as self-power pressure sensor. As shown in Fig. 2.35c, the voltage-output signal of various patterned-PDMS based sensor devices was obtained by a pressure induced by a droplet of water. The sensitivities of the line-, cube- and pyramid-featured sensors were about five, ten, and fifteen times, respectively, larger than that of the unstructured film-featured sensor. Moreover, the pyramid-featured device even can measure the pressure as low as 13 mPa, which is equivalent to the generated pressure caused by a piece of feather (Fig. 2.35d). [302]

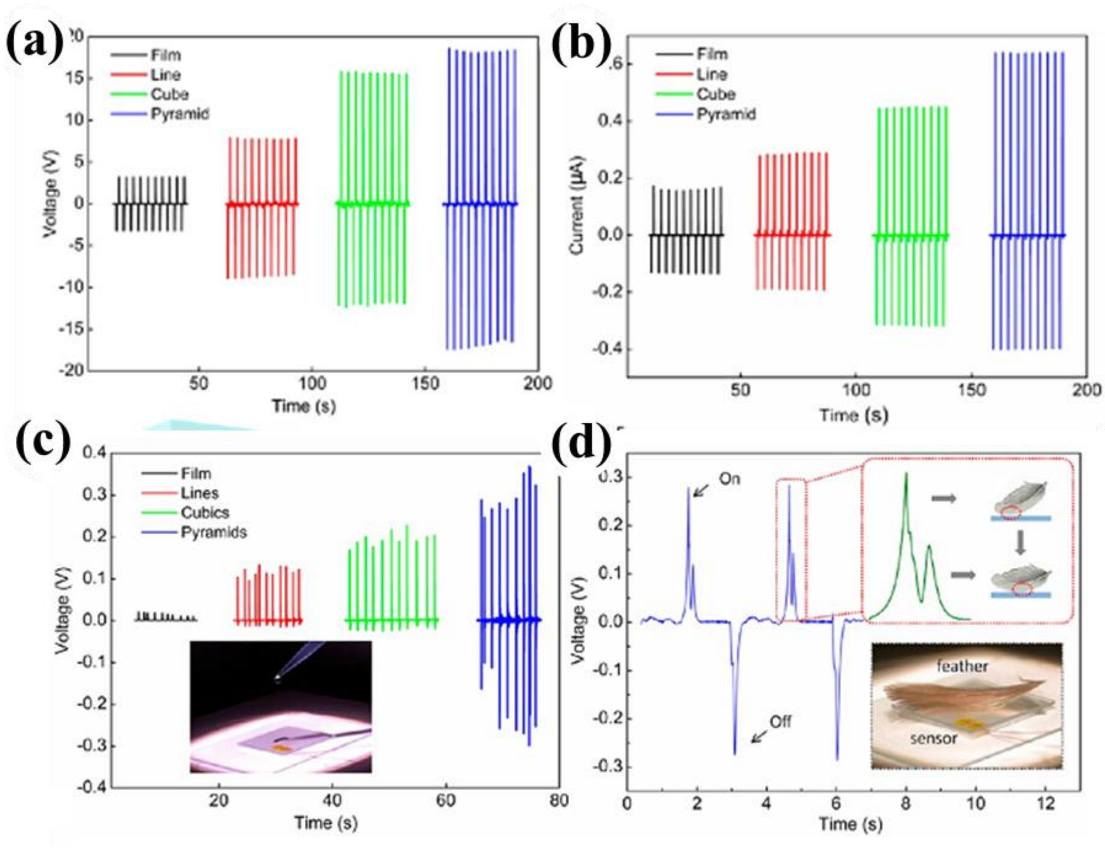

Figure 2. 35 (a) Output voltage and (b) output current of the TENG based PDMS films with flat surface and various patterned features respectively. (c) Performance of the pressure sensor device induced by (c) a droplet of water falling from about 5 cm high and (b) a piece of feather. The voltage responses of various types of sensor devices were measured[302]

Nanostructured materials prepared from block copolymers were also employed for the TENG applications. Jeong and coworkers fabricated the TENG devices based on the incorporation of various silica nanostructures templated from the self-assembly of silicon-containing BCPs.[303] Spatially defined spherical, cylinderal, and lamellar PDMS microdomains in PS matrix were firstly prepared from PS-*b*-PDMS by self-assembling in different solvent vapors, followed by the process of removing the PS and oxidizing the PDMS, silica nanodots, nanogrates, and nanomeshes. Finally, a PTFE-based Teflon thin film on an indium tin oxide (ITO)-coated polyethylene terephthalate (PET) substrate and PTFE-based Teflon ranks was used as counterpart triboelectic surface for the assembly of TENG on different nanopatterned substrates (Fig. 2.36I). Nonpatterned silica surface and three different types of nanopatterns including spherical nanodots, fingerprint-like nanogrates, and perforated lamellar nanomeshes were employed to assemble TENGs respectively (Fig. 2.36II). The nanostructured-based TENGs showed a great improvement in output performance of harvesting mechanical energy, as shown in Fig. 2.36III. Particularly, for the nanomesh-based TENG, approximately 6.3 times enhancement in power generation was achieved in comparison to the nonpatterned TENG. Its generated peak voltage and current were about ~130 V and~2.8 mA when a vertically compressive force of 50 N was applied.[303] By introducing large-area nanodot pattern on a flexible gold substrate with BCPs as template, Kim et al. also found that the electric performance of TENG can be obviously enhanced. The maximum instantaneous current and output power of their TENG were 1.6 mA and 93.2 W m^{-2}, respectively.[304]

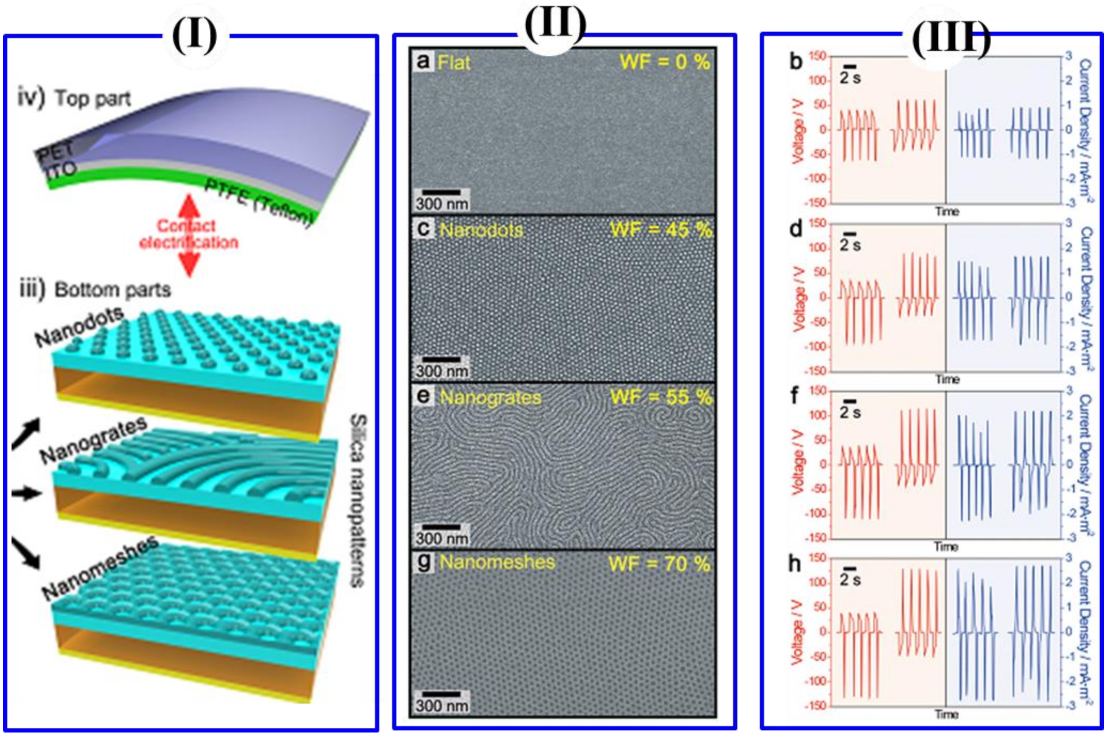

Figure 2. 36 (I) Flowchart of assembling TENG based on different nanopatterned template from BCPs. SEM images (II) of bottom parts' surface morphologies and the forward/reverse signals (III) of generated electricity of flat TENG, nanodots BCP-TENG, nanogrates BCP-TENG, and nanomeshes BCP-TENG, respectively[303]

More recently, through the optimization of polymeric materials, microstructures, working mode and triggering conditions, the output area power density of 500 W m^{-2}, instantaneous conversion efficiency of ~71%, and total energy conversion efficiency of 85% have been achieved by polytetrafluoroethylene film-based TENG,[305] liquid-metal-based TENG,[306] and grating-structured freestanding,[307] respectively. TENGs have been employed for harvesting multifarious mechanical energy extensively distributed in daily life, such as vibration and rotation caused by human motion[308-313] or natural phenomenon involving rain and wind,[314-316] and shown numerous promising applications in self-powered systems and sensors. Examples range from self-powered tactile imaging,[317,318] tracking[319-324] and electrodeposition[325] to active strain,[326] force,[327] and chemical sensors[17,328] without the need of power supply.

2.4 Applications of BFAs and their derived materials

BFA films prepared from different polymers and materials by the BF technique can meet the requirements of most applications stated above. So far, it has been demonstrated that BFA films and their derived materials are valuable in the fields of templating[263] and microfabrication,[329] biomaterials,[330,331] superhydrophobic surfaces,[177,182] sensors,[332,333] catalysis,[334] separation,[243] gas storage,[335] responsive surfaces,[198] surface enhanced Raman scattering (SERS) substrates,[336] and optical [259] and conductive materials.[202-206] Recently, Bao et al. used BFA films as negative molds for templating fabrication of PDMS dielectric structures to prepare capacitive pressure sensors. In comparison to similar sensing devices, such prepared sensors not only improved the sensitivity at high pressures up to 100 kPa, but also showed little-hysteresis pressure response with high sensitivities at applied pressures (<10 kPa).[337] This study provides an economical and scalable strategy for the production of pressure-sensing pixels which can act as "electronic skin" to mimic human skin pressure sensitivity in a broad range. Based on the BFA films on Cu thin film coated PET substrate, Ma et al. successfully prepared metal meshes with good flexible, optical and electrical properties. After modifying the obtained Cu meshes with silver deposition and UV/ozone treatment, they further applied them as flexible transparent electrodes for the assembly of organic photovoltaic devices, which can possess a power conversion efficiency of up to 2.04%.[338] These studies on the applications of BFA derived materials in energy-related fields are significant and promising. Unfortunately, the applications of BFAs and their derived materials in energy conversion and storage are still significantly less developed, although polymeric materials and their microstructures have been demonstrated to play key roles on the generation, accumulation, and retainment of triboelectric charges, which decisively determine the final electric performance of TENGs.[299-304] And to the best of our knowledge, there are still no reports on the fabrication and performance evaluation of TENGs based on BFA films.

2.5 Summary

In this chapter, prior work on the porous materials and polymers, BFs and their applications in porous polymers, and applications of porous polymers in energy harvesting has been broadly reviewed. The BF technique has been demonstrated as a unique strategy of using water droplet arrays as dynamic templates for fabricating the porous microstructures of diverse materials, which possesses simple, low-cost, time-saving, easily-scalable and non-destructive advantages. Because all the condensation, assembly and evaporation of BFs are spontaneous, this promising technique is straightforward and efficient, which requires no trivial work on the preparation and removal of templates. Although the BF technique is simple and straightforward, it actually involves complicated transfers of heat and mass at the interfaces among water, solvent and polymer, which has many thermodynamic and kinetic underpinnings that need to be further fully understood, such as the spreading behaviors of casting solution on substrate and condensed water droplets on solution surface, the role of water and its interaction with polymer solution, and the influence of solution concentration variation on the precipitation and gelation process.

The fabrication of BFAs has been widely studied on planar substrates, but the study of 3D conformal porous microstructures on nonplanar surface is significantly less developed, particularly on textile fabrics. Considering the extremely broad applications of textiles in life and industry, it is of great significance to fill this research gap by developing an efficient, time-saving and cost-competitive strategy for the conformal formation of porous microstructures on textiles, which may expectedly pave the way to a brand-new class of textile composites with promising prospects in flexible and wearable applications.

Towards the future practical applications, there are also several challenging issues that need to be addressed, such as the circumvention of film defects and cracks. It is still difficult to find a general and scalable fabrication approach of highly ordered porous films with commercial polymeric and non-polymeric materials on either planar or nonplanar substrates. Moreover, in comparison to the broad applications of porous polymers, more applications of BFA films can be developed. Particularly, the research gaps in energy-related applications should be filled, such as generating electricity based on TENGs by harvesting mechanical energy.

CHAPTER 3 Controllable Self-Assembly of Polymeric Microstructures Assisted by Different Nonsolvent Breath Figures

3.1 Introduction

The BF techniques performed in aqueous vapor have been widely reported for the fabrication of BFA films with the size ranging from several hundred nanometers to dozens of micrometers.[7,9-12] However, there are a few reports on the BF technique performed in non-aqueous vapor, although considerable organic solvents can form liquid droplets under appropriate conditions. It will be of theoretical and practical importance to investigate the formation of polymeric microstructures by developing the BF techniques to non-aqueous and more complex aqueous/nonaqueous mixed vapors. This may lead to the formation of diverse microstructures for some applications with specific requirements, and more importantly contribute to a comprehensive understanding of the complex mechanism behind the BF technique from a new perspective.

In this chapter, a series of linear PS hompolymers with well-defined M_ns and narrow M_w/M_n are first synthesized by ATRP. They are then employed as film-forming materials for systematic study of polymeric microstructures by the BF technique under water vapor, methanol (MeOH) vapor, and binary vapors of water and MeOH with different ratios, respectively. Besides molecular weights and nonsolvent vapors, other BF variables involving solution concentration and solvent types are also considered in this study. This leads to a range of polymeric microstructures including microspheres, pore arrays, and microspherical caps of different sizes, shapes and regularities. Through systematic comparison and analysis of these polymer microstructures, the complex mechanism behind the BF technique is thoroughly elucidated based on the physicochemical properties of polymer and the difference of vapor pressure, surface tension and miscibility between solvents and nonsolvents.

3.2 Synthesis of well-defined PS by ATRP

Polystyrene (PS) and its analogues, such as PS-based block, graft, star, and random copolymers, are some of the most widely used film-forming materials in the BF technique.[7,8] To avoid the unnecessary factors caused by multiple components, such as microphase separation caused by different polymer chain segments and mobility, herein single-component PS homopolymers with explicit linear structure, predetermined M_n and narrow M_w/M_n were specifically synthesized by atom transfer radical polymerization (ATRP) of styrene (St), and chosen for better studying the formation of polymeric microstructures by the BF technique. As shown in Fig. 3.1, the employed PS samples were generally prepared by the homopolymerization of St at 90 ºC-100 ºC in toluene (Tol) with Methyl-2-bromopropionate (MBP), Copper(I) bromide (CuBr) and N’, N’, N, N”, N”-pentamethyldiethylenetriamine (PMDETA) as initiator, catalyst and ligand, respectively.

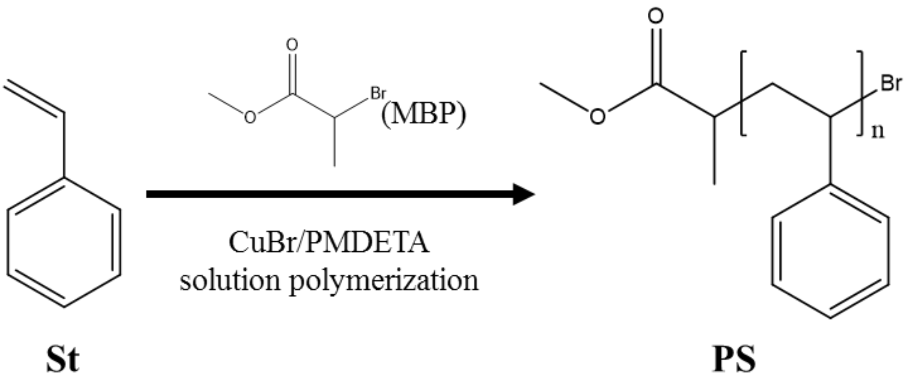

Figure 3. 1 Scheme of synthesizing PS homopolymer by ATRP

MBP (Acros, 98%) and PMDETA (Aldrich, 99%) were used as received. CuBr (Acros, 99.9%) was stirred in glacial acetic acid overnight, filtered through a Buchner funnel, and then washed three times with ethanol and diethyl ether, dried in a vacuum overnight. St (Aldrich, 99%) was dried over calcium hydride for 24 hours under nitrogen. THF and Tol were refluxed over sodium/benzophenone. They were distilled under nitrogen atmosphere respectively before use. The polymerization reactions were performed in a Schlenk flask containing a Teflon coated magnetic stir bar. In a typical procedure, CuBr (0.257 g, 1.79 mmol) was firstly added in the flask, vacuumed and back-filled with dry nitrogen for three times. Then St (41.2 mL, 0.36 mol), PMDETA (0.75 mL, 3.59 mmol), and MBP (0.2 mL, 1.79 mmol) were successively added under nitrogen atmosphere respectively. And finally 42 mL toluene was added and used as solvent. The prepared solution was degassed with three freeze-pump-thaw cycles, and followed by heating at 90 °C with the protection of nitrogen atmosphere in an oil bath. After 24 hours, the polymerization reaction was quenched by immersing the flask into a liquid nitrogen bath. The reaction mixture was diluted with THF, and poured into a neutral aluminum oxide (Al_2O_3) column for the removal of CuBr. White precipitation occurred by pouring the obtained solution into MeOH under magnetic stirring. It was collected by filtering, and further dried in a vacuum for further use.

ATRP is the most widely used methods for controlled/living radical polymerization of polymers with predictable molecular weight and designed molecular weight distribution owing to the mild reaction systems.[35,36] Through controlling the reaction temperature, reaction time and the mole ratios of monomer and initiator, a series of PS samples were well synthesized. Their M_n and M_w/M_n were measured by a gel permeation chromatography (GPC) system equipped with a Waters 1515 Isocratic HPLC pump, a Waters 2414 refractive index detector (RI), a Waters 2487 dual λ absorbance detector (UV) and a set of Waters Styragel columns (HR3, HR4 and HR5, 7.8 ×300 mm). The GPC measurements were carried out at 35 °C using THF as eluent with a 1.0 mL min^{-1} flow rate. The system was calibrated with polystyrene standards. Table 1 summarizes the M_n and M_w/M_n of different PS samples determined by GPC. Five PS homopolymers with a M_n ranging from 1600 to 19500 were successfully prepared. They were named as PS-02, PS-07, PS-11, PS-14 and PS-20, respectively. Their GPC curves are shown in Fig. 3.2. All of them display a sharp and monodisperse peak in GPC traces, indicating the narrow molecular weight distribution of PS homopolymers. Actually, the M_w/M_n of all samples determined by GPC were below 1.1.

Table 3. 1 Different M_n and M_n/M_w of synthesized PS homopolymers

No.	Sample Name	M_n	M_n/M_w
1	PS-02	1,600	1.100
2	PS-07	6,600	1.051
3	PS-11	10,900	1.084
4	PS-14	14,000	1.079
5	PS-20	19,500	1.088

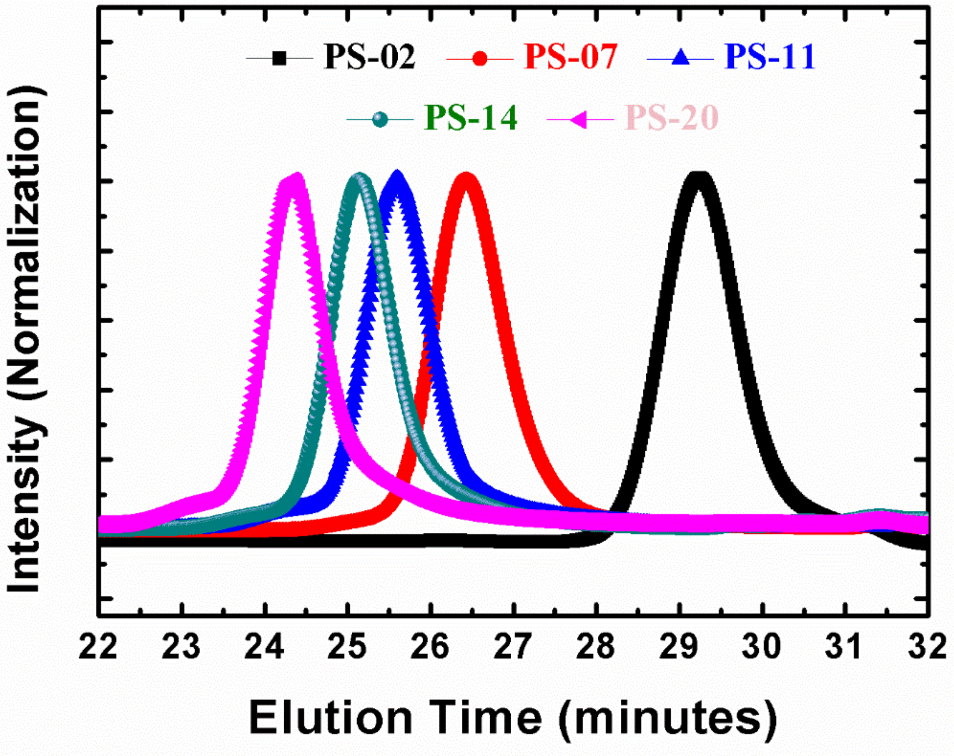

Figure 3. 2 GPC traces of different PS homopolymers

The chemical structure of PS homopolymer was also characterized by proton nuclear magnetic resonance ^{1}H NMR, which was performed on a Bruker AV 500 spectrometer at room temperature with $CDCl_3$ as the solvent. A typical ^{1}H NMR spectrum of linear PS terminated with bromo is shown in Fig. 3.3. Two broad signals at 6.25~7.21 ppm and 1.18~2.13 ppm are assigned to the aromatic protons in the styrene units, and the methene and methine protons of main chain, respectively, while the weak signals between 3.4 and 3.6 can be ascribed to methine protons adjacent to oxygen. These characteristic chemical shifts well confirmed the successful synthesis of PS.

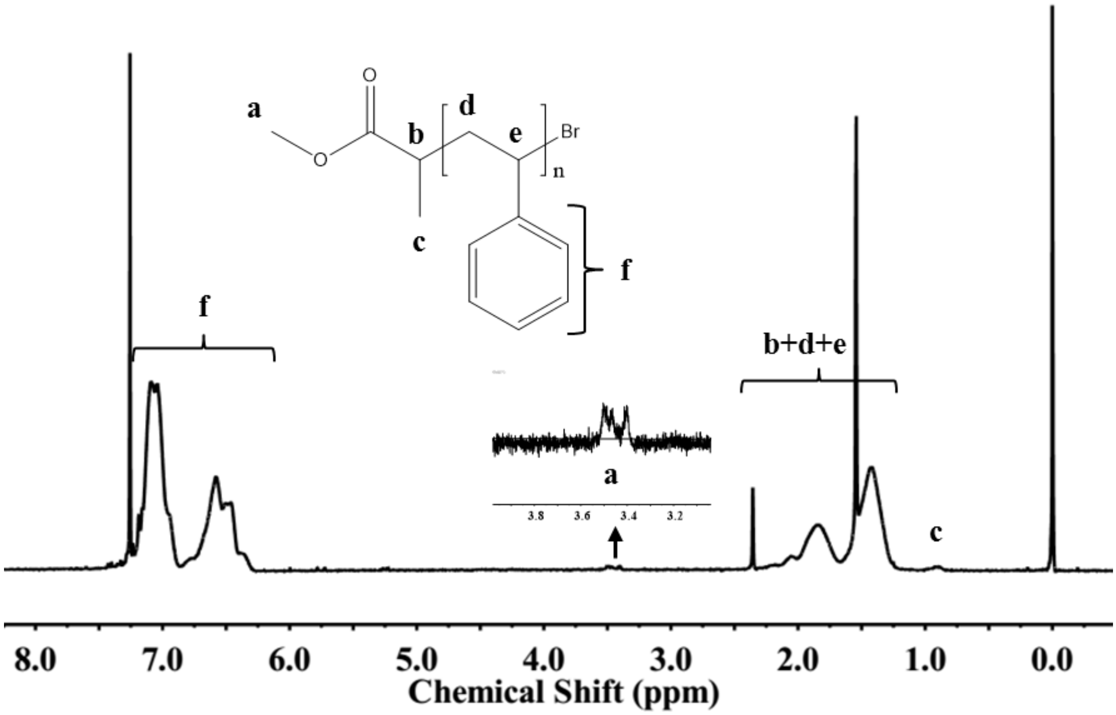

Figure 3. 3 A typical ^{1}H NMR spectrum of PS homopolymer with $CDCl_3$ as solvent

3.3 Polymeric microstructures prepared by BF in different nonsolvent vapors

The synthetic PS samples were employed for the construction of polymeric microstructures in a wide solution concentration by the static BF technique under different nonsolvent vapors. The BF process was performed at ambient temperature in a 50-mL sealed vessel saturated with nonsolvent vapor, which was generated by the liquid of MeOH, water or binary mixtures of MeOH and water with given weight ratios. The volume of added liquids was fixed at 2 mL. The obtained PS samples were dissolved in THF, $CHCl_3$ and CS_2 respectively for the preparation of solution with desired concentration. A typical BF process was carried out by casting about 25 μL polymer solution with a desired concentration onto a glass substrate, which was placed in the sealed vessel beforehand. The substrate was 1 cm higher than the liquid level. With the evaporation of organic solvent, the transparent solution film would gradually be turbid. After solidification, it was taken out of the vessels, and dried in air for further characterizations. The obtained PS film samples were directly placed under a Nikon optical microscope for optical photographs. Then they were coated with a thin layer of gold (around 2 nm) for further imaging by SEM (Hitachi TM-3000 or JEOL Model JSM-6490). A 15 keV (or 20 keV) electron beam was used for the observation with a working distance of 10 mm.

3.3.1 Fabrication of honeycomb porous microstructures by BF in aqueous vapor

3.3.1.1The influence of molecular weight

PS homopolymers with different M_ns were dissolved in CS_2 respectively to investigate the influence of molecular weight on the formation of polymeric microstructures. The solution concentration was fixed at 320 mg mL^{-1}. By the aqueous BF technique under the same conditions, five different polymer films were prepared for SEM observation. The typical surface features of PS-02, PS-07, PS-11, PS-14 and PS-20 films are shown in Fig. 3.4a-e, respectively. Their SEM images at a lower magnification are shown in Fig. 3.4f-j, correspondingly.

Randomly distributed pores were observed for PS samples with a low M_n. With the increase of M_n, the porous microstructure became dense, while the pore size tended to decrease. As M_n reaching at 14,000, homogeneous round pores and relatively ordered pore arrays were obviously observed. When using PS-20 as film-forming material, similar results were also obtained. This indicates that PS with a large M_n tends to form densely and regularly porous films with a small size by the BF technique under aqueous vapor.

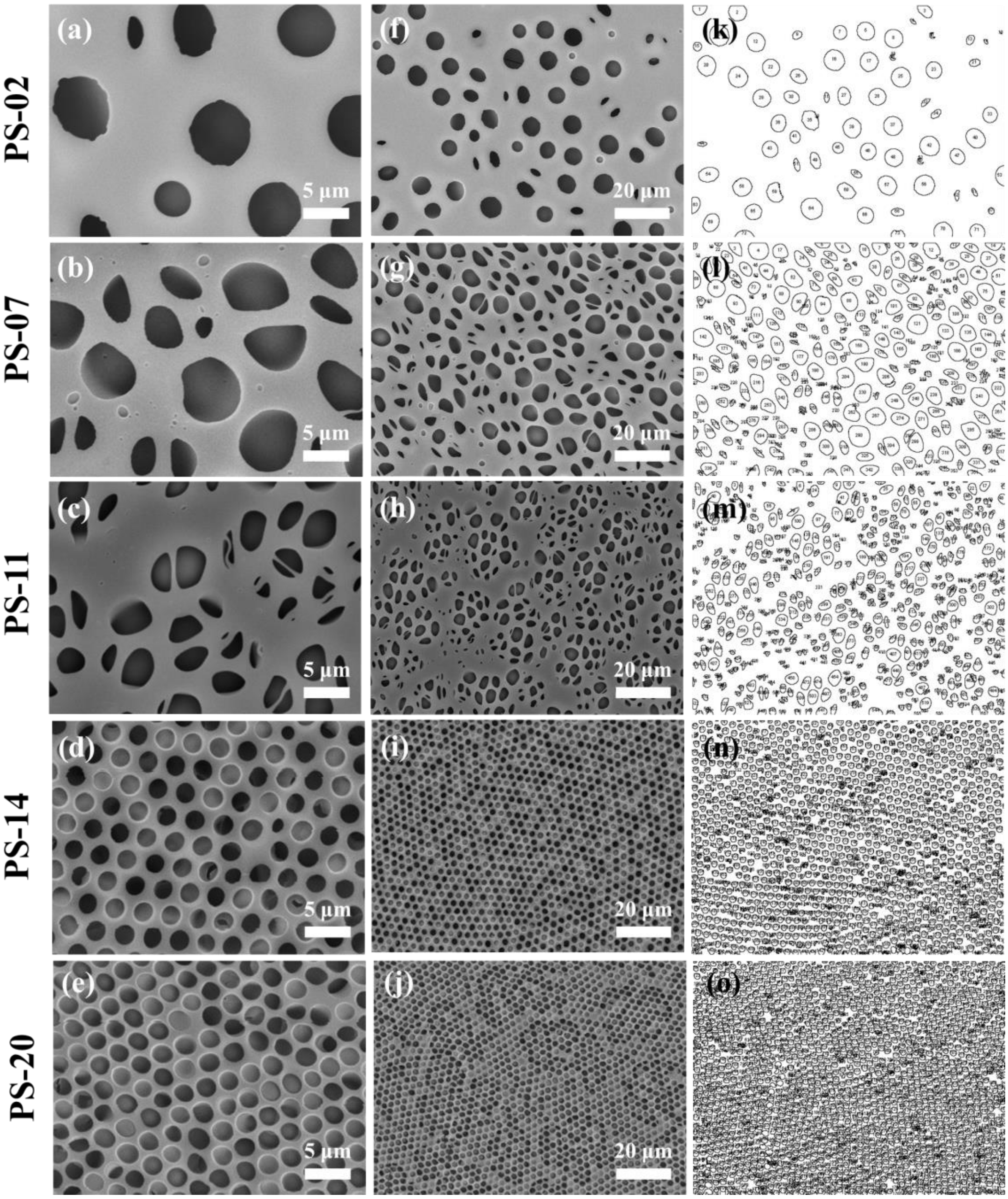

Figure 3. 4 Typical surface microstructures prepared from different PS homopolymers, (a) PS-02, (b) PS-07, (c) PS-11, (d) PS-14, and (e) PS-20. Their SEM images at a lower magnification are shown in (f)-(j), respectively. And (k)-(o) are corresponding outline pictures of (f)-(j) obtained by ImageJ

A reliable image processing software ImageJ was further employed for further quantitative analysis of the obtained porous microstructures.[339] The images in

Fig. 3.4f-j were first converted into black and white (BW) binary images by adjusting the threshold levels for ImageJ analysis. Fig. 3.4k-o show the obtained outline pictures correspondingly. Three parameters involving pore density (the number of pores per unit area), pore size (the diameter of circle area equivalent to the pore area), and surface porosity (the fraction of surface area of pores over the total film area) were used for quantitative analysis of the obtained porous films. The analysis results were summarized and plotted against M_n, as shown in Fig. 3.5. With the increase of M_n, the pore number of films per square meter increases drastically, while the average pore size decreases gradually. Specifically, as shown in Fig. 3.5a, the pore density of PS films with M_n at 1,600 (PS-02) is only about 7.59 x 10^9 m^{-2}. After a gradual increase to 5.79 x 10^{10} m^{-2} at 10,900, it drastically arises to 1.52 x 10^{11} m^{-2} at 14,000. With further increase of M_n, the rise trend becomes slow again. When PS-20 (M_n=19,500) was used as film-forming material, the resultant pore density is approximately 1.84 x 10^{11} m^{-2}. Different from the increasing trend of pore number with M_n, the average pore size of PS films shows a gradual decrease from 4.76 μm at 1,600 to 1.60 μm at 19,500 (Fig. 3.5b). Moreover, their standard deviations (SDs, i.e., bar height in Fig. 3.5b) correspondingly vary from 2.07 to 0.60, which indicates the pore size distribution possesses a narrowing trend with the increase of M_n. This indicates that PS with a higher M_n can lead to the formation of more regular porous microstructures with narrower size distribution. Owing to the rapid increase of pore number, the surface porosity of polymer film also shows a general increase trend with M_n (Fig.

3.5c).

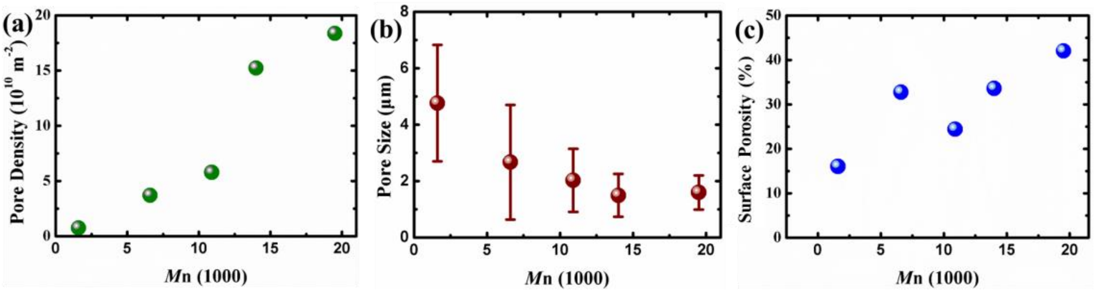

Figure 3. 5 Plot of the dependence of (a) pore density, (b) pore size and (c) pore proportion on the molecular weight (M_n) of used PS. The scale bars in (b) primarily represent the distribution of pore diameter

3.3.1.2 The influence of solution concentration

PS-14 and PS-20 solutions were diluted to study the influence of solution concentration on the formation of porous microstructures, respectively. When they were diluted to 160 mg mL^{-1}, the porous microstructures of PS-20 film became irregular (Fig. 3.6), while PS-14 led to form more regular pore arrays. As shown in Fig. 3.7a and b, hexagonally packed round pore arrays are clearly observed in large area. The pore arrays of PS-14 film became disordered when its casting solution was further diluted to 80 mg mL^{-1} (Fig. 3.7d and e). And there is no obvious change on the irregularity of porous microstructures as the concentration of casting solution was further decreased to 40 mg mL^{-1} (Fig. 3.7g and h). Fig. 3.7b, e, and h were then converted into BW binary images by ImageJ for pore analysis, as shown in Fig. 3.7c, f and i respectively. The analysis results were collected in Fig. 3.10, which will be discussed later. When PS-14 solution was diluted at 20 mg mL^{-1}, naked substrate was observed (Fig. 3.8a-c). With the continuous decrease of solution concentration, the naked area of substrate became larger (Fig. 3.8d-f). The resultant films are consisted of distorted and continuous polymer skeletons. Small pores with the size ranging from hundreds of nanometers to several micrometers randomly were distributed on the skeletons (Fig. 3.8a and d). When the PS-14 solution was diluted as low as 5 mg mL^{-1}, spreading polymer areas are still found, with numerous microscale pores distributed (Fig. 3.8g-i). The pore sizes are larger than those of polymer skeletons.

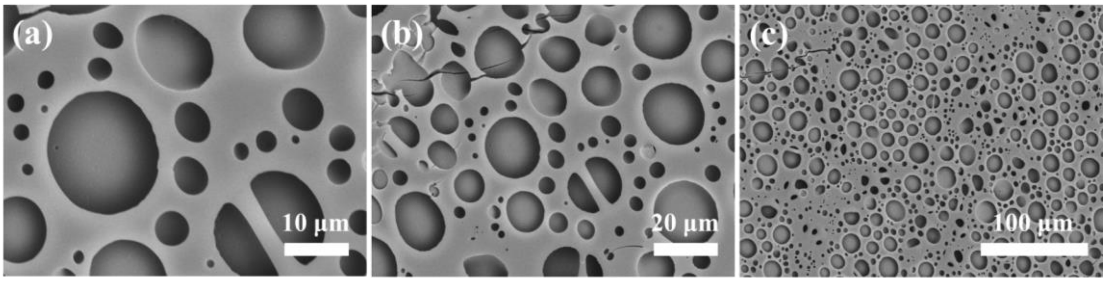

Figure 3. 6 Disordered porous microstructures at different magnifications from 160 mg mL^{-1} PS-20/CS$_2$ solution

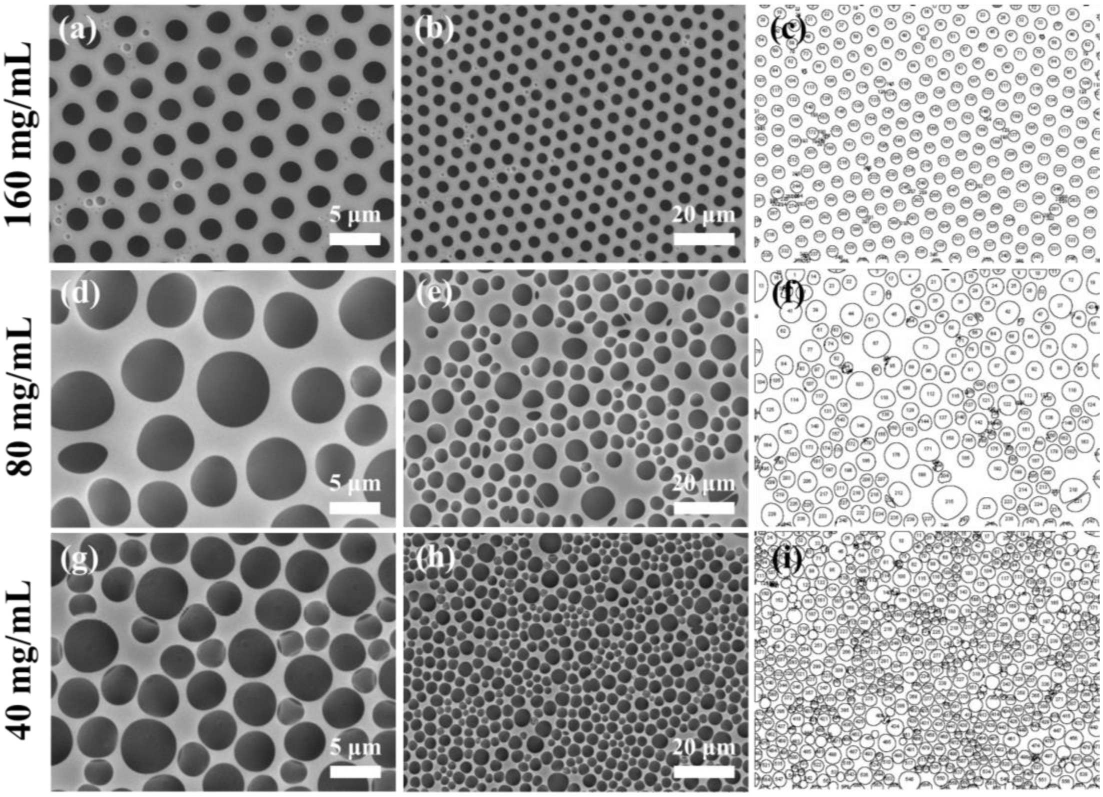

Figure 3. 7 Different porous microstructures prepared from PS-14/CS_2 solutions with (a) 160 mg mL^{-1}, (d) 80 mg mL^{-1} and (g) 40 mg mL^{-1}, respectively. Their SEM images at a lower magnification are shown in (b), (e) and (h). And (c), (f) and (i) are corresponding outline pictures of (b), (e) and (h) obtained by ImageJ

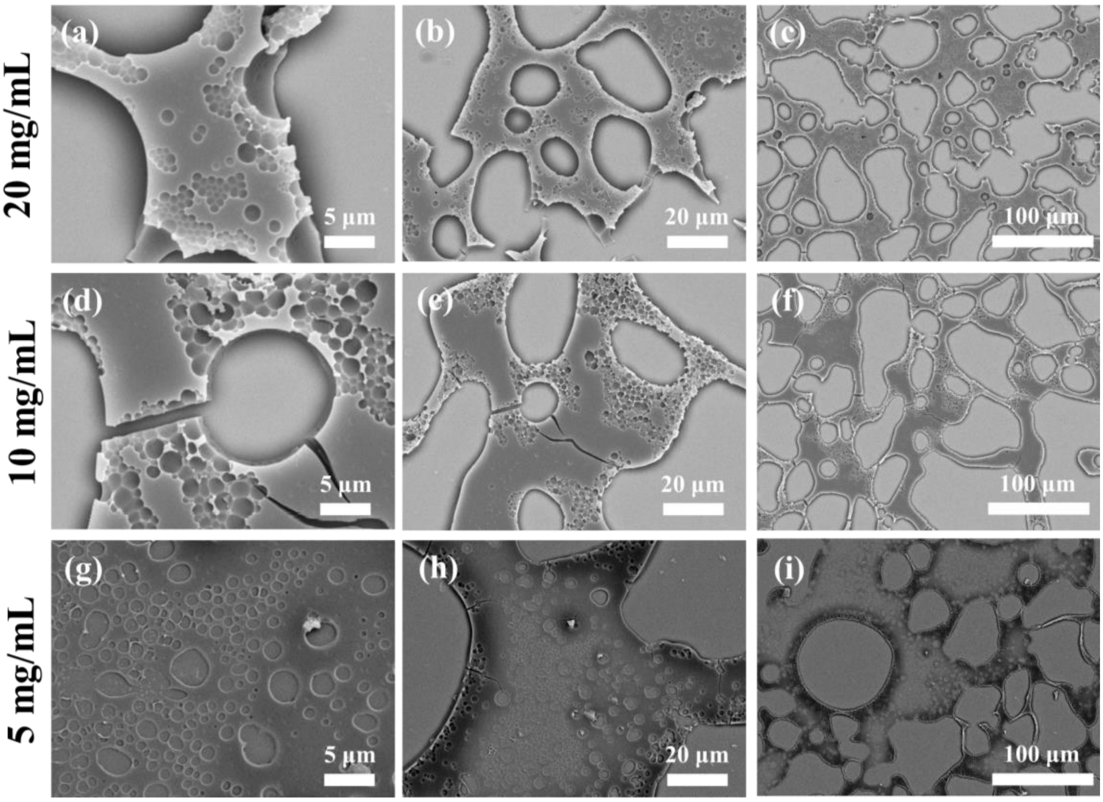

Figure 3. 8 Distorted porous microstructures at different magnifications from PS-14/CS_2 solution with (a)-(c) 20 mg mL^{-1}, (d-f) 10 mg mL^{-1} and (g)-(i) 5 mg mL^{-1}, respectively

PS-14 solution with polymer content up to 640 mg mL^{-1} was also studied by the BF technique. When it was dropped on the glass substrate, it cannot spread out to form a thin liquid film. Instead, a polymer monolith with a similar shape of casting solution droplet formed, as shown in Fig. 3.9a. It was due to the high viscosity caused by the high solution concentration, but this did not influence the formation of porous microstructures on monolithic surface. As shown in Fig. 3.9b-d and f, numerous pores with small size were clearly observed. Fig. 3.9d was further converted into a BW binary image for pore analysis (Fig. 3.9e).

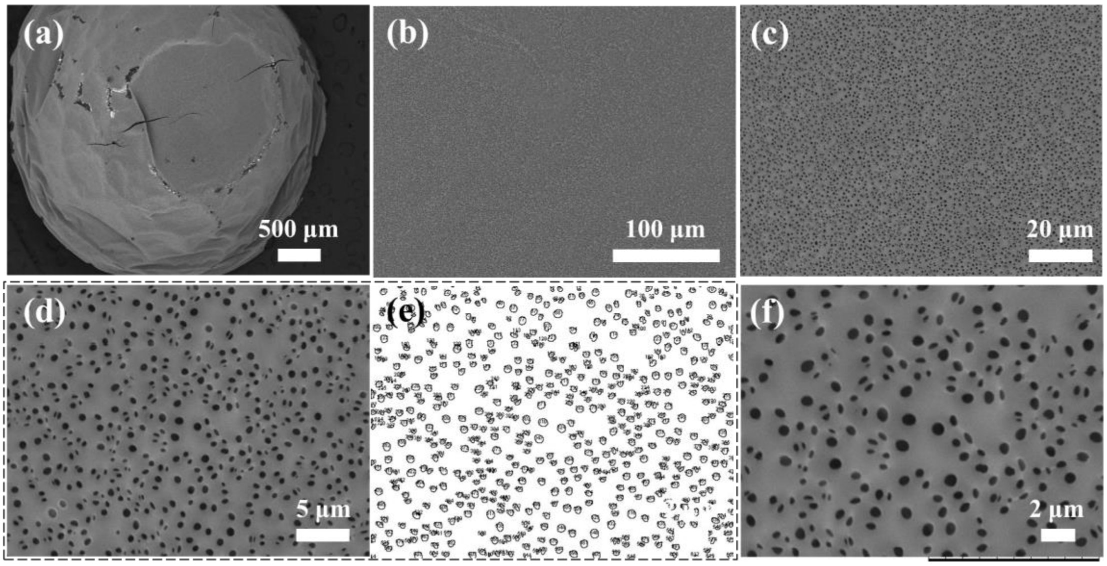

Figure 3. 9 Porous microstructures at different magnifications from PS-14/CS_2 solution with 640 mg mL^{-1}

The pore density, pore size and surface porosity of PS-14 films prepared from the solutions with concentration from 40 mg mL^{-1} to 640 mg mL^{-1} were summarized and plotted against the solution concentration for a further study, as shown in Fig. 3.10. Specifically, the pore density of PS-14 films basically possesses a rising trend with the increase of solution concentration (Fig. 3.10a), while the average pore size shows a general decrease tendency (Fig. 3.10b). Although the number of pores increases, the surface porosity of polymer films still shows a decrease trend with the increase of solution concentration approximately (Fig. 3.10c). This is probably due to the decrease of pore size.

Increasing solution concentration appropriately leads to the improvement of pore homogeneity and regularity. Highly hexagonal ordered arrays consisted of homogeneous round pores were obtained at 160 mg mL^{-1} (Fig. 3.7a and b) and 320 mg mL^{-1} (Fig. 3.4d and i). Their surface porosities are very close (31.66% and 33.623%, respectively), but the pore density of films at 160 mg mL^{-1} is approximately 3.7 x10^{10}, which is much less than that of films at 320 mg mL^{-1} (1.5 x 10^{11}). This indicates that the former pore size is larger than the latter one. Actually, the pore sizes of films at 160 mg mL^{-1} and 320 mg mL^{-1} are 3.03 μm (SD = 1.29) and 1.50 μm (SD = 0.76), respectively (Fig. 3.10b).

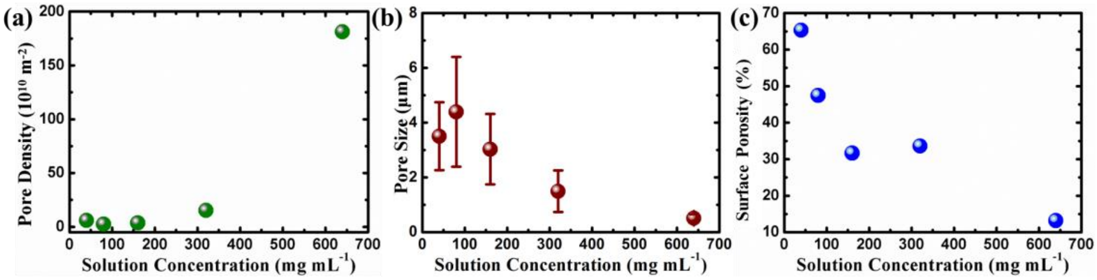

Figure 3. 10 Plot of the dependence of (a) pore number, (b) pore size and (c) surface porosity on the concentration of PS-14/CS$_2$ solution. The scale bars in (b) primarily represent the distribution of pore diameter

3.3.1.3 The influence of solvent type

Besides CS$_2$, CHCl$_3$ and THF are other two most common used solvents for dissolving polymers in the BF technique.[7,9,10] Like PS-14/CS$_2$ solution, it was difficult for their solutions at 640 mg mL^{-1} to spread on a glass substrate during the BF process, which was also due to the high viscosity caused by the high polymer concentration. This finally resulted in the formation of thick membranes. Their panorama views are shown in Fig. 3.11a and e, respectively. The vesicle-like morphology in Fig. 3.11a was probably caused by the rapid evaporation of residual solvent during the vacuum pumping process for Au coating. This also led to the generation of some cracks, as observed in both Fig. 3.11a and e. Another reason can be ascribed to the high glass transition temperature (T_g) of PS. The resultant PS films are usually brittle and fragile. Irregular porous microstructures were observed for both samples (Fig. 3.11b and f). In a closer view, as shown in Fig. 3c and g, pores distributed on polymer membranes from $CHCl_3$ solution seem to be smaller and sparser than those from THF solution. Quantitative pore analysis was conducted by ImageJ based on BW binary images in Fig. 3.11d and h, which were derived from Fig. 3.11c and g, respectively. Polymer films from $CHCl_3$ solution possess a pore density of 9.40 x 10^{11} m^{-2}, pore size of 0.23 μm (SD = 0.063), and surface porosity of 4.28%, while the corresponding values of film samples with THF as solvent are 1.97 x 10^{12} m^{-2}, 0.25 μm (SD = 0.102), and 11.62 %, respectively.

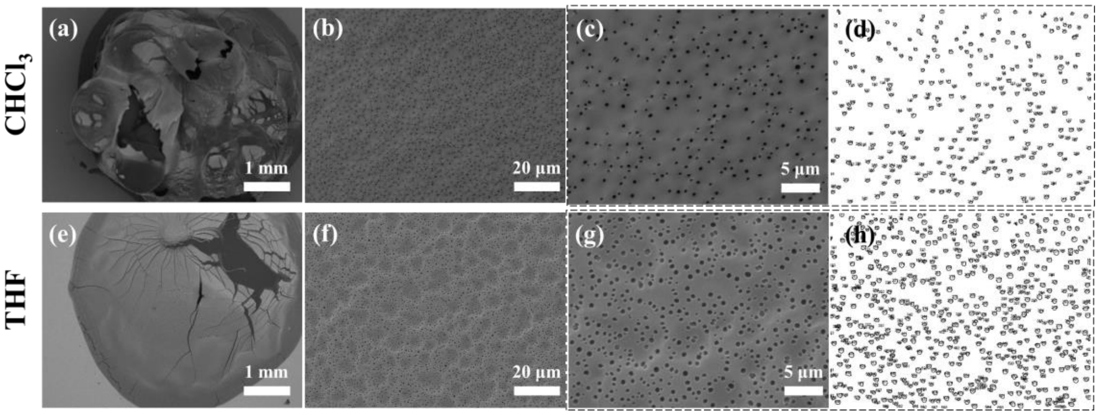

Figure 3. 11 Porous microstructures prepared from 640 mg mL^{-1} PS-14 solutions with (a)-(d) $CHCl_3$ and (e)-(h) THF as solvent, respectively

Like CS_2 solution above, $CHCl_3$ solution and THF solution were both gradually diluted by half to study the influence of solution concentration on the formation of porous microstructures. The typical surface microstructures from PS-14/$CHCl_3$

solution with the concentration ranging from 5 mg mL^{-1} to 320 mg mL^{-1} are summarized in Fig. 3.12 and Fig. 3.13 respectively. Relatively regular porous microstructures are observed for polymeric films cast between 40 mg mL^{-1} and 320 mg mL^{-1}. Especially at 160 mg mL^{-1}, the resultant displays highly ordered hexagonal pore arrays. With the solution concentration gradually decreasing to 5 mg mL^{-1}, the obtained porous microstructures become less and less regular.

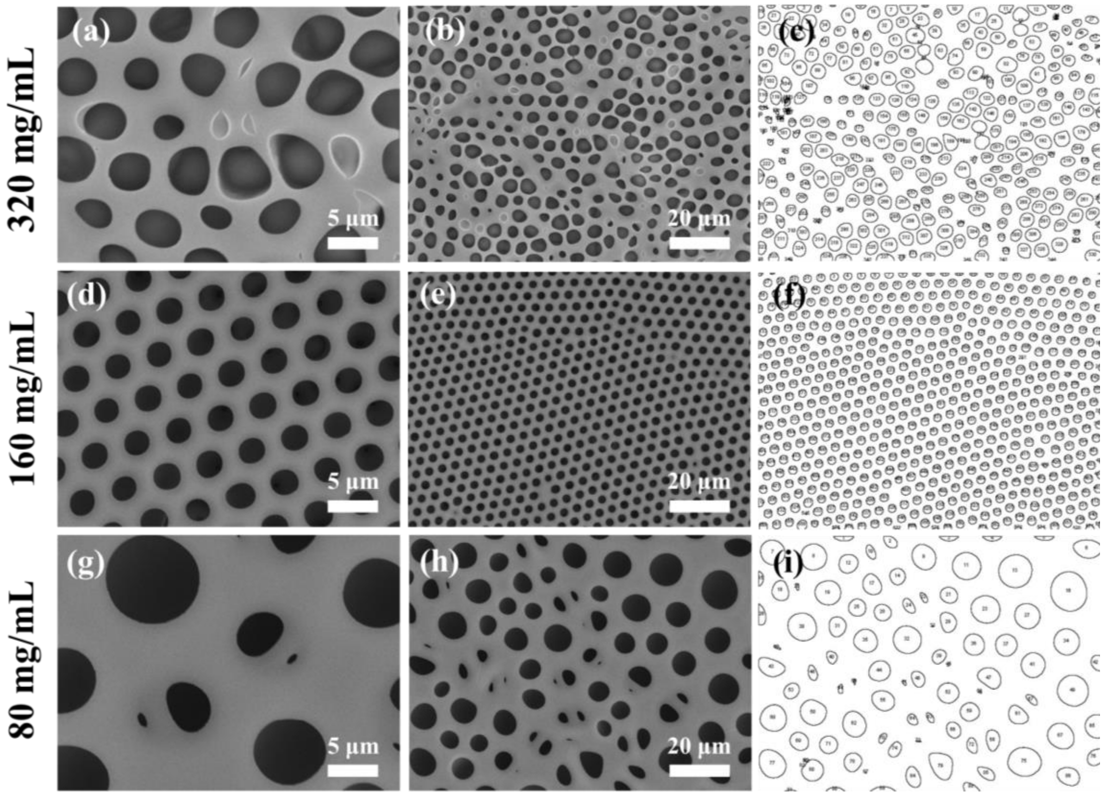

Figure 3. 12 Typical surface microstructures from PS-14/CHCl$_3$ solution with different concentrations, (a) 320 mg mL^{-1}, (d) 160 mg mL^{-1} and (g) 80 mg mL^{-1}. Their SEM images at a lower magnification are shown in (b), (e) and (h), respectively. And (c), (f), (i) are corresponding outline pictures of (b), (e) and (h) obtained by ImageJ

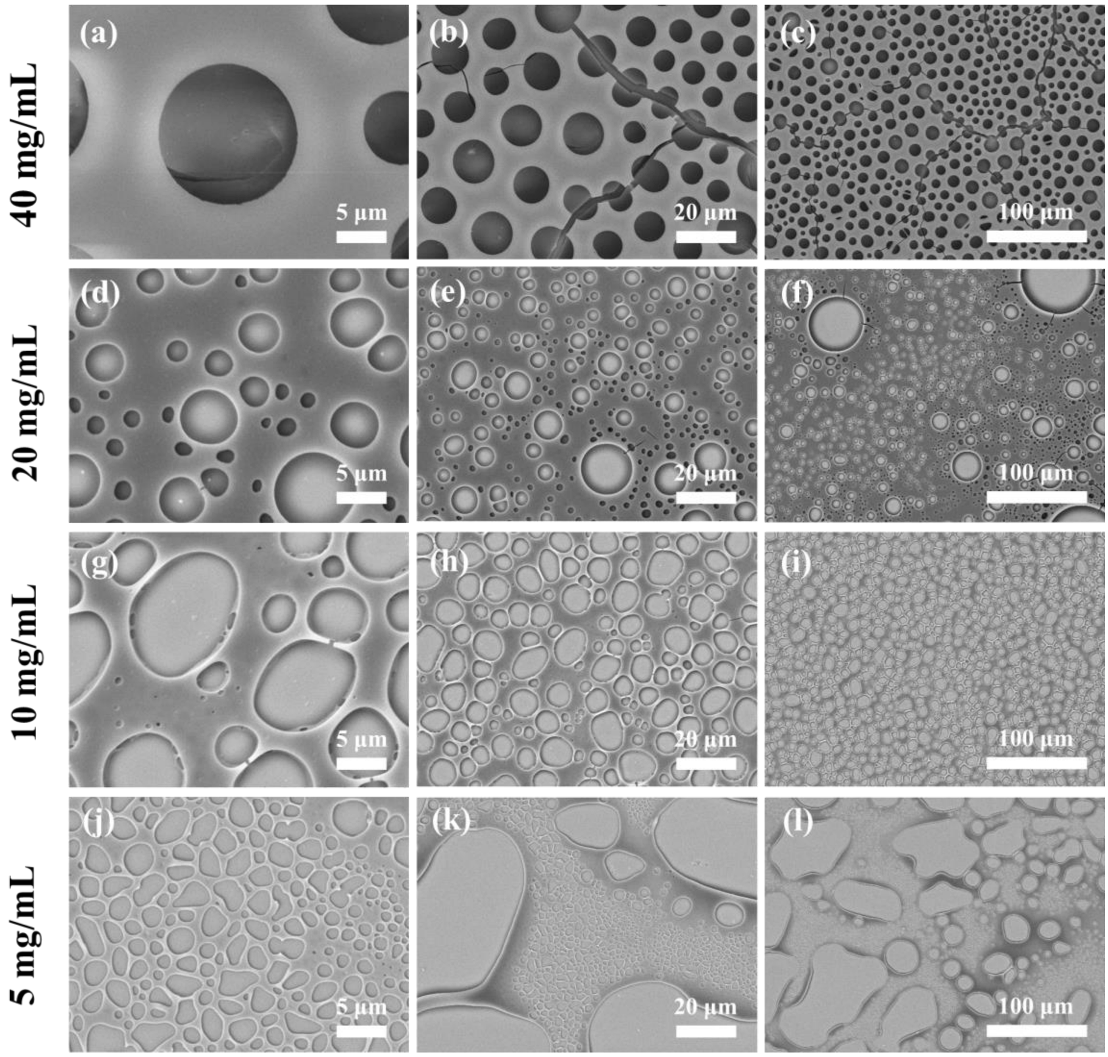

Figure 3. 13 Typical surface microstructures at different magnifications from PS-14/$CHCl_3$ solution with different concentrations, (a)-(c) 40 mg mL^{-1}, (d)-(f) 20 mg mL^{-1}, (g)-(i) 10 mg mL^{-1} and (j)-(l) 5 mg mL^{-1}

The pore analysis was performed based on the SEM images of polymer films prepared from 640 mg mL^{-1}, 320 mg mL^{-1}, 160 mg mL^{-1} and 80 mg mL^{-1}. Their analysis results were summarized and plotted against solution concentration, as shown in Fig. 3.14. The pore densities of polymer films cast from 80 mg mL^{-1} to 320 mg mL^{-1} range from 0.95 x 10^{10} m^{-2} to 6.00 x 10^{10} m^{-2}, which are much smaller that of polymer film prepared from 640 mg mL^{-1} (Fig. 3.14a). The pore size as well as the pore size distribution generally show a decrease trend with the increase of solution concentration (Fig. 3.14b). The size distribution of porous microstructures at 160 mg mL^{-1} is very narrow (SD = 0.39), and its average pore size is calculated as 2.55 μm. Polymer films prepare from solution between 80 mg mL^{-1} and 320 mg mL^{-1} have a surface porosity of up to 36.39% (Fig. 3.14c). Although the pore density of films obtained at 640 mg mL^{-1} is remarkably large, its pore size is very small (only 0.23 μm with a SD of 0.06), resulting in a low porosity (about 4.28%).

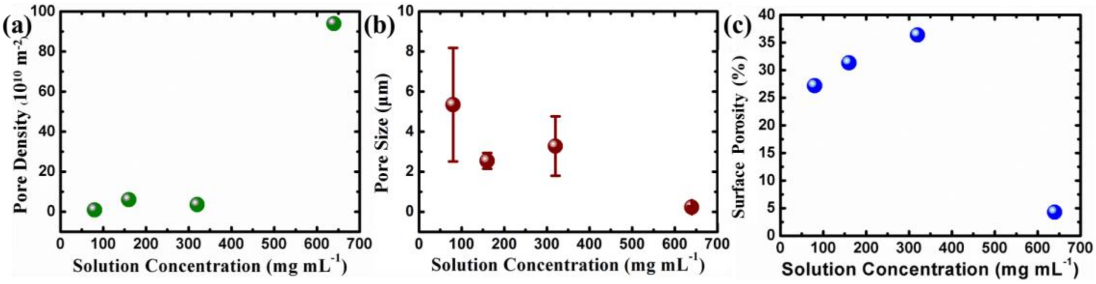

Figure 3. 14 Plot of the dependence of (a) pore density, (b) pore size and (c) pore proportion on the concentration of PS-14/$CHCl_3$ solution. The scale bars in (b) primarily represent the distribution of pore diameter

For PS-14/THF system, similar surface morphology evolution of polymer films is observed when its casting solution concentration increases from 5 mg mL^{-1} to 640 mg mL^{-1}. Polymer solutions with a high polymer content over 80 mg mL^{-1} lead to the formation of relatively regular porous microstructures (Fig. 3.15), while low polymer content solutions usually result in the generation of random and irregular pores. When the solution concentration was below 40 mg mL^{-1}, more and more irregular microstructures were obtained with the decrease of solution concentration (Fig. 3.16). Pore analysis was further performed on SEM images in Fig. 3.15b, e and h, which were converted into BW binary images for quantitatively evaluating the relatively regular porous microstructures (Fig. 3.15c, f and i). Their analysis results were summarized and plotted against the solution concentration over 80 mg mL^{-1}. The pore densities between 80 mg mL^{-1} and 320 mg mL^{-1} range from 2.03 x 10^{10} m^{-2} to 5.79 x 10^{10} m^{-2}, which are much smaller than that at 640 mg mL^{-1} (Fig. 3.17a). Their pore sizes and variations generally decrease with the increase of solution concentration (Fig. 3.17b). The average pore sizes at 80 mg mL^{-1}, 160 mg mL^{-1} and 320 mg^{-1} are 5.01 μm (SD = 1.20), 3.47 μm (SD = 0.86) and 2.97 μm (SD = 0.71), respectively. They are over a dozen larger than the pore size at 640 mg mL^{-1}. This significantly influences the final porosity of films. As shown in Fig. 3.17c, the surface porosity from 80 mg mL^{-1} to 320 mg mL^{-1} fluctuates between 42.27% and 46.04%, which is much larger than that at 640 mg mL^{-1} (only about 11.62%).

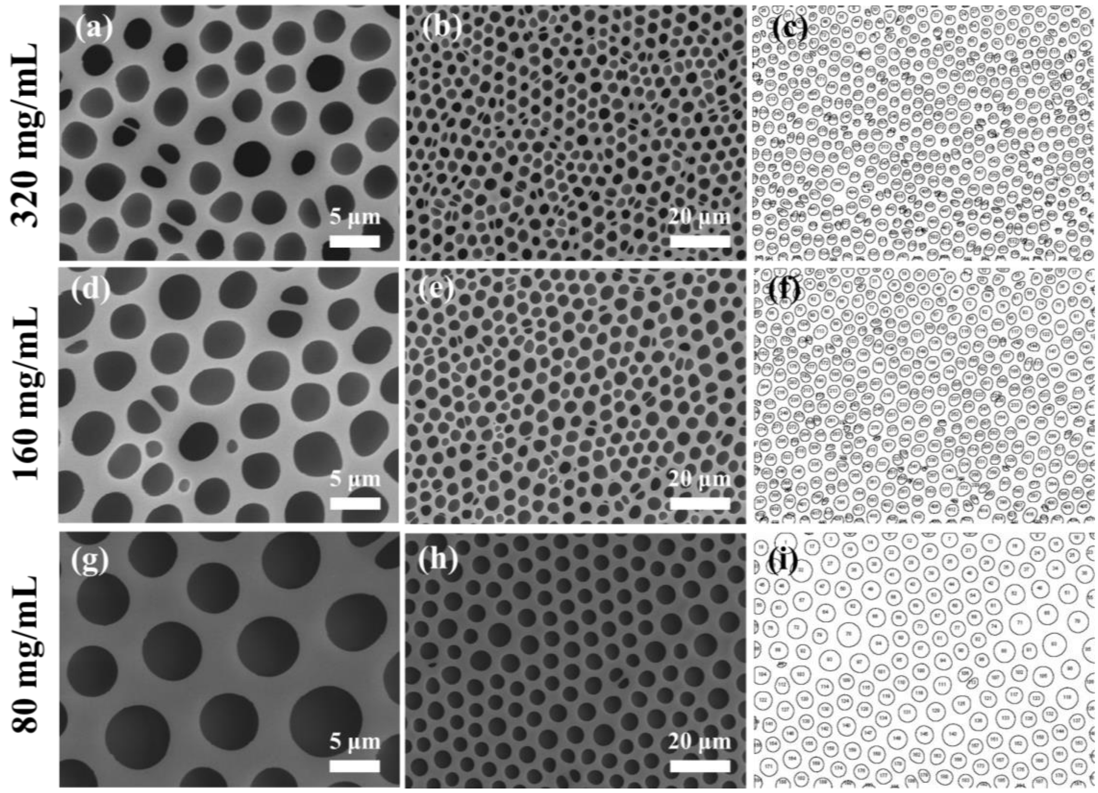

Figure 3. 15 Typical surface microstructures from PS-14/THF solution with different concentrations, (a) 320 mg mL^{-1}, (d) 160 mg mL^{-1} and (g) 80 mg mL^{-1}. Their SEM images at a lower magnification are shown in (b), (e) and (h), respectively. And (c), (f), (i) are corresponding outline pictures of (b), (e) and (h) obtained by ImageJ

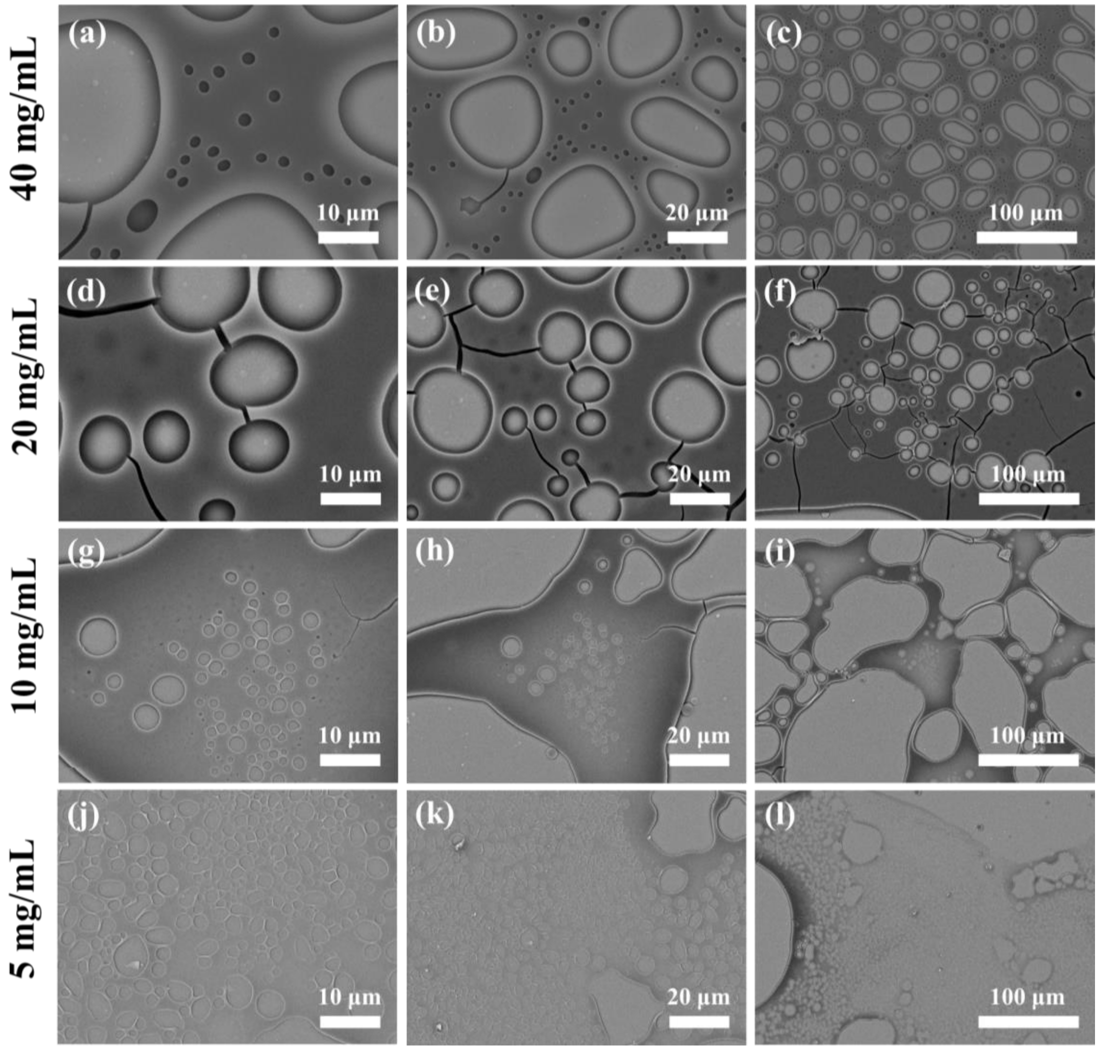

Figure 3. 16 Typical surface microstructures at different magnifications from PS-14/THF solution with different concentrations, (a)-(c) 40 mg mL^{-1}, (d)-(f) 20 mg mL^{-1}, (g)-(i) 10 mg mL^{-1} and (j)-(l) 5 mg mL^{-1}

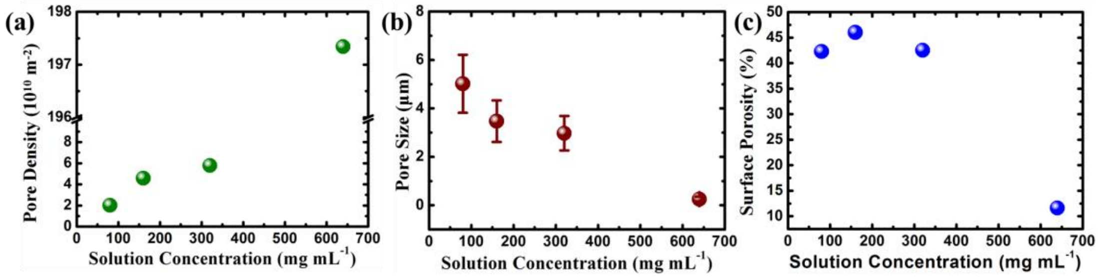

Figure 3. 17 Plot of the dependence of (a) pore number, (b) pore size and (c) pore proportion on the concentration of PS-14/THF solution. The scale bars in (b) primarily represent the distribution of pore diameter

3.3.2 Fabrication of microspheres by BF in MeOH vapor

3.3.2.1 The influence of CS_2 solution concentration

The polymeric microstructures by the BF technique under MeOH vapor were first studied from CS_2 solutions. Specifically, PS-14 was dissolved in CS_2 with a given concentration of 640 mg mL^{-1}. Then the obtained solution was gradually diluted with solvent by half to obtain a series of solutions with the concentrations of 320 mg mL^{-1}, 160 mg mL^{-1}, 80 mg mL^{-1}, 40 mg mL^{-1}, 20 mg mL^{-1}, 10 mg mL^{-1}, and 5 mg mL^{-1}. These solutions were cast on glass substrates under MeOH vapor, respectively. During the MeOH BF process, the shrinkage of PS solution on substrate was observed. Although the volume of casting solution was kept at the same, the finally resultant polymer film area from a low solution concentration was smaller than that from higher solution concentration. This indicated that, with the decrease of solution concentration, the shrink phenomenon became more serious, thereby resulting in the enrichment of polymers in a smaller area. For example, when a droplet of 40 mg mL^{-1} was cast on substrate, a liquid film area at square centimeter scale can be rapidly obtained by spreading. However, with the continuous evaporation of solvent, the finally obtained polymer area was shrunk at square millimeter scale. The resultant polymer films were revealed by SEM and are shown in Fig. 3.18. The panorama views in Fig. 3.18m, Fig. 3.18o and the insets of Fig. 3.18i and Fig. 3.18k clearly show that the polymer area decreases with the decrease of the solution concentration. This well demonstrates that more serious shrinkage phenomenon occurs during the MeOH BF process when the concentration of casting solution was at a lower concentration. All samples possess a porous surfaces regardless of solution concentration. However, in comparison to the pores with several micrometers formed in aqueous vapor, the resultant pores or holes are very irregular and ultra-huge. Their sizes range from dozens of micrometers to hundreds of micrometers.

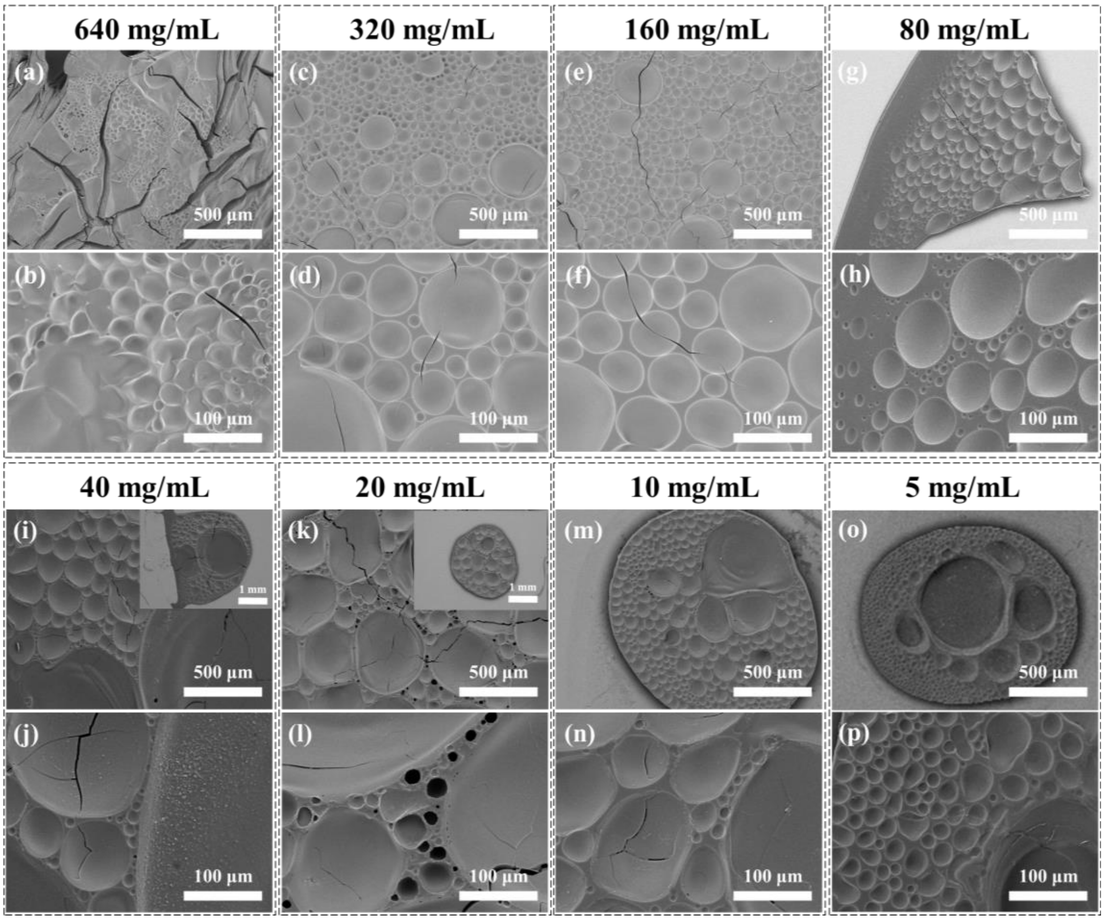

Figure 3. 18 Polymeric microstructures prepared by the MeOH BF technique from PS-14/CS_2 solution with (a) 640 mg mL^{-1}, (c) 320 mg mL^{-1}, (e) 160 mg mL^{-1}, (g) 80 mg mL^{-1}, (i) 40 mg mL^{-1}, (k) 20 mg mL^{-1}, (m) 10 mg mL^{-1}, and (o) 5 mg mL^{-1}. Their SEM images at a high magnification are shown in (b), (d), (f), (h), (j), (l), (n) and (p), respectively

$CHCl_3$ solution and THF solution at the concentration of 640 mg mL^{-1} were also prepared and cast on glass substrates by the MeOH BF technique, respectively. As stated above, the high viscosity of solution caused by high polymer contents would result in a difficult spreading behavior. This always leads to the formation of polymer membranes with thick layers. Fig. 3.19a and c reveal that the membrane surfaces prepared from both $CHCl_3$ solution and THF solution are decorated with numerous dimples. Further close views in Fig. 3.19b and d show their dimple sizes both roughly range within 5 μm. These surface microstructures are quite different from the large holes prepared from CS_2 solution.

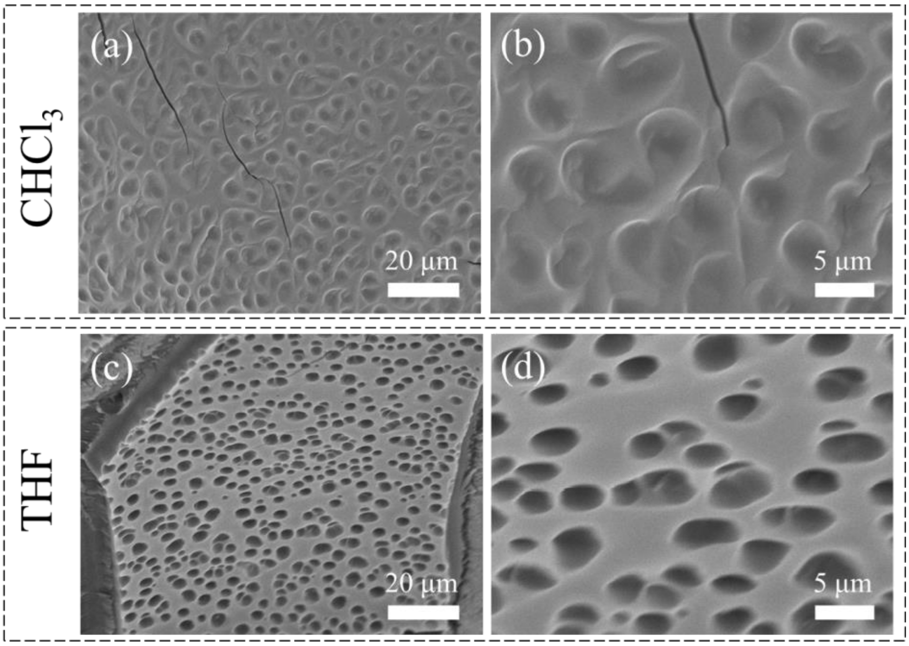

Figure 3. 19 Polymeric microstructures of PS-14 prepared by the MeOH BF technique from 640 mg mL^{-1} (a) $CHCl_3$ solution and (c) THF solution. SEM images at a high magnification are shown in (b) and (d) correspondingly

3.3.2.2 The influence of THF solution concentration

PS-14/THF solution was further diluted for studying the influence of solution concentration on the formation of polymer microstructures under MeOH vapor.

The shrinkage of solution film with the initial concentration of 320 mg mL^{-1} was not obviously observed by naked eyes during the MeOH BF process. An integral polymer stratum was finally obtained after complete evaporation of solvent. Fig. 3.20a shows that some polymers were left on substrate near the stratum edge. The close view demonstrates that they are dense separated microspheres (Fig.3.20d). The different regions on polymer stratum were also checked by SEM at higher magnifications. Two mains surface features, small dimples (Fig. 3.20b) and sparsely distributed microspheres (Fig. 3.20c) were observed. Similar polymer microstructures involving polymer stratums, dimples and microspheres substrates were also observed for PS solutions at 160 mg mL^{-1} (Fig. 3.20e-h) and 80 mg mL^{-1} (Fig. 30i-l). The area of microsphere region on substrate increases with the decrease of solution concentration, while the region area of polymer stratum shows an obvious decrease trend. The diameters of microspheres on substrate (excluding the microspheres on polymer stratum) were measured for further particle analysis, as shown in Fig. 3.22e-g.

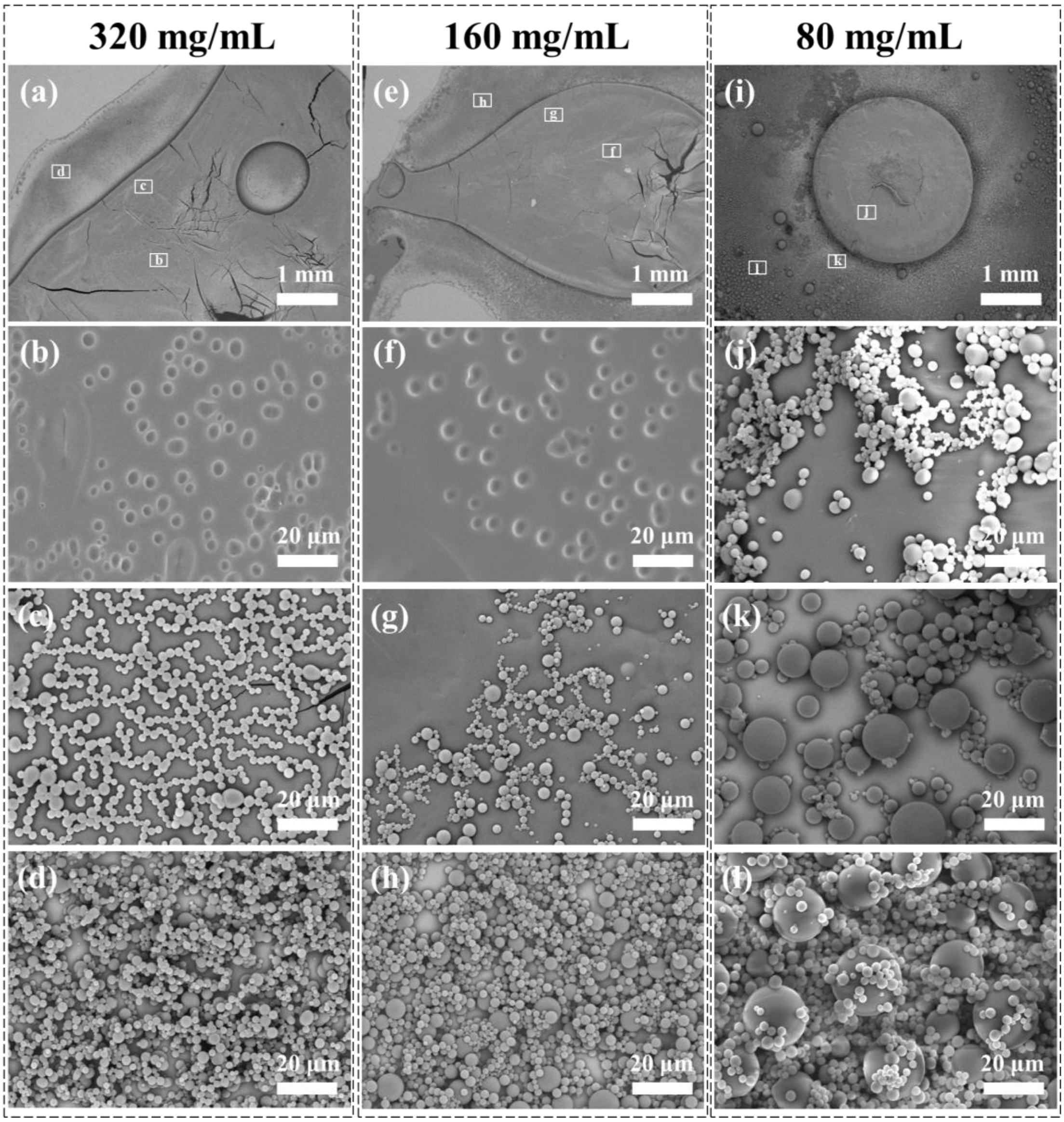

Figure 3. 20 Polymeric microstructures prepared by the MeOH BF process from PS-14/THF solution with (a) 320 mg mL^{-1}, (e) 160 mg mL^{-1} and (i) 80 mg mL^{-1}. (b)-(d), (f)-(h), and (j)-(l) are the magnifications of corresponding areas shown in (a), (e), and (i), respectively

The polymer stratum gradually disappeared with the further decrease of initial concentration of casting solution. Fig. 3.21 shows the polymeric microstructures prepared from 40 mg mL^{-1}, 20 mg mL^{-1}, 10 mg mL^{-1}, and 5 mg mL^{-1}, respectively. Only microspheres were observed for these samples. The resultant microsphere region was roughly as large as the spreading area of solution film. Microspheres with various sizes were observed at 40 mg mL^{-1} (Fig. 3.21a-c). And the particle size seems to become homogeneous with the decrease of solution concentration, as shown in Fig. 3.21d-f (20 mg mL^{-1}) and g-i (10 mg mL^{-1}). When the solution concentration was decreased to 5 mg mL^{-1}, no obvious large microspheres were observed, as shown in Fig. 3.21j-l.

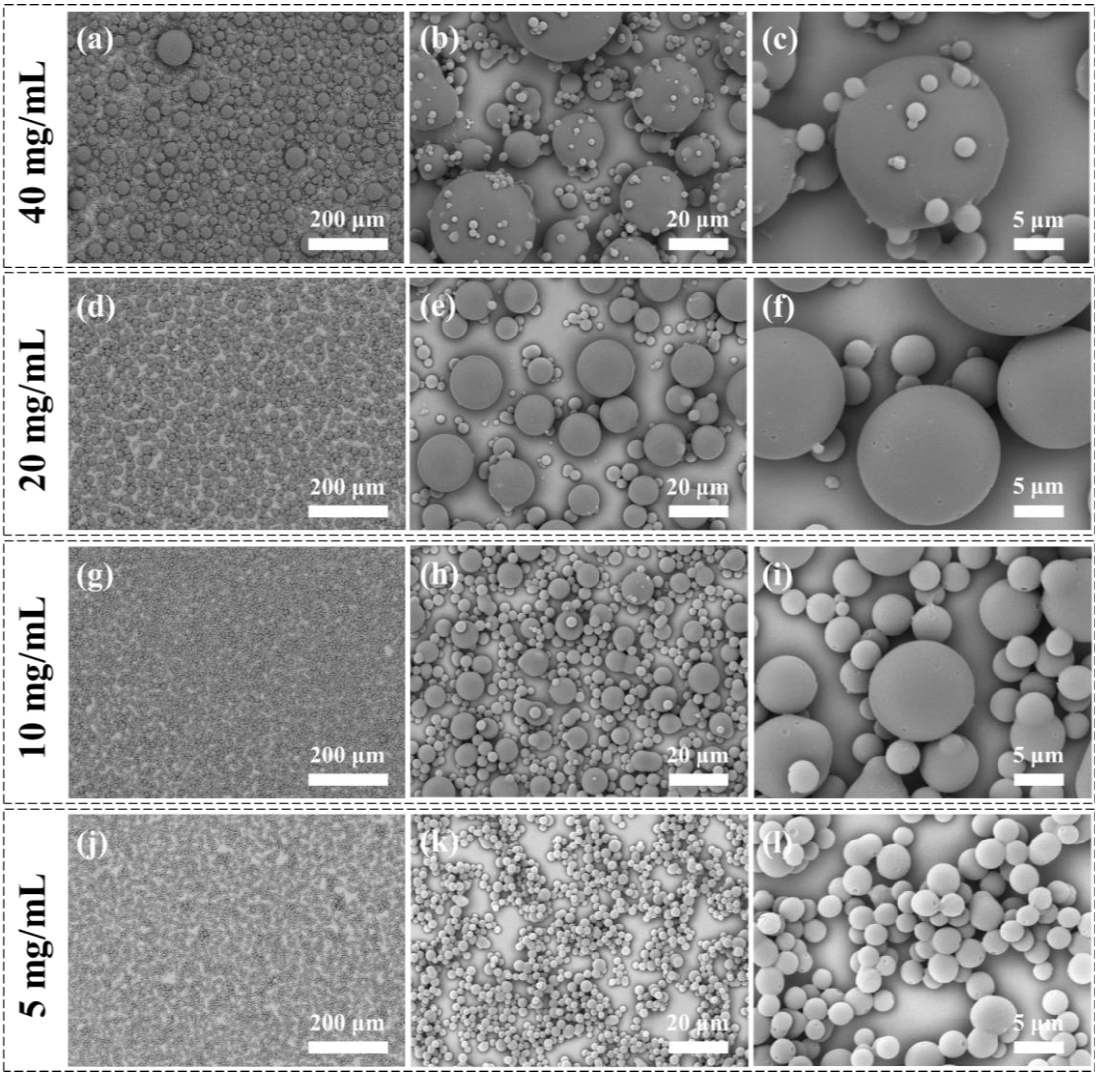

Figure 3. 21 Polymeric microspheres prepared by the MeOH BF process from PS-14/CS$_2$ solution with (a) 40 mg mL^{-1}, (d) 20 mg mL^{-1}, (g) 10 mg mL^{-1} and (j) 5 mg mL^{-1}. Their corresponding higher magnifications were shown in (b)&(c), (e)&(f),

(h)&(i), and (k)&(l), respectively

The diameters of microspheres on substrate were measured and grouped by every 1 μm in a histogram to give a direct and clear particle size distribution. The particle size distributions for the samples with the concentration of casting solution ranging from 5 mg mL^{-1} to 320 mg mL^{-1} are shown in Fig. 3.22a-g, respectively. And their average particle size and particle size distribution plotted against the solution concentration are shown in Fig. 3.22h. Fig.3.22a indicates that 83.72% of the resultant microspheres at 5 mg mL^{-1} mainly possess a diameter of 2 to 3 μm. The calculated average microsphere diameter is 2.55 μm, with a SD of 0.50 indicating a relatively narrow particle size distribution. At 10 mg mL^{-1}, the average size of microspheres increases to 3.95 μm with a SD of 1.88. The proportion of 2 ~ 3 μm microspheres reduces to 27.78%. And about 43.33% microspheres range from 3 to 4 μm. The particle size distribution becomes mere flat at 20 mg mL^{-1}. Microspheres with the size ranging from 1 to 20 μm can be observed. The proportion of 2 ~ 4 μm microspheres becomes less than half (47.11%). Due to the broad size distribution of microspheres, the obtained average particle size and SD are 5.55 μm and 4.03, respectively. The resultant microspheres from 40 mg mL^{-1} solution have a much broader size range from 1 to 39 μm, but 84.27% of them are between 2 and 4 μm. When the solution concentration was over 80 mg mL^{-1}, small microspheres with the particle size below 1 μm start to appear, but their proportions are all less than 5.0%. The sizes of microspheres at 80 mg mL^{-1} mainly range from 1 to 6 μm (80.10%), while 160 mg mL^{-1} and 320 mg mL^{-1} solutions both lead to the formation of relatively homogeneous microspheres. Their particle sizes are both concentrated on 1 μm~4μm, with a proportion of 89.52% and 94.59%, respectively. Correspondingly, their average microsphere diameters and SDs are 4.27 μm (SD = 3.04) at 80 mg mL^{-1}, 2.47 μm (SD = 1.20) at 160 mg mL^{-1}, and 2.17 μm (SD = 0.80) at 320 mg mL^{-1}, respectively.

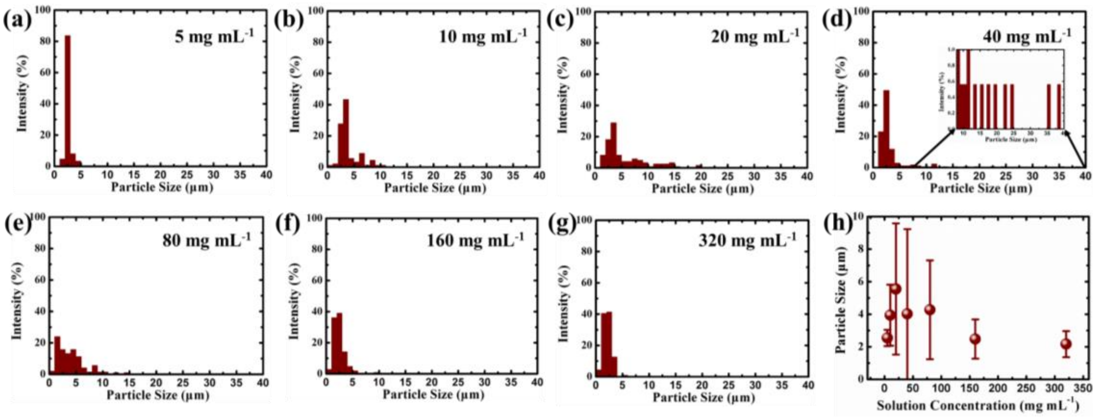

Figure 3. 22 The size distribution of polymeric microspheres prepared by the MeOH BF process from PS-14/THF solution with (a) 5 mg mL^{-1}, (b) 10 mg mL^{-1}, (c) 20 mg mL^{-1}, (d) 40 mg mL^{-1}, (e) 80 mg mL^{-1}, (f) 160 mg mL^{-1} and (g) 320 mg mL^{-1}. (h) the dependence of particle size on solution concentration. The particle diameter was measured and grouped by every 1 μm in histograms

3.3.2.3 The influence of $CHCl_3$ solution concentration

Replacing THF with $CHCl_3$ led to a similar surface morphology evolution with the decrease of solution concentration. When the concentration of PS-14/$CHCl_3$ solution varied between 80 mg mL^{-1} and 320 mg mL^{-1}, dense polymer stratums with separated microspheres sparsely distributed on substrates were obtained, as shown in Fig. 3.23. And dimple-like pores on the stratum surface were also observed. With the decrease of solution concentration, the region area of polymer stratum showed a decrease trend, and completely disappeared when the concentration of casting solution was decreased to 40 mg mL^{-1}.

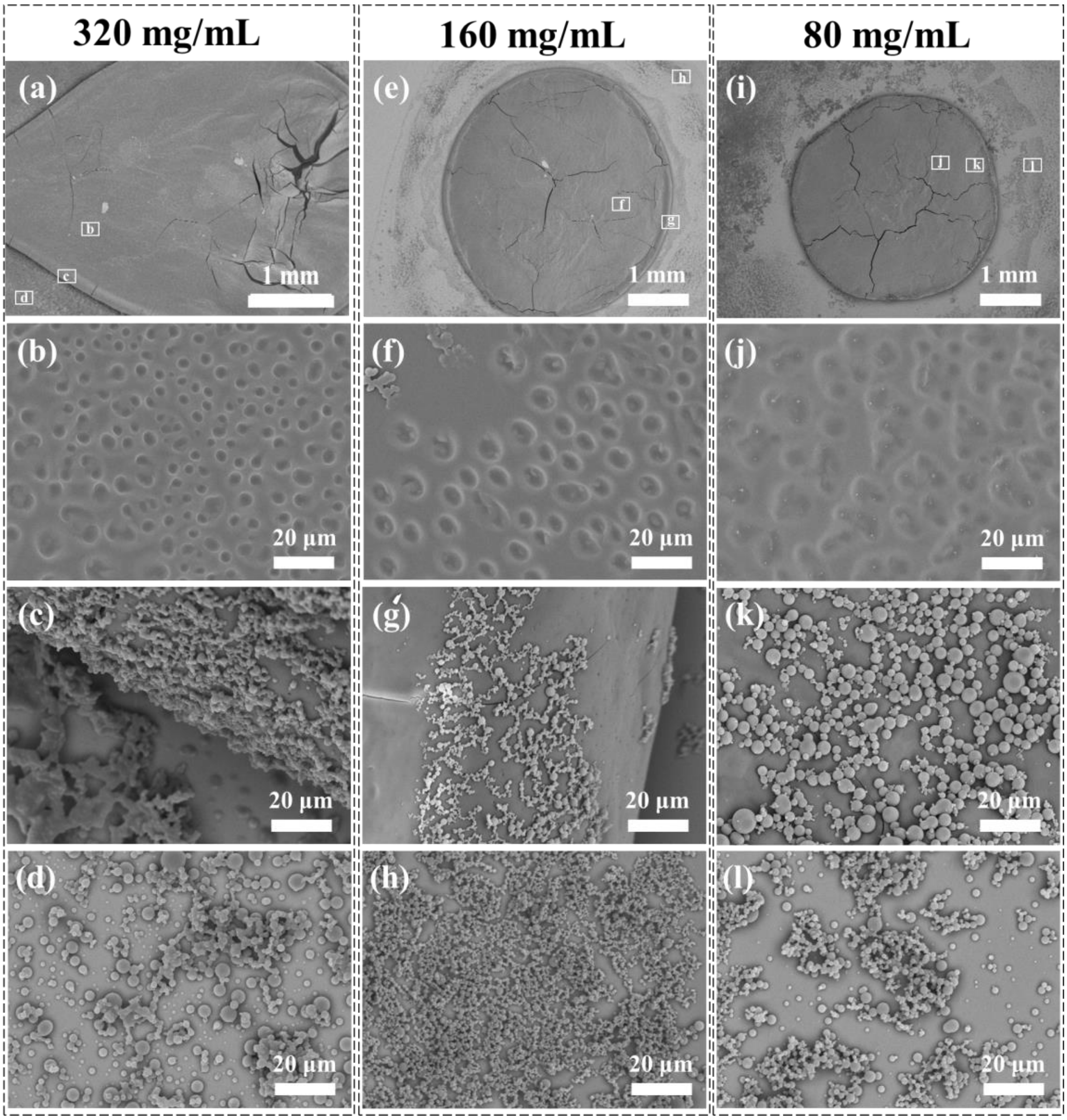

Figure 3. 23 Polymeric microstructures prepared by the MeOH BF process from PS-14/$CHCl_3$ solution with (a) 320 mg mL^{-1}, (e) 160 mg mL^{-1} and (i) 80 mg mL^{-1}. (b)-(d), (f)-(h), and (j)-(l) are the magnifications of corresponding areas shown in (a), (e), and (i), respectively

Only microspheres are observed for PS-14 samples prepared from the solutions below 40 mg mL^{-1}, as shown in Fig. 3.24. Their microsphere diameters were measured were measured for further particle analysis. And the analysis results are shown in Fig. 3.25a-d, respectively. These results clearly indicate that the diameters of microspheres all mainly varied between 1 and 3 μm. The proportions of microsphere size within this interval are 71.05% at 5 mg mL^{-1}, 76.14% at 10 mg mL^{-1}, 75.21% at 20 mg mL^{-1}, and 74.26% at 40 mg mL^{-1}. Although there are some small microspheres with the size below 1 μm at 40 mg mL^{-1}, the proportion is very small, which is less than 1%.

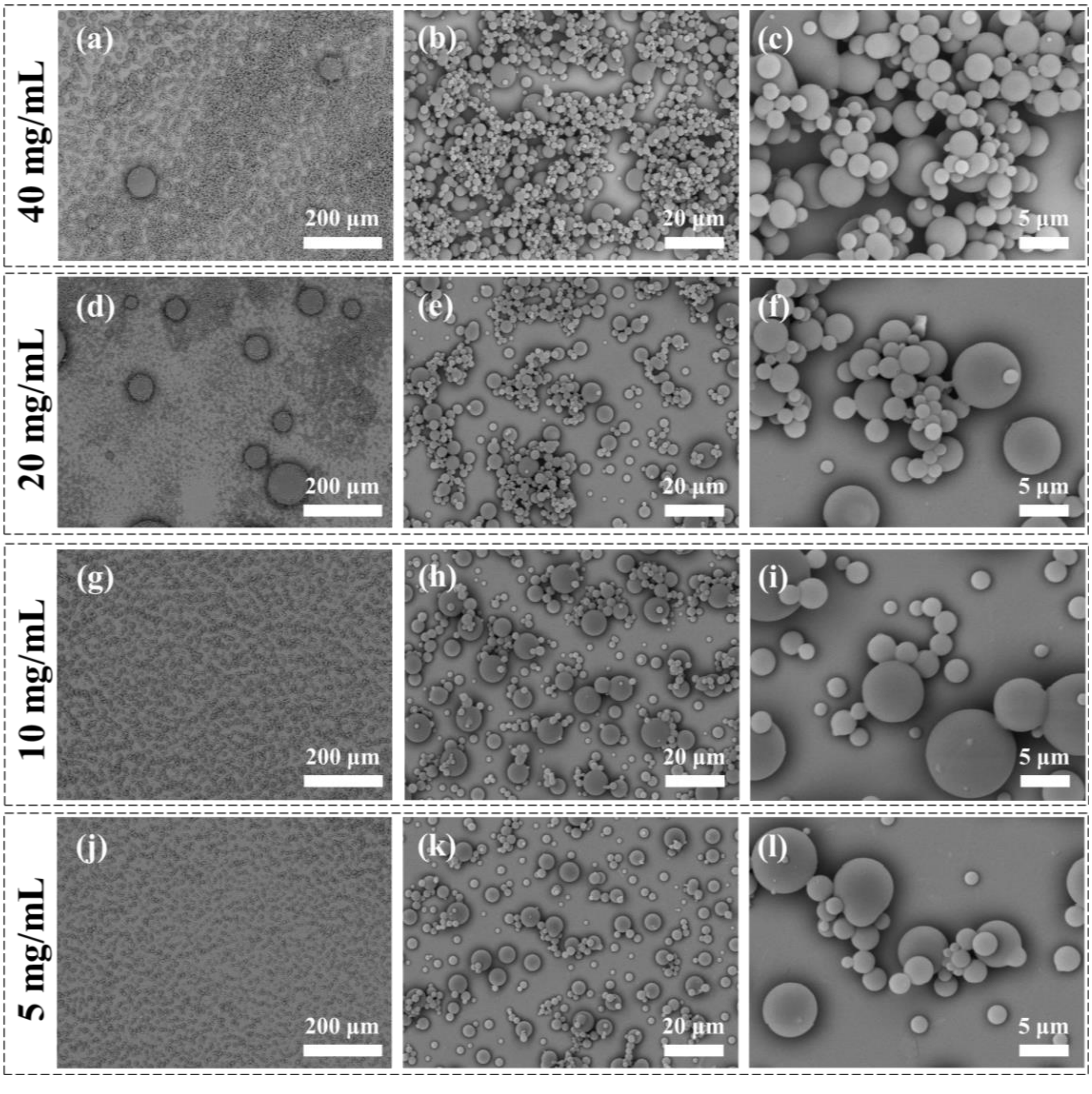

Figure 3. 24 Polymeric microspheres prepared by the MeOH BF process from PS-

14/CS_2 solution with (a) 40 mg mL^{-1}, (d) 20 mg mL^{-1} and (g) 10 mg mL^{-1} and (j) 5 mg mL^{-1}. Their corresponding higher magnifications were shown in (b)&(c), (e)&(f), (h)&(i), and (k)&(l), respectively

For the samples with the solution concentration over 80 mg mL^{-1}, the diameters of microspheres on substrate were also measured, which were summarized and grouped by every 1 μm in histogram. Fig. 3.25e-g show that the particle size generally shifts toward smaller value, mainly ranging between 0 and 2 μm. Their proportions are 76.51% at 80 mg mL^{-1}, 94.17% at 160 mg mL^{-1}, and 74.30% at 320 mg mL^{-1}. And among them, the proportions of microspheres with the diameter below 1 μm are 17.42%, 35.92%, and 34.72% respectively, which tends to increase with the increase of solution concentration. Fig. 3.25h shows the dependence of average particle size and particle size distribution on the concentration of casting solution. The calculated average microsphere diameters vary between 1.19 μm and 2.99 μm. They generally possess a decrease trend with the increase of solution concentration.

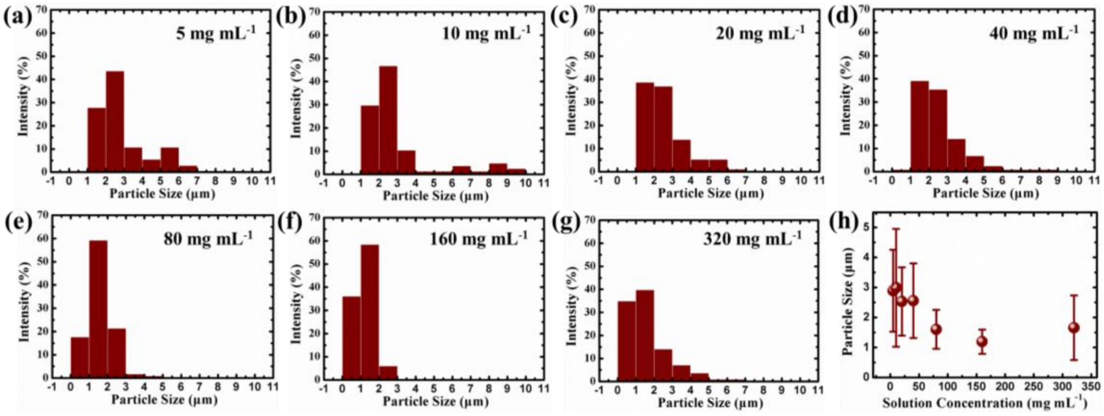

Figure 3. 25 The size distribution of polymeric microspheres prepared by the MeOH BF process from PS-14/$CHCl_3$ solution with (a) 5 mg mL^{-1}, (b) 10 mg mL^{-}

^{1}, (c) 20 mg mL^{-1}, (d) 40 mg mL^{-1}, (e) 80 mg mL^{-1}, (f) 160 mg mL^{-1} and (g) 320 mg mL^{-1}. (h) the dependence of particle size on solution concentration. The particle diameter was measured and grouped by every 1 μm in histograms

3.3.3 Fabrication of microspherical caps by BF in binary vapors of water and MeOH

To study the formation of polymer microstructures by binary BF technique, MeOH was further used as co-solvent to construct binary vapors of water and MeOH. The choice of MeOH as co-solvent is owing to its large surface tension difference and excellent water-miscibility. Through simply controlling the mixture ratio of MeOH to water, binary BFs with different properties and surface tensions can be adjusted.

3.3.3.1 The influence of M_n and solution concentration

The influences of M_n and solution concentration on the formation of polymeric microstructures were further studied by the BF technique under the binary vapors of water and MeOH. The MeOH weight ratio of binary liquids sealed in the vessel was fixed at 80%. PS-11, PS-14 and PS-20 were employed for the construction of polymeric microstructures in the binary vapors of MeOH and water. They were dissolved in THF for the preparation of 80 mg mL^{-1} solutions, and then cast on a glass substrate in MeOH/water binary vapors by the BF technique, respectively. After complete evaporation of solvent, they were coated with a thin gold layer for SEM observation. A novel asymmetrical particulate microstructure is surprisingly observed for all PS-11, PS-14 and PS-20 samples, as shown in Fig. 3.26a, d and g respectively. The resultant asymmetrical particles just look like a portion of a sphere cut off by a plane. Herein this novel microstructure is defined as microspherical cap because it is quite different from the microstructures prepared by the BF technique discussed before.

To study the influence of solution concentration, the three different solutions were further diluted to 40 mg mL^{-1} and 20 mg mL^{-1}, respectively. After the same binary BF process, the resultant polymeric microstructures revealed by SEM are shown in in Fig. 3.26b, e and h (40 mg mL^{-1}), and Fig. 3.26c, f and i (20 mg mL^{-1}), respectively. They all have a similar shape of microspherical caps at 80 mg mL^{-1}. These results confirm the direct formation of microspherical caps in the binary vapors of MeOH and water, and indicate that M_n and solution concentration were not the key factors on controlling the final shapes of particles under such experimental conditions.

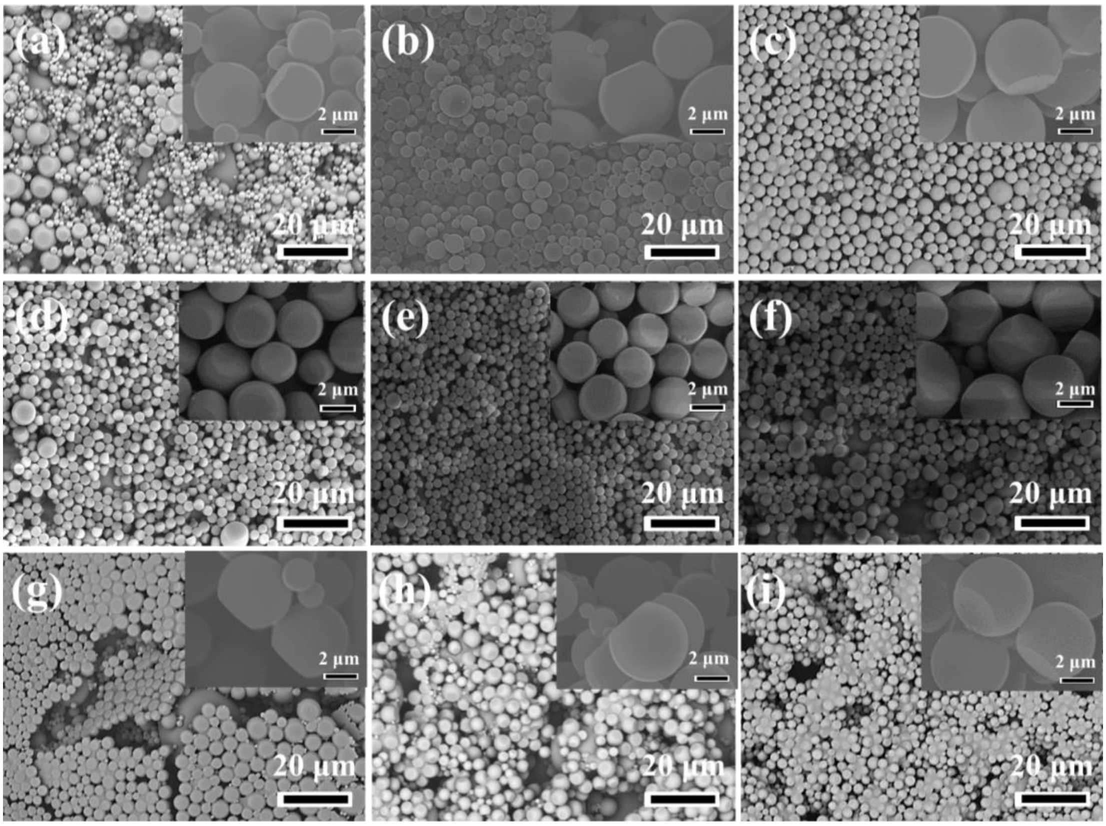

Figure 3. 26 Microspherical caps prepared in binary vapors generated by MeOH and water from (a) 80 mg mL^{-1}, (b) 40 mg mL^{-1} and (c) 20 mg mL^{-1} PS-11/THF solutions, (d) 80 mg mL^{-1}, (e) 40 mg mL^{-1} and (f) 20 mg mL^{-1} PS-14/THF solutions, and (g) 80 mg mL^{-1}, (h) 40 mg mL^{-1} and (i) 20 mg mL^{-1} PS-20/THF solutions, respectively. The ratio of MeOH was fixed at 80 wt%. The insets were close views of spherical caps correspondingly

The sphere diameters of microspherical caps prepared from PS with different molecular weights and solution concentration were also measured for statistical analysis. The resultant average particle size and particle size distribution are shown in Fig. 3.27. For PS-20 sample, its average particle size and particle size variation both have a decreasing trend with the decrease of solution concentration, while for PS-11 and PS-14 samples, no special relationships are found for the particle size with the solution concentration. PS-11 microspherical caps have a relatively wide distribution of particle sizes, which roughly fluctuates between 3 and 5 μm. The micropherical caps from PS-14 solutions all possess a homogeneous particle size, especially at 80 mg mL^{-1} and 40 mg mL^{-1}. They have a very similar average particle size of approximately 3 μm.

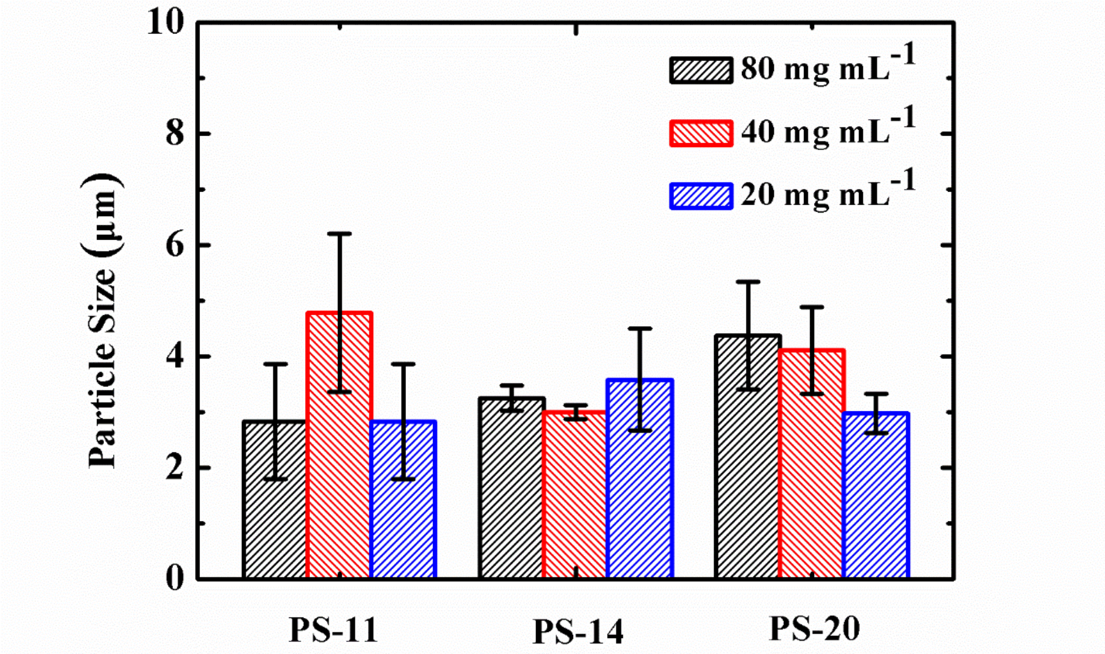

Figure 3. 27 The particle size and size distribution of microspherical caps prepared from PS with different molecular weights and solution concentration. The sphere diameter of microspherical cap was measured for statistical analysis

3.3.3.2 The influence of MeOH/Water ratio

PS-14/THF solution was fixed at 40 mg mL^{-1} to investigate the influence of MeOH/water ratios on the formation of microscpherical caps. The ratios of MeOH in MeOH/water liquids for the generation of binary vapors ranged from 95 wt% to 30 wt%. The typical microstructures prepared at different MeOH/water ratios of binary vapors are shown in Fig. 3.28. Different shapes of microspherical caps, like a sphere cut off by a plane at different positions, were obtained with the change of MeOH content. Specifically, polymer solution evaporated in MeOH/water vapor with a ratio up to 70 wt% tended to form the large portion of a sphere (Fig. 3.28a-e), while the ratio below 50 wt% led to obtaining the small portion of sphere (Fig. 328g-i). And hemispheres were observed around the ratio of 60 wt% (Fig. 3.28f). The morphology evolution clearly indicates that desired spherical caps can be prepared by elaborately tuning the components of binary BFs. Generally, the smaller portion of a sphere prefers to be formed in the binary vapors with lower MeOH ratio.

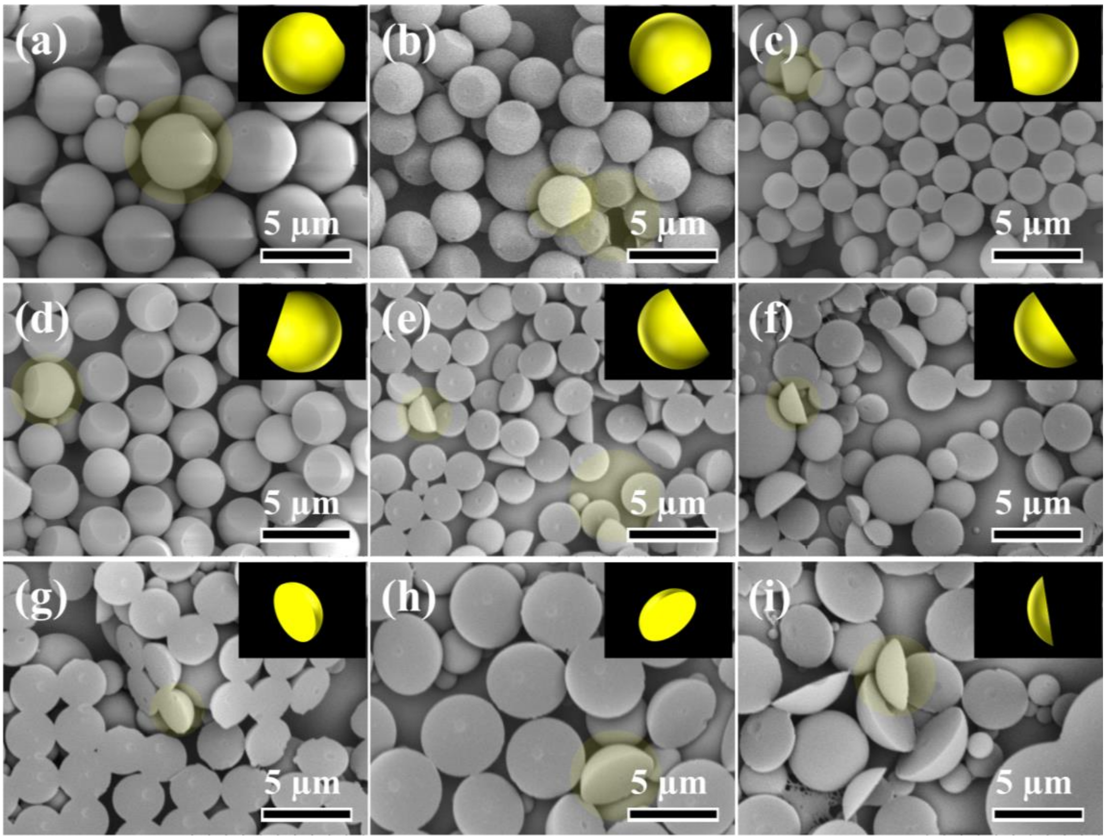

Figure 3. 28 Microspherical caps with tunable shapes prepared from evaporation of 40 mg mL^{-1} PS-14/THF solution in binary vapors generated by MeOH/water with different ratios. The weight ratios of MeOH were (a) 95%, (b) 90%, (c) 85%,

(d) 80%, (e) 70%; (f) 60%, (g) 50%, (h) 40%, and (i) 30%, respectively

Considering the different particle shapes, two kinds of particle size were measured for statistical analysis, namely the sphere diameter of large-portion microspherical cap and the base diameter of small-portion microspherical cap. They were summarized and plotted against the weight ratio of MeOH, as shown in Fig. 3.29. With the decrease of MeOH content, the former generally possesses a decrease trend while the latter shows an increase trend. The average sphere diameter of large-portion microspherical caps roughly ranges from 2.09 μm to 4.30 μm when the MeOH content was between 95 wt% and 70 wt%. It should be pointed out that the microspherical caps obtained at 80wt% and 70 wt% are very homogeneous, their average particle sizes are 2.96 μm and 2.30 μm, respectively. When MeOH content was decreased to 60 wt%, the resultant microspherical caps become small-portion. Their average base diameter is approximately 2.54 μm. With the content of MeOH further decreasing to 40 wt%, the average base diameter of resultant small-portion microspherical caps increases to 4.59 μm. Then at 30 wt%, the average particle size decreases slightly, but their particle size distribution becomes very broad.

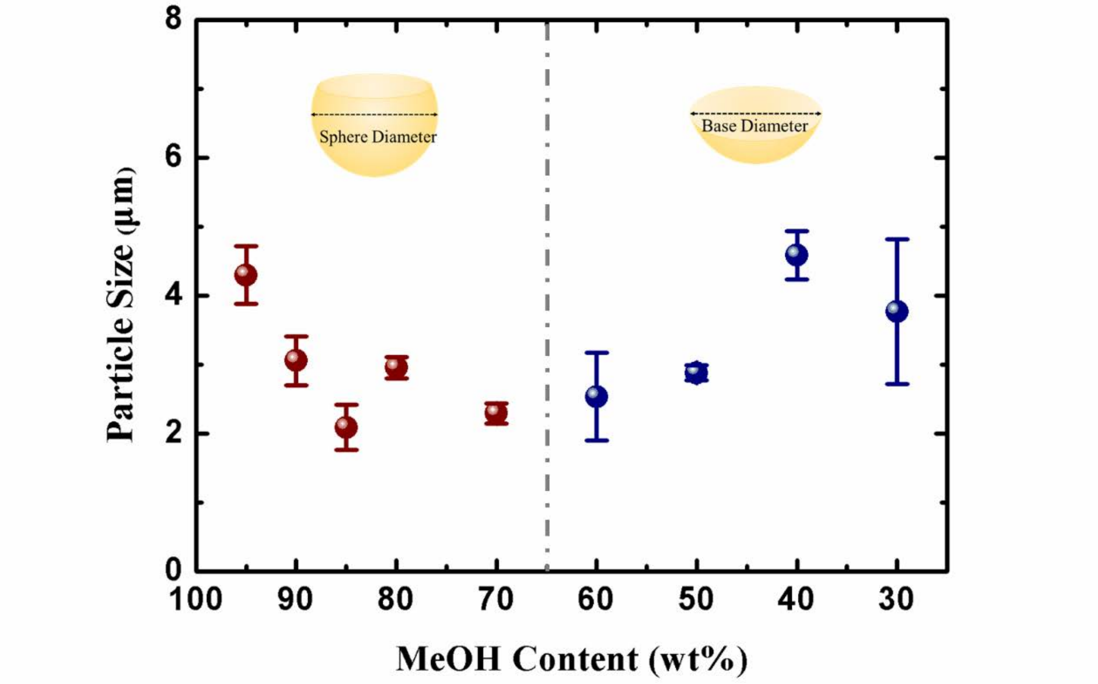

Figure 3. 29 The particle size of microspherical caps plotted against on the MeOH contents. The scale bars indicate the particle size distribution. The sphere diameter of large-portion microspherical cap and the base diameter of small-portion microspherical cap were measured for statistical analysis, respectively

3.3.3.3 The influence of solvent type

The influence of solvent types on the formation of microspherical caps by the binary BF technique was also investigated. When THF was replaced by $CHCl_3$, PS-14/$CHCl_3$ can lead to the formation of microspherical caps at 20 mg mL^{-1}. Through adjusting the ratios of MeOH and water, a similar evolution of microspherical caps from large portions to small portions was observed, as shown in Fig. 3.30. CS_2 solution was also cast on glass substrate under the binary vapors of MeOH and water by the BF technique. However, no microspherical caps were observed regardless of the concentration of casting PS/CS_2 solution. These results indicated that binary BFs were key factors for the successful formation of microspherical caps. And the formation of microspherical caps was also partially influenced by solvent types.

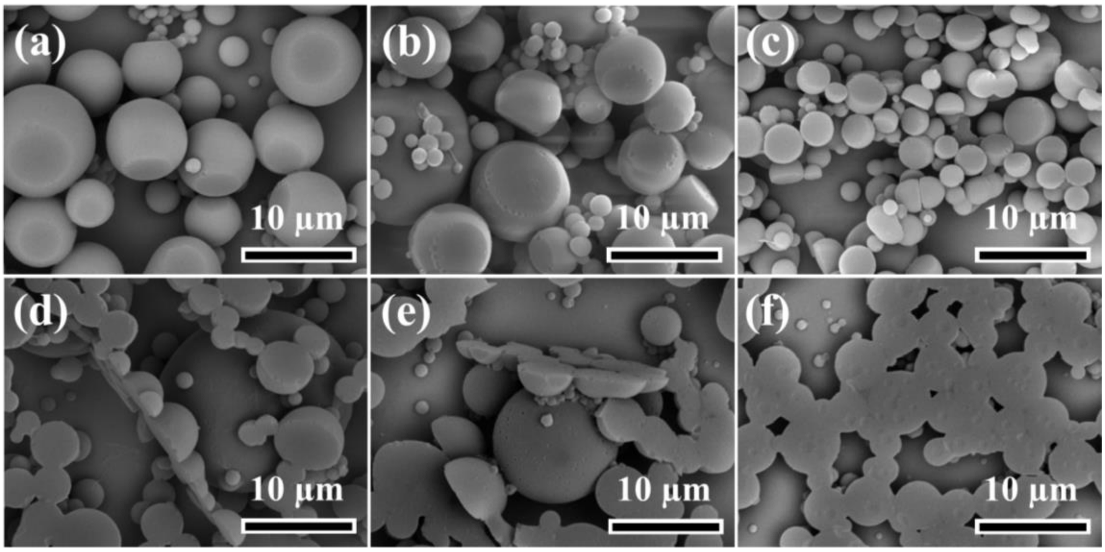

Figure 3. 30 Microspherical caps with tunable shapes prepared from evaporation of 20 mg mL^{-1} PS-14/$CHCl_3$ solution in binary vapor generated by different MeOH/water weight ratios: (a) 95/5; (b) 90/10; (c) 85/15; (d) 80/20; (e) 70/30; (f) 60/40

3.4 Formation mechanisms of different polymeric microstructures

Fig. 3.31 shows the principal procedures of a typical BF process for the fabrication of microstructured film from a droplet of polymer solution.

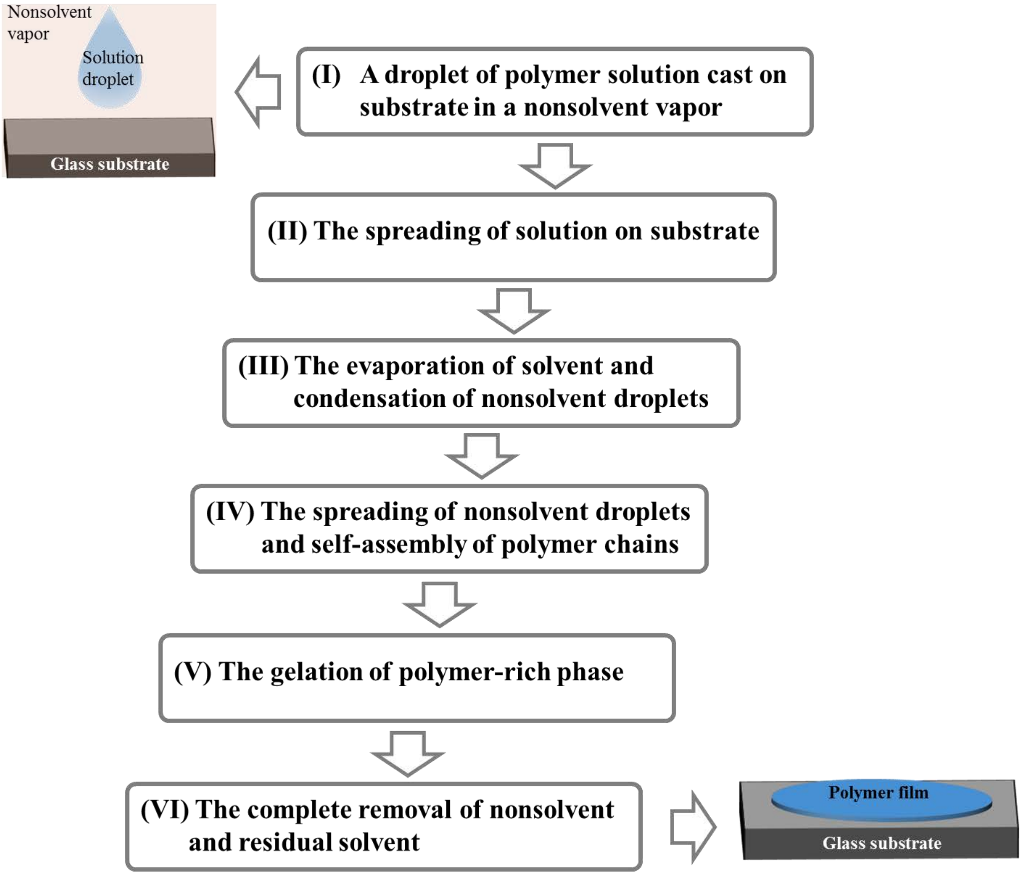

Figure 3. 31 Principal procedure of forming polymer film on substrate from a droplet of polymer solution by the BF process

3.4.1 The spreading of solution on substrate

When a droplet of liquid is placed on a solid substrate with flat surface, three associated forces at the liquid/vapor interface, solid/vapor interface and solid/liquid interface will drive it to spread on substrate for energy minimization, as shown in Fig. 3.32a. θ is the initial angle when the droplet contacts the substrate surface. After it reaches an equilibrium, the contact angle will become stable at θ'. Their relationships at equilibrium can be described by the following Young's Equation.[340]

$$\gamma_{sv} = \gamma_{lv} \cos(\theta') + \gamma_{sl} \qquad (1)$$

Where γ_{sv}, γ_{lv} and γ_{sl} are solid/vapor interfacial tension (or surface tension of solid substrate), liquid/vapor interfacial tension (or the surface tension of liquid), and solid/liquid interfacial tension, respectively. θ and θ' represent the contact angle between the liquid surface and solid surface at initial state and at the equilibrium state, respectively.

PS solution at low concentration can quickly spread out on the glass substrate to form a thin liquid film because the surface tension of pristine glass substrate is approximately 300 mN m^{-1} at room temperature, which is far larger than those of employed solvents and polymers (generally below 50 mN m^{-1}). After reaching at the equilibrium state, the contact angle will be very small and may even be close to zero, as shown in Fig. 3.32b. The viscosity of solution cannot be neglected when the solution concentration is very high. Because of the high solution viscosity caused by high polymer content, the spreading process will become slow on the glass substrate. With the evaporation of solvent and condensation of nonsolvent, the gelation time induced by nonsolvent may become shorter than the spreading time. And the spreading behavior terminates when the polymer solution becomes gelation. Therefore, polymer films with a thicker layer are usually obtained at a higher solution concentration of casting solution. Especially at 640 mg mL^{-1}, a polymer stratum with convex surface can be obtained. This is due to the slow spreading rate and short spreading time for polymer solution on substrate.

(a) A liquid droplet cast on substrate at initial state (b) A liquid film on substrate at the equilibrium state

Figure 3. 32 A thin liquid film formed on glass substrate from a droplet of liquid

3.4.2 Formation of nonsolvent BFs

Introducing nonsolvent onto the formed solution film from nonsolvent vapor is the primary requirement for the microstructure of polymer films. When a droplet of polymer solution cast on substrate under a nonsolvent vapor, the nonsolvent can be either directly drawn to the solution by the affinity with solvent or condensed onto the solution surface in the formation of nonsolvent BFs (droplets) through the evaporative cooling. The former way is obviously slow and inefficient. And considering the rapid process of the BF technique, the formation of nonsolvent BFs from its vapor is the main way for the introduction of nonsolvent onto solution. This is mainly determined by the vapor pressure of employed solvents and nonsolvents. Fig. 3.33 is the vapor pressure of different liquids at a temperature ranged from approximately -100 ºC to 100 ºC.[341] It shows that the vapor pressures of THF, $CHCl_3$ and CS_2 are higher than those of MeOH and water between -35 - 50 ºC. This indicates that the evaporation of the used solvents within this temperature can lead to the condensation of MeOH and water from their saturated vapors to form BFs. And according to the previous study, evaporative cooling of a low-boiling-point solvent can decrease the temperature of its solution surface as low as -6 °C. Therefore, during the film-formation process at the working temperature ranging from -6 °C to ambient temperature (about 25 °C), MeOH and aqueous BFs are always created onto the solution surface from the saturated vapor by the evaporative cooling of solvents.

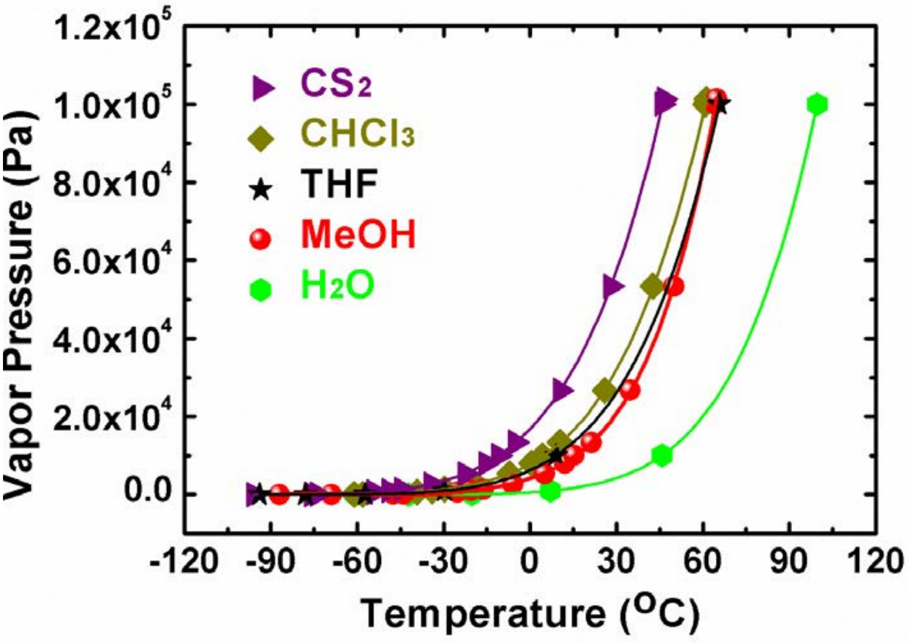

Figure 3. 33 Vapor pressures of solvents THF, CS_2 and $CHCl_3$, and nonsolvents MeOH and water plotted against temperature. The data were collected from CRC Handbook of Chemistry and Physics[341]

3.4.3 Influential factors of spreading behavior of BFs

When numerous nonsolvent BFs are condensed onto the solution surface, their spreading behaviors will determine the following phase morphology of polymer-rich phase and the self-assembly of polymer chains. This is similar to a droplet of solution cast on the glass substrate stated above. The difference is that the solid glass substrate is replaced by the soft solution film. Therefore, similarly, the surface tensions of liquid are used for illustrating the spreading behavior of

MeOH and water BFs in polymer solution. And for an explicit and direct explanation, a spreading coefficient ($S_{n\text{-}s}$) based on the surface and interfacial tensions of liquids is further employed.[342] Here $S_{n\text{-}s}$ is defined as Gibbs free energy change in spreading nonsolvent over a unit area of the solvent, and it is calculated as

$$S_{n\text{-}s}=\gamma_s-\gamma_n-\gamma_{n\text{-}s} \tag{2}$$

Where γ_s is the surface tension of solvent, γ_n is the surface tension of nonsolvent, and $\gamma_{n\text{-}s}$ is the interfacial tension between solvent and nonsolvent. $S_{n\text{-}s}<0$ stands for partial wetting, indicating that BFs tend to form spheres. $S_{n\text{-}s}>0$ stands for complete wetting, meaning that the nonsolvent BFs will spread on the solvent surface.

It is clear that $S_{n\text{-}s}$ is determined by γ_s, γ_n and $\gamma_{n\text{-}s}$. The surface tensions of used solvents and nonsolvents were plotted against temperature and are shown in Fig. 3.34. $\gamma_{n\text{-}s}$ is mainly dependent on the liquid-liquid miscibility between nonsolvents and solvents. Their Hansen Solubility Parameters (HSPs), involving Dispersion cohesion (solubility) parameter (δD, dispersion component), polar cohesion (solubility) parameter (δP, polar component), and hydrogen bonding cohesion (solubility) parameter (δH, hydrogen bonding component), were plotted in a three-dimensional model figure (Fig. 3.35).[343] Because the interaction radius (R) of PS is about 12.7 MPa$^{1/2}$, the HSPs of THF, $CHCl_3$, and CS_2 lie within the solubility sphere of PS, while the HSPs of MeOH, water and their binary mixtures lie outside of it.[343] This indicates that THF, $CHCl_3$, and CS_2 are good solvents for PS, while MeOH, water and their mixtures are poor solvents (nonsolvents) for it. These results are coincident with the experimental phenomenon. The solubility parameter distance between two liquids can also be directly employed for approximately evaluating their affinity with each other. The shorter distance between MeOH and solvents indicates that MeOH possesses higher affinity with solvents than water.[343] For example, water is immiscible with CS_2 and their HSP distance is the largest among different nonsolvent-solvent pairs, while MeOH is more miscible with it owing to the shorter distance.

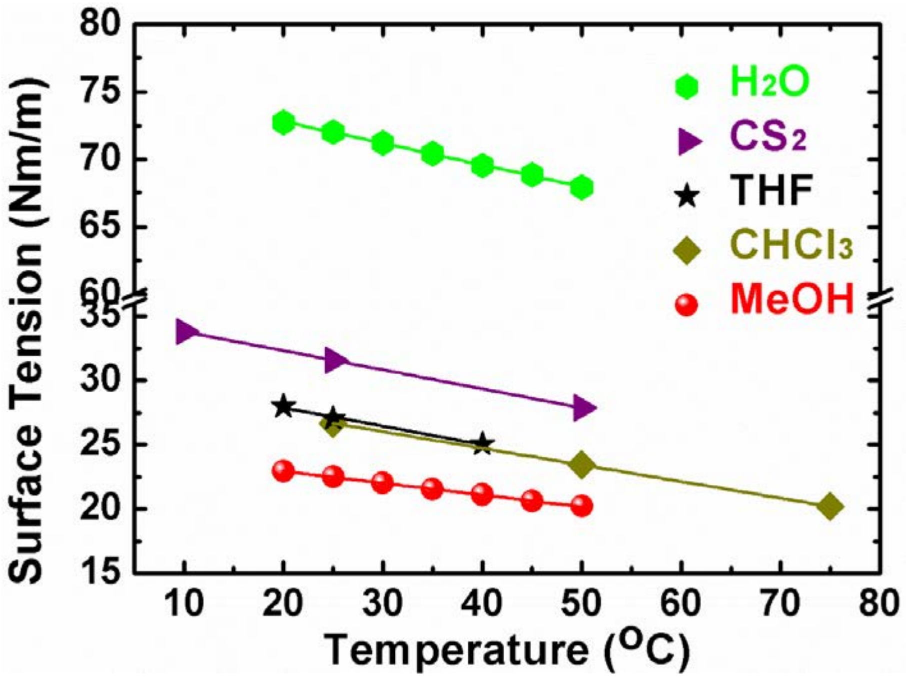

Figure 3. 34 Surface tensions of solvents THF, CS_2 and $CHCl_3$, and nonsolvents MeOH and water plotted against temperature. The data were collected from CRC Handbook of Chemistry and Physics[341]

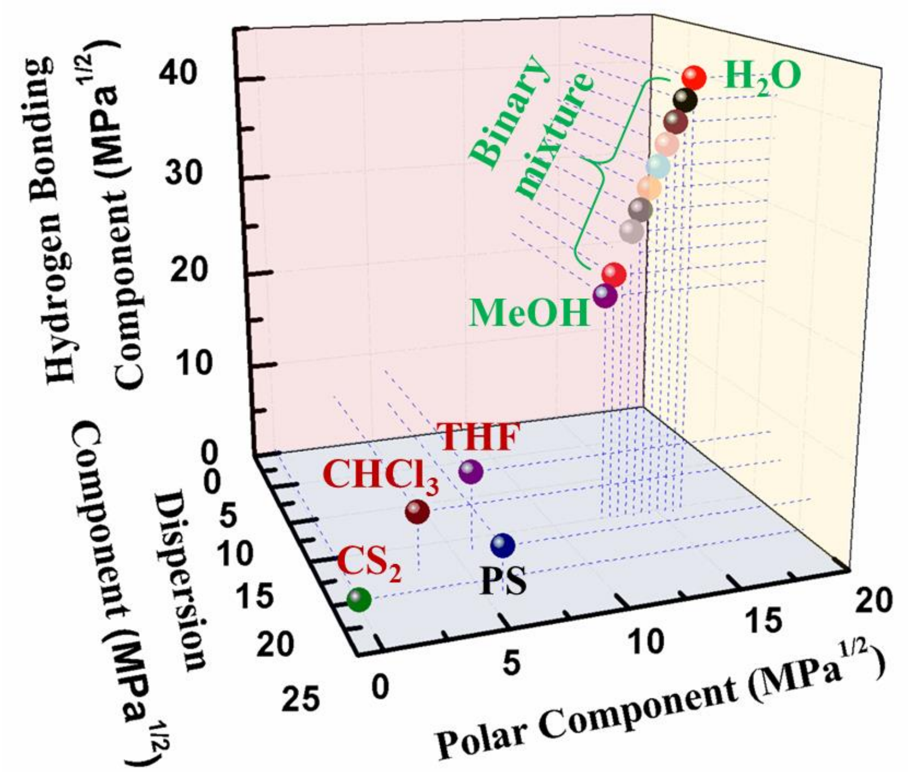

Figure 3. 35 Three-dimensional plot of the HSPs of PS (black letters), solvents (red letters), nonsolvents and binary nonsolvent mixtures (green letters) at 25 ºC, where each axis is one of the HSPs. The data were collected from Physics and Hansen Solubility Parameters: A User's Handbook[343]

3.4.4 Formation mechanism of honeycomb porous microstructures templated by aqueous BFs

Fig. 3.34 shows that water possesses the largest surface tension in a wide temperature range. Specifically, the surface tension of water (γ_w) ranges from 67.9 to 72.8 mN m^{-1} in the 20-50 ºC temperature range, while the surface tensions of used solvents (γ_s) involving CS_2, $CHCl_3$ and THF roughly vary from 20 to 30 mN m^{-1}. As γ_w is much larger than γ_s, and the interfacial tension between water and solvent ($\gamma_{w\text{-}s}$) are always positive (because water is less miscible with THF and

$CHCl_3$ than MeOH, and immiscible with CS_2), the spreading coefficient of aqueous BFs in a solvent is constantly negative ($S_{w\text{-}s}=\gamma_s-\gamma_w-\gamma_{w\text{-}s}<0$). The surface energy of PS ((γ_{PS}) is approximately 30 ~ 40 mN m^{-1}, which is similar to γ_s, and still much smaller than γ_w. Adjusting the solution concentration (polymer contents) can hardly change the surface tension of polymer solution in a significant range. Therefore, $S_{n\text{-}s}<0$ will always drive the water droplets on the solution surface to keep in a spherical shape. Water is a nonsolvent for PS. Through inducing the coiled PS chains aggregating and precipitating along the interface between water phase and polymer-rich phase, spherical water droplets act as templates for the formation of porous microstructures. This well explains why only porous microstructures are obtained in aqueous vapor regardless of the M_n of PS, solvent type and solution concentration.

For a polymer solution film in aqueous vapor, the evaporative cooling of the solvent leads to the condensation of small aqueous droplets which act as numerous nuclei for subsequent growth of spherical water droplets (Fig. 3.36a). In the beginning, the growth of water droplets is mainly dependent on the uptake of moisture from the surrounding water vapor. If the precipitated polymers cannot effectively stabilize the water droplets, later collision and coalescence of neighboring droplets will attribute to form water droplets with a larger size quickly (Fig. 3.36b). Actually, Beysens and Knobler have semi-quantitatively pointed out that the radius *R* of the water droplets on an oil surface dependent on time (*t*) is proportional to $R \sim t^{1/3}$ in the beginning, and then becomes $R \sim t$ at the end. With the decrease of solvent by evaporation and increase of water by condensation, more and more polymer chains will continually aggregate and precipitate at the interfaces between water droplets and polymer-rich phase until physical gelation occurs. This indicates that the precipitation of polymers plays a role of stabilizing the formed droplets. However, at gelation point, the effective growth of water droplets will be terminated. Further evaporation of solvent and condensation of water will have little influence on the phase morphology, but their exchange can enable the polymer-rich phase become more solidified. After complete evaporation of water and residual solvent, porous microstructures will be left on the glass substrate (Fig. 3.3.6c). Polymer solution with a higher concentration usually needs a shorter time to achieve the physical gelation state under the same BF conditions. This is because less nonsolvent requires to be introduced from the nonsolvent vapor by evaporative cooling. Therefore, the size of water droplets will possess a decrease trend with the increase of solution concentration. Namely, increasing the concentration of casting solution will lead to the decrease of pore size in the resultant polymer films. This generally coincides with the experimental results discussed before.

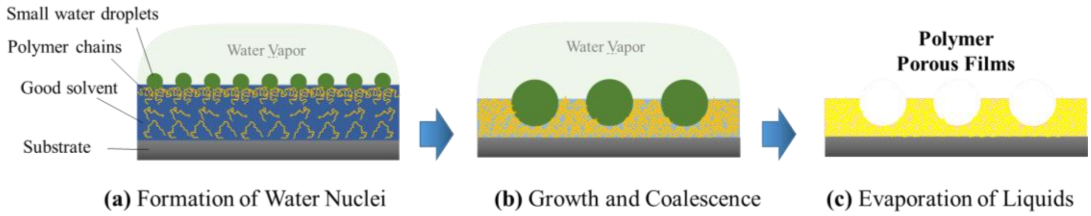

Figure 3. 36 Schematic diagram of the formation mechanism of polymer porous films in aqueous vapor by the BF technique

Benefiting from the softness and flexibility of liquid surface, the formed water droplets can move freely during the BF process by the drive of Marangoni convection and the capillary effect. The Marangoni effect is the mass transfer along an interface between two fluids caused by a surface tension gradient. When such mass transfer is induced by temperature gradient, it may also be called thermo-capillary convection.[344] The surface tension of water is much larger than those of employed solvents. The temperature is also different near the contact line and the center of solution film due to their different evaporation rates. And because the evaporation only occurs at the solution surface, the temperature at the solution surface is lower than that at the bottom of solution. Therefore, both surface tension gradient and temperature gradient exist during the BF process. The Marangoni convection plays an important role of driving the condensed water droplets to move and assemble at/in the solution film. Such convective motion among droplets can also suppress their coalescence. Moreover, the thin layer of air between two neighboring water droplets may act as a lubricant to avoid their coalescence. The capillary effect contributes to the attractive interactions among water droplets. The increase of water droplet size and/or the decrease of the distance between water droplets will increase the attractive force caused by capillary effect. When the water droplets cannot be separated stably, the merge of water droplets occurs. Therefore, the pore size and shape of film pores templated from the water droplets at gelation point can be regarded as the competitive results of Marangoni convection and the capillary interactions.

Under optimal BF conditions, such as proper solution concentration, the formed water droplets with homogenous size can self-assemble into regularly hexagonal arrays. This will lead to the formation of hexagonally ordered pore arrays with monodispersed size. However, irregular pores with a wide size distribution will be obtained when the solution concentration is either too low or too high. The resultant porous microstructures are especially irregular and disordered at a low solution concentration. This is because when the water droplets are self-assembled in a highly ordered state, the amount of polymers is too little for the immediate gelation of polymer-rich phase. When the polymer-rich phase achieves the gelation state, the size of water droplets becomes very large and the coalescence of water droplets is very serious. Therefore, irregular pores with very large size are always observed when the concentration of casting solution is small. While for the casting solution with a high polymer content, the gelation of polymer-rich phase generally occurs before the water droplets grow and self-assemble into regular arrays. This will lead to the formation of small pores with a relatively narrow size distribution.

Owing to the higher segment density, the nonpolar PS with a larger M_n are easier to precipitate along the water/solution surface at the same concentration of casting solution. The M_n of polymer plays a similar role of solution concentration on the formation of porous microstructures by the BF technique. Under specified BF conditions (such as fixed solution concentration), PS possessing an optimal M_n range can lead to the formation of homogeneous round pores arranged into regularly hexagonal arrays. If M_n is too low, PS chains will precipitate too late for the gelation of polymer-rich phase to stabilize the regular water droplets. While M_n is too high, the gelation of polymer-rich phase will occur before the water droplets become homogeneous and ordered.

CS_2 and $CHCl_3$ are more workable than THF for the preparation of ordered porous microstructures. This is due to their different vapor pressure, surface tension, and miscibility (or affinity) with water. Solvents with high vapor pressure and water immiscibility are conducive to the condensation and stabilization of water droplets. And the condensed water droplets more prefer to keep a spherical shape on the solvent film with less surface tension. Therefore, under optimal BF conditions, both CS_2 and $CHCl_3$ can lead to the formation of round pores arranged in regularly hexagonal arrays, while the porous microstructures prepared from THF solution are generally less regular and ordered. This can be ascribed to the high miscibility of THF with solvent, which results in less ability of stabilizing the formed water droplet shapes and arrays. Briefly, under similar BF conditions, CS_2 and $CHCl_3$ tend to form more regular BFA arrays with relatively smaller pore size, while the obtained BFAs prepared from THF are irregular and disordered, but they have a larger surface porosity.

The pore density and surface porosity of polymer films are greatly dependent on the concentration of casting solution. At the initial stage of BF process under the same conditions (involving the same humidity, temperature and solvent), the density of water nuclei condensed onto the liquid film with different solution concentrations can be regarded as the same. With more water introduced by the continue evaporation of solvent, the formed water nuclei will grow to obtain large-size droplets. The collision and coalescence of neighboring droplets also occur during this period. This will lead to the formation of water droplets with larger size, but result in the decrease of total number of water droplets. The time of achieving the gelation point (gelation time) determines the final number of water droplets. Generally, the shorter the gelation time is, the less the water droplet number decreases. Therefore, the pore number of films generally decreases with the decrease of solution concentration due to the gradual increase of gelation time. The proportion of porous area to solid area (i.e. surface porosity) in the polymer film is roughly equivalent to the ratio of nonsolvent phase to the polymer-rich phase at gelation point. The general increase of surface porosity with the decrease of solution concentration can also ascribed to the gelation time. Polymer solution with a lower concentration allows a longer gelation time for the condensation of more nonsolvent. This contributes to increasing the proportion of nonsolvent phase, and finally leading to the increase of porous area in the resultant polymer film.

3.4.5 Formation mechanism of Microspheres induced by MeOH BFs

The surface tension of MeOH (γ_m) ranges from 20.2 to 23.0 mN m^{-1} between the temperature of 20 °C and 50 °C. The excellent linear fitting indicates that the surface tension of liquid decreases with the increase of temperature, and the surface tensions of solvents (γ_s) are always above γ_m, as shown in Fig. 3.34. Considering the high miscibility of MeOH with THF and $CHCl_3$, the interface tensions between MeOH and solvent ($\gamma_{m\text{-}s}$) are regarded as zero. Therefore, the spreading coefficient of MeOH BFs in a solvent is always positive ($S_{m\text{-}s}=\gamma_s-\gamma_m>0$). This drives the generated MeOH BFs to spread as a film on the solution surface. And owing to the high miscibility of MeOH to solvent, MeOH BFs will then quickly and homogeneously dissipate into the solution. MeOH is a poor solvent for PS. Its introduction results in the extended polymer chains in a good solvent becoming compact coils. The aggregation of some coiled chains leads to the formation of nuclei (Fig. 3.37a). With the decrease of solvents caused by evaporation and increasing condensation of MeOH caused by evaporative cooling, they induce the symmetrical growth of polymer microspheres by continually aggregating the precipitated polymer chains until gelation occurs (Fig. 3.37b). After gelation, further evaporation of solvent and condensation of MeOH will have little influence on the phase morphology, but enable the microsphere phases become more solidified. Finally, the formed polymer microspheres will be left on substrate after complete evaporation of liquids, as shown in Fig. 3.37c.

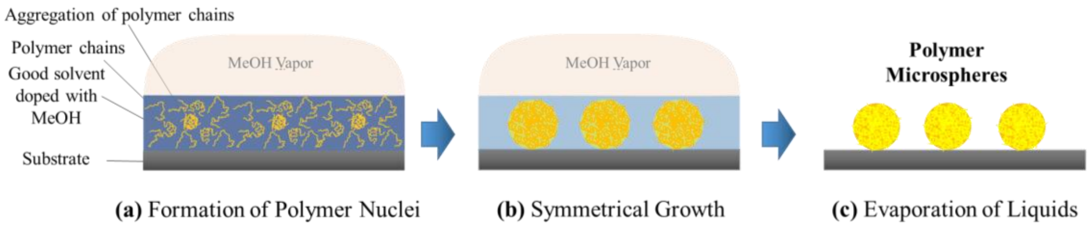

Figure 3. 37 Schematic diagram of the formation mechanism of polymer microspheres in MeOH vapor by the BF technique

High miscibility of solvent with MeOH is the primary requirement for the successful formation of microspheres by the BF technique under MeOH vapor. As demonstrated above, no microspheres but large holes in most cases have been observed for PS samples prepared from CS_2 solutions regardless of the solution concentration. This is ascribed to the less miscibility of nonpolar CS_2 with polar MeOH. Although $S_{\mathrm{m\text{-}CS2}}>0$ can drive the MeOH BFs to spread as a film on the solution surface, the low miscibility disables the penetration of condensed MeOH into polymer/CS_2 solution. Consequently, the formation of polymer nuclei cannot be effectively induced for further growth of polymer particles. Instead, with the evaporation of solvent and condensation of MeOH, the solution will be driven to shrink wholly. During the shrinking process, some of the condensed MeOH BFs gather together to form large liquid droplets and float on the solution surface, which finally results in the formation of large holes on the seriously shrunken polymer film.

Like the aqueous BF process, the gelation time dependent on the solution concentration also plays a significant role on the formation of polymer microstructures by the MeOH BF technique. When the casting solution is at an ultrahigh concentration, polymer gelation will quickly occur from the solution surface to the inner. The condensed MeOH droplets are difficult to spread and dissipate into the solution. Therefore, regardless of solvent type, only dimple-like pores are observed for the samples prepared at 640 mg mL^{-1}. When the solution concentration is not very high, the solution will tend to shrink from the edge to center gradually driven by $S_{\text{m-s}}$ until gelation occurs. The self-assembly of polymer microspheres will meanwhile start from the edge of solution film. Therefore, polymer film with numerous microspheres distributed around the edge and a dense stratum at the center can be observed on substrate. The decrease of solution concentration will lead to the increase of microsphere region and the decrease of the polymer stratum region owing to the increase of gelation time. When the gelation time is long enough for all polymer microspheres to finish their self-assembling process, the polymer stratum will totally disappear. Therefore, polymer films composed of whole microsphere region can be obtained under a specified solution concentration. The decrease of solution concentration includes two opposite roles on the growth of polymer microspheres: (a) the increase of growth time (determined by gelation time) and (b) the decrease of solute. Therefore, if the solution concentration is too low, although the growth becomes very long, there is no enough solute for microspheres to increase their sizes.

3.4.6 Formation mechanism of microspherical caps induced by binary BFs

The well understanding of the formation mechanisms of polymer microspheres in pure MeOH vapor and porous microstructures in aqueous vapor can contribute to exploration of the formation mechanism of microspherical caps in binary vapors of MeOH and water, though the spreading behavior of the binary BFs in the latter system is more complex than the simplex BFs in the former two systems. Fig. 3.38 shows that the surface tension of MeOH/water (γ_{mw}) mixtures gradually decreases with the increase of MeOH content. The γ_{mw} becomes smaller than the surface tension of THF (γ_{THF}) after increasing to 70 wt%. This indicates that at a high MeOH ratio the binary BFs tend to spread as a film on the solution surface. Owing to the higher affinity with THF, MeOH penetrates and diffuses into polymer solution more quickly than water. This would make MeOH, water and solvent to form a gradient layer at the vapor/solution interface, as illustrated in Fig. 3.39A-i. At the center of interface layer, water is the dominant component because MeOH prefers to quickly diffusing into solution. Polymer chains become compact coils due to the introduction of poor solvents, aggregate at the formed interface to lessen the interface tension, and thereby give rise to the formation of nuclei. With the solvent evaporated and more nonsolvent introduced, they induce the asymmetrical growth of polymer particles at the air/solution interface by constantly assimilating the precipitated polymers (Fig. 3.39A-ii) until gelation occurs. After complete evaporation of liquids, large-portion microspherical caps will be left on the substrate (Fig. 3.39A-iii). The water component at the interface layer can be increased by decreasing the MeOH ratio in the binary vapors (Fig. 3.39B-i), resulting in the formation of larger nuclei (Fig. 3.39B-ii). And due to more water existing, the time for gelation becomes shorter, which disables the sufficient growth of particles. This finally leads to the formation of microspherical caps with a smaller portion (Fig. 3.39B-iii). Therefore, microspherical caps with different shapes including hemispheres can be prepared by simply adjusting the MeOH ratio of binary BFs. Owing to their close miscibility and surface tension, similar results can also be obtained by replacing THF with $CHCl_3$. However, nonpolar solvent CS_2 cannot lead to form microspherical caps due to its poor miscibility with nonsolvents.

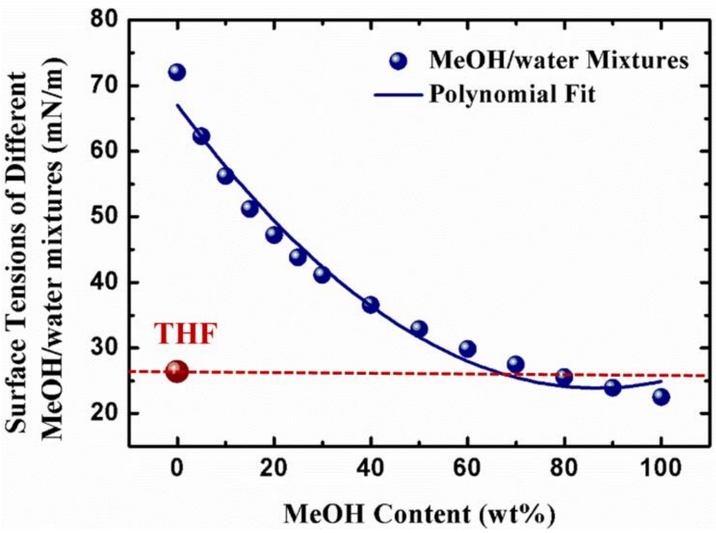

Figure 3. 38 The dependence of the surface tensions of MeOH/water mixtures on the MeOH content at 25 ºC. The data were collected from CRC Handbook of Chemistry and Physics[341]

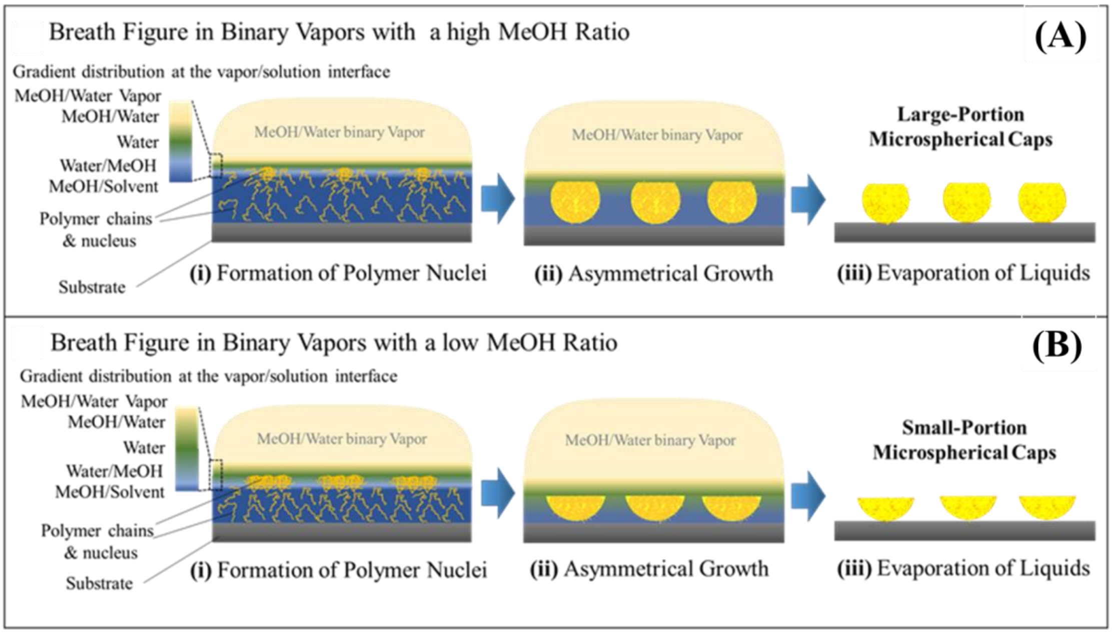

Figure 3. 39 Schematic diagram of the formation mechanism of microspherical caps with different shapes in binary vapors of MeOH and water: (a) large-portion

microspherical caps formed in the binary vapors with a high MeOH ratio, and (b) small-portion microspherical caps formed in the binary vapors with a low MeOH ratio

A precipitation trial similar to the BF process was designed for direct observation to further verify the mechanisms stated above. To replace the relatively slow condensation process of nonsolvent from the vapor atmosphere, a droplet of water, MeOH and MeOH/water mixture (50/50, w/w) dyed with Rhodamine B (RhB) was directly dripped into a clear PS solution, respectively. It was found that water was quickly separated into two parts, which were located at the top and bottom layers of solution respectively. They kept stable when holding statically (Fig. 3.40a). The upper part can be ascribed to the large surface tension of water and the stabilization of polymer chains, while the lower part was due to the higher density of water. Therefore, when water is gently condensed from vapor atmosphere by evaporative cooling, it is feasible for water BFs to nucleate and grow on the solution surface for further templating fabrication of porous microstructures. The solution quickly became clear again (after about two seconds) when a droplet of MeOH was dripped (Fig. 3.40b). Even a little more MeOH was added, the solution can still keep clear. This verifies that MeOH can be dispersed rapidly and homogeneously in polymer solution owing to the good miscibility of MeOH with THF, which enables the nuclei and growth of symmetrical microspheres. The stratification phenomenon was also observed when a droplet of MeOH/water mixtures was introduced into the solution (Fig.

3.40c). This indicates that water can still remain at the solution surface when MeOH diffuses into the solution quickly, which can be ascribed to their different affinities with solvent as discussed above. Therefore, polymers can precipitate, nucleate, and grow up asymmetrically to form microspherical caps with the gradual increase of nonsolvent by condensation and the decrease of solvent by evaporation.

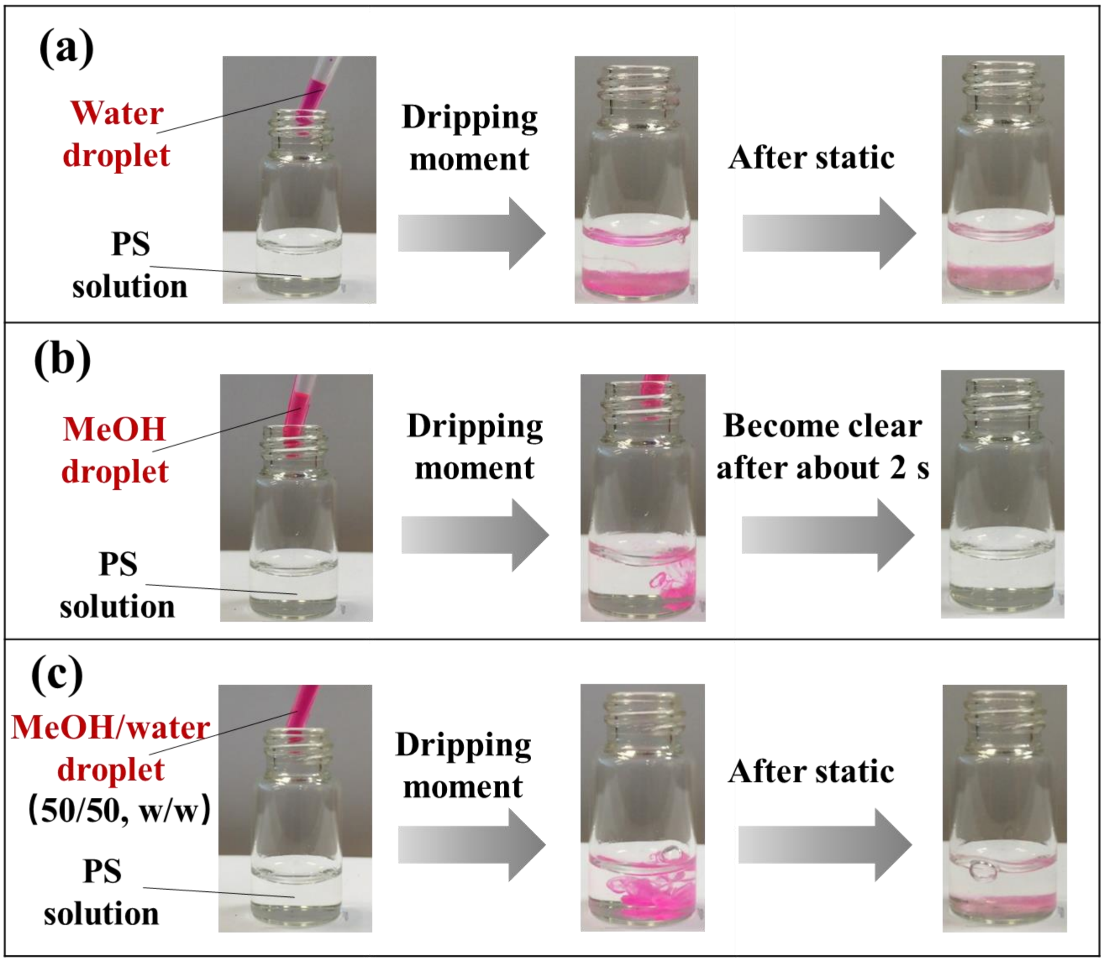

Figure 3. 40 (a) The diffusion status of a droplet of (a) water, (b) MeOH, and (c) MeOH/water mixtures (50/50, w/w) dripped into a 40 mg mL^{-1} PS solution, respectively. The nonsolvent droplets were dyed with RhB for clear observation

The influence of solution concentration on the size of asymmetrical particles by the binary BF technique is similar to the MeOH BF process. Increase the solution concentration can provide enough solute for particle growth but will result in the decrease of growth time (because the gelation process becomes short). Water is a better nonsolvent for PS than MeOH. When the solution concentration is fixed, increasing the ratio of water can lead to a little faster gelation process. This will result in the formation of microspherical caps with smaller sphere size due to the shorter growth time. However, if the water ratio in the vapor is too large, polymer chains prefer to aggregate along the interface with solution film. Increasing water ratio may also lead to the formation of asymmetric nuclei with tabular surface. Therefore, the base diameter of small-portion microspherical caps will increase with the increase of water ratio.

3.5 Summary

In summary, this work has systematically prepared a series of porous microstructures with various pore size, size distribution and regularity under different experimental conditions based on well-defined PS homopolymers by the BF technique in aqueous vapor, and successfully developed the BF principle of water to non-aqueous liquid (i.e. MeOH) for the formation of symmetrical microspheres and more complex binary aqueous/non-aqueous liquids (i.e. water and MeOH) for novel fabrication of asymmetrical particles with adjustable microspherical caps by controlling the ratio of water and MeOH. This greatly enriches the polymer microstructures generated by the BF technique. Moreover, the size range of BFs-generated porous microstructures was extended from submicrometer (low to 0.23 μm) to submillimeter (up to hundreds of μm). These polymer films with adjustable microstructures and sizes can meet various requirements in practical uses, which are believed to have a broader range of potential applications.

The different morphology features obtained are mainly ascribed to the difference of surface tension and miscibility between the employed solvents and nonsolvents. The precipitation of polymers also has an important influence on the final polymer microstructures. Their formation mechanisms have been thoroughly elucidated from the initial spreading of solution film on substrate, the formation and spreading of nonsolvent BFs on solution film, the physical gelation of polymer-rich phase to the final formation of polymer microstructures by complete removal of liquids for better and more comprehensive understandings. The explicit clarifications of formation mechanism behind the BF techniques will benefit the improvement of controlling polymer microstructures and further development of new BF approaches for more novel microstructures and advanced functions.

CHAPTER 4 General Fabrication of Highly Ordered Breath Figure Arrays with Commercial Polymers *via* Additive-Assisted Strategy

4.1 Introduction

Fabrication of highly ordered porous microstructures based on commercially available materials with more time-saving and cost-efficient techniques always receives a central level of research interest because it is a prerequisite for many potential applications. [7,20] The BF techniques can rapidly and economically produce highly ordered honeycomb pore arrays (breath figure arrays, BFAs) based on elaborate synthesis of polymers in lab. But unfortunately, most commercial polymers and inorganic materials are not good candidates for BF techniques. They usually require laborious work on further chemical modification or elaborate optimization of BF conditions. Therefore, it is highly desirable to develop a universal strategy for the preparation of highly ordered BFA films in more easily accessible BF conditions.

In this chapter, a robust and universal BF strategy is developed for general fabrication of highly ordered BFA with easily-obtained commercial polymers by exploring an efficient oligomer additive. The influences of additive type, additive amount, solution concentration and planar substrate types are investigated on the film microstructures. Different 3D objects such as copper grids, inorganic particles, and fabrics are also used as nonplanar surfaces for demonstrating the feasibility of additive-assisted BF technique. Moreover, non-polymeric nanoparticles are directly incorporated into the porous films for more advanced functionalization. One of their applications in harvesting luminous energy is exemplified for photocatalytic degradation of pollutants.

4.2 Film microstructures without an additive

To demonstrate the feasibility of additive-assisted BF technique, a commercial polystyrene (cPS) with linear chain structure and nonpolar groups was employed as film-forming material. It was first used as received to study its film microstructures by the BF technique without an additive.

The M_n and M_w/M_n of cPS were first measured by a GPC system equipped with a Waters 1515 Isocratic HPLC pump, a Waters 2414 refractive index detector (RI), a Waters 2487 dual λ absorbance detector (UV) and a set of Waters Styragel columns (HR3, HR4 and HR5, 7.8 ×300 mm). The GPC measurements were carried out at 35 °C using THF as eluent with a 1.0 mL min^{-1} flow rate. The system was calibrated with polystyrene standards. The determined M_n and M_w/M_n of PS were 129600 and 2.24, respectively. And its GPC curve is shown in Fig. 4.1.

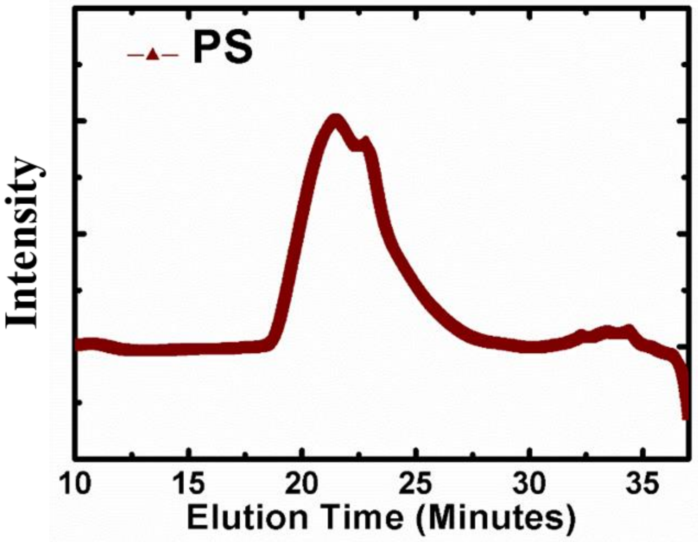

Figure 4. 1 The GPC curve of used cPS in THF eluent

CS_2 was used to dissolve cPS for the preparation of solutions with different concentrations. Water was fixed for the use of constructing nonsolvent vapor. This is because CS_2, which possesses high vapor pressure and water immiscibility, has been demonstrated as a good solvent for ATRP-synthetic PS (aPS) to form hexagonally ordered porous microstructures under aqueous vapor by the BF process in a relatively wide solution concentration. The prepared cPS/CS_2 solutions were cast on glass substrates under aqueous vapor by the BF technique. The resultant polymer films were sputter-coated with a gold layer of about 2 nm thickness for SEM observation. Fig. 4.2 shows the typical film microstructures prepared from cPS solutions with the concentrations ranging from 10 mg mL^{-1} to 50 mg mL^{-1}, respectively. Porous microstructures were observed on the films prepared from all the solution samples regardless of their polymer contents.

The pore size of the porous films was dependent on the solution concentration.

And through adjusting the solution concentration, the regularity of porous microstructures can be slightly improved. Specifically, the casting solution at either low concentration (10 mg mL^{-1}, Fig. 4.2a and e) or high concentration (50 mg mL^{-1}, Fig. 4.2d and h) solutions would result in a disordered porous microstructure with a broad size distribution. While at 20 mg mL^{-1} (Fig. 4.2b and f) and 30 mg mL^{-1} (Fig 4.2c and g), the film pore sizes were both relatively homogeneous. The former presents a better round pore shape than the latter. Graphical histograms visually reflect the pore size distribution of each PS film samples. As shown in Fig. 4.2j, the pore size distribution of films cast at 20 mg mL^{-1} was the narrowest in comparison to other three film samples (Fig. 4.2i, k and l).

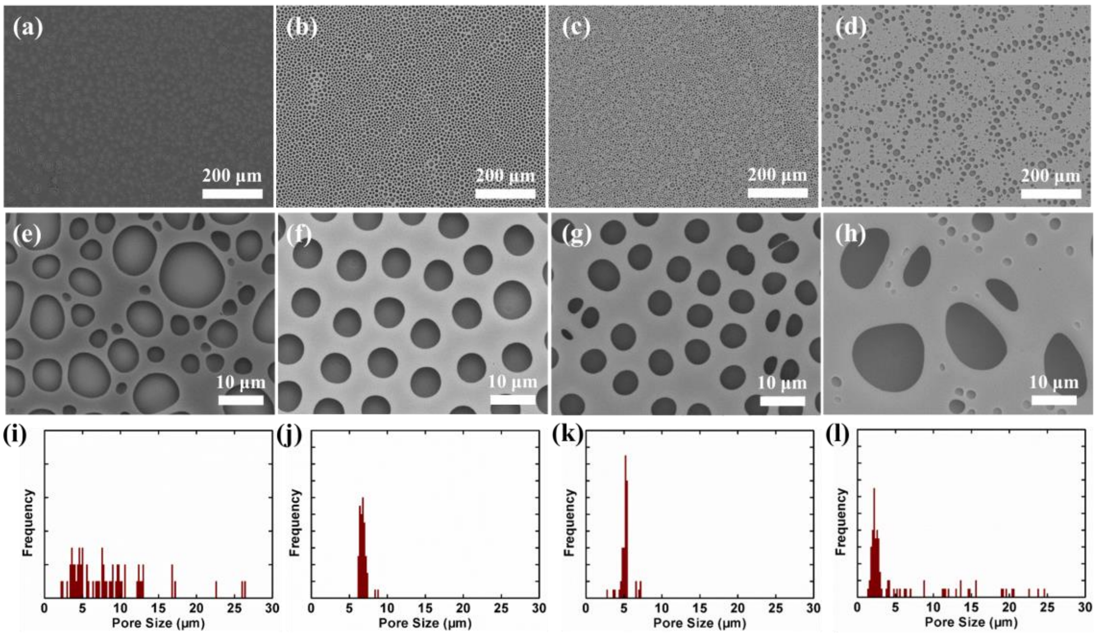

Figure 4. 2 Typical SEM images with different magnifications and pore size distribution of and cPS films cast from different solution concentration: (a), (e) and (i) 10 mg mL^{-1}, (b), (f) and (j) 20 mg mL^{-1}, (c), (g) and (k) 30 mg mL^{-1}, (d),

(h) and (l) 50 mg mL^{-1}. The pore size was measured along the major axis of pores and grouped by every 0.2 μm in histograms

The dependence of pore size on the concentration of cPS solution was further plotted in Fig. 4.3a and b. The average pore sizes of cPS films at the concentrations of 10 mg mL^{-1}, 20 mg mL^{-1} and 30 mg mL^{-1} were 8.50 μm, 6.89 μm, and 5.43 μm respectively. Their corresponding standard deviations (SDs) indicating the pore size distributions were 5.22, 0.47, and 0.68, respectively. At high concentration (50 mg mL^{-1}), the resulted PS films roughly appeared a bimodal size distribution because of the coexistence of small satellite pores (2.41 μm, 0.93) and large main pores (12.00 μm, 8.07). Generally, the average size of porous PS films presents a decreasing trend with the increased concentration. And cPS/CS_2 solution at 20 mg ml^{-1} tends to form relatively homogeneous microstructures with a relatively narrow pore size distribution.

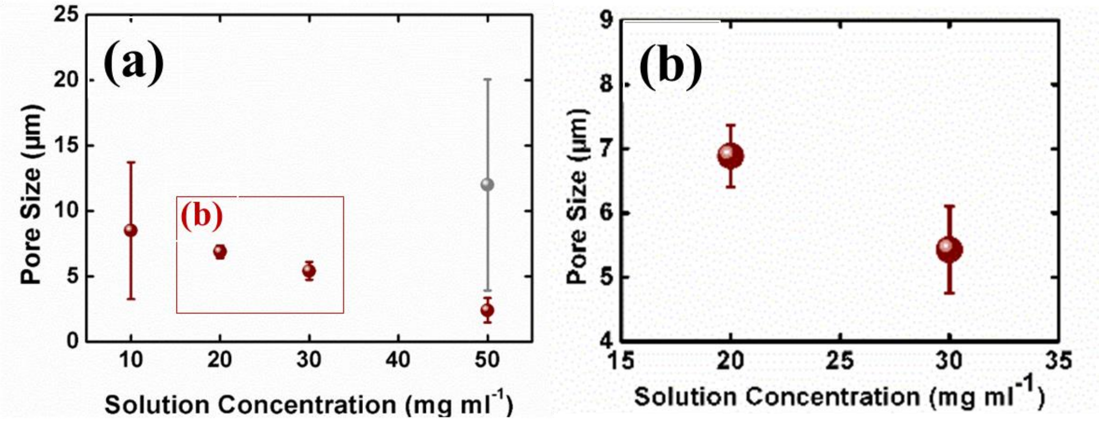

Figure 4. 3 (a) Plot of the dependence of pore size on the concentration of cPS solution. (b) The magnification of read area in (a)

In the previous chapter, we have demonstrated the feasibility of ATRP-synthesized (aPS) for highly ordered pore arrays by the aqueous BF technique through increasing the concentration of casting solution. Fig. 4.4 shows the obvious morphology evolution from disordered at 40 mg mL^{-1} to ordered porous microstructures at 160 mg mL^{-1}. The regular arrays formed in large scale display beautiful textures at a low magnification by SEM (Fig. 4.4c). However, regardless of solution concentration, the generation of cracks was also found in all film samples. When such aPS film was introduced on a nonplanar substrate by the BF technique, the cracking phenomenon became more serious. Even an intact film cannot be obtained because gentle disturbance can result in cracking and flaking.

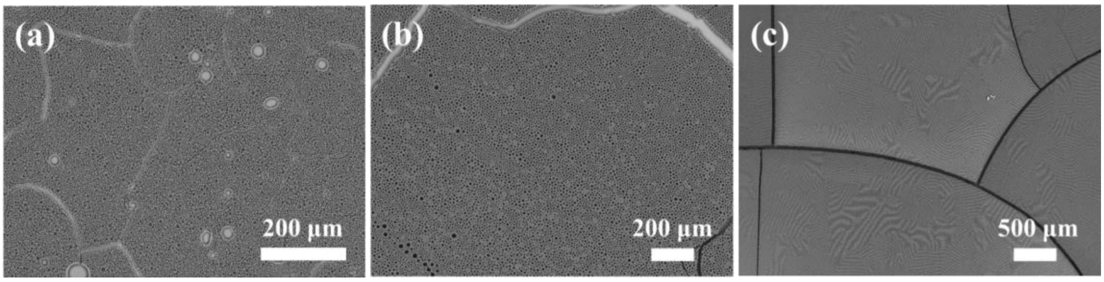

Figure 4. 4 Cracks generated in the PS-14 film prepared by the aqueous BF technique from (a) 40 mg mL^{-1}, (b) 80 mg mL^{-1} and (c) 160 mg mL^{-1}, respectively

Obviously, in comparison to the porous films of aPS, cPS tends to form porous films with few cracks under similar BF conditions, although the resultant porous microstructures are irregular and disordered. The generation of cracks in aPS film samples is due to the brittle property of PS caused by its high T_g (about 100 °C).[33] While for cPS films samples, the non-cracking phenomenon can be ascribed to the wide molecular weight distribution of commercial PS (M_w/M_n=

2.24, which is much larger than that of aPS (<1.1)). The low M_n PS molecules play a role of plasticizer to improve the flexibility of polymer films. However, due to the high T_g of PS, the resultant films are still brittle, which can be crumbed very easily by a small external force. Brittle polymer films obviously cannot be employed for further applications. It will inevitably result in the degraded performance and poor reproducibility of ordered porous films in some practical applications.

Increasing solution concentration is not a good strategy for cPS to improve its pore regularity by the BF technique. Because the M_n of cPS (129600) is much larger than aPS (<20000), the solution viscosity of cPS solution will drastically increase with the increase of solution concentration. It is not easy for cPS solution with high concentration to spread out on desired surface for the formation of homogeneous liquid film. Moreover, increasing solution concentration will inevitably result in the waste of raw materials and may aggravate the degradation of some film properties caused by thick layer, such film flexibility.

4.3 Film microstructures with an additive

To meet the rigorous demands of some applications, on the premise of film stability, both the regularity and flexibility of porous cPS films by the BF technique should be improved regardless of the concentration of casting solution. Recently, using polymers with a T_g below 48 °C as film-forming materials, such as PDMS-based star polymers, has been demonstrated as an effective strategy for the formation of non-cracking porous microstructures with good regularity on both planar and nonplanar surfaces by the BF technique.[246] This indicates that the low T_g of polymers played an important role on the formation of non-cracking porous films. Based on these valuable work and inspired by the role of PS with low M_n, the strategy of using an efficient oligomer with low T_g (such as PDMS and asphalt) as plasticizer will be developed in this study to modify commercial PS film for further improvement of its flexibility. The addition of oligomer is also expected to assist cPS chains to stabilize the formed water droplet arrays, thereby giving rise to improving the regularity of final porous microstructures.

4.3.1 The influence of PDMS additive on film microstructures

Based on the reported literatures and commercial availability, linear PDMS hompolymer was first considered to modify the film properties of cPS films. The used PDMS has a M_n of 4000. It was dispersed in cPS solution with a given weight ratio, and cast on substrate by the BF process. It was expected that high T_g and high M_n of cPS ensure the stability of resultant films while the soft-flowing nature of low T_g PDMS component can endow the films with improved flexibility. Specifically, linear PDMS has an extremely low T_g of below -120 °C.[345] However, PDMS is not miscible with most ordinary polymers involving PS. Due to the strong repulsive interaction between PS and PDMS,[346] serious phase separation occurred during the BF process, resulting in inhomogeneous films. Even when PDMS was added in its copolymer solution, such as a silicone-containing graft copolymer PDMS-*g*-PAs solution, polymer films with different surface microstructures can be observed after the BF process (Fig. 4.5a). Although no cracks were found in the resultant films, two kinds of porous surface microstructures are clearly observed, as shown in Fig. 4.5b and d respectively. They are correspondingly the main aggregation areas of PDMS-*g*-PAs and PDMS. Fig. 4.5c shows the obvious border between the two different surface regions.

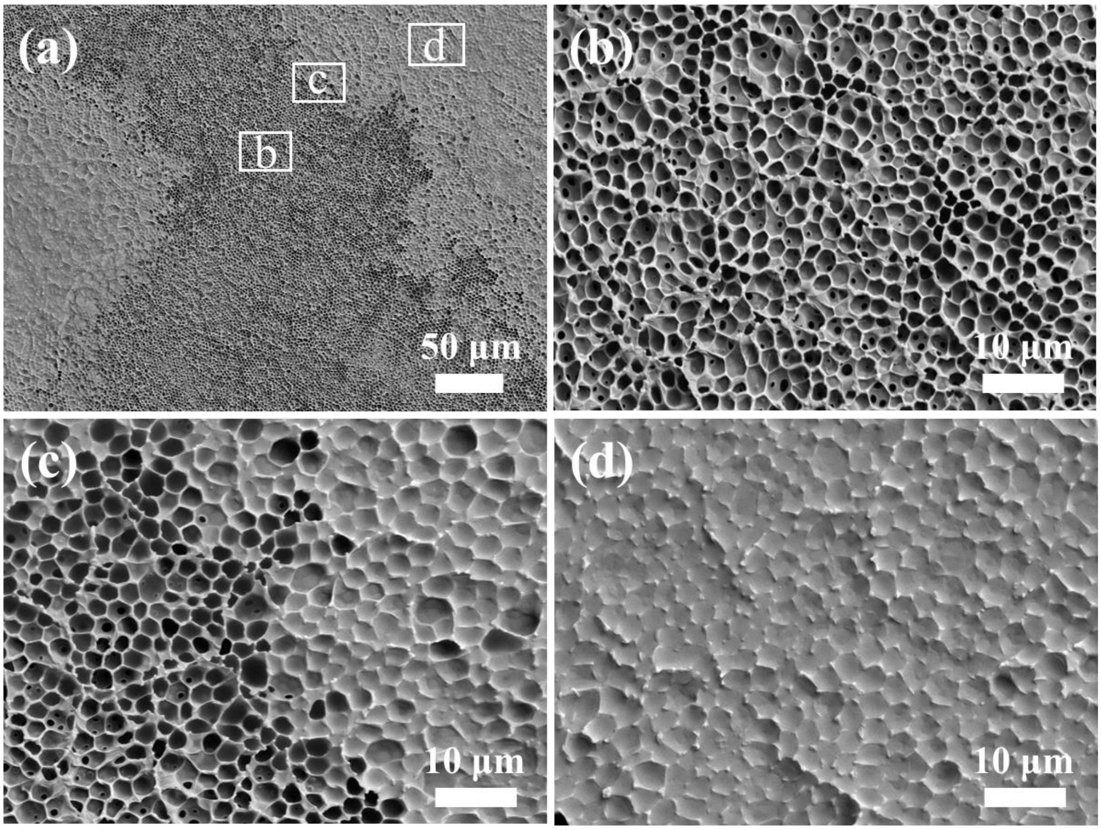

Figure 4. 5 (a) SEM image of cPS film after the addition of linear PDMS homopolymer. (b)-(d) Magnified views of white edge regions highlighted in (a) display different porous microstructures in a film

4.3.2 The influence of asphalt additive on film microstructures

The phase separation phenomenon of PDMS modified polymer films indicates that besides the low T_g, the compatibility of oligomer additive with cPS should also be considered seriously. Asphalt is generally a mixture of oligomers that consist of saturated hydrocarbons, resins, naphthene aromatics, polar aromatics, and macromolecular asphaltenes.[347] Most of them have similar Flory-Huggins interaction parameters with PS. And their molecular weights are usually several thousand at most. The low molecular weight and multiple component characters enable asphalt good miscibility with most polymers, particularly for the polymers possessing aromatic groups and/or hydrocarbon chains. And the T_g of asphalt is approximately -20 °C.[347] This indicates that asphalt will be a good candidate to modify the films properties of cPS films by the BF technique.

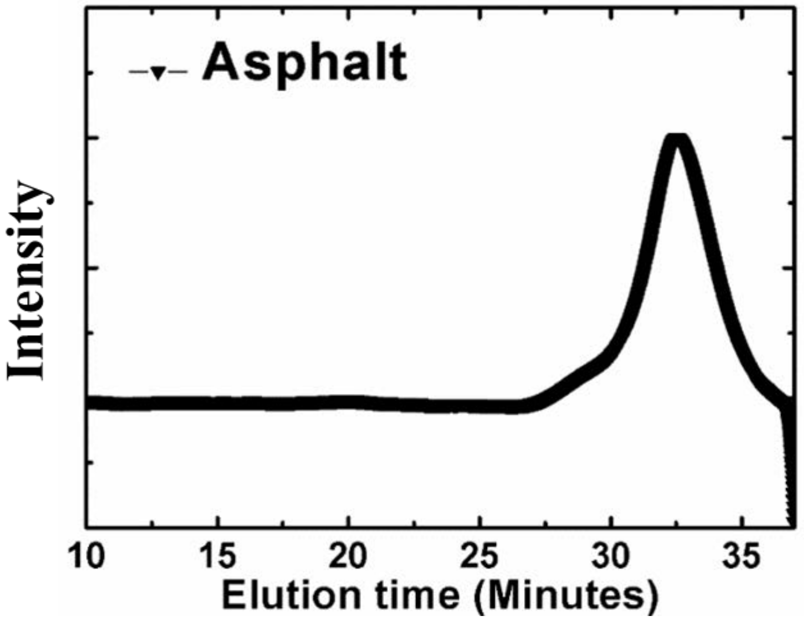

Figure 4. 6 A GPC curve of used asphalt in THF eluent

cPS/asphalt (PSA) solutions with different asphalt contents were prepared by dissolving cPS and asphalt in CS_2 according to a certain weight ratio, and cast on the glass substrate by the static BF technique to systematically study the influence of asphalt on the final film microstructures. The M_n and M_w/M_n of used asphalt determined by GPC are 1,000 and 1.96, respectively (Fig. 4.6). The total concentration of casting solution was fixed at 25 mg mL^{-1}. The resultant films were sputter-coated with a gold layer of about 2 nm for SEM observation. Fig. 4.7 shows the surface microstructures of PSA films with the asphalt content ranging from 0 to 100 wt%. The surface morphologies of film evolving from disorder to ordered and finally to disorder porous microstructures can be clearly observed. Without the assistance of asphalt, only irregular pores with largely different sizes were observed in PS films (Fig. 4.7a). While after introducing 10 wt% asphalt, the pore size was decreased obviously and became relatively homogeneous (Fig. 4.7b). And further increasing asphalt content was conducive to form more uniform pores, as shown in Fig. 4.7c. When the content was increased to 30 wt%, uniform round pores were found in local film regions, coexisting with irregular pores (Fig. 4.7d). Slightly increasing the asphalt fraction to 35 wt%, ordered arrays with round pores, namely the typical honeycomb porous microstructures, were observed as expected in large scale (Fig. 4.7e). The continuing increase of asphalt could further enhance the regularity of pore arrays, as demonstrated in Fig. 4.7f. And the similar highly ordered microstructures illustrated that enlarging the fraction of asphalt to 50 wt% has no influence on the regularity of pore arrays (Fig. 4.7g). Even when the asphalt content exceeded PS, highly regular honeycomb porous arrays could still be obtained (Fig. 4.7h). Only the average pore size was decreased from 4.42 μm (35 wt% asphalt) to 3.02 μm (60 wt% asphalt). Nevertheless, further raising the asphalt proportion would result in the formation of less regular honeycomb microstructures. As shown in Fig. 4.7i, some distorted pores were found to intersperse in the pore arrays after 5% more asphalt was added. And a mottled surface involving the deformed pores and non-porous areas was obtained when the added asphalt was over 80 wt% (Fig. 4.7j). This is probably because rigid PS component is plasticized and softened seriously by semi-solid asphalt, which thus cannot effectively maintain the formed microstructures. Only few isolated pores were irregularly distributed in non-porous areas when asphalt content was up to 90%. In some partial film areas, the imprint of water droplets could be observed (Fig. 4.7k), which clearly indicates that over addition of asphalt will result in the collapse of microstructures. And this can be further demonstrated by casting asphalt/CS_2 solution on a glass substrate where only buckling features were observed in the asphalt film rather than porous structures, as demonstrated in Fig. 4.7l. The morphology evolution of PSA films above suggests that asphalt can efficiently assist PS solution to form ordered porous microstructures in a wide additive range (from 35 wt% to 60 wt%). More importantly, there are no cracks found on all of these samples. This demonstrates that the addition of asphalt during the BF process is a good strategy to improve the regularity and flexibility of porous cPS films.

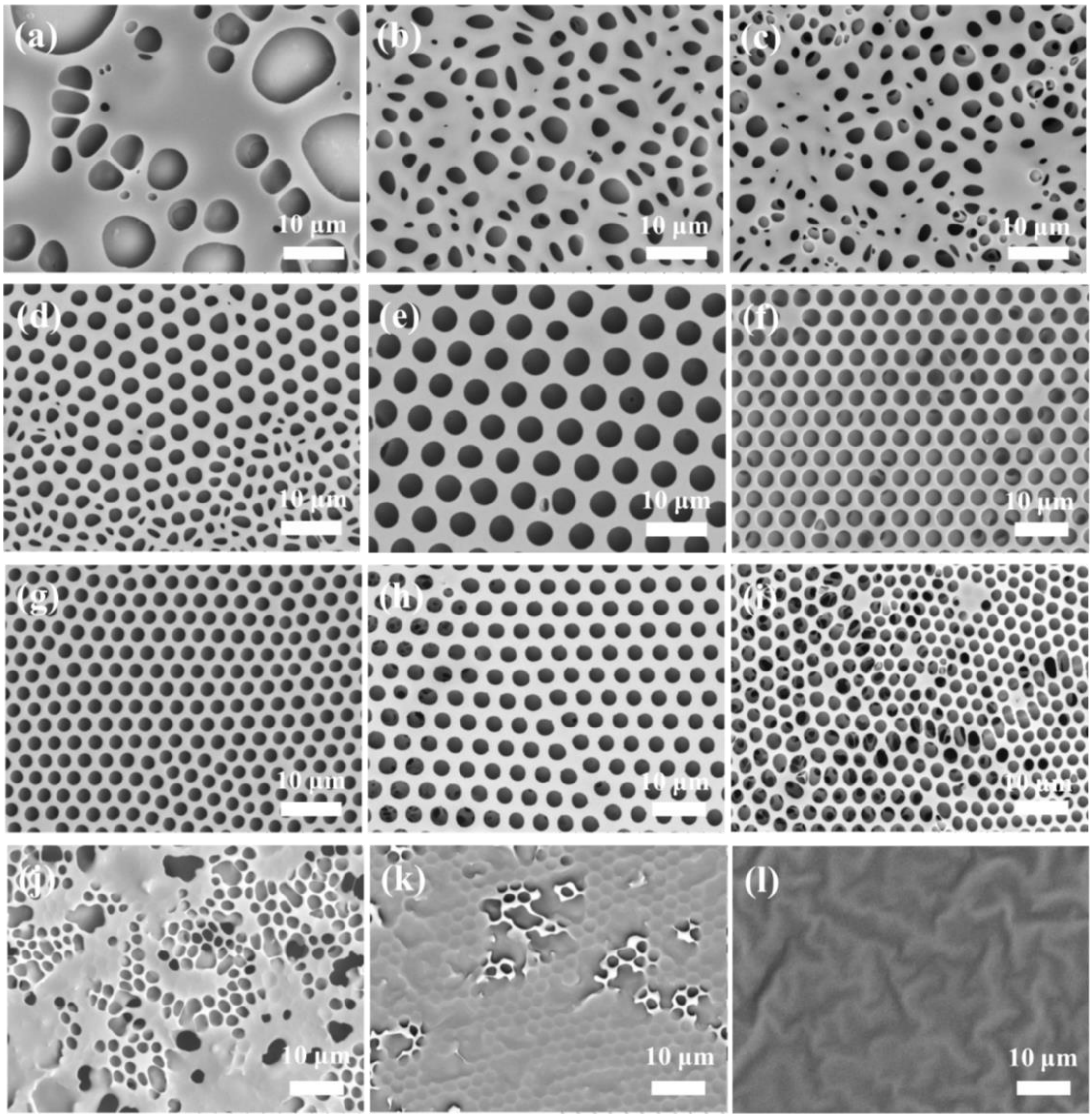

Figure 4. 7 SEM images of morphological evolution of PSA films on glass substrates with increasing asphalt contents: (a) 0, (b) 10 wt%, (c) 20 wt%, (d) 30 wt%, (e) 35 wt%, (f) 40 wt%, (g) 50 wt%, (h) 60 wt%, (i) 65 wt%, (j) 80 wt%, (k) 90 wt%, and (l) 100 wt%. The concentration of all casting solutions was fixed at 25 mg mL^{-1}

4.4 Different influencing factors on the film microstructures prepared by asphalt assisted BF technique

4.4.1 The influence of solution concentration

The influence of solution concentration on the polymer film morphology was further investigated by fixing the weight ratio of cPS to asphalt at 1. The PSA solutions with the concentration from 10 mg mL^{-1} to 50 mg mL^{-1} were cast on the glass substrate by the aqueous BF technique, respectively. Regardless of the solution concentration, non-cracking and regular porous microstructures are found on the substrate in large scale, as shown in Fig. 4.8a, d, g and j. Their corresponding magnified views in Fig. 4.8b, e, h, and k further reveal that the pore microstructures all display a highly ordered hexagonal arrays. The pore size and pore size distribution were measured and summarized in Fig. 4.8c, f, i and l respectively. The graphical histograms visually reflect the narrow pore size distribution, which indicates the formation of uniform pores. These are quite different form the porous microstructures of cPS films without the addition of asphalt. As revealed in Fig 4.2, neat cPS films cast from a wide solution concentration displayed a disordered porous microstructure with a broad size distribution. Only the pore size of cPS films cast at 20 mg mL^{-1} was relatively homogeneous. This means that the addition of asphalt contributes to the formation of ordered porous films by extending the workable concentration of casting solution from 10 mg ml^{-1} to 50 mg ml^{-1}.

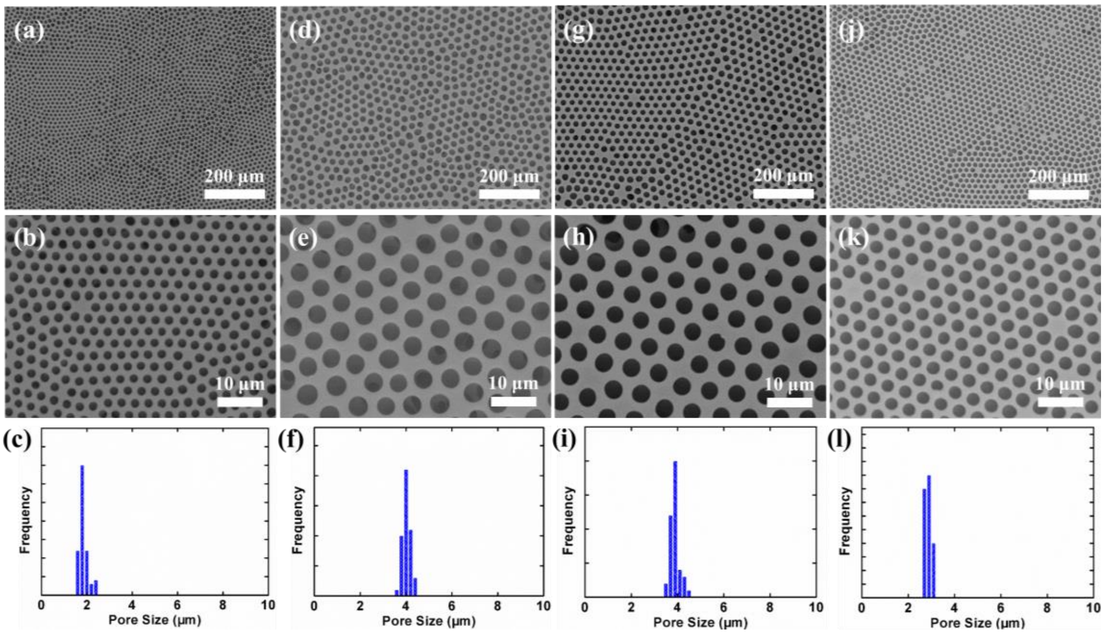

Figure 4. 8 Typical SEM images and pore size distribution of PSA films cast from different solution concentrations: (a)-(c) 10 mg mL^{-1}, (d)-(f) 20 mg mL^{-1}, (g)-(i) 30 mg mL^{-1}, (j) and (l) 50 mg mL^{-1}. The introduced weight amount of asphalt in PSA films is equal to PS. The pore size was measured along the major axis of pores and grouped by every 0.2 µm in histograms

The dependence of pore size on the concentration of PSA solution was further plotted in Fig. 4.9. The average pore sizes of PSA films with a standard deviation were 1.93 µm (0.12) at 10 mg mL^{-1}, 4.11 µm (0.17) at 20 mg mL^{-1}, 3.89 µm (0.19) at 30 mg mL^{-1}, and 2.86 µm (0.12) at 50 mg mL^{-1}, showing a decreasing trend with the increased concentration of solution after 10 mg mL^{-1}. Correspondingly at the same concentrations summarized in Fig. 4.3, the average sizes and standard deviations of porous PS films were much larger than PSA samples. These results clearly indicate that, in a similar BF condition, the introduction of asphalt can effectively reduce the pore size and greatly narrow the size distribution of polymer films.

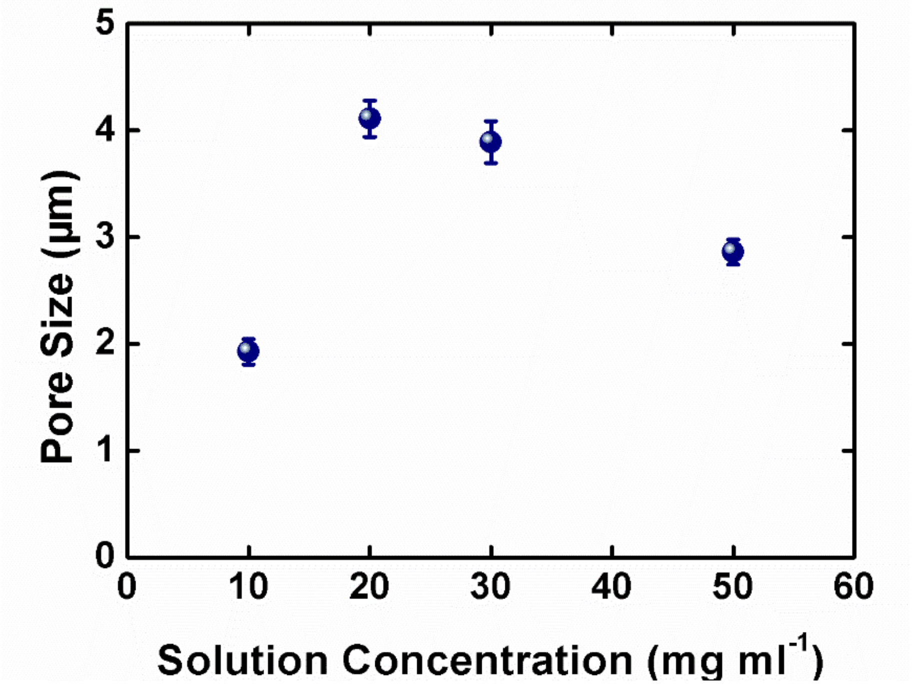

Figure 4. 9 Plot of the dependence of pore size on the concentration of PSA solution

4.4.2 The influence of substrates

The addition of asphalt in the casting solutions of cPS during the BF process has been demonstrated as an effective strategy to prepare ordered porous microstructures without cracks on glass substrates. However, in most cases, such microstructures are always required to be constructed on a specific substrate to meet the demand of certain uses. Moreover, uneven and curved surfaces are usually encountered in many practical applications. Therefore, this section will study the film-forming properties of PS/asphalt blends by the BF technique on different planar substrates and nonplanar substrates.

4.4.2.1The influence of substrate materials

The influence of substrate materials on the formation of PSA films microstructures was studied by casting the desired solutions on the planar substrates with different materials. The employed substrates included silicon wafers, organic sheets (or films), metal foil and even water surface. Their surface energies ranged from 18 mN m^{-1} to 73 mN m^{-1}.[341] The used PSA/CS_2 solution was fixed at 25 mg mL^{-1}. And the weight ratio of cPS to asphalt was fixed at 1. PSA solution at this concentration can well spread on all of the employed substrates. After the same BF procedures, the resultant films on different substrates were revealed by SEM and are shown in Fig. 4.10, respectively. All of them show a honeycomb patterned porous microstructure. Hexagonally ordered pore arrays are observed on all substrates, involving the low surface energy perfluoro substrate polytetrafluoroethylene (PTFE) plate (ca. 18 mN m^{-1}) and the high surface energy water surface (ca. 73 mN m^{-1}). After the removal of water, the latter can lead to the formation of free-standing films conveniently. These results well indicate that PSA can form ordered porous microstructured films on the planar surfaces of most commonly used materials by the asphalt-assisted BF strategy.

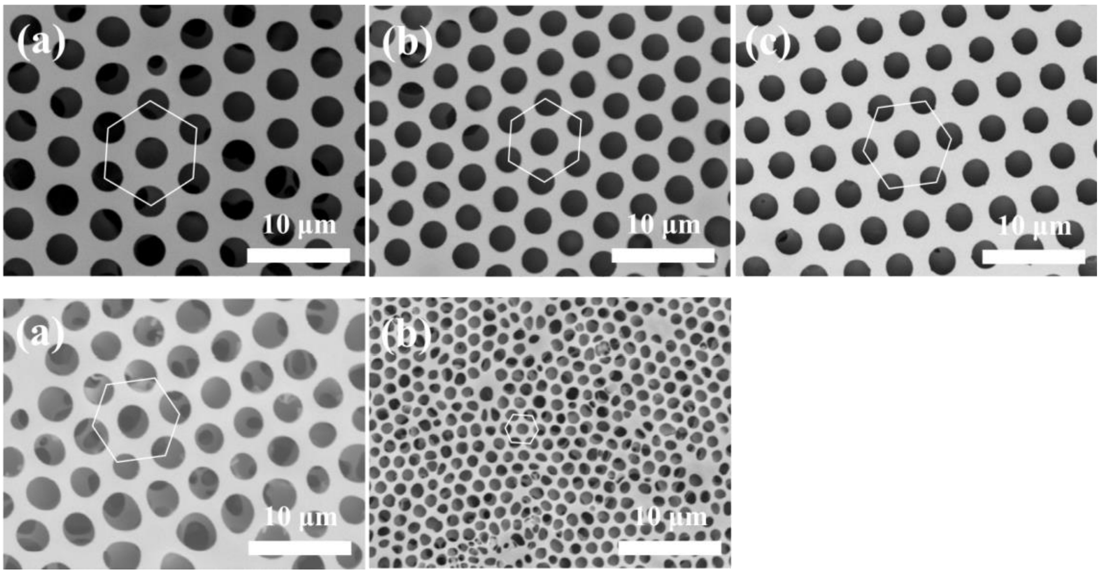

Figure 4. 10 SEM images of PSA films on different planar substrates: (a) copper foil, (b) silicon wafer, (c) water surface, (d) PET sheet and (e) PTFE surface

4.4.2.2 The influence of nonplanar surfaces

Three different categories of object, including two different types of transmission electron microscope (TEM) copper grid, two different types of woven fabric and two different types of inorganic particle, were further employed as nonplanar substrates to investigate the influence of nonplanar surfaces on the formation of porous PSA films by the asphalt-assisted BF technique. The resultant surface features were revealed by SEM, and are shown in Fig. 4.11, respectively. The formed porous microstructures are found to effectively contour the whole object regardless of the surface pattern, texture, shape and size. More interestingly, no cracks were found on all the prepared PSA film samples. This can be ascribed to the soft-flowing property of asphalt, which enables the PSA film to act as a flexible coating to cover the nonplanar surfaces. The magnified views (insets in Fig. 4.11) reveal that honeycomb pore arrays exist around the surface profile of objects, giving rise to a hierarchical surface morphology. These results well demonstrate the robustness and universality of PSA films on the formation of non-cracking porous microstructures on complex surfaces by the asphalt assisted BF technique. This simple strategy provides a direct route to prepare 3D conformal porous microstructured films.

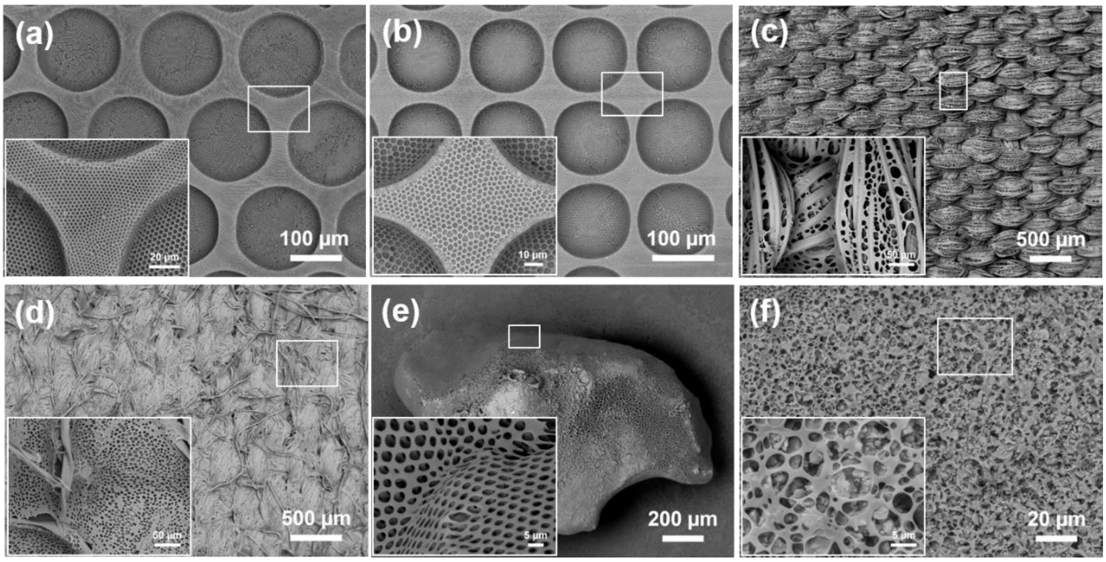

Figure 4. 11 SEM images of PSA (asphalt/PS=1/1, w/w) films covering on different nonplanar objects: (a) 150 mesh copper TEM grid with hexagonal pattern, (b) 230 mesh copper TEM grid with square pattern; (c) woven cotton fabric with regular texture, (d) PET fabric with irregular texture; (e) millimeter-size silica particle with irregular shape, and (f) basalt powder with the particle size ranging from hundreds of nanometers to several micrometers. The insets are the corresponding magnified images of highlighted areas in a-f respectively

4.4.3 The influence of polymer types

The robustness and university of asphalt assisted technique for assisting target materials to form highly ordered porous microstructures were further demonstrated by employing more different commercial polymers as film-forming materials. The employed commercial polymers are commonly used in different fields, involving a thermoplastic SBS (M_n=113,800), an engineering plastic PC (M_n=26,500), and a biodegradable polymer PEO (M_n=500,000). For comparison, they were dissolved in CS_2 or chloroform ($CHCl_3$), and cast on glass substrates by the same BF procedures, respectively. The irregular patterns revealed by optical microscopy (OM) indicate that both SBS/CS_2 and PC/$CHCl_3$ solutions at 12.5 mg mL^{-1} were not suitable for the formation of ordered porous films (Fig. 4.12a and b). While after the addition of small asphalt, the pore size became more homogeneous obviously. And ordered porous films with uniform size were obtained when about 30 wt% and 35 wt% asphalt were introduced into the SBS films (Fig. 4.12d) and PC films (Fig. 4.12e), respectively. PEO generally shows a semicrystalline nature. Nonporous microstructures were found when its $CHCl_3$ solution was cast under aqueous vapor (Fig. 4.12c). Large spherulites tightly interconnected with each other were clearly observed by polarizing OM (POM, insets of Fig. 4.12c). Instead, porous microstructures with relatively uniform size were observed by OM when 50 wt% asphalt was introduced (Fig. 4.12f). And POM shows that the size of PEO spherulites was reduced drastically, which is space-filling evenly in the PEO/asphalt film (insets of Fig. 4.12f). These three different examples powerfully demonstrate that asphalt assisted BF technique is suitable for different polymers to form improved regularity of porous microstructures.

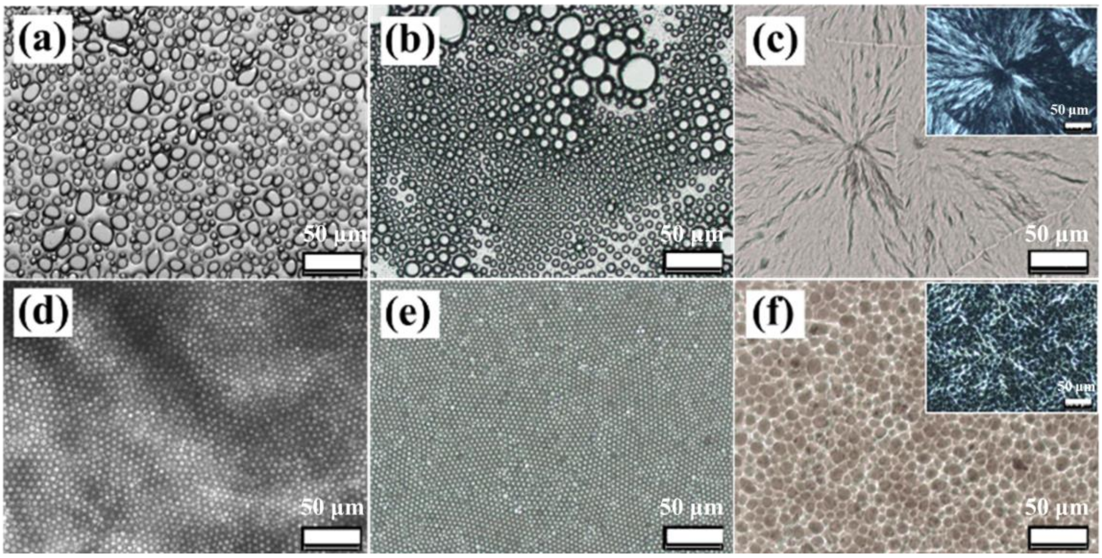

Figure 4. 12 Optical micrographs of polymer films without asphalt cast from 12.5 mg ml^{-1} (a) SBS/CS_2, (b) PC/$CHCl_3$, and (c) PEO/$CHCl_3$ solutions. Optical micrographs of (d) SBS/asphalt, (e) PC/asphalt, and (f) PEO/asphalt films after introducing 30 wt%, 35 wt%, and 50 wt% asphalt. The insets are polarized optical micrographs

4.5 The role of asphalt on the formation of highly ordered BFAs

As stated in chapter 3.4.4, the generation of pores by the aqueous BF approach is templated from the water droplets. During the BF process, water droplets nucleate from aqueous vapor and grow on the solution surface by the evaporative cooling of solvent until gelation occurs. The arrangement, shape and size of water droplets at gelation point largely determine the final regularity, shape and size of pores formed in polymer films. Driven by the Marangoni convection and capillary interactions, water droplets with homogenous size can self-assemble into regularly hexagonal arrays under suitable BF conditions. Polymer-rich phase just gelling at such state will lead to the formation of hexagonally ordered pore arrays with monodispersed size after complete evaporation of residual solvents and water. In other words, any factors that can stabilize the regular state of formed water droplet arrays till the gelation of polymer-rich phase can lead to the formation of highly regular pore arrays finally.

Adjusting the initial concentration of casting solution is a commonly used strategy to obtain ordered porous films by the BF technique.[222-225] At a low concentration of casting solution, the resultant porous microstructures are usually irregular and disorder. This is because when the water droplets are self-assembled in a highly ordered state, the amount of polymers is too little to stabilize the formed regular water droplet arrays until gelation occurs. Increasing the solution concentration will lead to a quicker precipitation of polymer chains, thereby producing more polymers precipitated at the water/solution interface to stabilize the water droplets. It will also result in a shorter time for the gelation of polymer-rich phase. Therefore, the regularity of porous microstructures can be improved by increasing the concentration of cPS/CS_2 solutions. However, no very ordered pore arrays can be found in the cPS films. This indicates that cPS are not very good solute to precipitate at the water/solution interface to stabilize the formed water droplets, which can be mainly ascribed to its hydrophobic and nonpolar properties.

In the same concentration range of casting solution, cPS solutions with the addition of asphalt can lead to form hexagonally ordered pore arrays in large scale by the same BF procedures. This indicates that asphalt plays a key role during the BF process. Specifically, asphalt can assist cPS to stabilize the formed regular water droplet arrays more effectively than the simple action of cPS. The morphology evolution with the increase of asphalt weight ratio in Fig. 4.7 clearly demonstrates that the addition of asphalt can effectively cPS to form more regular and ordered porous microstructures. This also indicates the important role of asphalt on stabilizing the regular water droplet arrays during the BF process, which can be mainly ascribed to its polar components and colloidal particle properties. As stated above, asphalt is generally a complex mixture that mainly consists of saturated hydrocarbons, resins, naphthene aromatics, polar aromatics, and macromolecular asphaltenes. Owing to hydrophilic-lipophilic balance, the polar components will be selectively enriched on water/solution interfaces to stabilize the formed water droplets. The colloidal particle property of asphalt is mainly due to the macromolecular asphaltenes. The predominate molecular architecture of asphaltenes is a single, moderately large polycyclic aromatic hydrocarbon with peripheral alkanes (PAHs).[347] With the induction of nonsolvent water, it is easy for PAHs to form nanoaggregates and nanoclusters by stacking and aggregating. Driven by the Pickering effect,[348] the formed asphaltenes nanoaggregates and nanoclusters will aggregate at the water/solution interfaces, thereby acting the role of stabilizing the formed water droplets. Asphalt is a good film-forming material for the stabilization of water droplets, but it should be noted that excess increase of asphalt would result in the less regular porous arrays again. This can be ascribed to the low T_g and low M_n of asphalt. The used asphalt is semi-solid at ambient temperature, which always tend to flow as a level surface. The cPS film will be plasticized and softened seriously when the addition amount of asphalt is excessive. Therefore, the resultant film microstructures will collapse again, resulting in the formation of disordered polymer films with less porosity.

4.6 Functionalization of porous PSA films for photocatalytic applications

4.6.1 Functionalization of porous PSA films by incorporating nanoparticles

Incorporating desired components into the porous microstructures is an effective strategy to functionalize the porous polymer films.[203,249,272] The existence of porous microstructures can also ensure the functional activity of incorporated components by avoiding them completely embedded in the solid matrix. To study the influence of incorporating nanocomponents on the formation of porous microstructures, three kinds of nanomaterials involving titanium dioxide nanoparticles (TiO_2 NPs), silver nanowires (Ag NWs) and Cu nanowires (Cu NWs) were doped into the PSA/CS_2 solutions, and cast on the glass substrate by the same BF procedures, respectively. The resultant organic/inorganic hybrid films were first revealed by SEM, as shown in Fig. 4.13a-c. The highly similar regular honeycomb porous microstructures with PSA films indicate that the incorporated nanocomponents have little influence on the regularity of pore arrays. No collapsed porous microstructures can be found. Through the pore holes, some nanocomponents, such as TiO_2 NPs and Ag NWs, were clearly observed from a close view (Fig. 4.13d-f). Energy dispersive X-ray spectrometer (EDX) was further employed for the characterization of these hybrid films. Fig. 4.13g-i show the typical and strong signals of Ti, Ag, and Cu elements, respectively. These results further confirm the successful incorporation of desired functional nanoparticles without the influence of pore regularity of porous PSA films. This direct functionalization of porous polymer films with nanomaterials by the BF technique is a simple and facile strategy to prepare porous hybrid materials with hierarchical microstructures. Such microstructured hybrid films combine the merits of polymer micropores and functional nanocomponents.

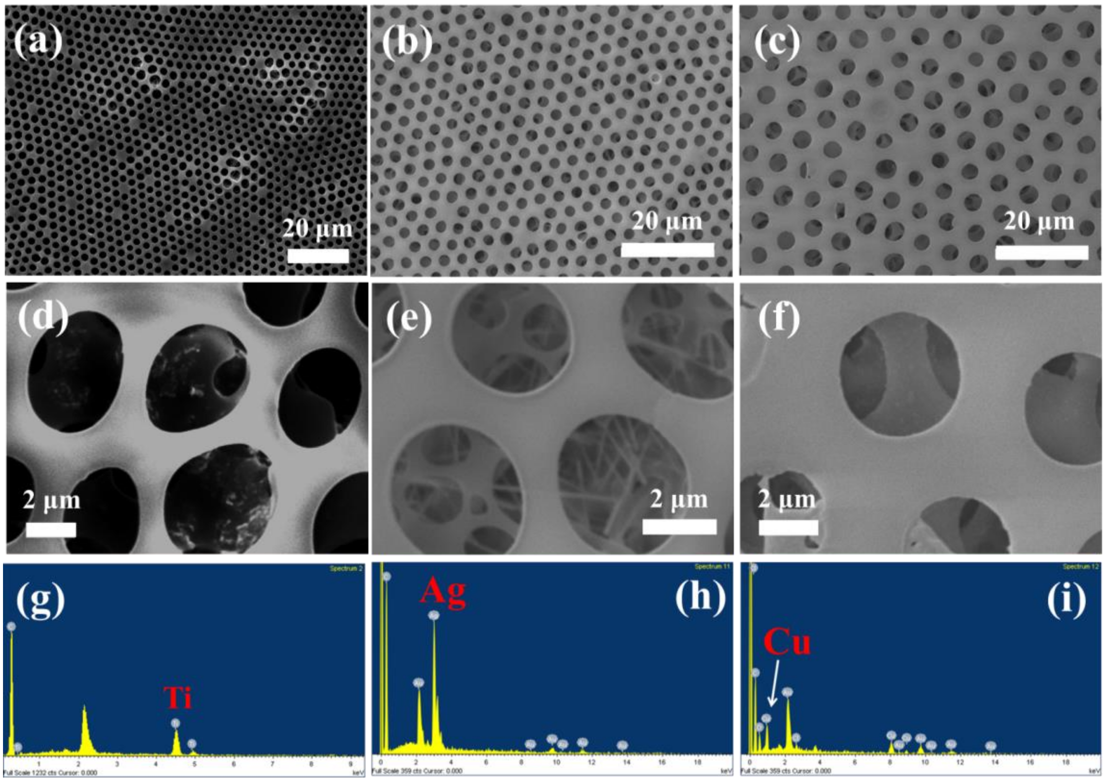

Figure 4. 13 SEM images with different magnifications and EDX spectrums of PSA films incorporated with 10 wt% TiO_2 NPs (a, d and g), 5 wt% Ag NWs (b, e and h), and 3 wt% Cu NWs (c, f and i)

The incorporation of functional nanoparticles into porous PSA microstructures on nonplanar surface were also be carried out by the same BF procedures. Flexible woven cotton fabric was used to replace the planar solid glass substrate. After casting PSA/TiO_2 solution by the BF technique, the white cotton fabric became black immediately, as shown in the inset of Fig. 4.14a. Through the observations at different magnifications by SEM, the resultant PSA/TiO_2 coated cotton textile displays typical multilevel structures, including fabric texture and twisted yarn (Fig. 4.14a), porous PSA film coated on fiber (Fig. 4.14b), and TiO_2 nanoparticles decorated on pore walls (Figure 4.14c). This indicates that the incorporation of small amounts of functional nanoparticles does not alter the excellent film-forming properties of PSA to cover the 3D surfaces of nonplanar substrates by the BF technique. By contrast, when the cotton fabric was simply immersed in PSA/TiO_2 solution and then dried in ambient conditions, no porous microstructures were found on the resultant surface (Figure 4.14 d and e). The introduced nanoparticles were found to aggregate and adhere to the fiber together with PSA, as shown in Fig. 4.14f.

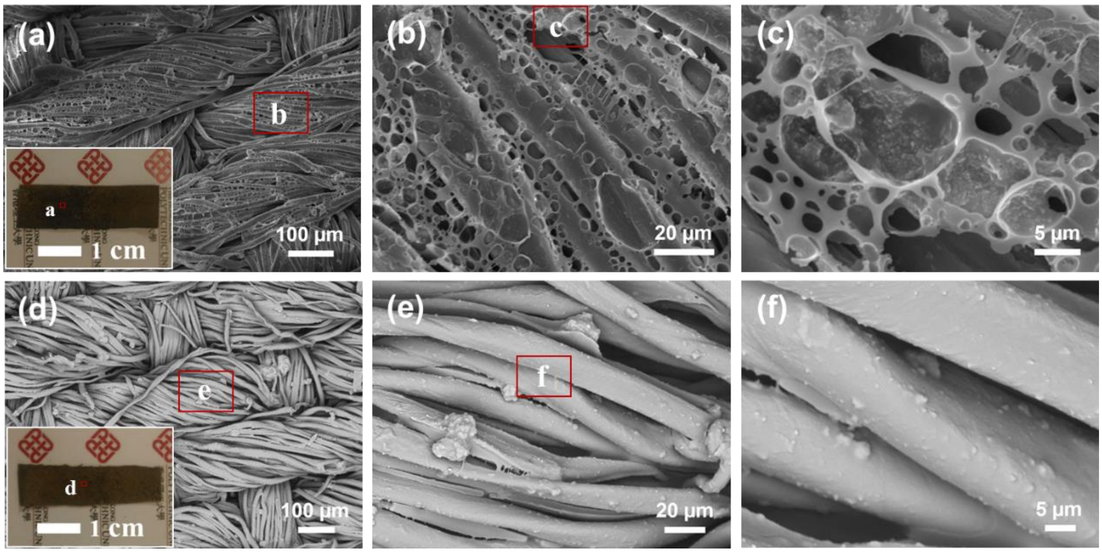

Figure 4. 14 SEM images of TiO_2-hybrid porous (a)-(c) and solid (d)-(f) PSA films

coated on flexible cotton fabrics, the magnifications of the corresponding areas marked with a, b, c, d, e, and f responsively. The insets of (a) and (d) were a 1 cm x 4 cm hybrid porous, and hybrid solid film-coated cotton fabric respectively

The experimental results indicate that the incorporated nanoparticles prefer to selectively aggregate at the pore walls rather than embedding in the solid matrix. This can be ascribed to the Pickering emulsions effect during the BF process.[348] The Pickering emulsions effect is a kind of emulsion phenomenon stabilized by solid particles, which was named after S.U. Pickering. When solid particles are mixed with water and oil to prepare emulsions, they will be absorbed onto the liquid-liquid interfaces, and stabilize the formed emulsions by preventing the small droplets from coalescing. [348,349]

In the typical BF process, numerous water droplets are introduced onto the solution surface by evaporative cooling, which will lead to the formation of liquid/liquid interfaces. Fig. 4.15a schematically shows a water droplet floating on the surface of the PSA solution blended with desired nanocomponents, such as TiO_2 nanoparticles. Before the liquid film becomes viscous, the blended nanoparticles will tend to move with the polymer chains towards the interface of water and solution (Fig. 4.15b). They can aggregate at the interface and form a nanoparticle/precipitated polymer layer to stabilize the formed water droplet (Fig. 4.15c). With the decrease of solvent by evaporation, the gelation of polymer/nanoparticle mixtures will occur. This will lock the incorporated nanoparticles at the interface. After the complete evaporation of residual solvent and water, spherical pores with the decoration of nanoparticles will be formed in the polymer films.

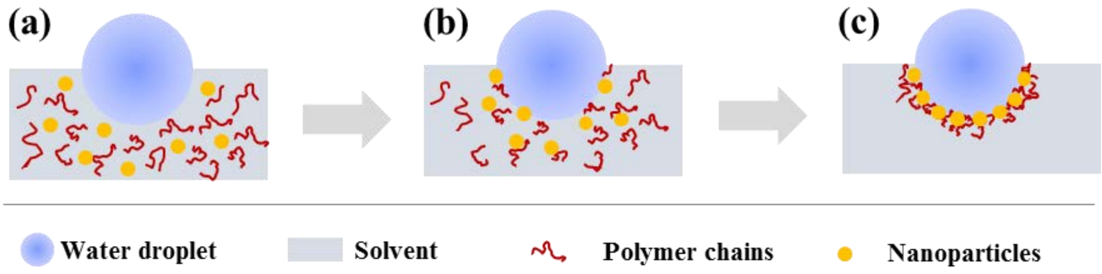

Figure 4. 15 Schematic diagram of the introduced nanoparticles assembling on the water/solution interface caused by the Pickering Emulsions effect during the BF process

4.6.2 Photocatalytic degradation of pollutants based on TiO_2-incorporated PSA porous microstructures

The functionality of porous PSA microstructures can be tailored for different applications through choosing the incorporated nanoparticles. And based on the used substrates, the nanoparticles-incorporated PSA porous microstructures can be applied in different ways. Taking the photocatalytic characteristic of TiO_2 NPs as example, when the TiO_2-incorporated PSA porous microstructures were introduced on a solid substrate as film by the BF technique, they can be employed for the removal of vehicle emissions in air with the assistance of UV irradiation;[350] when the TiO_2-incorporated PSA porous microstructures were coated on the flexible cotton fabric, the resultant textile composites with hierarchical microstructures can be used for photocatalytic degradation of dyes in water.[351,352]

4.6.2.1 Photocatalytic degradation of air pollutants

Nitrogen oxides (NO_x, mainly involving NO and NO_2) are some of the main air pollutants from vehicle emissions.[350,353] They are also the major precursors of particulate matter 2.5. With the assistance of UV irradiation, there have been a few reports about the removal of NO_x by using the fascinating photocatalytic characteristic of TiO_2. Here porous PSA microstructures with the incorporation of 25 wt% TiO_2 NPs were specifically prepared on a solid substrate with the area of about 81 cm^2 by the BF technique. For a comparison, a control sample without honeycomb microstructures was also prepared by traditional spraying TiO_2 method. Their performances on the mitigation of NO_x were quantitatively evaluated and compared by a custom-designed environmental test setup. The setup system that can test the NO_x removal efficiency consists of four main parts: the gas source, light source, data analysis system and reacting chamber equipped with gas inlet and outlet.

In a typical test, the testing sample was placed in the reacting chamber beforehand. The temperature and humidity of reacting chamber were controlled at 20°C and 10%, respectively. The fluorescent lamp that can emit UV irradiations with the wavelength of 365 nm was used as light source. And the luminosity was fixed at 2 mW cm^{-2}. NO_x was carried inside the reacting chamber by a gas flow rate of 1.5 L min^{-1}. The gas flow was adjusted to obtain an initial NO_x concentration (C_{initial}). After C_{initial} reaching at 1000 parts per billion (ppb) and keeping stable, the UV light was turned on. Then the variation of NO_x concentration was monitored and recorded by computer. The change of NO_x reduction efficiency during the whole process was calculated based on the data analysis system. The variations of NO_x concentration for different samples were plotted against time. As shown in Fig. 4.16, the NO_x concentration in the reacting chamber approached stable again after about 25 minutes, which was recorded as C_{stable}. In comparison to the solid hybrid film sample without porous microstructures, the porous hybrid film sample incorporated with the same amount of TiO_2 shows an obviously enhanced ability of removing NO_x. Based on the values of C_{initial} and C_{stable}, the efficiency of removing NO_x can be further calculated by the Eq.4.1:

$$\text{Efficiency of removing NOx } (E\%) = \frac{C_{initial} - C_{stable}}{C_{initial}} \times 100\% \qquad (4.1)$$

Where C_{initial} and C_{stable} are the stable NO_x concentrations before and after the UV irradiation, respectively.

The efficiency of control sample without porous microstructures was calculated as 24%, while the efficiency of PSA/TiO_2 hybrid film increased to 40 % after the introduction of porous microstructures by the BF technique. Moreover, from Fig. 4.16, the photocatalytic efficiency of control sample shows a gradual decrease with time after 5 minutes, while the porous film sample always keeps at high NO_x reduction efficiency with no attenuation.

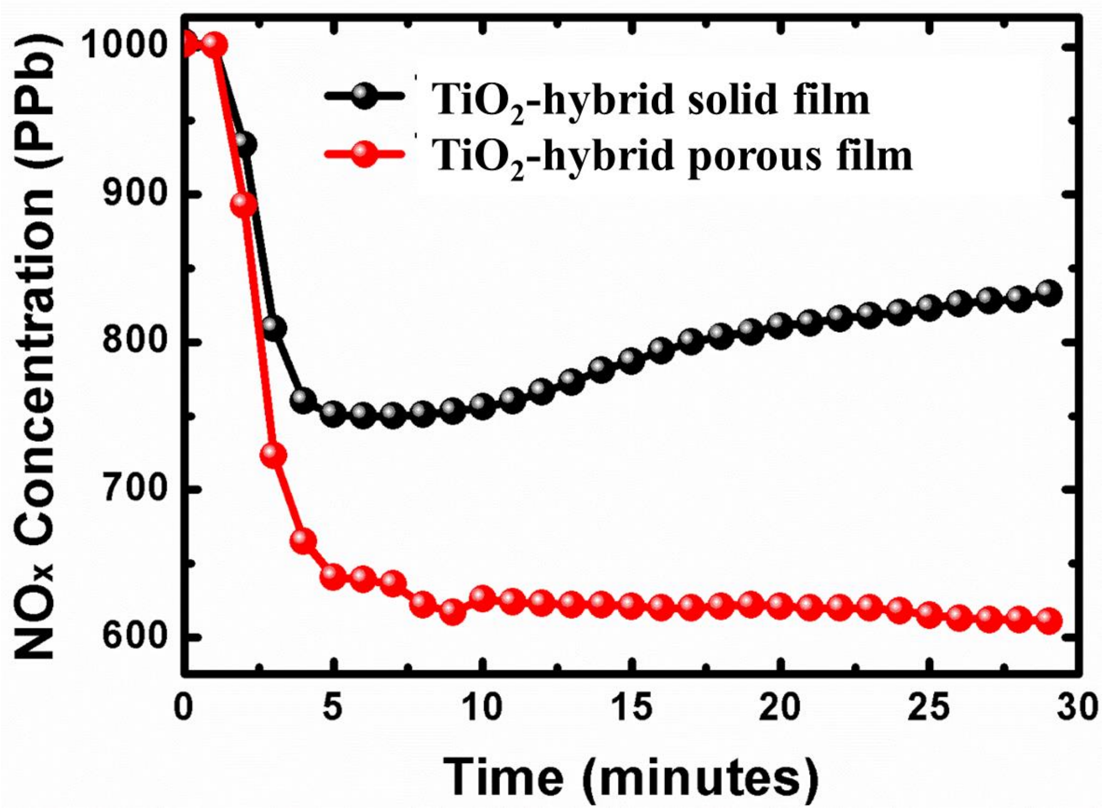

Figure 4. 16 Variation of NO_x concentration for solid (black dot line) and porous (red dot line) film samples with the exposure time of UV irradiation. Here both solid and porous film samples were incorporated with 25 wt% TiO_2

The mechanism of mitigating NO_x by the TiO_2/PSA hybrid films is based on the photocatalytic oxidation property of incorporated TiO_2 NPs, which has been well demonstrated by Agrios et al.[354] In the presence of UV irradiation with appropriate wavelength, NO_x pollutants can be oxidized into water-soluble nitrates with the catalysis of TiO_2. The whole heterogeneous photocatalytic oxidation process can be described by the following equations. First, TiO_2 is excited by the photon with the energy larger than or equal to the band gap of 3.2 eV. This will lead to the generation of conduction band electron (e^-) and valence band hole (h^+) pairs (Eq.4.2) on the surfaces of TiO_2 NPs. Then, owing to the strong oxidization of h^+, OH^- dissociated from water will be oxidized to active hydroxyl radical (OH*) (Eq.4.3). While e^- is a powerful reducing agent, and it can reduce oxygen (O_2) to superoxide anion (O_2^-) (Eq.4.4). And O_2^- can further react with H^+ for the generation of HO_2* radical (Eq.4.5). Both HO_2* and OH* are powerful oxidants. The former radical can oxide NO to NO_2 and generate a radical of OH* (Eq.4.6). Finally, the hazardous NO_2 will be oxidized by OH* to produce water soluble nitrates (NO_3^-), as described by Eq.4.7.[354-356]

$$TiO_2 + h\nu \rightarrow h^+ + e^- \qquad (4.2)$$

$$h^+ + OH^- \rightarrow OH^* \qquad (4.3)$$

$$e^- + O_2 \rightarrow O_2^- \qquad (4.4)$$

$$H^+ + O_2^- \rightarrow HO_2^* \qquad (4.5)$$

$$NO + HO_2^* \rightarrow NO_2 + OH^* \qquad (4.6)$$

$$NO_2 + OH^* \rightarrow HNO_3 \qquad (4.7)$$

The performance of removing NO_x by PSA/TiO_2 hybrid films is greatly dependent on the exposing area of TiO_2 on the film surface. This is because the photocatalytic oxidization process can only occur when UV irradiation and pollutants both contact with TiO_2 NPs. For the TiO_2 NPs embedded in the solid matrix, the diffusion of NO_x is slow and difficult, and the UV light will be shielded. The obviously enhanced and sustainable efficiency of removing NO_x for the porous film sample by the BF technique can be attributed to two factors: (1) the Pickering emulsions effect during the BF process and (2) the porous microstructures templated from the water droplets. The former enables the incorporated TiO_2 NPs prefer to exposing at the pore surface rather than embedding in the solid matrix, while the latter increases the specific surface area of film, thereby providing a larger contact surface for TiO_2 NPs to catalyze the oxidization reaction of removing NO_x with the assistance of UV irradiation.

4.6.2.2 Photocatalytic degradation of dyes in water

Owing to containing large amounts of sorption-active cellulose,[93,357] the flexible and permeable cotton fabrics are usually colored by different dyes for various textile applications. Moreover, taking advantages of its easy dying characteristic, cotton fabrics are also ideal materials for the removal of waste dyes by physical adsorption. After introducing the porous microstructures of PSA/TiO_2 hybrid materials by the BF technique, the modified cotton fabric can undergo a “first adsorption, then chemical degradation” process to totally remove the waste dyes without secondary pollution with the assistance of UV irradiation. To demonstrate this novel application, an azo dye, mordant orange 1 (MO1), was used as the model pollutant. PSA/TiO_2-hybrid porous microstructures coated on the cotton fabric prepared above were cut into 1 cm x 4 cm strip and immersed into a 10 mL bottle filled with MO1 aqueous solution (5×10^{-5} M). PSA/TiO_2 modified cotton fabric with the same size but without porous microstructures was also immersed into MO1 solution as control sample. The photochemical degradation process was performed by placing the bottles in a chamber within two UV light tubes. Each light tube generated UV emissions at a wavelength of 365 nm and power of 18 W. The distance between the UV source and fabric was 10 cm. A digital camera and an ultraviolet/visible (UV/vis) spectrometer (Lambda 18 UV/VIS Spectrometer) were employed to examine the color and MO1 concentration of solution with time respectively.

Under 365 nm UV irradiation, the generation process of h^+, e^-, OH* and HO_2* radicals on the surface of TiO_2 NPs in water is similar to the process in air (Eqs. 4.2-5). The dye molecule absorbed in the pores can be either reduced by electrons (Eq. 4.8) or oxidized by holes (Eq.4.9). The generated OH* and HO_2* radicals are also responsible for the decomposition of dyes though a series of complex heterogeneous reactions (Eq.4.10). Based on the reported literatures, the possible photo-degradation pathways of MO1 catalyzed by TiO_2 with the assistance of UV irradiation are shown in Fig. 4.17.[351,352]

$$e^- + \text{Dye} \rightarrow \text{reduction products} \quad (4.8)$$

$$h^+ + \text{Dye} \rightarrow \text{oxidation products} \quad (4.9)$$

$$HO_2^* + \text{Dye} \rightarrow \text{degradation products} \quad (4.10)$$

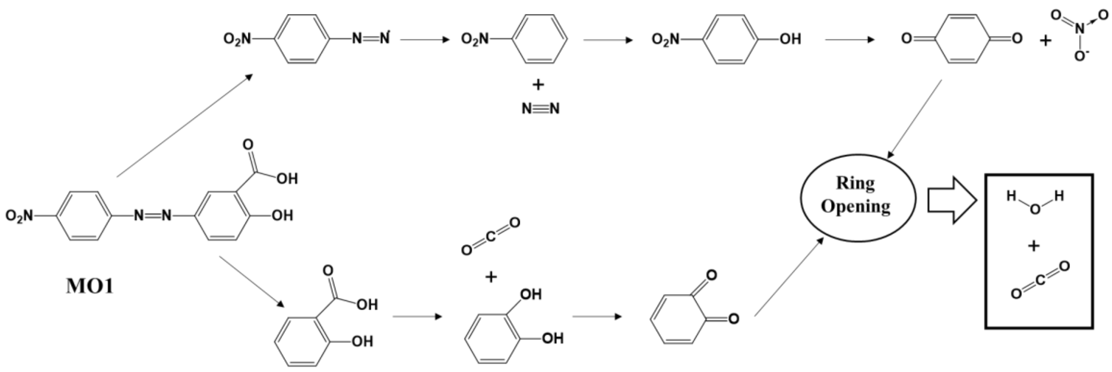

Figure 4. 17 Molecular structure of MO1, and possible photo-degradation pathways of MO1 with TiO_2 as catalyst under UV irradiation

Fig. 4.18a shows the UV-visible absorption spectra of MO1 aqueous solution of porous PSA/TiO_2 hybrid microstructures coated cotton fabric statically placed under 365 nm UV lamp with different time of durations. MO1 shows a strong absorption band at 371 nm (0 h, black line). The band intensity decreases with the increasing UV exposure time. After 128 h, the absorbance decreased by ca. 91.5%. And the yellow solution becomes colorless, reflecting that most of MO1 was degraded. By contrast, when TiO_2-hybrid PSA coated fabric sample without porous microstructure was immersed in MO1 solution with the same initial concentration for 128 h UV exposure, the solution color becomes light yellow, but the declination of band intensity is only about 36.1% (Fig. 4.18b). The removal efficiency of MO1 by the fabric-based samples with different microstructures was further plotted against time, as shown in Fig. 4.18c. It clearly indicates the fabric sample coated with the porous microstructures of PSA/TiO_2 hybrids possesses a quicker and strong capacity of removing MO1 than the control sample without porous microstructures. This reason for the low efficiency of control sample can be ascribed to the aggregation of TiO_2 nanoparticles and their embedment in solid PSA film.

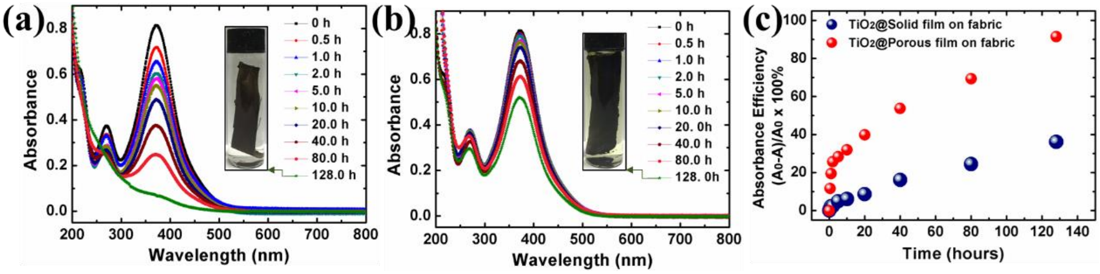

Figure 4. 18 UV-visible spectral changes of MO1 aqueous solution (5 x 10^{-5} M) in the presence of hybrid porous (a) and solid (b) film-coated cotton fabrics with the exposure time of 365 nm UV irradiation. The insets of (a) and (b) were their photographs of immersing in MO1 aqueous solution after 128 h UV irradiation respectively. (c) The plot of removal efficiency of MO1 against time by different fabric-based samples

4.7 Summary

In summary, this work successfully developed a robust asphalt-assisted BF strategy for general fabrication of noncracking ordered porous films with narrowed size distribution and greatly promoted regularity based on easily obtained polymers, such as commercial PS, SBS, PEO and PC. Various material surfaces including nonplanar surface, such as glass, silicon, copper, copper grid, fabric, irregular particle, and even water surface, were used as substrates for the formation of highly ordered BFAs. Moreover, when desired functional nanocomponents, such as TiO_2 NPs, Ag NWs, and Cu NWs, were incorporated into porous films, little influence on the regularity of pore arrays was found. This contributes to uncovering the incorporated nanoparticles, thereby maintaining their excellent properties to the utmost extent. In comparison to TiO_2 embedded solid films, for example, a greatly enhanced efficiency was obtained when the TiO_2-incorporated BFA films was used for photocatalytic degradation of pollutants in either air or water.

This study not only provides an effective solution for direct and general fabrication of ordered porous films with commercial polymers and materials but also enables their optimal BF conditions to be more easily accessible. Moreover, the additive principle can be extended to direct incorporation of different nanoparticles for customized functionalization of BFA films. This study is believed to accelerate development of BF techniques and BFA films for more commercial applications.

CHAPTER 5 Fabric-based Three-Dimensionally Conformal Breath Figure Arrays with Adjustable Dimensional Architectures

5.1 Introduction

Fabrics are flexible and versatile materials consisting of natural or synthetic yarns (or fibers) that can be knitted, woven or nonwoven into designable network structures for a broad spectrum of applications.[358,359] They are often further treated by surface modification (e.g. plasma treatment) or coating (e.g. knife coating) techniques in practical uses.[360,361] Unfortunately, the incorporated properties for coated textiles always cannot achieve a maximum performance due to the limited effective areas of solid surface layer. Physical modification of fabrics with the porous microstructures of desired materials conformably formed on the uneven surface of textile substrates may provide an effective solution of combining multifunctional properties of introduced materials, inherent excellent fabric properties and unique texture features of fabrics. However, this study is significantly less developed.

In this chapter, 3D conformal honeycomb pore arrays (or 3D conformal breath figure arrays, 3C-BFAs) on nonplanar substrates, particular on flexible fabrics with complex surface textures, are developed and studied based on a novel silicon-containing graft copolymer poly(dimethylsiloxane)-*graft*-polyacrylates (PDMS-*g*-PAs). The excellent film-forming properties of PDMS-*g*-PAs is first investigated on a planar substrate by the BF technique. Then based on a special metal fabric, Cu/Ni-coated fabric, the formation of fabric-based 3C-BFAs (F3C-BFAs) is systematically studied to find an optimal concentration range of casting solution that can meanwhile form ordered BFAs and maintain elaborate surface features of fabric. Finally, taking advantages of the silicon-containing characters, PDMS-*g*-PAs BFA films is explored as single-source precursor for in situ formation of honeycomb microstuctured ceramics.

5.2 Chemical structure of PDMS-g-PAs

The employed PDMS-*g*-PAs was purchased from Sigma-Aldrich, Ltd and used as received. Its chemical structure is shown in Fig. 5.1. It is composed of a linear backbone of PDMS and randomly distributed branches of polyacrylates. According to the functional groups, the side chains can be generally classified into two types: hydrophilic segments (polyacrylic acid (I) and polymethacrylic acid (I)) and hydrophobic segments (including series of polyacrylates (II and III) and polymethacrylates (II and III)). The chemical PDMS-g-PAs was further characterized by GPC and HNMR respectively. GPC analysis was performed with a Waters 1515 pump and Waters 1515 differential refractive index detector (set at 30 °C). It used a series of three linear Styragel columns (HT2, HT4, and HT5) at an oven temperature of 45 °C. The eluent was tetrahydrofuran at a flow rate of 1.0 mL min^{-1}. A series of low-polydispersity polystyrene standards were employed for the GPC calibration. Proton nuclear magnetic resonance (^{1}H NMR) spectra of PDMS-g-PAs was collected by using an AV 500 MHz spectrometer in dimethyl sulfoxide-d$_6$ (DMSO-d$_6$) at 25 °C.

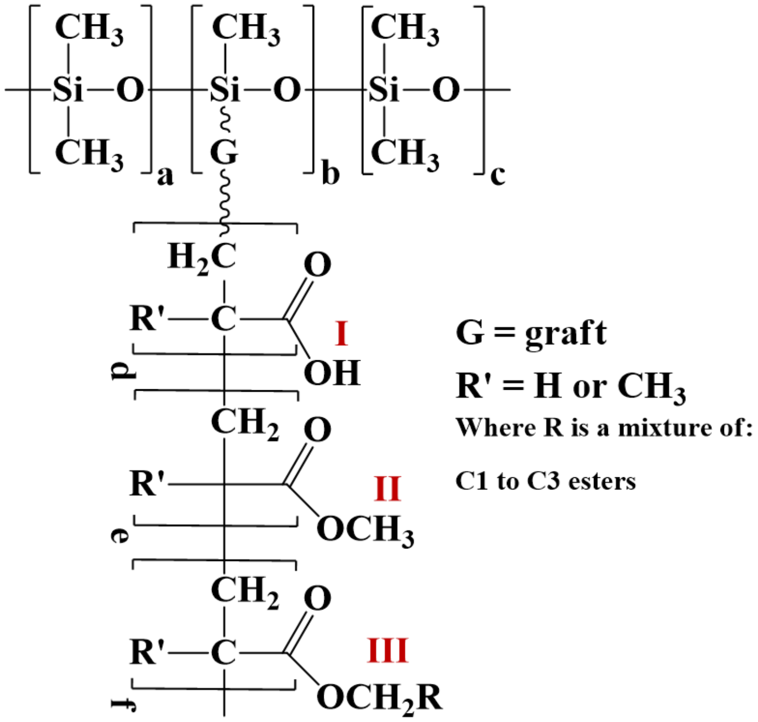

Figure 5. 1 Chemical structure of graft silicon-containing polymer PDMS-*g*-PAs

The M_n of this silicon-containing graft copolymer is 26,000, with approximately 80 wt% PDMS, which enables further formation of silicon oxide by oxidation. Its M_w/M_n determined by GPC in THF is 1.88, and the GPC trace exhibits a relatively narrow peak, as demonstrated in Fig. 5.2a. ^{1}H NMR analysis of the graft copolymer (Fig. 5.2b) shows distinct resonances at 3.41, 3.61 and 12.54 ppm, corresponding to methyl protons of -COOCH$_3$ (II), methylene protons of -COOCH$_2$R (III), and carboxyl proton (-COOH, I) respectively. The ratio of the relative proton numbers in carboxyl group to ester groups is 1: 54.40, wherein the ratio of protons in methyl group to methylene groups is 1:1.80 by dividing the integral of ester groups. Comparing the resonances associated with carboxyl proton to those associated with ester groups, and combining the molecular formula, it was possible to determine that the ration of hydrophilic segments to hydrophobic segments in the graft copolymer is about 1: 24.05.

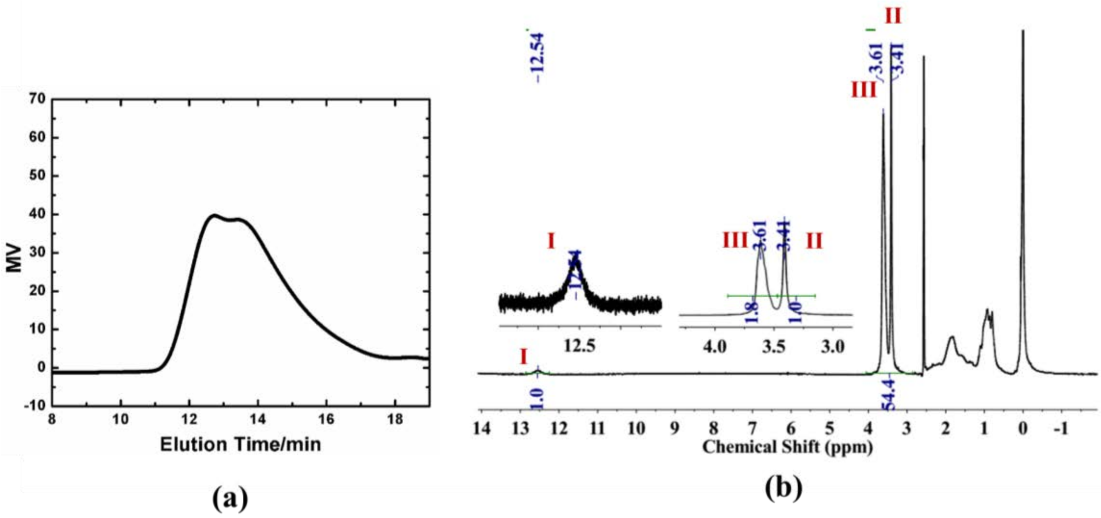

Figure 5. 2 GPC trace (a) and ^{1}H NMR spectra (b) of PDMS-*g*-PAs

5.3 Film-forming properties of PDMS-*g*-PAs

5.3.1 Surface morphology evolution of BFAs with solution concentration

Comparing with nonpolar linear homopolymer stated previously, herein the employed linear polymer with branching chains is believed to be a promising candidate for fabricating more ordered porous films. This is because the branched chains can promote the segment density of polymer, which can effectively stabilize water droplet arrays during the precipitation process of BF.[10] Moreover, the existence of hydrophilic groups endows polymers with a certain degree of hydrophilicity. The proper interaction of the water with the hydrophilic segments is available for further enhancement of formed droplet arrays.[7] Actually, when this polymer was dissolved in $CHCl_3$, and applied to form polymer films by the static BF process in aqueous vapor, regular honeycomb porous microstructures were obtained in a wide solution concentration, ranging from a very low content 0.30 mg mL^{-1} to 45 mg mL-^{1}, as demonstrated in Fig. 5.3b-k. Only for the solution concentration at 0.15 mg mL^{-1}, the honeycomb features on film surface are completely disappeared (Fig. 5.3a). On the other hand, when increasing polymer content to 60 mg mL^{-1}, less regular hierarchical porous films are observed (Fig. 5.3l), with smaller pores in cell-like structures. A SEM image with low magnification shows that cellular pores are distributed evenly in the whole surface area. At relatively low solution concentrations, it is observed from the SEM views of film surfaces that a single layer of uniform holes reaching the bottom of films arranges hexagonally on substrates (Fig. 5.3b-e). As the solution concentration reaching at 1.50 mg mL^{-1}, the top view of SEM indicates the existence of pores inside the film. With the continuing increase of solution concentration, the pores in the second layer are observed clearly through the top surface of the film, as demonstrated in Fig. 5.3g-k.

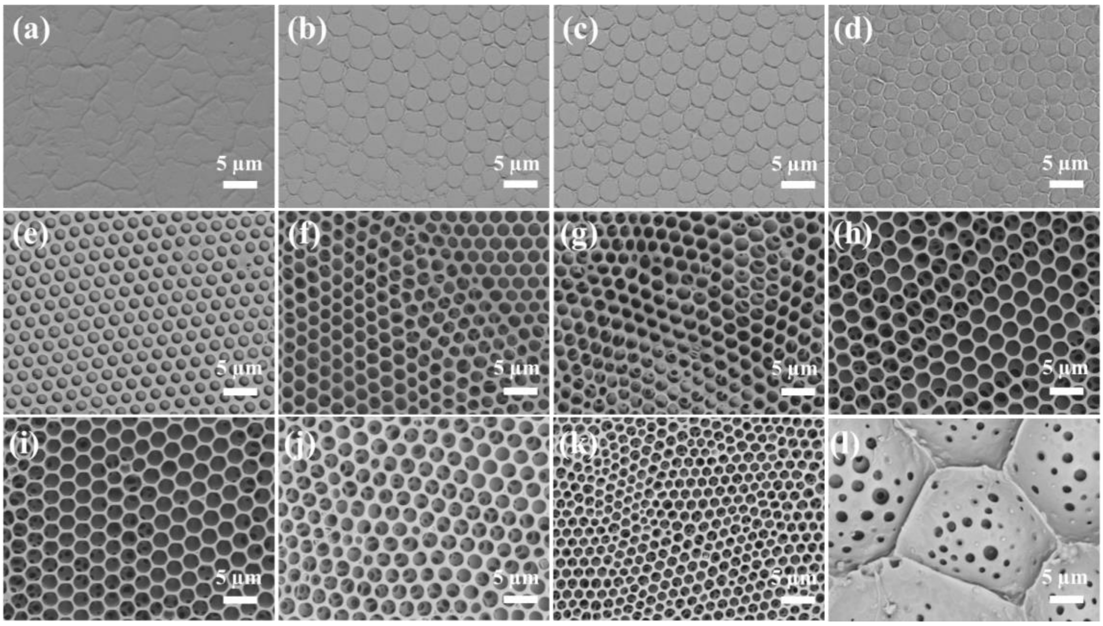

Figure 5. 3 Morphology evolution of film surfaces investigated by SEM with the increasing solution concentration. The films are prepared by casting from

PDMS-*g*-PAs/$CHCl_3$ solutions with different concentrations: (a) 0.15 mg mL^{-1}; (b) 0.30 mg mL^{-1}, (c) 0.45 mg mL^{-1}, (d) 0.75 mg mL^{-1}, (e) 1.20 mg mL^{-1}, (f) 1.50 mg mL^{-1}, (g) 4.50 mg mL^{-1}, (h) 7.50 mg mL^{-1}, (i) 15.00 mg mL^{-1}, (j) 30.00 mg mL^{-1}, (k) 45.00 mg mL^{-1}, and (l) 60.00 mg mL^{-1}

The obtained polymer films with different porous layers exhibit several typical topographies under optical microscopy (OM), as demonstrated in Fig.5.4. Generally, if the concentration of casting solution is extremely low, randomly distributed structures are observed on substrates (Fig. 5.4a). The regular lightspot arrays indicate that the surface of the film is covered by a single layer of ordered pores, while the ambiguous shades reflect that the film possesses multilayer porous structures, as shown in Fig. 5.4b-e, respectively. Cellular structures embedded with small pores obtained at high concentration can also be observed clearly, as shown in Fig. 5.4f, which are consistent with the morphology revealed by SEM above.

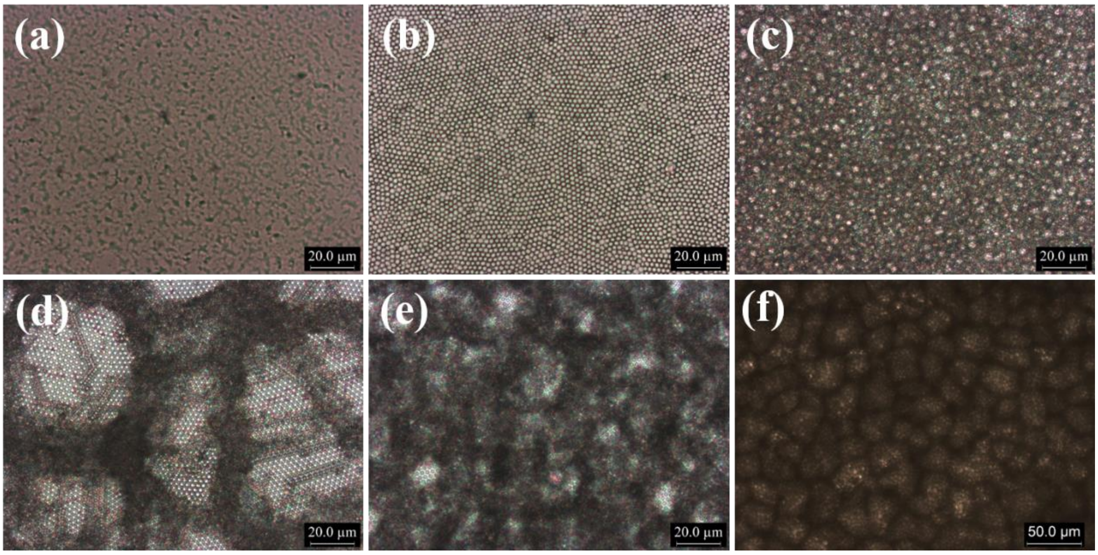

Figure 5. 4 Optical micrographs of PDMS-*g*-PAs films cast on glass substrates

from different solution concentration: (a) 0.15 mg mL^{-1}; (b) 0.45 mg mL^{-1}, (c) 4.5 mg mL^{-1}, (d) 7.5 mg mL-1, (e) 15 mg mL^{-1}, and (f) 65 mg mL^{-1}

The results revealed by SEM and OM clearly demonstrate that PDMS-*g*-PAs is an excellent material for the preparation of ordered BFAs by the aqueous BF technique in a wide solution concentration. However, it should be noted that the BFA films cannot be prepared by direct use of linear PDMS. This is because the extremely low T_g (less than -120 ºC) and high theological properties of PDMS cannot effectively maintain the formed porous microstructures at ambient conditions. While for PDMS-*g*-PAs, the T_gs of its grafted poly(meth)acrylates and poly(meth)acrylic acid are approximately 100 ºC.[33] This contributes to the increase of the T_g of PDMS-g-PAs, thereby maintaining its formed porous microstructures.

5.3.2 Dimensional architecture evolution of BFAs with solution concentration

The cross-sectional views of BFAs prepared form PDMS-*g*-PAs/$CHCl_3$ solutions with the concentration ranging from 0.15 mg mL^{-1} to 60 mg mL^{-1} by the aqueous BF technique were also examined by SEM respectively. As shown in Fig. 5.5, the revealed inner structures of BFAs show an obvious evolution of dimensional architecture with the increasing solution concentration. Except the films cast from the solution with extremely low concentration (Fig. 5.5a), porous structures throughout the whole film are observed at the solution concentration less than 4.5 mg mL^{-1}. Especially, single-layer structures are obtained when the casting solution is below 1.2 mg mL (Fig. 5.5b-e), while two- and three-layer pores are found at 1.5 mg mL^{-1} (Fig. 5.5f) and 4.5 mg mL^{-1} (Fig. 5.5g) respectively. Besides multiple porous layers, a dense polymer stratum emerges in the film bottom at the concentration of 7.5 mg mL^{-1} (Fig. 5.5h), which can be obviously observed when the casting solution is more than 15.00 mg mL^{-1} (Fig. 5.5i-l). The thickness of dense stratum increases gradually with the rising concentration of casting solution while the thickness of porous layers decreases slightly, as shown in Fig.5.5h-l.

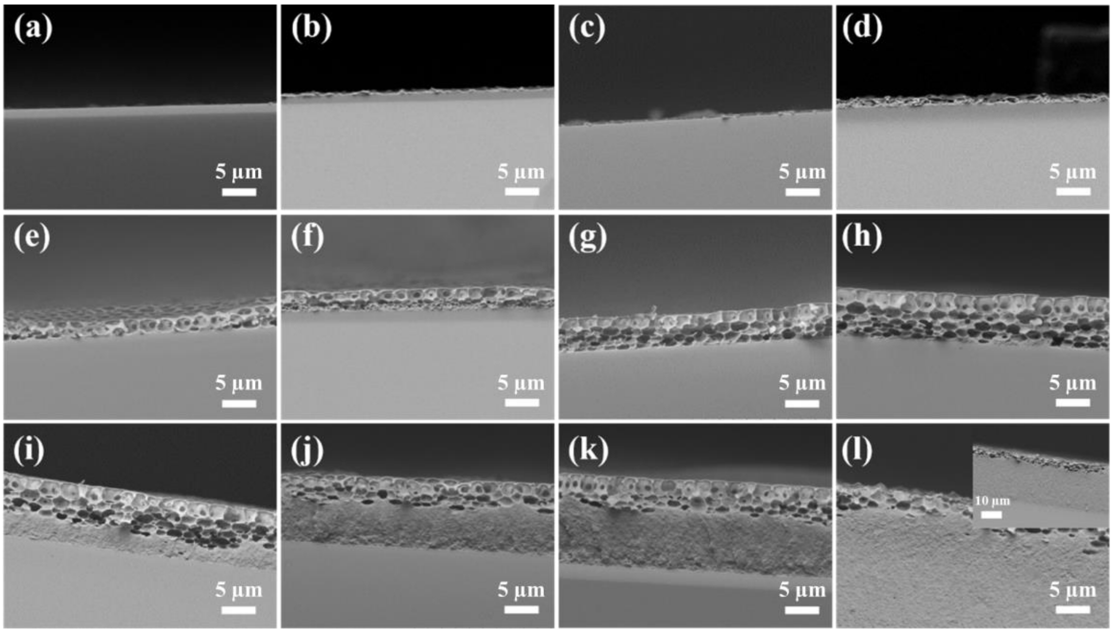

Figure 5. 5 SEM cross-sectional views of the honeycomb structured films cast from different solution concentrations. (a) 0.15 mg mL^{-1}; (b) 0.30 mg mL^{-1}, (c) 0.45 mg mL^{-1}, (d) 0.75 mg mL^{-1}, (e) 1.20 mg mL^{-1}, (f) 1.50 mg mL^{-1}, (g) 4.50 mg mL^{-1}, (h) 7.50 mg mL^{-1}, (i) 15.00 mg mL^{-1}, (j) 30.00 mg mL^{-1}, (k) 45.00 mg mL^{-1}, and (l) 60.00 mg mL^{-1}

The influences of solution concentration on the microstructures of BFAs are further studied by analyzing pore sizes, the thickness of porous layers and dense stratum, as shown in Fig. 5.6. It is obvious that the average sizes of pores on film surface fluctuates with the solution concentration (Fig. 5.6a), while the film thickness shows an upward trend (Fig. 5.6b). More exactly, the thickness of the emerging dense stratum in the film at 7.5 mg mL^{-1} drastically increases from about 0.62 μm to 22.11 μm at 65 mg mL^{-1}, but the porous layers' thickness decreases to 4.15 μm finally after a steady rise to the peak of 6.55 μm from approximately 0. 26 μm at 0.15 mg mL^{-1}. Porous structured films without dense stratums can be classified into two types: monolayer porous films and multilayer porous films. The pore sizes of the monolayer porous films obtained at low concentrations exhibit downward trends, decreasing from 2.75 μm at 0. 30 mg mL^{-1} to 1.64 μm at 1.20 mg mL^{-1}, while the sizes of multilayer porous structures obtained between 1.50 and 4.50 mg mL^{-1} show a slightly increase. However, only films with multilayer porous structures on a dense stratum were fabricated when increasing to 7.5 mg mL^{-1}, and their pore sizes decline again, from 2.35 μm to 1.42 μm at 45.00 mg mL^{-1}. Hierarchically structured film cast from the solution of 65 mg mL^{-1} displays a pore size of 1.49 μm but with a large standard deviation of 0.47, indicative of the less regularity of pore arrays.

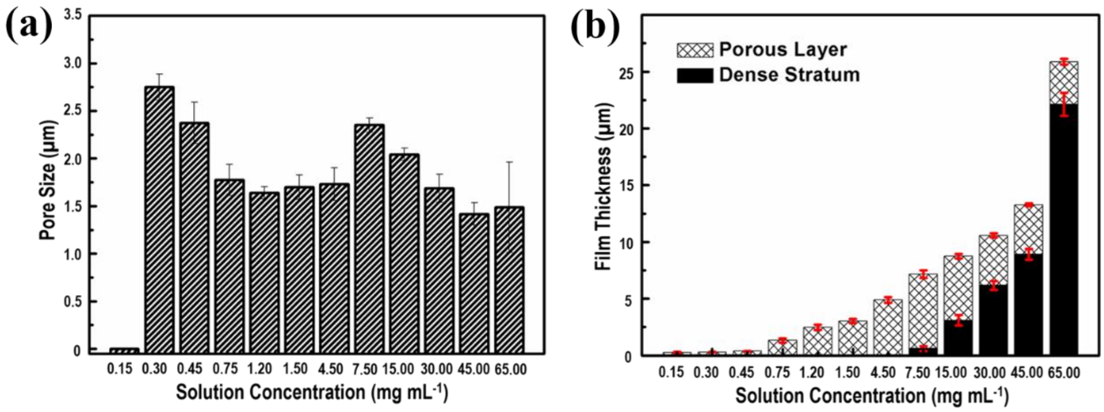

Figure 5. 6 (a) Plot of the dependence of pore sizes on solution concentrations. (b) Graphical comparison of the thickness of porous layers and dense stratum in the films cast from different solution concentrations

5.4 Study of 3C-BFAs on flexible and nonplanar Fabrics

Owing to its rapid process and spontaneous formation and evaporation of water droplets, it is feasible for the BF technique to prepare 3D porous microstructures those contour to the curved surfaces of nonplanar substrates. In section 4.4.2.2, we have demonstrated that directly casting PSA solution by the aqueous BF technique can effectively and rapidly prepare noncracking 3D conformal BFAs (3C-BFAs) on different nonplanar surfaces with the assistance of semisolid asphalt. Benefiting from the low T_g of PDMS component, PDMS-*g*-PAs is also a good film-forming material for the formation of 3C-BFAs. In this section, the formation of 3C-BFAs on nonplanar surfaces will be systematically investigated based on PDMS-*g*-PAs. PDMS-*g*-PAs that can form non-cracking and ordered BFAs in a wide solution concentration facilitate to investigate the influence of the solution concentration on the formation of 3C-BFAs on nonplanar surfaces. To prepare fabric based 3C-BFAs (F3C-BFAs) possessing both the 3D surface profiles of fabric substrates and BFAs templated from water droplet arrays, a kind of commercial Cu/Ni-coated fabric brought from 3M Corp. was explored as flexible and nonplanar substrates for the BF technique. The influence of solution concentration on the surface microstructures of F3C-BFAs was investigated systematically.

The employed Cu/Ni-coated fabric is flexible (Fig. 5.7a) and can be easily tailored according to required size. It is copper-nickel coated conductive polyester fabric with one surface coated with electrically conductive acrylic adhesive. SEM was employed to further reveal its surface microstructures. As shown in Fig. 5.7b and c, the conductive fabric is directly plain weaved by numerous Cu/Ni coated polyester fibers. The diameter of fiber is around 20 μm, which fluctuates in several micrometers. Fig. 5.7d shows the threadlike fibers which have a coarse surface with particulate features. This can be clearly observed by further close view (the inset of Fig. 5.7d). The size of particulate protuberances ranges from dozens of nanometers to several micrometers. These results reveal that the employed Cu/Ni-coated fabric possesses a multilevel surface structure composed of millimeter-scale plain fabric texture, microscale fiber, and nanoscale particulate features. The cross-sectional views in Fig. 5.7e-g indicate that the thickness of Cu/Ni-coated fabric is approximately 100 μm.

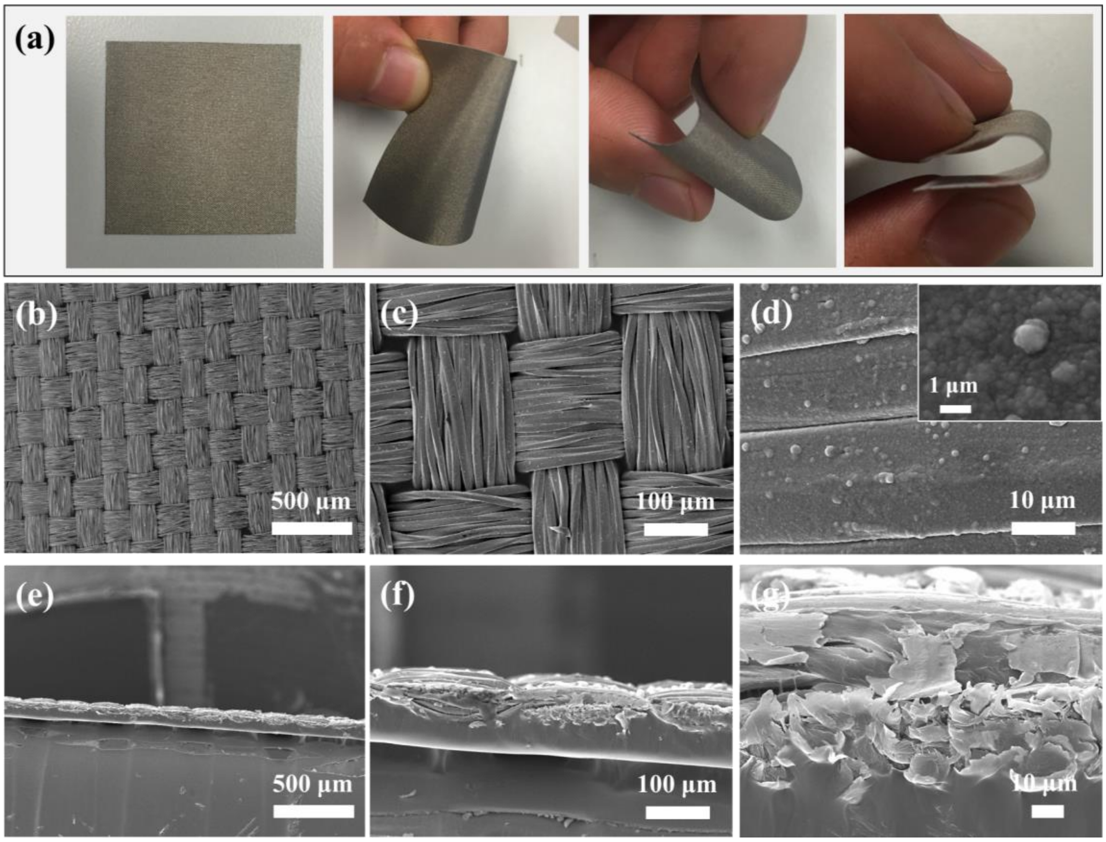

Figure 5. 7 (a) Digital photographs and (b)-(g) SEM images of flexible Cu/Ni-coated fabric with (b)-(d) top views and (e)-(g) cross-sectional views

The PDMS-*g*-PAs solution of 60 mg mL^{-1} was first prepared by dissolving a given amount of PDMS-g-PAs in $CHCl_3$. Then it was gradually diluted with solvent to obtain a series of solutions with the concentrations of 45 mg mL^{-1}, 30 mg mL^{-1}, 15 mg mL^{-1}, 7.5 mg mL^{-1}, and 3.0 mg mL^{-1}. These solutions were cast on Cu/Ni-coated fabric substrates with the same volume under aqueous vapor by the BF technique, respectively. All of them can well spread on the Cu/Ni-coated fabric substrate with good wettability. And it was found that the spreading area of casting solution possessed a general increasing trend with the decrease of solution concentration. According to the concentration of casting solution, the finally resultant F3C-BFAs are named as F3C-BFA-60, F3C-BFA-45, F3C-BFA-30, F3C-BFA-15, F3C-BFA-7.5 and F3C-BFA-3.0, respectively.

The surface microstructures of F3C-BFA-60 revealed by SEM at different magnifications are shown in Fig. 5.8. No obvious surface feature of fabric substrate is found (Fig. 5.8a and b). Higher magnified views show that F3C-BFA-60 displays disordered cellular microstructures in large area (Fig. 5.8c and d). And small pores can be found inside the open cells (Fig. 5.8e and f), which is very similar to BFAs prepared from 60 mg mL^{-1} on a planar substrate. These results indicate that the surface textures of Cu/Ni-coated fabric substrate are almost totally concealed by the BFs-generated porous microstructures. This is mainly due to the high concentration of casting solution, which contains enough polymers to smooth the uneven surface, and finally results in the formation of a thick porous film on fabric.

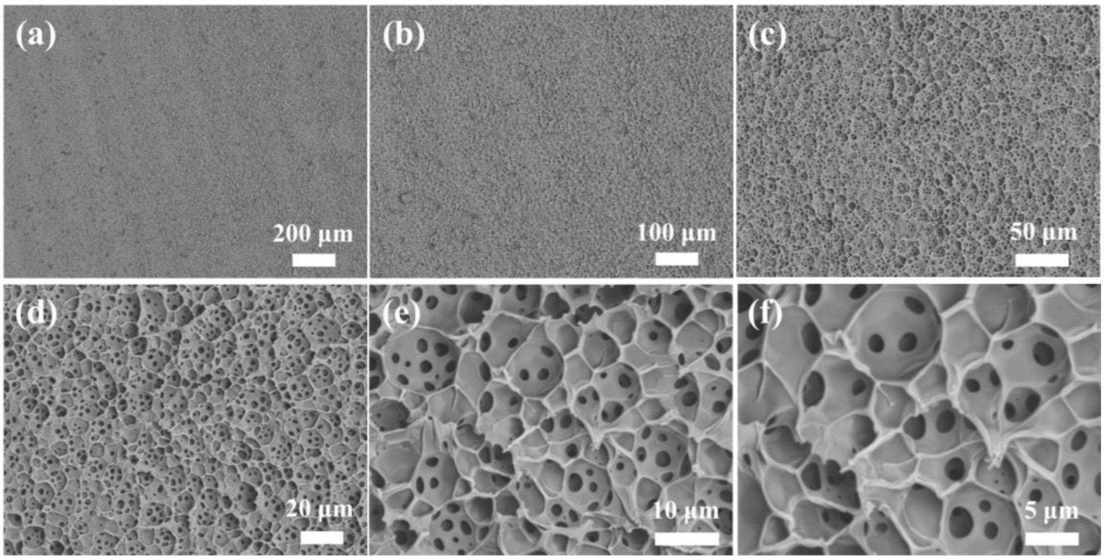

Figure 5. 8 SEM images at different magnifications of F3C-BFA-60 film prepared by the BF technique from 60 mg mL^{-1} PDMS-g-PAs/CHCl$_3$ solution

The fabric textures of F3C-BFA-45 become observable when the concentration of casting soluton was decreased to 45 mg mL^{-1} (Fig. 5.9a and b). And some of its fiber profiles are roughly distinguishable (Fig. 59c and d). They are fully covered with continuous porous film, which displays highly ordered BFAs at higher magnifications (Fig. 5.9e and f). When the solution concentration was further decreased to 30 mg mL^{-1}, the resulant F3C-BFA-30 possesses similar texture features of fabric substrate and regularly honeycomb porous microstructures templated from water droplets, as shwon in Fig. 5.10. These results demonstrate that the flexible and nonplanar surface of fabric has no influence on the formation of highly ordered porous microstructues. And most importantly, they indicate that decreasing the solution concentration may be an effective strategy for maintaing the unique surface features of fabric when coating it with the porous microstructures by the BF technique.

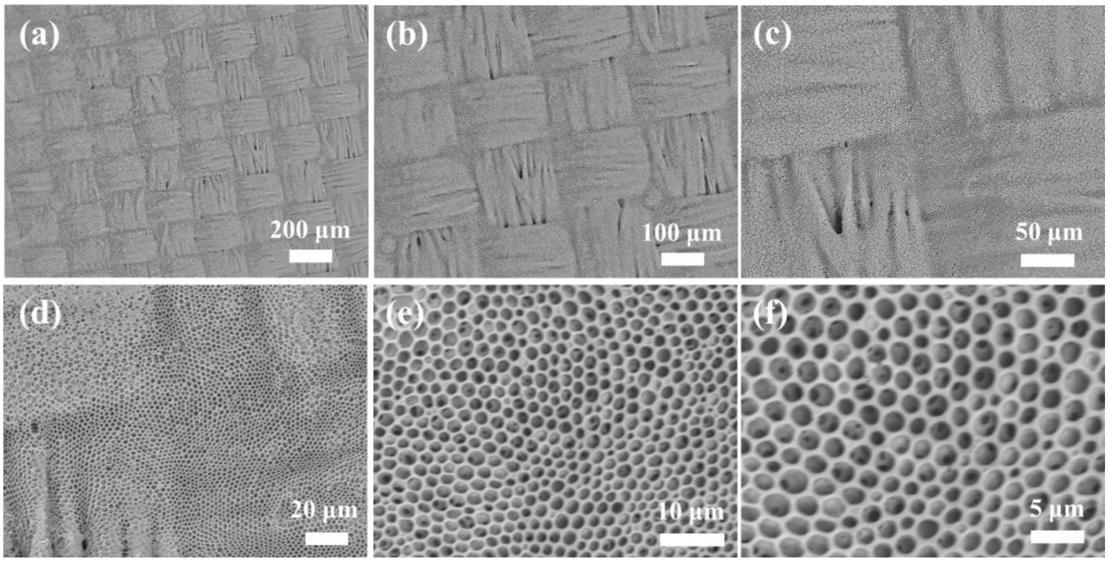

Figure 5. 9 SEM images at different magnifications of F3C-BFA-45 film prepared by the BF technique from 45 mg mL^{-1} PDMS-g-PAs/$CHCl_3$ solution

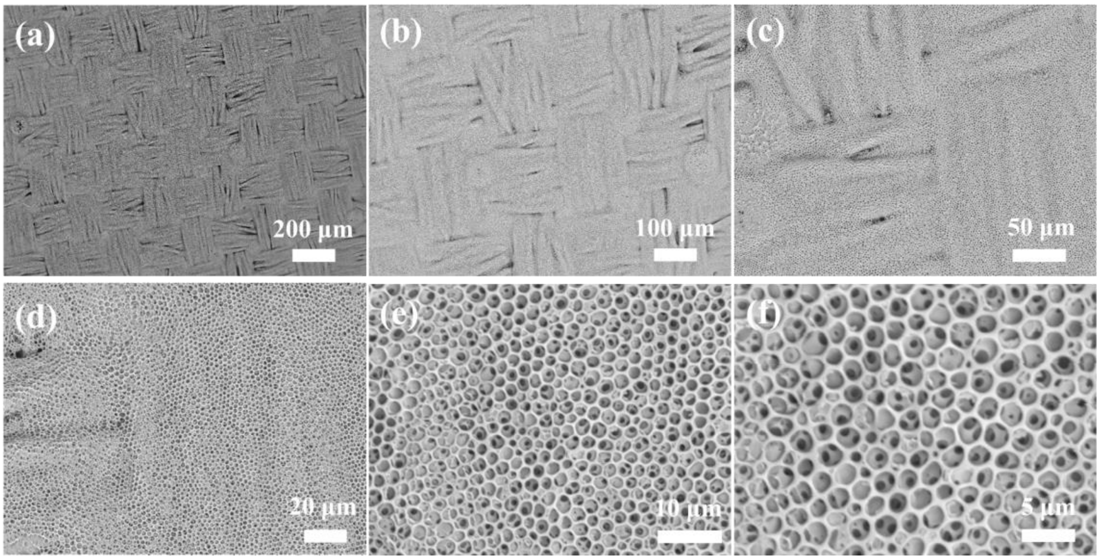

Figure 5. 10 SEM images at different magnifications of F3C-BFA-30 film prepared by the BF technique from 30 mg mL^{-1} PDMS-g-PAs/$CHCl_3$ solution

It is encouraging to further cast the solution concentrat at 15 mg mL^{-1} on Cu/Ni-coated fabric substrate for the preparation of F3C-BFA-15. A dinstinct veiw of surface morphology highly similar to the texture features of origin Cu/Ni-coated fabric is observed as expected, as shown in Fig. 5.11a. And the surface profiles of fibers in both longitudinal and latitudinal directions become dinstictly observable (Fig. 5.11b). They are actullay comformably covered with porous microstructures, as revealed in Fig. 5.11c. Three typical areas of F3C-BFA-15 at different positions, i.e. the crossover area between the longitudinal fibers and latitudinal fibers (white region of d in Fig. 5.11a), the area of longitudinal fibers (white region of e in Fig. 5.11a) and the area of latitudinal fibers (white region of f in Fig. 5.11a), are further observed at different magnifications, as shown in Fig.5.11d-d_2, Fig. 5.11e-e_1, and Fig. 5.11f-f_2, respectively. Regardless of the complexity of fabric surface, all of them show an intact film of highly ordered

BFAs. The formed BFAs well conform to the surface profile of fiber arrays without any cracks observed. These results explicitly demonstrate that materials can be introduced as highly ordered and noncracking porous microstructures onto the fabric surface by the BF technique without concealing the unique surface features of fabric substrate.

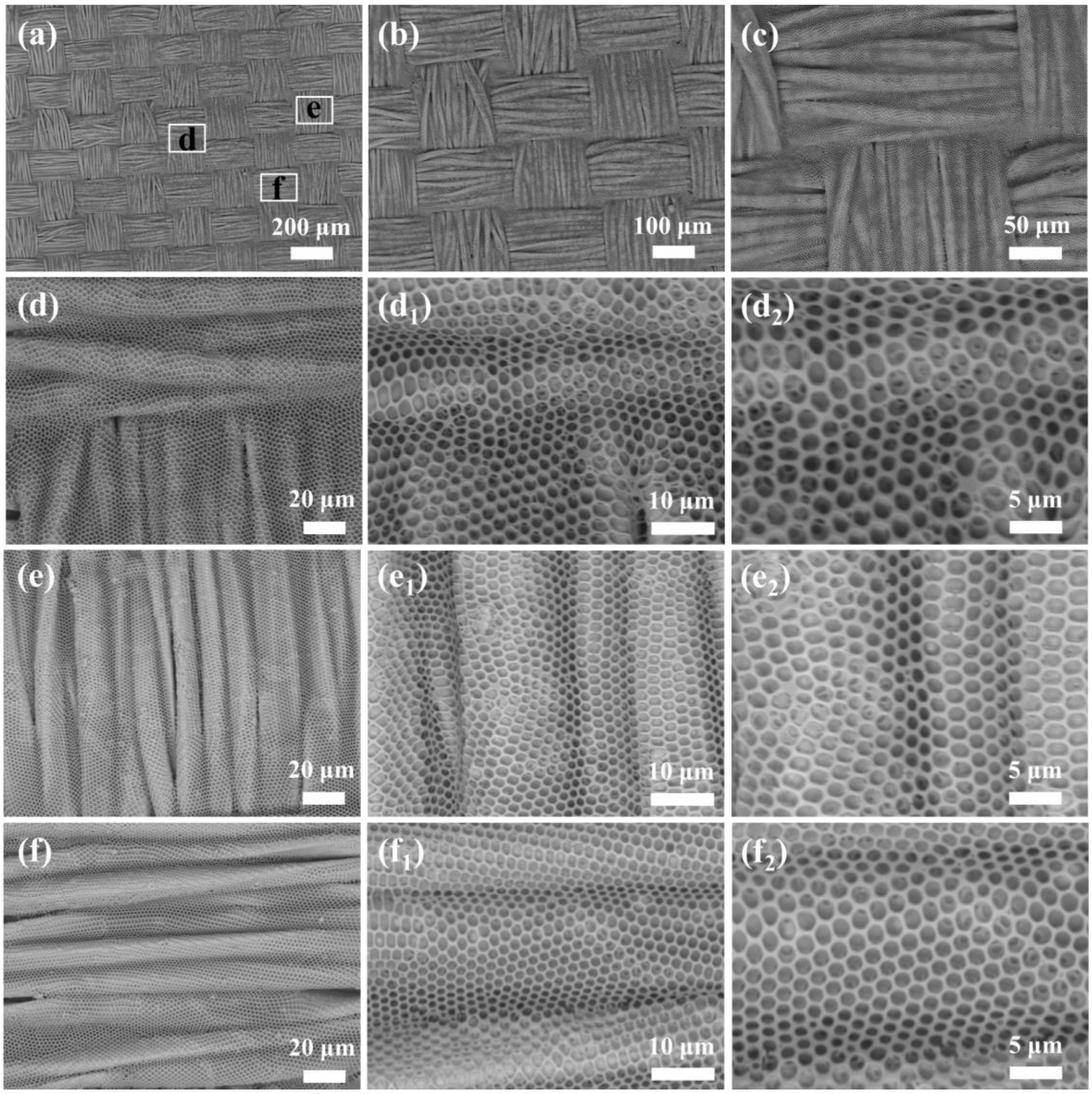

Figure 5. 11 (a)-(c) SEM images at different magnifications of F3C-BFA-15 film prepared by the BF technique from 15 mg mL^{-1} PDMS-g-PAs/$CHCl_3$ solution. (d), (e) and (f) are the magnification of white areas highlighted in (a). (d$_1$) and (d$_2$), (e$_1$) and (e$_2$), (f$_1$) and (f$_2$) are their further magnifications correspondingly

When the concentration of casting solution is further reduced by half, the obtained F3C-BFA-7.5 possesses a more dinstinct view of Cu/Ni-coated fabric textures (Fig. 5.12a-c). Honeycomb porous microstructures conformably on the fiber surfaces are still observed, but they become less ordered and regular (Fig.5.12f). At some areas, the porous microstructures are discontinuous (Fig.5.12e). More seriously, no porous microstrures are found at the crossover areas of longitudinal fibers and latitudinal fibers (Fig. 5.12d). Continuous decrease of the solution concentration will aggravate this situation, although it can enable the surface morphology of F3C-BFAs more close to that of fabric substrate. As shown in Fig. 5.13a-c, F3C-BFA-3.0 prepared from solution at 3.0 mg mL^{-1} no longer has continuous porous films on fabric surfaces. Only some disordered BFAs distribute among the fiber arrays sparsely (Fig. 5.13d-f). This indicates that the amount of PDMS-*g*-PAs is too little to form an intact film.

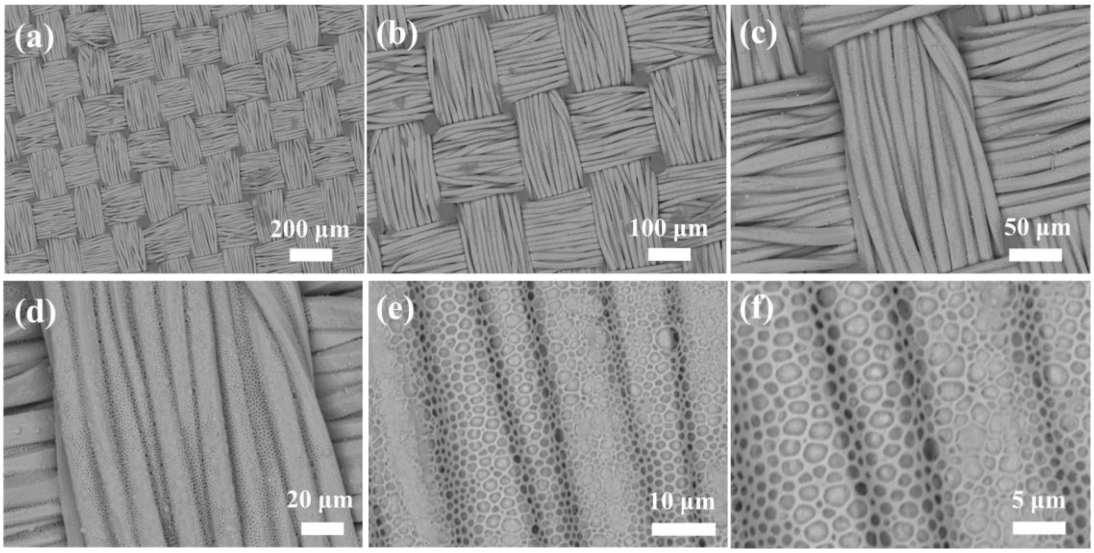

Figure 5. 12 SEM images at different magnifications of F3C-BFA-7.5 film prepared by the BF technique from 7.5 mg mL^{-1} PDMS-g-PAs/$CHCl_3$ solution

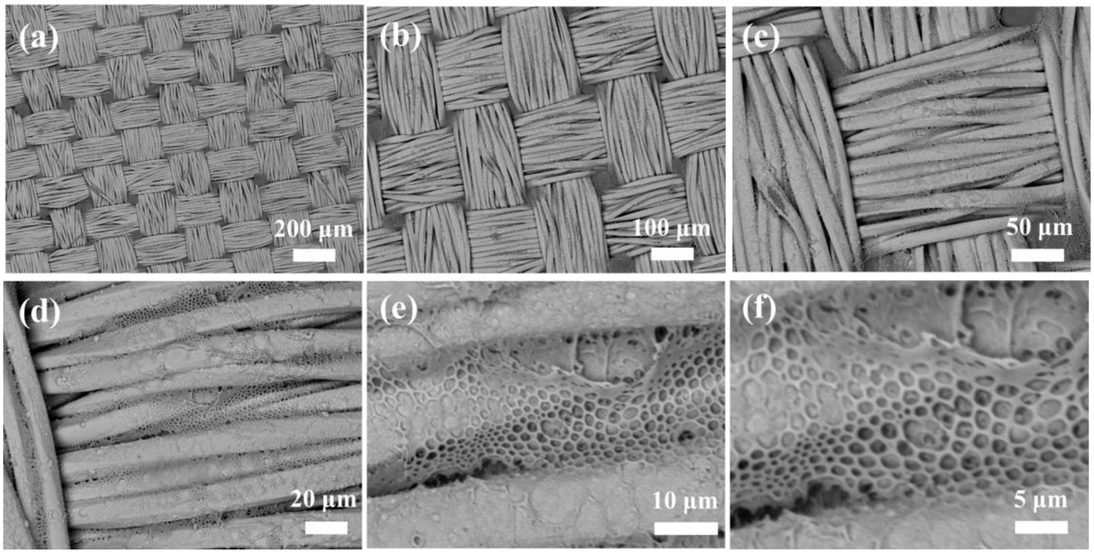

Figure 5. 13 SEM images at different magnifications of F3C-BFA-3.0 film prepared by the BF technique from 3.0 mg mL^{-1} PDMS-*g*-PAs/$CHCl_3$ solution

Highly ordered 3C-BFAs can also be introduced on nonplanar substrates with different surface features. Three kinds of TEM grids with different patterns and meshes placed on a glass substrate were further used as nonplanar surfaces. The PDMS-g-PAs solution of 15 mg mL^{-1} was directly cast on the surface regions of glass substrate where they rested by the aqueous BF technique, respectively. The panorama views of 3C-BFAs on 100 mesh square grid, 230 mesh square grid and 150 mesh grid are shown in Fig. 5.14a, d and g, respectively. Fig. 5.14b, e and h reveal that they are covered with a noncracking and continuous 3C-BFAs, respectively. These can be clearly observed by their further magnified reviews (Fig. 5.14c, f and i). Honeycomb porous microstructures are formed on both the bottom surfaces of glass substrates and the skeleton of copper grids. And the formed PDMS-*g*-PAs 3C-BFAs well conform to the surface profiles of copper grids, involving irregular shapes and corners with different angles. These results demonstrate that 3C-BFAs can also be prepared on solid nonplanar substrates, and indicate that fabric substrates with more different and complex surface textures can be employed for the formation F3C-BFAs.

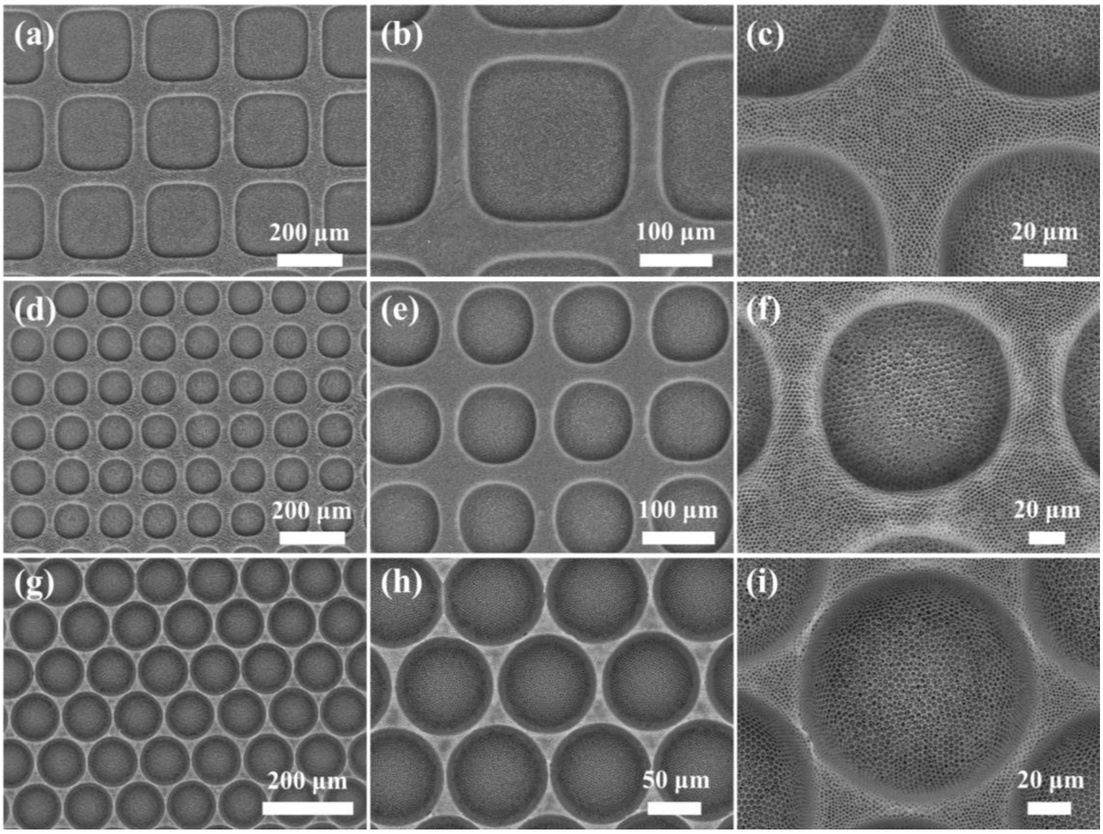

Figure 5. 14 SEM images at different magnifications of 3C-BFAs prepared from PDMS-g-PAs/$CHCl_3$ by the aqueous BF technique on copper grids with different meshes and patterns: (a)-(c) 100 mesh grid with square patterns, (d)-(f) 230 mesh grid with square patterns, and (g)-(i) 150 mesh grid with hexagonal patterns

5.5 Formation mechanisms of 3C-BFAs

The formation mechanism of BFAs from polymer solution by the aqueous BF technique has been elaborately described in Chapter 3.4.4. Herein the formation reason of PDMS-*g*-PAs BFAs by the aqueous BF technique is similar to the generally accepted mechanism. For a droplet of PDMS-g-PAs/$CHCl_3$ solution cast on a glass substrate under a sealed vessel saturated with water vapor, it will firstly spread on the substrate to form a liquid film immediately. Due to the evaporation of volatile $CHCl_3$, the temperature of the solution surface decreases rapidly, leading to the condensation of water droplets from humid atmosphere onto the surface of solution. The condensed water can induce the precipitation of polymers at the interface of water/solution to stabilize and keep the water droplets from coalescence. With the drive of Marangoni effect and Capillary effect, the polymer encapsulated water droplets can self-assemble into hexagonally ordered arrays on the solution surface or be drawn into the solution. The successive sinking of water droplets into the solution will lead to form multiple layers of water droplet arrays in the solution. With the continuous evaporation of solvent, the self-assembly behavior of water droplets terminates at the gelation point of polymer. After complete evaporation of residual solvent and water droplets, honeycomb porous microstructures will be finally left on the substrate.

It is interesting to find the polymer film conformably formed on uneven surface rather than simply filled in the sunken areas, because due to gravity it is quite difficult for a flowing liquid to spread on nonplanar substratre homogeneously. The successful formation of well-defined F3C-BFAs is mainly ascribed to the rapid film-forming process of BF technique and appropriate viscosity of polymer solution, which can be explained as follows. We know that dissolving polymers in a solvent can endow the formed solution with certain viscosity. And the viscosity usually possesses a increase trend with the increase of solution concentration. Therefore, when the solution is cast on nonplanar substrate, it is reasonable to speculate that a relatively homogeneous liquid coating can be formed, and remained transiently by contouring to its surface profile. And owing to the rapid evaporation of solvent during the BF process, the condensation of nonsolvent droplets, increase of solution concentration and decrease of solution temperature will drastically increase the viscosity of liquid system. This contribute to retain the liquid film on the nonplanar surface. When the retaining time is long enough for the gelation of polymer solution, the sedimentation of polymers in sunken areas will not occur. Therefore, after complete removal of residual solvent and water droplets, 3D porous microstructures contouring to the curved surface of substrate will be left. The formation of non-cracking of F3C-BFA films can be ascribed to the low T_g PDMS component of PDMS-*g*-PAs. It can endow PDMS-*g*-PAs films with excellent elasticity to alleviate the possible stress concentration caused by uneven surfaces and during the drying process.

5.6 In situ formation of honeycomb patterned ceramics from BFAs

Taking advantage of the high silicon content and honeycomb porous microstructure of PDMS-*g*-PAs films, honeycomb patterned ceramics could be obtained under appropriate oxidation environments. However, when directly pyrolyzing BFA films, no special features were found by SEM (Fig. 5.15). In other words, the regular honeycomb features of films were completely destroyed during the pyrolysis process. The reason can be ascribed to the poor thermal stability of PDMS-*g*-PAs. Honeycomb structures of films melt and collapsed when heating up to its T_g (T_g of PAs and PDMS are approximately 102 and -120 °C, respectively[33]).

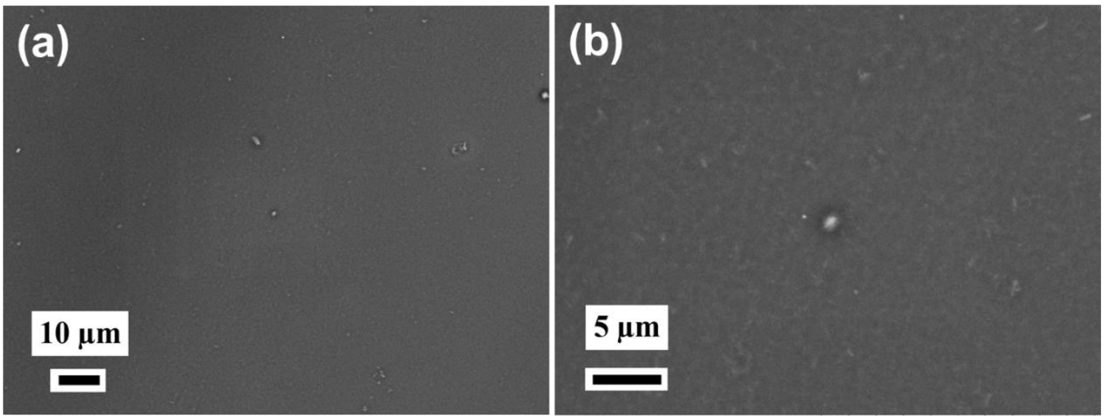

Figure 5. 15 SEM images of surface features on substrate at different magnifications after direct pyrolysis of PDMS-*g*-PAs BFAs

To solve this problem, a hybrid approach involving plasma modification was developed. The schematic strategy is shown in Fig. 5.16. Firstly, regularly PDMS-*g*-PAs BFAs were constructed from polymer solution by a static BF process (Fig. 5.16a). Then, the as-cast BFA film was treated by oxygen plasma for rapidly modifying the film surface at ambient conditions (Figure 5.16b). Finally, the easy accessible modified BFA film acts as a template for the formation of honeycomb patterned ceramics by further in situ pyrolysis (Figure 5.16c).

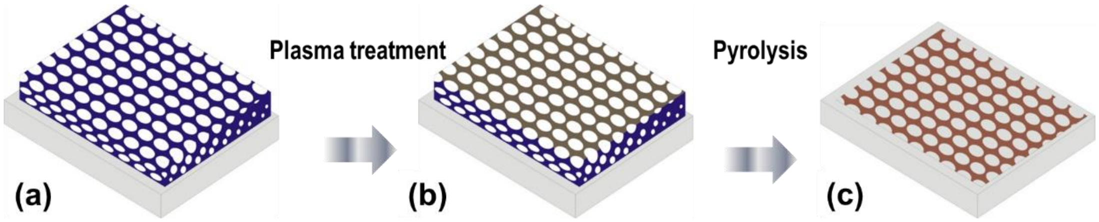

Figure 5. 16 Schematics of fabricating honeycomb patterned ceramics by in situ pyrolysis of plasma-modified BFA film: (a) PDMS-*g*-PAs BFA film, (b) Modification of BFA surface by oxygen plasma treatment, and (c) Honeycomb

patterned ceramic by in situ pyrolysis of plasma-modified BFA film

5.6.1 Modification of BFAs by oxygen plasma treatment

Plasma-related technique is a versatile technique for the surface modification of materials.[362,363] To minimize the influence of high temperature on film morphology, the treatment of BFAs was carried out by an atmospheric pressure plasma jet apparatus at ambient temperature. Through adjusting the processing conditions, such as output power, oxygen gas flow and exposure time, BFAs with different etching degrees can be controlled. When we treated BFAs under the processing conditions of 190 W (output power) and 0.6 L min^{-1} (oxygen flow) for just one second (1 s), the surface wettability was drastically changed from superhydrophobic (153.2°) to hydrophilic (38.9°) (Fig. 5.17a and b). And the advancing and receding CAs for as-cast BFA (155.3° and 111.6°), after plasma treatment, become 40.9° and 30.7° respectively (Fig. 5.17c and d). It indicates that the chemical nature of film is altered after plasma treatment because the contact angle is sensitive to the compositional variability of surface chemistry. Specifically, it is generally agreed that the advancing angle is sensitive to the low-energy components of the surface, while the receding angle is sensitive to the high energy components of the surface.[364,365]

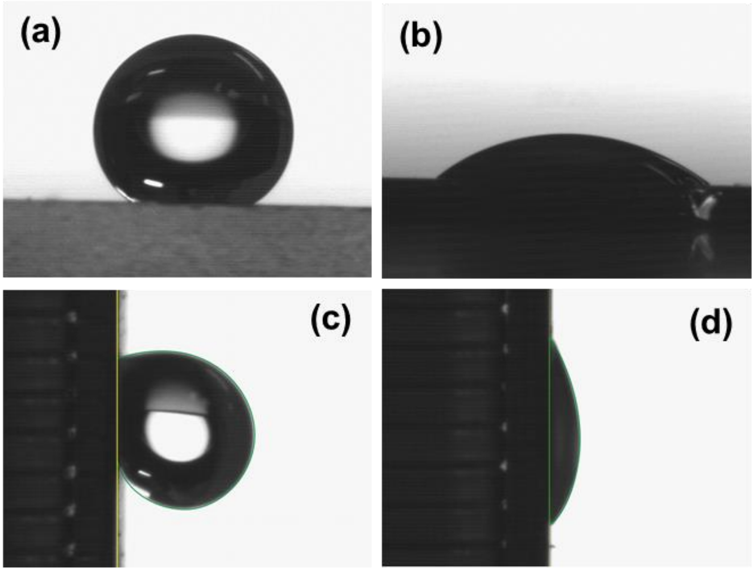

Figure 5. 17 Water droplets on a BFA film (a) before and (b) after oxygen plasma treatment. Water drops adhered to BFA surface (c) before and (d) after oxygen plasma treatment under very high substrate inclinations (tilt angle: 90°)

The difference in chemical nature between the as-cast and plasma-modified BFAs was examined on the basis of XPS analysis, as shown in Fig. 5.18. The intensity of C 1*s* at 285 eV decreases after the oxygen plasma treatment (Fig. 5.18a), while O 1*s* peak at 532 eV exhibits a shift to a higher binding energy and its intensity increases (Fig. 5.18b). Moreover, Si 2*p* peak shifts to 103.5 eV from the characteristic peak of silicon at 102 eV in the neat PDMS-*g*-PAs, and its intensity also increases obviously (Fig. 5.18c). The obtained results indicate that PDMS near the film surface is oxidized whereas the PAs segments are degenerated by oxygen plasma. More importantly, SEM image reveals that both the honeycomb patterns and spatial structures in the film are highly maintained without any collapse after rapid plasma treatment, as demonstrated in Fig. 5.19a.

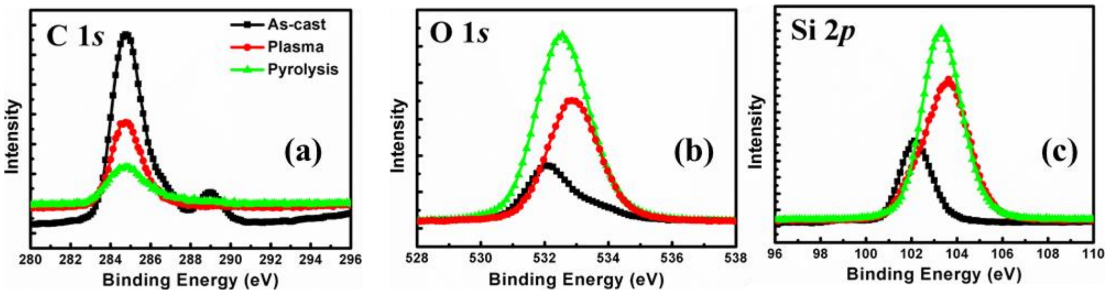

Figure 5. 18 XPS spectra of (a) C 1*s*; (b) O 1*s* and (c) Si 2*p* of as-cast BFA film (black square line), plasma-modified BFA film (red cyclic line) and plasma-modified BFA film after pyrolysis (green triangular line)

It seems feasible to prepare honeycomb patterned ceramic if the exposure time of oxygen plasma is extended to long enough. However, we found that the regular microstructures of film were destroyed when extending the plasma treating time. And the degree of damaging structures increases with the exposure time. As shown in Fig. 5.19b, cracks begin to appear in some pores as PDMS-*g*-PAs film was treated 3 s by oxygen plasma. With the increase of exposure time, the spreading destroyed microstructures were observed evidently (Fig. 5.19c-e). When the plasma treating time is up to 50 s, the observed area of honeycomb microstructures is almost completely destroyed (Fig. 5.19f). And the generated cracking can be visually observed. EDX analysis was further used to monitor the element variation in the BFA film surface with exposure time. The C fraction is found to decrease while the fractions of both O and Si increase in comparison to the film without plasma treatment. This change becomes more evident at longer exposure time. As shown in Fig. 5.20, when increasing to 25 s (log value of 1.41), the atomic fractions of O and Si increase from 19.74% and 11.31% in the as-cast

PDMS-*g*-PAs film to 28.86% and 20.79% respectively, while the C fraction decreases to 50.36%. However, further extending the exposure time to 50 s (log value of 1.71), the variation of the three elements is not obvious, indicating that simply increasing the exposure time has little influence on promoting the converting rate of PDMS-*g*-PAs into ceramic by plasma treatment. And the cross-sectional view shows that the thickness of plasma-modified film almost has no change. It can be explained that the formation of thin inorganic layer on the BFA film surface resists the further etching of oxygen plasma. Consequently, it is impassable to fabricate regularly honeycomb patterned ceramic from micrometer-thickness PDMS-*g*-PAs film only by oxygen plasma treatment. Further combining pyrolysis will contribute to the complete formation of silicon-based ceramics.

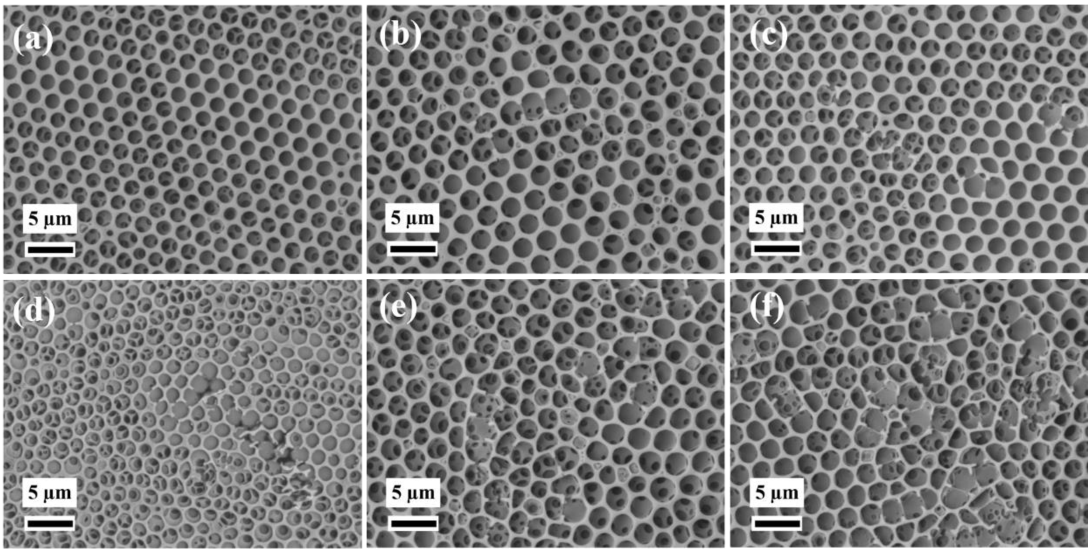

Figure 5. 19 SEM images of BFAs treated by oxygen plasma treatment with different exposure time under the processing conditions of 190 W (output power) and 0.6 L min^{-1} (oxygen gas flow): (a) 1 s, (b) 3 s, (c) 5 s, (d) 10 s, (e) 25 s, (f) 50

s

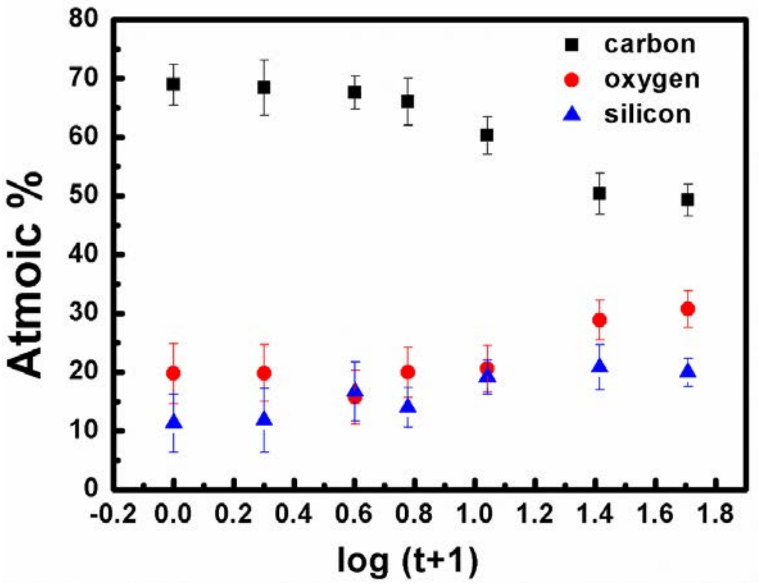

Figure 5. 20 EDX analysis results of BFAs treated by oxygen plasma treatment with different exposure time under the processing conditions of 190 W (output power) and 0.6 L min^{-1} (oxygen gas flow). **t** represents the time of plasma treatment. The **t** values of the seven plotted samples from left to right are 0 s, 1 s, 3 s, 5 s, 10 s, 25 s and 50 s, respectively

5.6.2 In situ pyrolysis of plasma-modified BFAs for honeycomb patterned ceramics

BFAs treated by oxygen plasma with 1 s possess highly maintained honeycomb features and were used as templates for further pyrolysis. The film samples were heated with a heating rate of 2.5 ºC under an air atmosphere and held till no weight loss was found. XPS was also used to monitor the change of binding energy after pyrolysis (Fig. 5.18). Both Si 2*p* and O 1*s* peaks shift to a higher binding energy, and they are consistent with the oxidized PDMS-*g*-PAs film, but their intensities increase more obviously. The intensity of the C 1s peak decreases evidently, but it does not disappear after pyrolysis. These results indicate that the formed ceramics are consisted of Si, O, and C elements. The obtained ceramics were further revealed by microscopy, as demonstrated in Fig. 5.21. We can find that regular honeycomb features of the film templates after pyrolysis are well preserved (Fig. 5.21a and b). Through the top sheet layer, the pores in the second layer are clearly observed (Fig. 5.21c). The average diameter of pores on the surface sheet is about 1.893 μm with a standard deviation of 0.095 μm. The cross-sectional view shown in Fig. 5.21d suggests that the formed sheet is large-area and continuous, and the thickness decreases to below 1 μm. The well-preserved sheets have the identical surface features with those of the as-prepared film surface, indicative of the in situ formation of ceramic on the honeycomb structures. Compared with the as-cast film template, the pore size after pyrolysis increases while the thickness drastically decreases from nearly ten micrometers to hundreds of nanometers. It can be ascribed to the collapse of inner multilayer pore structures and degradation of polymers. AFM height image (Fig.5.21e) shows the multilayerd ceramic honeycomb surface possessing an average pore size about 1.910 μm, which is coincided with the results revealed by SEM. Its height profile also gives the information on the sheet thickness. As shown in Figure 5.21e and f, the areas where red, yellow and green triangles are marked represent the top surface of the first layer, the second layer and the third layer respectively. The possible reason for the indistinct third layer is that the AFM tip could not reach the bottom of the pores. Calculated from the height difference of the first two layers, the thickness of top layer sheet is approximately 300 nm. The formed ceramics exhibit no change under solvent or thermal treatment, indicating their high thermal and chemical resistance properties.

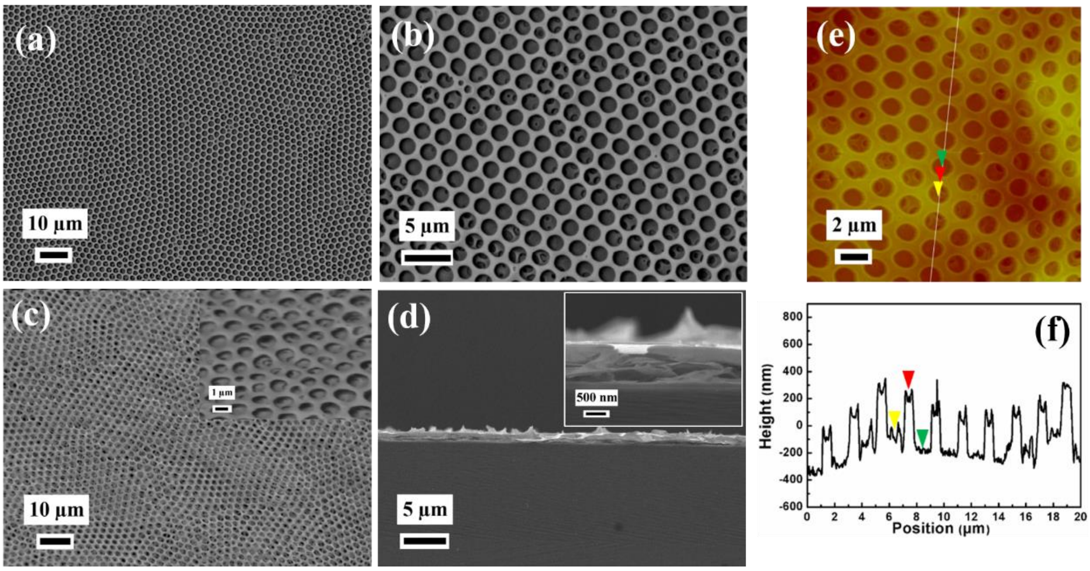

Figure 5. 21 (a) and (b) Top views of honeycomb patterned ceramic with different magnifications. (c) 45° side view and (d) vertical cross-sectional view of honeycomb patterned ceramic on substrate. (e) AFM tapping-mode topographical height image of honeycomb patterned ceramic. (f) Height profiles taken from the corresponding white line in the AFM image. The insets show a higher magnification

The good results illustrate that in situ pyrolysis of plasma-modified PDMS-*g*-PAs BFAs is an effective strategy to form orderedly patterned ceramics. Plasma treatment is considered to be a key step during this process. Because the movement of polymer chains can be neglected during the rapid processing of plasma treatment at ambient temperature with just 1 s, the outermost surface layers of PDMS-*g*-PAs film were modified without destroying the regular microstructures. The formation of thin cross-linked organic/inorganic hybrid composites on the surface during the plasma process locates on the unmodified matrix as a honeycomb mask, and thus can act as a structuring-directing role for the subsequent pyrolysis. When pyrolysing the BFAs without plasma treatment in the same procedure, the reason for no special features found on substrate is ascribed to the poor thermal stability of PDMS-*g*-PAs. Heating unmodified PDMS-*g*-PAs films from ambient temperature to high temperatures (500 ºC) will inevitably lead to the melt of whole films, and then the collapse of regular honeycomb features on film surface. Therefore, the structure-directing action of surface microstructures without plasma modification becomes invalid during the pyrolysis process, while PDMS-*g*-PAs film after proper exposure time of oxygen plasma can be used as robust templates for in situ formation of honeycomb patterned ceramics.

More interestingly, we observed that warps or curls of single-layer sheet on honeycomb patterned ceramics were generated in the defects of multilayer porous film template, such as the man-made cracks scratched by tweezer. As shown in Fig. 5.22a-c, ceramic sheet curls up from the film crack, with the residual sheets stacked on the substrate. It may be caused by the stress generated by different pyrolysis rates of plasma treated film template between surface and inner structure. This phenomenon indicates the excellent mechanical strength and toughness of formed ceramics. It also suggests the possibility of obtaining 2D ceramic sheets by peeling off the top layer from substrate by external forces. Actually, when breaking off the wafer substrate decorated with multilayer honeycomb patterned ceramics, stripped and isolated monolayer nanosheets can be obtained (Fig. 5.22d). Close view of SEM demonstrates that the thickness of single top layer is about several hundreds of nanometers (Fig. 5.22e). The residual sheet layers with honeycomb patterns can be clearly observed after peeling off the top layer, as shown in Fig. 5.22f.

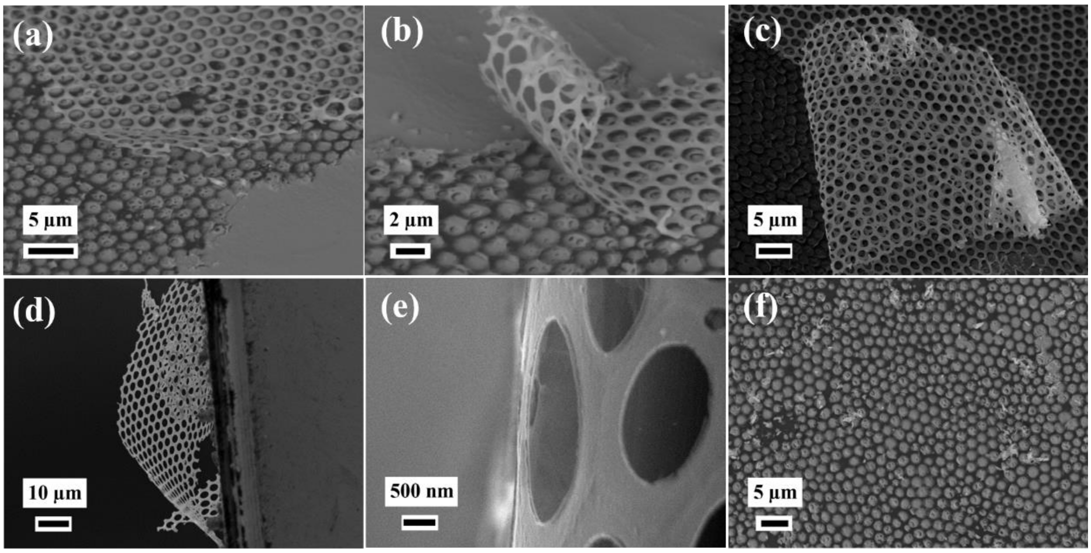

Figure 5. 22 (a)-(c) Different degrees of honeycomb ceramic warps in different positions observed by SEM. (d) SEM image of stripped and isolated ceramic sheet. (e) Close views of single-layer ceramic nanosheet. (f) Residual honeycomb pattern after stripping the surface ceramic sheet

5.7 Summary

In summary, the formation of 3C-BFAs on nonplanar surfaces has been studied based on flexible fabric substrate with complex surface textures. A silicon-containing graft copolymer PDMS-*g*-PAs that can form highly ordered BFAs in a wide solution concentration range has been first explored and demonstrated as the excellent film-forming material for this investigation. Non-cracking BFAs can be obtained on both planar and nonplanar substrates in large scale benefiting from the low T_g PDMS component of PDMS-g-PAs. It was found that the concentration of casting solution plays a decisive role on the formation of F3C-BFAs that maintain both regularly honeycomb porous microstructures and dinstinct surface textures of Cu/Ni-coated fabric substrate. Finally, taking advantages of the silicon-containing characters, PDMS-*g*-PAs BFA films were successfully used as single-source precursor for in situ formation of honeycomb microstuctured ceramics.

This study provides a novel, physical and nondestructive strategy for the surface modification of fabrics with conformal porous microstructures of materials *via* direct casting polymer solution on fabric with the BF technique, which may pave the way to a brand-new class of textile composites that can possess customized multifunctional properties of introduced materials, inherent excellent properties (such as breathability and flexibility) and unique texture features of fabrics. Such kind of fabric-based materials is believed to be promising materials for a wide spectrum of flexible and wearable applications.

CHAPTER 6 Templating Fabrication of Micro Lens Arrays for Triboelectric Nanogenerators from Breath Figure Arrays

6.1 Introduction

Polymer films prepared by the BF techniques have been demonstrated in a wide range of applications involving microfabrication, sensing, separation, catalysis, biology, optical and electronic devices.[7,9,11] In this chapter, BFA films prepared on planar substrates and nonplanar are first used as negative molds for templating fabrication of positive poly(dimethylsiloxane) (PDMS) film with micro lens arrays (MLAs) and hierarchical MLAs (HMLAs), respectively. Then the resultant PDMS films with different surface microstructures are employed for the assembly of triboelectric nanogenerators (TENGs). The influence of surface microstructures on the electric performance of TENGs is investigated and evaluated based on a vertical contact-separation mode under different triggering conditions. Finally, PDMS films with optimal surface microstructures are further used for wearable TENG devices to harvest the mechanical energy generated by human body motion.

6.2 Templating fabrication of (hierarchical) micro lens arrays from BFAs and Fabric based 3D conformal BFAs (F3C-BFAs)

6.2.1 Templating synthesis of MLAs from BFAs

PDMS is one of the most actively developed materials for the fabrication of TENGs to harvest mechanical energy owing to its excellent mechanical properties, chemical inertness, high negative polarity and dielectric properties. Fig. 6.1 illustrates the main processes for templating synthesis of PDMS MLAs from PDMS-*g*-PAs BFAs. The as-prepared PDMS-g-PAs BFA films by the BF technique acted as a negative mold (Fig. 6.1a). The used PDMS precursors were purchased from Momentive Performance Materials Japan LLC and used as received after homogeneously mixing. They were cast on the BFA mold according to the mass-to-surface-area ratio of 0.048 g cm^{-2} by a doctor-blading method. Then it was shifted to a vacuum oven for degassing at room temperature to obtain PDMS liquid film without air bubbles (Fig. 6.1b). After the liquid film becoming transparent, the temperature was increased to 80 °C for cross-linking reaction, which was held for three hours (Fig. 6.1c). The cross-linked PDMS film can be directly peeled off from the BFA mold carefully (Fig. 6.1d). The resultant PDMS film was robust and self-supported, which possesses a convex MLA pattern.

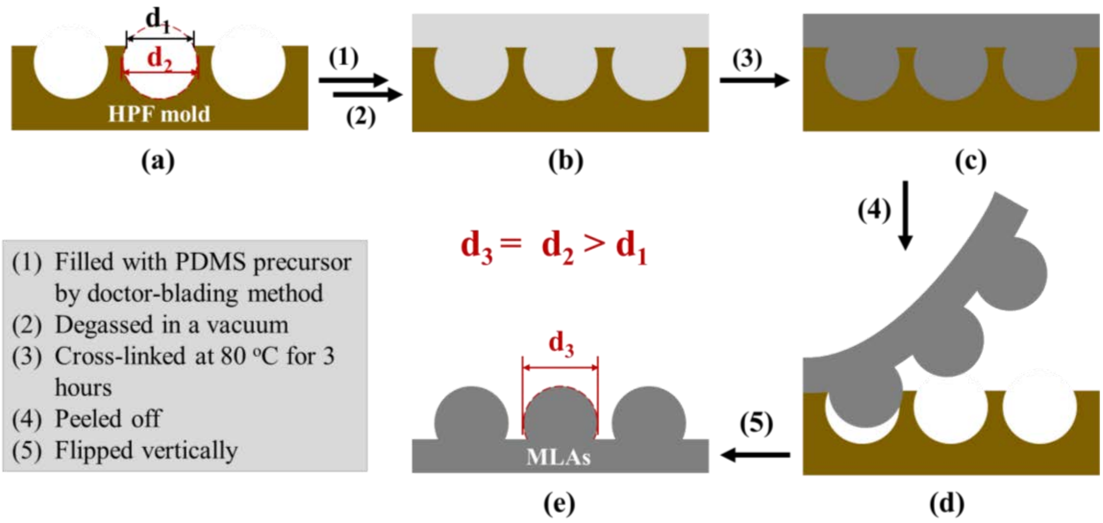

Figure 6. 1 Schematic of templating synthesis of PDMS MLAs with PDMS-g-PAs BFAs as negative mold

PDMS-*g*-PAs BFA films prepared from various concentrations of casting solution, including 0.5 mg mL^{-1}, 0.75 mg mL^{-1}, 1.5 mg mL^{-1}, 3.0 mg mL^{-1}, 5.0 mg mL^{-1}, 7.5 mg mL^{-1}, 15 mg mL^{-1}, 30 mg mL^{-1}, 45 mg mL^{-1}, and 60 mg mL^{-1} by the BF technique (for details, see section 5.3 in previous chapter 5) were used as negative molds for templating synthesis of PDMS films with MLAs respectively. According to the concentration of casting solution, the used BFA molds were marked as BFA-0.5, BFA-0.75, BFA-1.5, BFA-3.0, BFA5.0, BFA-7.5, BFA-15, BFA-30, BFA-45 and BFA-60. And correspondingly, their resultant PDMS MLAs were named as MLA-0.5, MLA-0.75, MLA-1.5, MLA-3.0, MLA-5.0, MLA-7.5, MLA-15, MLA-30, MLA-45 and MLA-60. All of them were firstly observed under OM, as shown in Fig. 6.2 and Fig. 6.3.

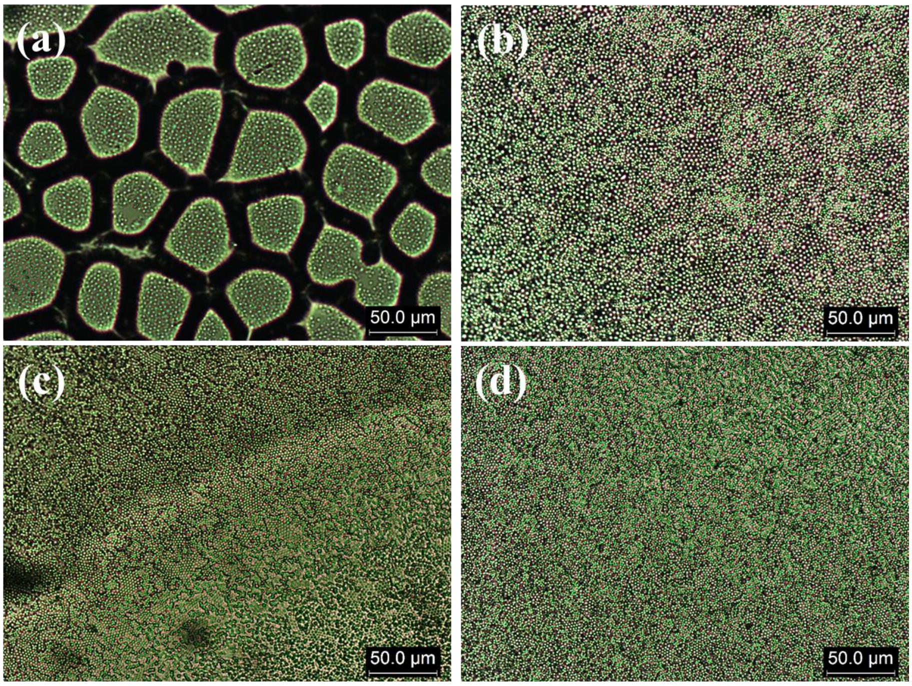

Figure 6. 2 OM images of (a) MLA-60, (b) MLA-45, (c) MLA-30 and (d) MLA-15

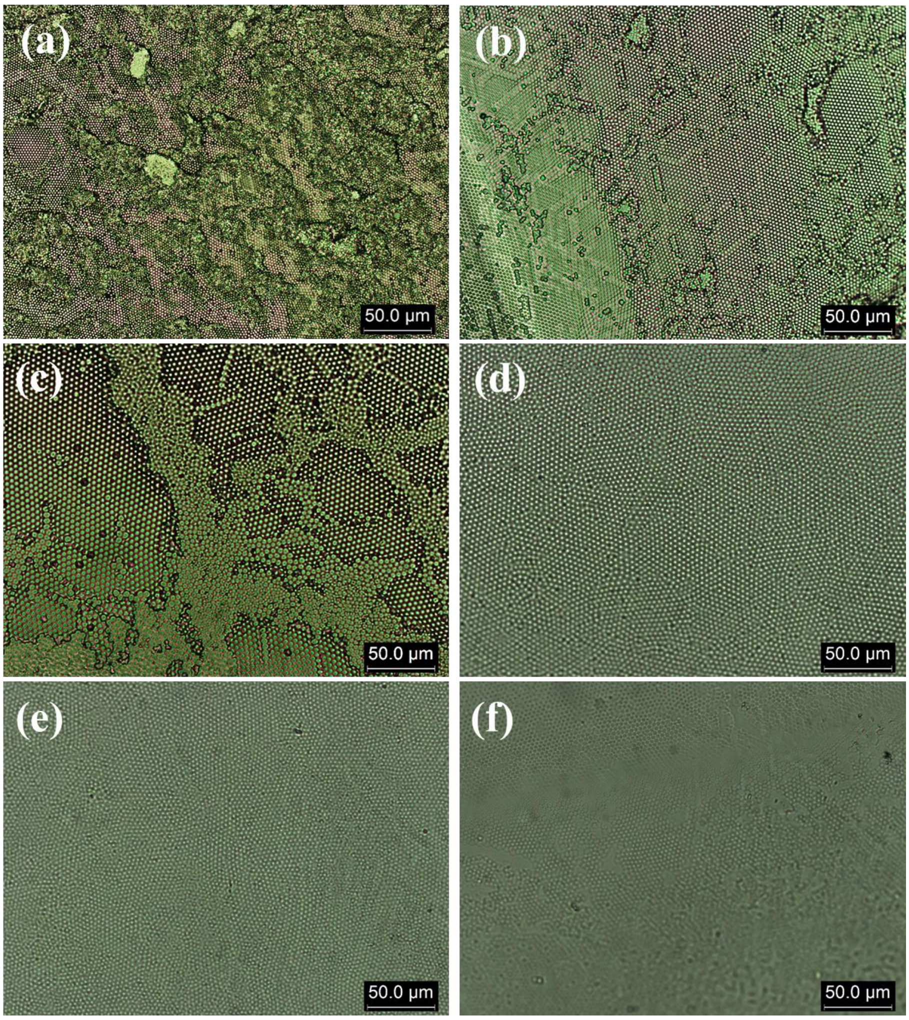

Figure 6. 3 OM images of (a) MLA-7.5, (b) MLA-5.0, (c) MLA-3.0, (d) MLA-1.5, (e) MLA-0.75 and (f) MLA-0.50

Generally, MLAs under OM possess similar surface morphologies as their BFA molds (Figs. 6.2 and Fig. 6.3). Microscale lightspots are observed for all samples. They are distributed on the PDMS film with different regularities, which are obviously dependent on their pore arrays of BFA molds.

The resultant PDMS films were coated with a thin layer of gold for further surface observation by SEM (JEOL Model JSM-6490). Their fracture surfaces were obtained by rapidly tearing and also examined by SEM for cross-section study.

The obtained SEM images are the secondary electron images acquired by using a 20 keV electron beam with a working distance of 10 mm.

The surface morphology of MLA-60 was first observed by SEM at different magnifications. As shown in Fig. 6.4a and b, lens-like microstructures with the size of dozens of micrometers are found in large scale. On the surface of lens, small protuberances with the size of several micrometers can be observed by SEM at a higher magnification (Fig. 6.4c). The hierarchical surface patterns are well coincident with the hierarchical porous microstructures of the used BFA mold. The cross-sectional view in Fig. 6.4d illustrates the resultant micro lens are convex. And the height of micro lens was approximately several micrometers, as shown in Fig. 6.4e. The close view in Fig. 6.4f also demonstrates the existence of small protuberances on the large size lens. These results well indicate that PDMS film can replicate the surface microstructures of BFA with high resolution.

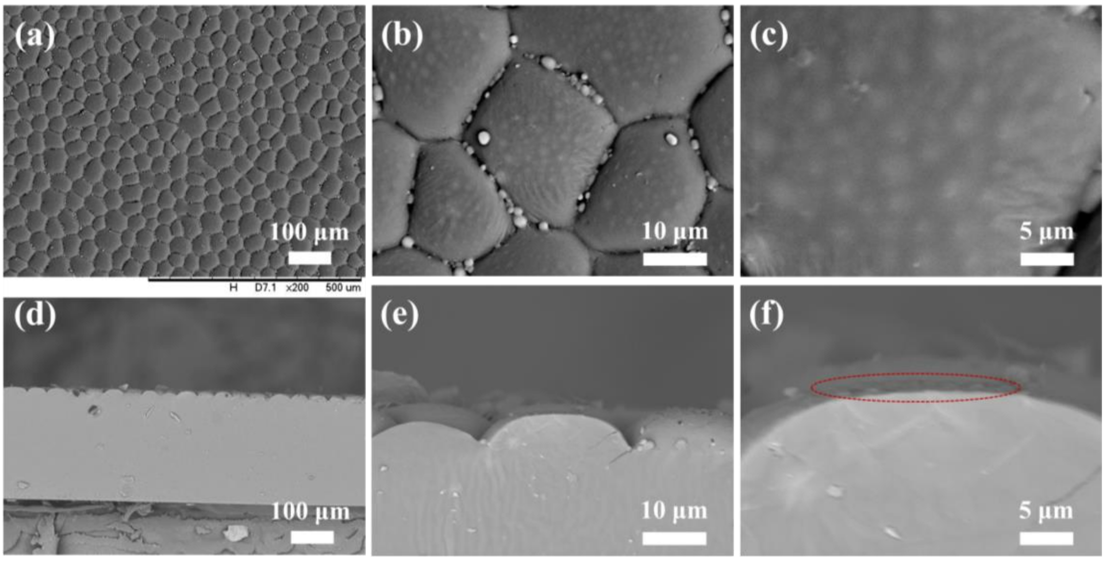

Figure 6. 4 (a)-(c) Top views and (d)-(f) cross-sectional views of MLA-60

Fig. 6.5 shows the top views and cross-sectional views of MLA-45 (Fig. 6.5a-c), MLA-30 (Fig. 6.5d-f), MLA-15 (Fig. 6.5g-i), and MLA-7.5 (Fig. 6.5j-l), respectively. Their BFA molds were prepared from PDMS-*g*-PAs solutions with a relatively high concentration, which all led to the formation of PDMS MLAs in large scale, as demonstrated in Fig. 6.5a, d, g, and j, respectively. Close views in Fig. 6.5b, e, h, and k reveal that the micro lens of MLA samples are arranged in a hexagonal array. The average micro lens sizes of these samples are approximately 3.34 μm, 3.32 μm, 3.16 μm, and 2.44 μm, respectively (Fig. 6.6a). The decreasing trend with the increase of solution concentration is similar to the pore size variation of BFA molds with solution concentration. However, it is noted that all the resultant micro lens sizes are larger than the pore size of their BFA molds. This can be ascribed to their different measurement methods. As shown in Fig. 6.1a, the pore shape of BFAs can be regarded as an air sphere, which is the imprint of a spherical water droplet after evaporation. The measured pore size of BFAs is actually the surface pore size of film. It is equivalent to the diameter of sphere latitude at the surface plane (d_1), which is obviously smaller than its equator diameter (d_2). The micro lens can be regarded as identical replica of air sphere. Therefore, its measured sphere size (d_3) is the equator diameter, which is equal to d_2 and larger than the surface pore size (d_1).

The stacked micro lens in some regions indicate that the formed MLAs are multiple. This is further confirmed by the corresponding cross-sectional views. As shown in the light orange regions of Fig. 6.5c and f, two or more layers of

MLAs are clearly observed for MLA-45 and MLA-30. Both MLA-15 and MLA-7.5 possess a monolayer in most regions (Fig. 6.5i and l, highlighted in light orange). The measured thickness of MLA region for these samples is approximately 8.7 μm, 7.6 μm, 5.4 μm and 4.0 μm, respectively. They display a general increasing trend with the increase of solution concentration, as shown in Fig. 6.6b.

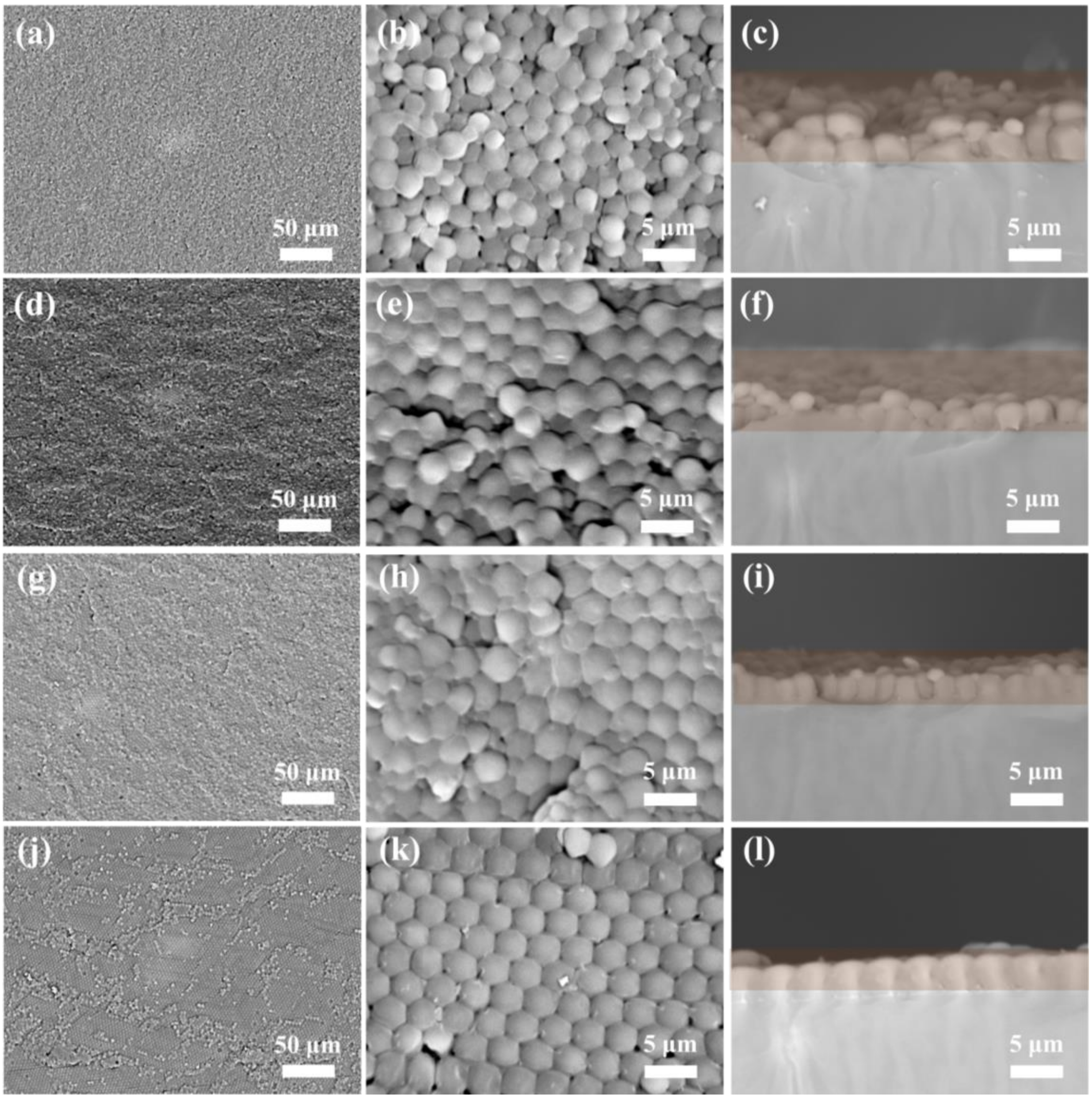

Figure 6. 5 SEM images of (a)-(c) MLA-45, (d)-(f) MLA-30, (g)-(i) MLA-15 and (j)-(l) MLA-7.5. The former two images in each line are the top views at different magnifications, while the third image is the cross-sectional view. The region of

MLAs in (c), (f), (i) and (l) are colored with light orange

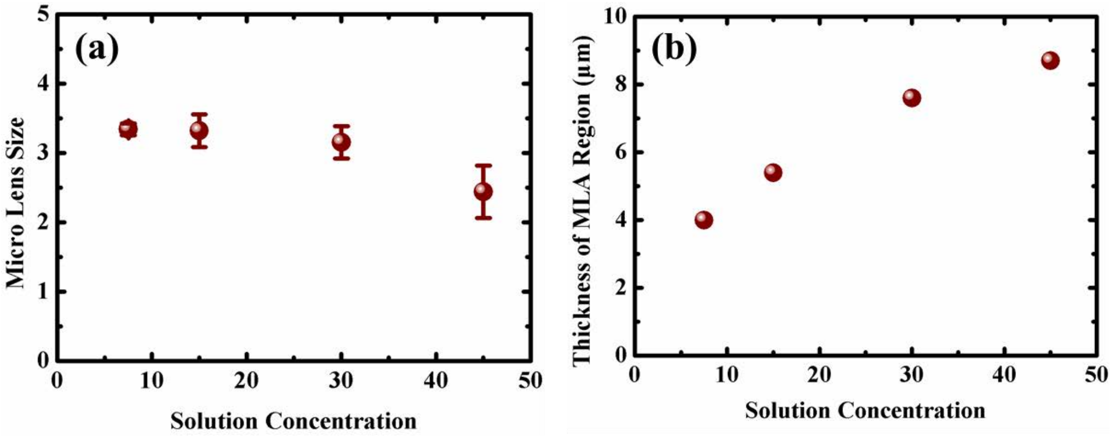

Figure 6. 6 Plot of the dependence of (a) micro lens size and (b) thickness of MLA region on the solution concentration

The PDMS films templated from BFA-5.0, BFA-3.0, BFA-1.5, BFA-0.75 and BFA-0.5 were also examined by SEM. Their top views and cross-sectional views are shown in Fig. 6.7. Similar hexagonal MLAs are observed for all these samples. However, with the decrease of solution concentration, the surface microstructures become more and more obscure. The cross-sectional views show that the height of MLAs is very small, which possesses an obviously decreasing trend with the decrease of solution concentration. For PDMS film templated from BFA-0.5, its MLA region becomes indiscernible, as shown in its cross-sectional view in Fig. 6.7o. The heights of PDMS MLA regions are actually determined by the pore layers and thickness of their used BFA molds.

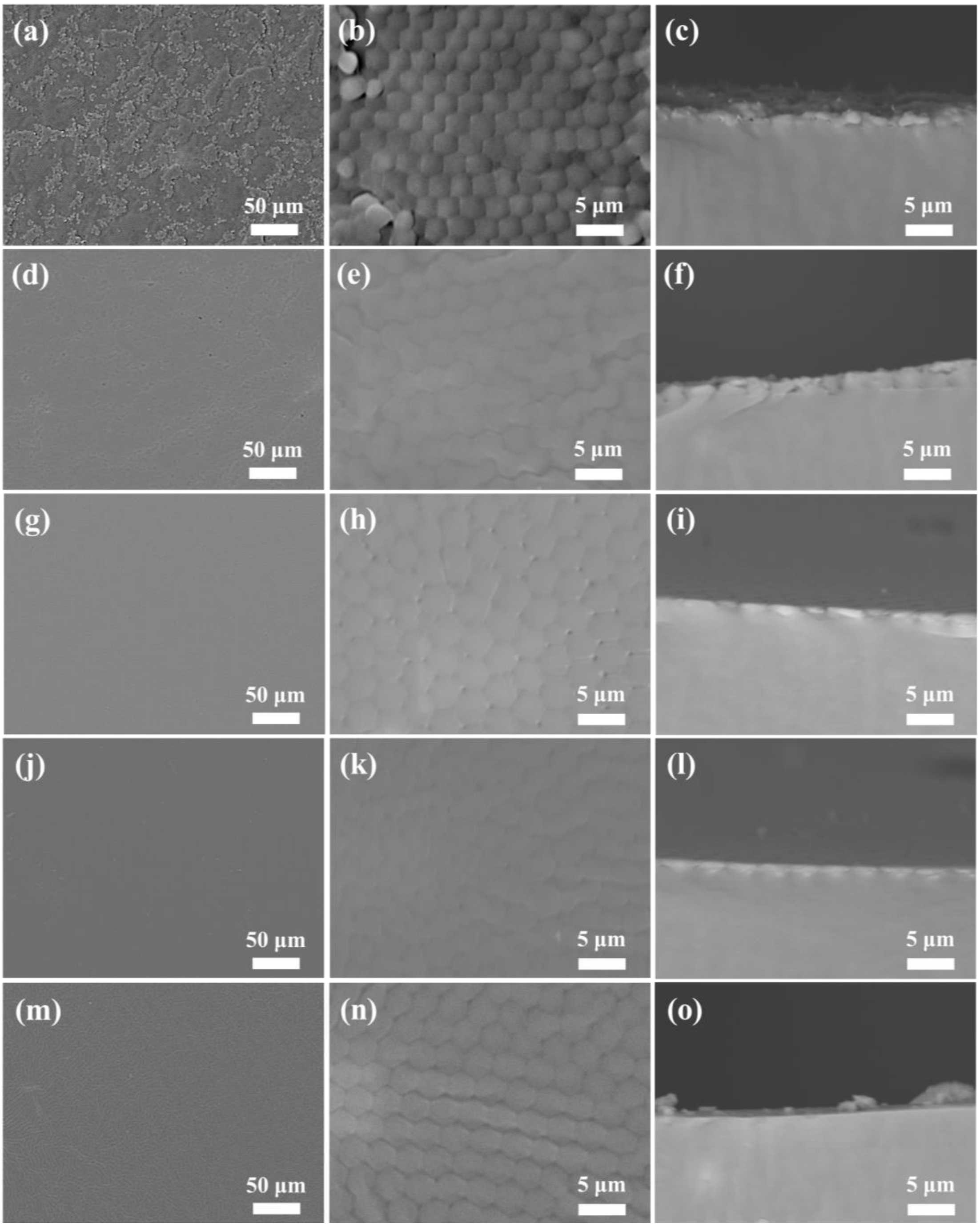

Figure 6. 7 SEM images of PDMS MLAs templated from PDMS-*g*-PAs BFAs prepared from solutions with (a)-(c) 5.0 mg mL^{-1}, (d)-(f) 3.0 mg mL^{-1}, (g)-(i) 1.5 mg mL^{-1}, (j)-(l) 0.75 mg mL^{-1} and (m)-(o) 0.50 mg mL^{-1} respectively. The former two images in each line are the top views at different magnifications, while the third image is the cross-sectional view

6.2.2 Templating synthesis of hierarchical MLAs (HMLAs) from F3C-BFAs

Fabric based 3D conformal BFAs (F3C-BFAs) prepared by the BF technique were employed as negative molds for the fabrication of hierarchical MLAs (HMLAs) with specific dimensional microstructures, as illustrated in Fig. 6.8. Its detailed procedures are identical with the synthesis process of honeycomb MLAs from BFAs. The difference is that, through the use of F3C-BFAs as negative molds, both fabric textures and honeycomb MLAs are expected to be introduced on PDMS films, thereby leading to the formation of hierarchical MLAs (HMLAs).

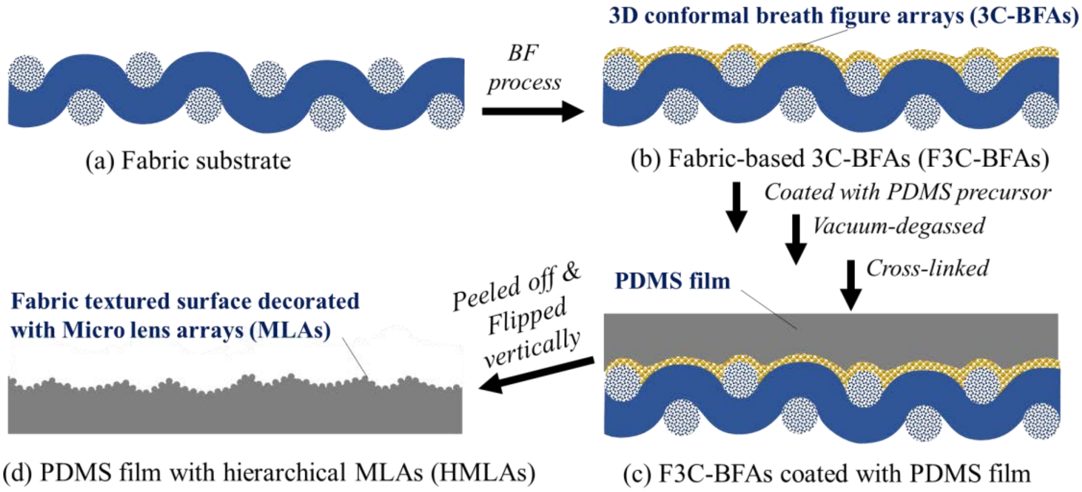

Figure 6. 8 Schematic of templating synthesis of HMLAs from F3C-BFAs prepared by the BF technique

The resultant samples molded from F3C-BFA-60, F3C-BFA-45, F3C-BFA-30, F3C-BFA-15, F3C-BFA-7.5 and F3C-BFA-3.0 by the BF technique (for details, see section 5.4 in previous chapter 5) are correspondingly named as HMLA-60, HMLA-45, HMLA-30, HMLA-15, HMLA-7.5 and HMLA-3.0, respectively. Their top views and cross-sectional views were systematically examined by SEM at different magnifications, and they are shown in Fig. 6.9-14, respectively.

The morphology evolution of HMLAs coincides with the dimensional microstructures of F3C-BFAs that evolve with the concentration of casting solution. When the employed F3C-BFA mold was prepared from a high solution concentration (60 mg mL^{-1}), the resultant HMLA-60 shows a micro lens patterned surface, but no obvious surface textures of Cu/Ni-coated fabric are observed, as shown in Fig. 6.9a-c. Cross-sectional view in Fig. 6.9f (highlighted in transparent red) confirms the formation of micro lens on the surface of PDMS film. At lower magnifications, it is found that the surface profile of HMLA-60 is not planar. It is slightly curved, and looks like a small and periodical wave (Fig. 6.9d and e). These cross-sectional views also indicate that the patterned PDMS film is consisted of three regions: the solid film matrix, the texture region (highlighted in 80%-transparent yellow in Fig. 6.9d) and the MLA region (highlighted in 80%-transparent red in Fig. 6.9e). The measured thickness of texture region for HMLA-60 is approximately 17 μm.

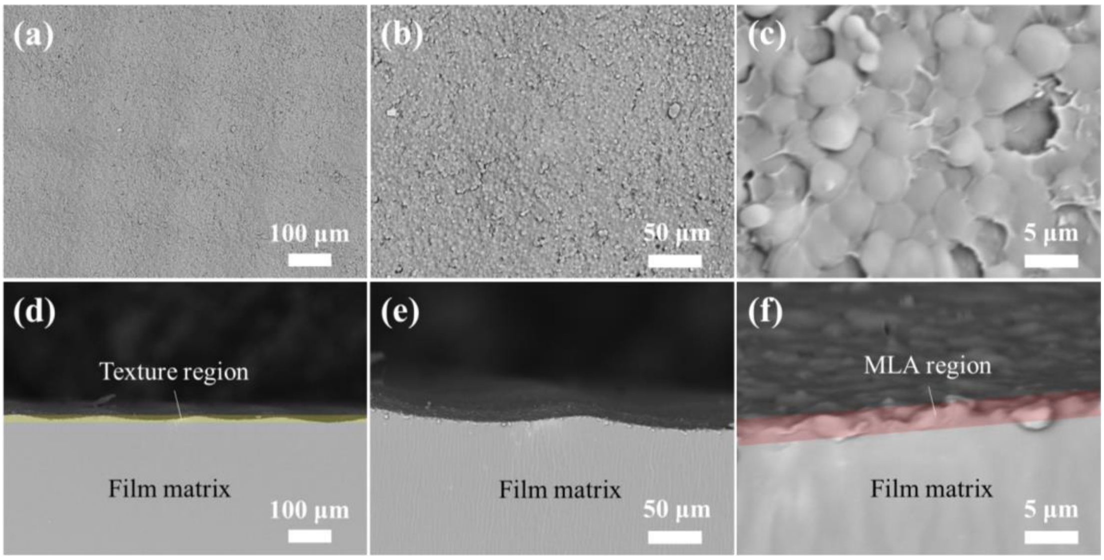

Figure 6. 9 SEM images of HMLA-60 molded from F3C-BFA-60: (a)-(c) top views and (d)-(f) cross-sectional views with different magnifications. The texture region and MLA region of PDMS films are highlighted in 80%-transparent yellow and red, respectively

Compared with HMLA-60, the fabric texture of HMLA-45, which is decorated with honeycomb MLAs (Fig. 6.10c), becomes distinguishable (Fig. 6.10a and b). And its cross-sectional views show that HMLA-45 has a similar wavy surface profile (Fig. 6.10d-f), but its texture region increases slightly, which is about 23 μm (highlighted in transparent yellow in Fig. 6.10d).

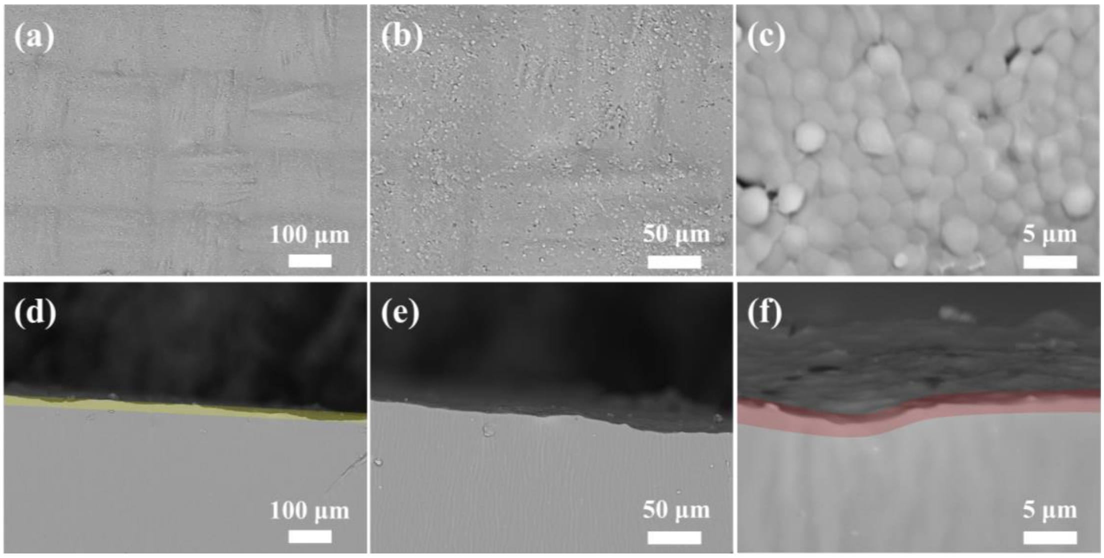

Figure 6. 10 SEM images of HMLA-45 templated from F3C-BFA-45: (a)-(c) top views and (d)-(f) cross-sectional views with different magnifications. The texture region and MLA region of PDMS films are highlighted in 80%-transparent yellow and red, respectively

HMLA-30 has a more distinct view of Cu/Ni-coated fabric texture than the samples above (Fig. 6.11a). And its thickness of texture region increases to around 31 μm (Fig. 6.11d, highlighted area). At a larger magnification, some fiber-like channels are observed in both meridional and parallel directions (Fig. 6.11b). They are further confirmed by the cross-sectional views at the same magnification (6.11e). Fig. 6.11c shows that the surface of HMLA-30 is completely decorated with honeycomb MLAs, involving the fiber channels. And MLAs formed along the curved surface profile is clearly observed (Fig. 6.11f, highlighted area).

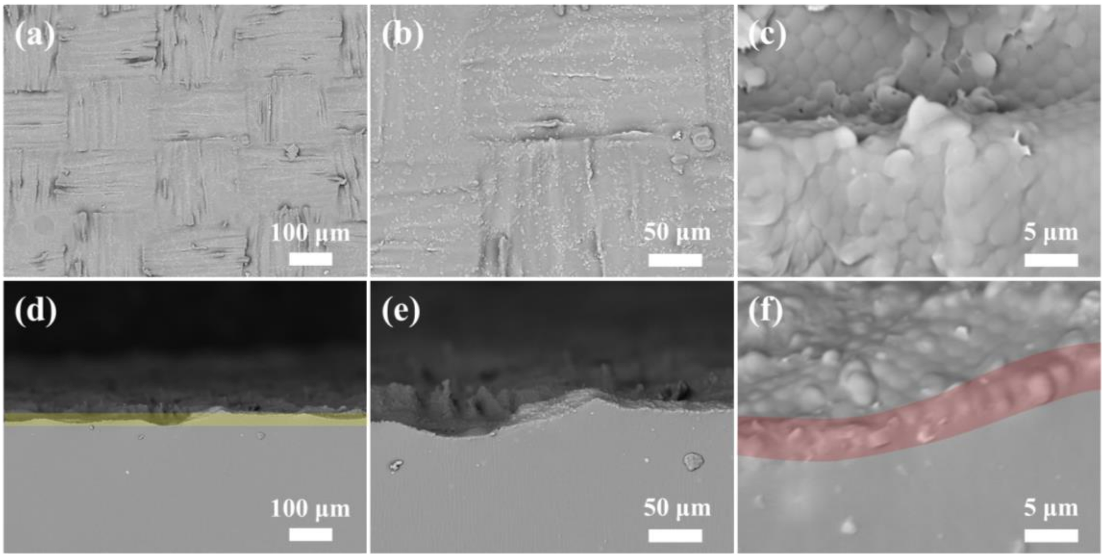

Figure 6. 11 SEM images of HMLA-30 templated from F3C-BFA-30: (a)-(c) top views and (d)-(f) cross-sectional views with different magnifications. The texture region and MLA region of PDMS films are highlighted in 80%-transparent yellow and red, respectively

When F3C-BFAs prepared from the solutions at or below 15 mg mL^{-1} were used as negative molds, the panorama views of resultant HMLAs, including HMLA-15, HMLA-7.5 and HMLA-3.0, are all very close to the surface textures of Cu/Ni-coated fabric, as shown in Fig. 6.12a, 6.13a and Fig. 6.14a, respectively. And the channels molded from the fibers of Cu/Ni-coated fabric are distinctly observable (Fig. 6.12b, 6.13b, and 6.14b). The cross-sectional views in Fig. 6.12d, 6.13d and 6.14d indicate that their thicknesses of texture region are about 35 μm, 38 μm and 42 μm respectively. Their corresponding views in a higher magnification also clearly confirm the formation of fiber channels (Fig. 6.12e, 6.13e and 6.14e).

The honeycomb MLAs of HMLA-15 are explicit and regular (Fig. 6.12c), which finely conform to the surface profile of Cu/Ni-coated fabric textures and fibers (Fig. 6.12f). Such similar hierarchical surface features can also be observed on HMLA-7.5 sample (Fig. 6.13c and f). However, it is noted that the MLA region of HMLA-3.0 is not obvious (Fig. 6.14f). And no explicit honeycomb MLAs can be observed from its top view. Only disordered micro lenses are found to intersperse in local areas, as shown in Fig. 6.14c. This can be ascribed to its used F3C-BFA-3.0 mold, which possesses an irregular and disordered porous surface caused by the low concentration of casting solutiong.

Briefly, the thickness of texture region generally possesses an increasing trend with the decrease of solution concentration that determines the dimensional microstructures of F3C-BFAs. However, the thickness variation of MLA regions is not obvious. In most HMLA samples, the thickness of MLA region roughly fluctuates between 2 μm and 3 μm. And the micro lens sizes of HMLAs are approximately identical with the pore size of F3C-BFAs. This indicates that the formation of MLA region is mainly dependent on the surface pore arrays of F3C-BFAs.

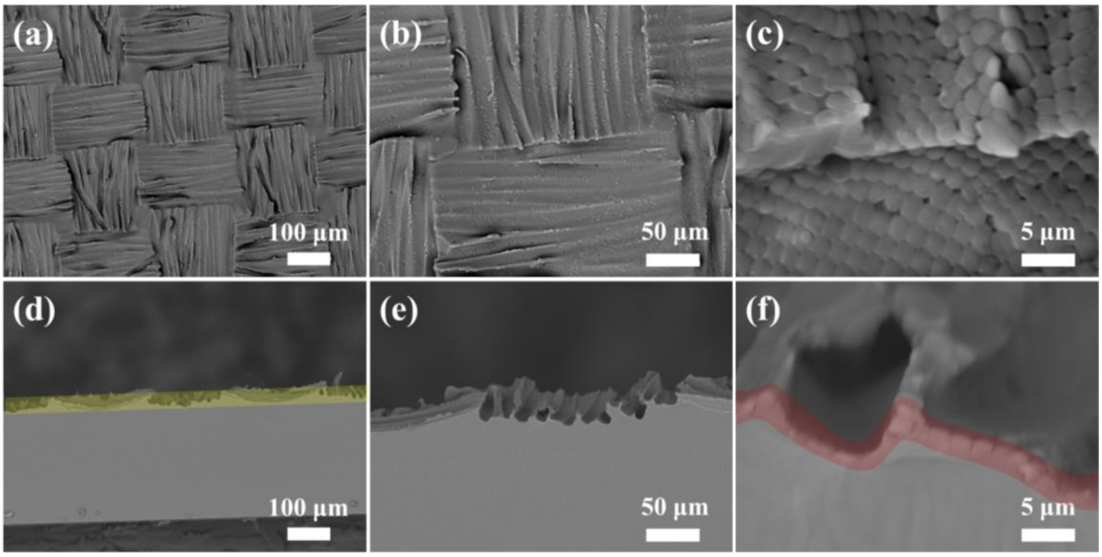

Figure 6. 12 SEM images of HMLA-15 templated from F3C-BFA-15: (a)-(c) top views and (d)-(f) cross-sectional views with different magnifications. The texture region and MLA region of PDMS films are highlighted in 80%-transparent yellow and red, respectively

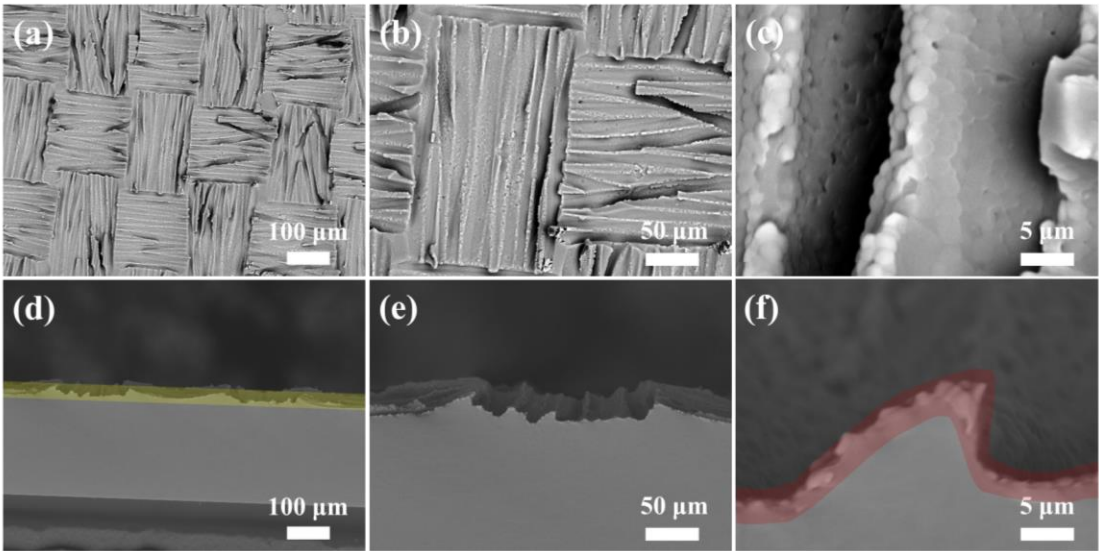

Figure 6. 13 SEM images of HMLA-7.5 templated from F3C-BFA-7.5: (a)-(c) top

views and (d)-(f) cross-sectional views with different magnifications. The texture region and MLA region of PDMS films are highlighted in 80%-transparent yellow and red, respectively

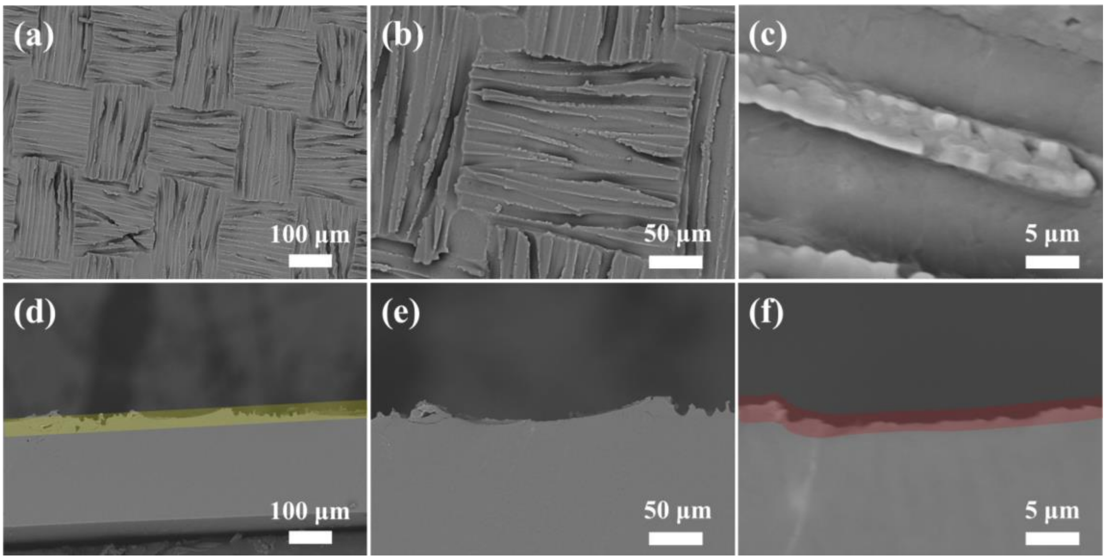

Figure 6. 14 SEM images of HMLA-3.0 templated from F3C-BFA-3.0: (a)-(c) top views and (d)-(f) cross-sectional views with different magnifications. The texture region and MLA region of PDMS films are highlighted in 80%-transparent yellow and red, respectively

6.3 Assembly of PDMS film-based TENGs and fundamental principle

6.3.1 Assembly of PDMS film-based TENGs

In this study, the main procedures for the assembly of TENGs based on the PDMS films prepared above were illustrated in Fig. 6.15.

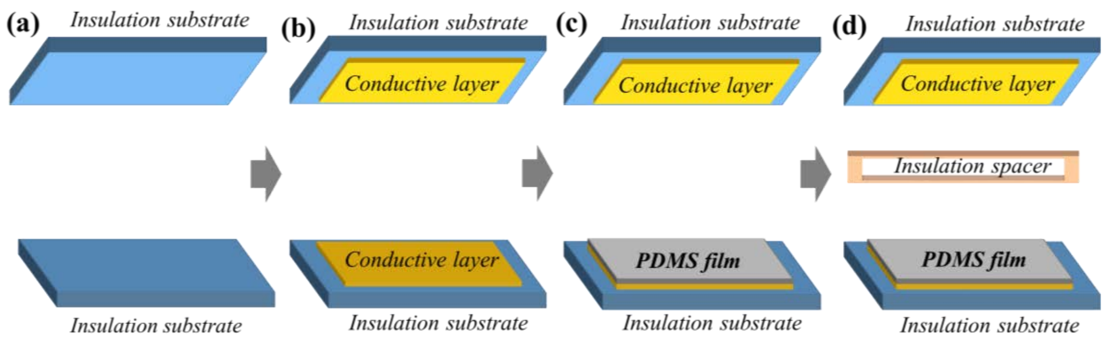

Figure 6. 15 Schematic of assembling a TENG based on PDMS film, (a) preparing two insulation substrates, (b) introducing a conductive layer on the inner surface for each substrate, (c) fixing a PDMS film on the conductive area of bottom substrate, and (d) Adding a hollow insulation spacer between the two substrates

Firstly, two polypropylene (PP) plates were used as top and bottom substrates respectively (Fig. 6.15a). Then an aluminum (Al) sheet was adhered to the inner surface of top substrate to act as dual roles of top electrode and contact (friction) surface. And a conductive adhesive film was adhered to the inner surface of another substrate to act as bottom electrode (Fig. 6.15b). Thirdly, PDMS film was fixed by adhering its smooth surface to the conductive adhesive, while its surface patterned with MLAs or HMLAs was used as the frictional surface (Fig. 6.15c). Finally, as shown in Fig. 6.15d an insulation spacer with good elasticity (such as polyurethane (PU) sponge) was placed between the two substrates for producing reciprocating motion under external forces.

6.3.2 Fundamental principle of PDMS film-based TENGs

It is generally accepted that the operation principle of the TENG for the case of electric-to-dielectric in vertical contact-separation mode is based on the coupling of triboelectric effect and electrostatic effect.[16,17]

Under open-circuit conditions (i.e. the top electrode is not connected with the bottom electrode), no charge is generated in the original separation state (Fig. 6.16a). When the top metal electrode is brought to contact with PDMS film by pressing, close contact enables the electrons, ions and/or molecules to transfer between the inner surfaces of two materials, leading to the creation of triboelectric charges at the contact area. Because PDMS possesses much higher high negative polarity than metal materials, electrons and ions are usually transferred from metal material. This leads to the creation of net positive charges at the metal surface and the same amount of net negative charges retained at the PDMS surface, respectively (Fig. 6.16b). An electric potential difference will be established when PDMS film and Cu/Ni-coated fabric become separated again. Such a potential difference can be gradually increased to a maximum value by repeatedly impacting. This is because repetitive friction can accumulate the triboelectric charges at the dielectric PDMS film until achieving a saturation state.

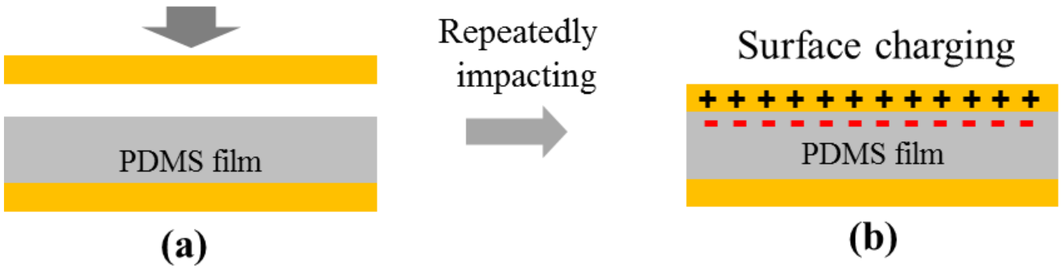

Figure 6. 16 Schematic of charging the surface of PDMS film under open-circuit conditions by friction cause by repeatedly impacting, (a) no charge generated in the original separation state, (b) surface charges generated and accumulated on the

surface of PDMS films after repeatedly impacting

As a load (such as pure resistance **R**) is electrically connected between the top electrode and bottom electrode, free electrons induced by the triboelectric charges on PDMS film will be driven to flow back and forth between the two electrodes for building an opposite potential to balance the electrostatic field generated during the separating and contacting processes, thereby leading to the generation of electric energy (current), as shown in Fig. 6.17. Specifically, when metal sheet (top electrode) is brought to completely contact with PDMS film (at contact state) after numerous times of impact, the positive triboelectric charges of top electrode are equal to the negative charges retained on the PDMS film (Fig. 6.17a). Once the top electrode is separated, the bottom electrode possesses a lower electric potential than the top electrode, leading to the production of an electric potential difference. Such potential difference will drive the electrons induced on the bottom electrode to flow through the external load for screening the positive triboelectric charges on the top electrode (Fig. 6.17b). When the top electrode is separated at a distance of **d**, positive triboelectric charges are completely screened on the top electrode, leaving an equal amount of induced positive charges on the bottom electrode (cause by the loss of electrons) (Fig. 6.17c). During the subsequent contacting process, an electric potential difference with reversed polarity will be produced with the decrease of separation distance. Correspondingly, the electrons are driven to flow in a reversed direction (Fig. 6.17d). They will keep screening the inductive positive charges on the bottom electrode until the top electrode is brought to completely contact with PDMS film again. An alternating voltage and an alternative current can be measured during the separating and contacting process, which are usually used to characterize the performance of TENG.

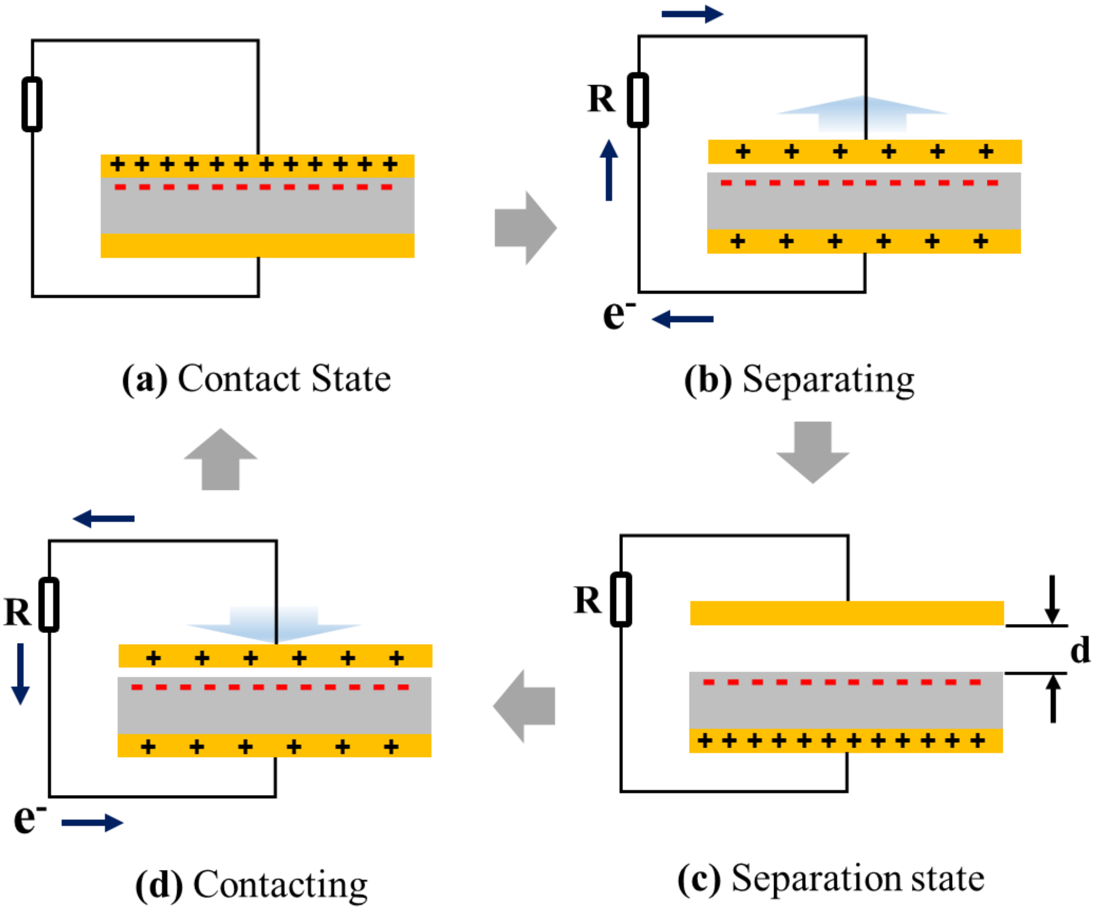

Figure 6. 17 Schematics of working principle of PDMS film-based TENG connected with a resistance load: (a) At contact state, positive triboelectric charges on top electrode are equal to the negative charges on PDMS film; (b) during the separating process, the potential difference drives electrons induced on the bottom electrode to flow through the external load for screening the positive triboelectric charges on the top electrode; (c) at the separation distance of d, positive triboelectric charges on the top electrode are completely screened, while an equal

amount of induced charges are produced on the bottom electrode; (d) During the subsequent contacting process, electrons are driven back for screening the induced positive charges on the bottom electrode

6.4 Investigation and evaluation of TENGs based on PDMS films with different surface microstructures

6.4.1 MLA-based TENGs

The electric performance of TENGs based on PDMS films with different MLAs was firstly evaluated by utilizing a mechanical compression system with a frequency of 3.3 Hz. For comparison, a TENG based on PDMS film with flat surface was used as control sample. During the compressing process, their open-circuit voltages (V_{oc}) were monitored by an oscilloscope of 1 MΩ internal resistance (Keisight DSO-X3014A) with a high voltage probe of 8 MΩ internal resistance (N2790A, maximum 1400V). For all TENG samples, their voltages were found to increase with the impacting time initially, and then stabilize at a maximum value with a small fluctuation in several minutes. The V_{oc} signals of each sample were recorded after impacting for 10 minutes.

The typical V_{oc} pulse signals generated by TENGs based on different PDMS films were compared, as shown in Fig. 6.18. It is found that TENGs based on all MLA samples possess larger peak voltages than the flat film-based TENG (Fig. 6.18a). And MLA-15 based TENG obviously has the largest peaks of V_{oc}. Fig. 6.18b and c show that each impact generates a pair of positive voltage pulse and negative voltage pulse. The positive peak voltage and negative peak voltage were produced during the contacting and separating process respectively, while the V_{oc} at zero corresponds to the contact position. The obvious performance improvement can be ascribed to the use of PDMS film with MLA surfaces. Such patterned PDMS film leads to obtain larger triboelectric contact area, and thereby producing more surface charges than the unpatterned (flat) PDMS film under the same impacting conditions.

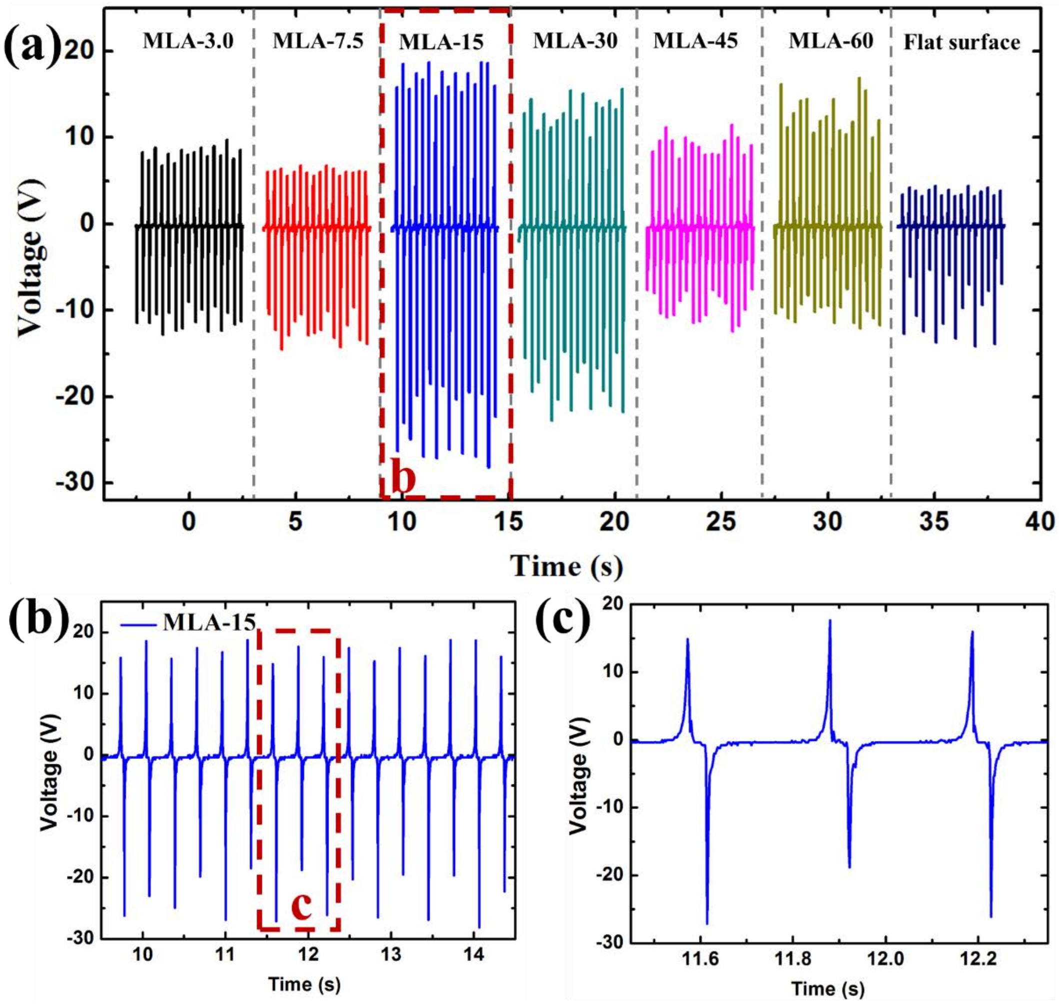

Figure 6. 18 Electric performance of TENGs based on PDMS films with different MLAs, (a) Typical open-circuit voltage signals generated by different TENGs, (b) magnified voltage signals of MLA-15 based TENG, and (c) its enlarged view of several voltage pulses

To more explicitly compare the electric performance of different TENGs, the absolute values of positive peak voltage and negative peak voltage generated by each impact were added for the calculation of average voltage. The calculated results are compared and shown in Fig. 6.19. Specifically, the average voltages of TENGs based on MLA-3.0, MLA-7.5, MLA-15, MLA-30, MLA-45 and MLA-60 are 19.40 V, 20.00 V, 40.80 V, 32.30 V, 19.34 V, and 23.22 V, respectively, while flat PDMS film-based TENG has only an average voltage of 13.83 V under the same impacting conditions. This clearly indicates that all MLA-based TENGs have a better electric performance than flat PDMS film-based TENG. Particularly for MLA-15 based TENG, an enhanced electric performance of approximately three times larger than that of flat PDMS film-based TENG was achieved.

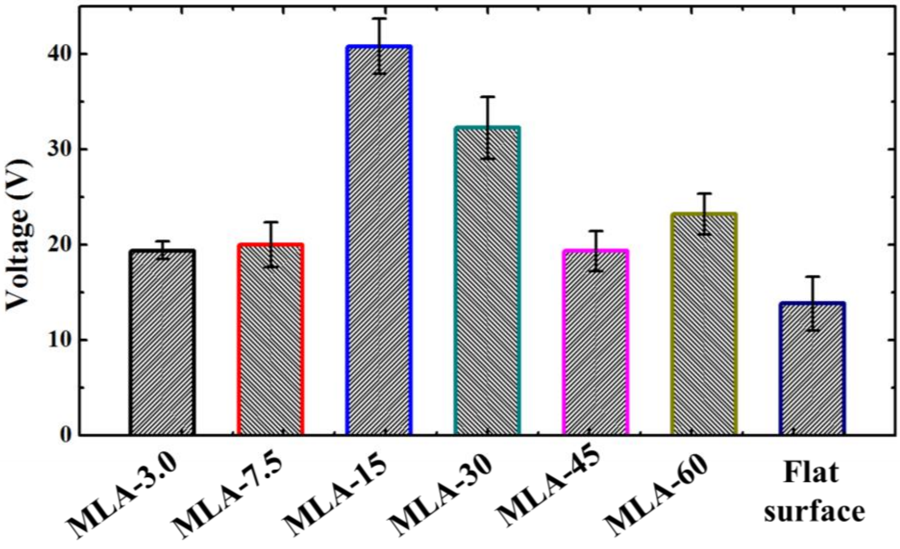

Figure 6. 19 Comparison of electric performance of TENGs based on PDMS films with different MLAs and a flat surface

The output performance of TENGs with an external load was evaluated based on different pure resistors. Fig. 6.20a shows the typical current pulse signals generated by MLA-15 based TENG under the load resistance of 20 MΩ, 10 MΩ, 5.1 MΩ, 1.0 MΩ and 0.51 MΩ respectively. Their peak currents generally possess a decreasing trend with the increase of load resistance (Fig. 6.20b), which is due to Ohmic loss. To find the matched external resistance that can generate maximum electric performance, the output current was used to calculate the instantaneous output power (P) based on the following equation.

$$P = {I_{peak}}^2 R \tag{6.1}$$

Where P, I_{peak} and R represent the instantaneous power, the average peak current and external resistance, respectively.

The dependence of instantaneous powers on the load resistance was plotted in Fig. 6.20c. It is clearly found that at the load resistance of 5.1 MΩ, the instantaneous power output of MLA-15 based TENG reaches the maximum.

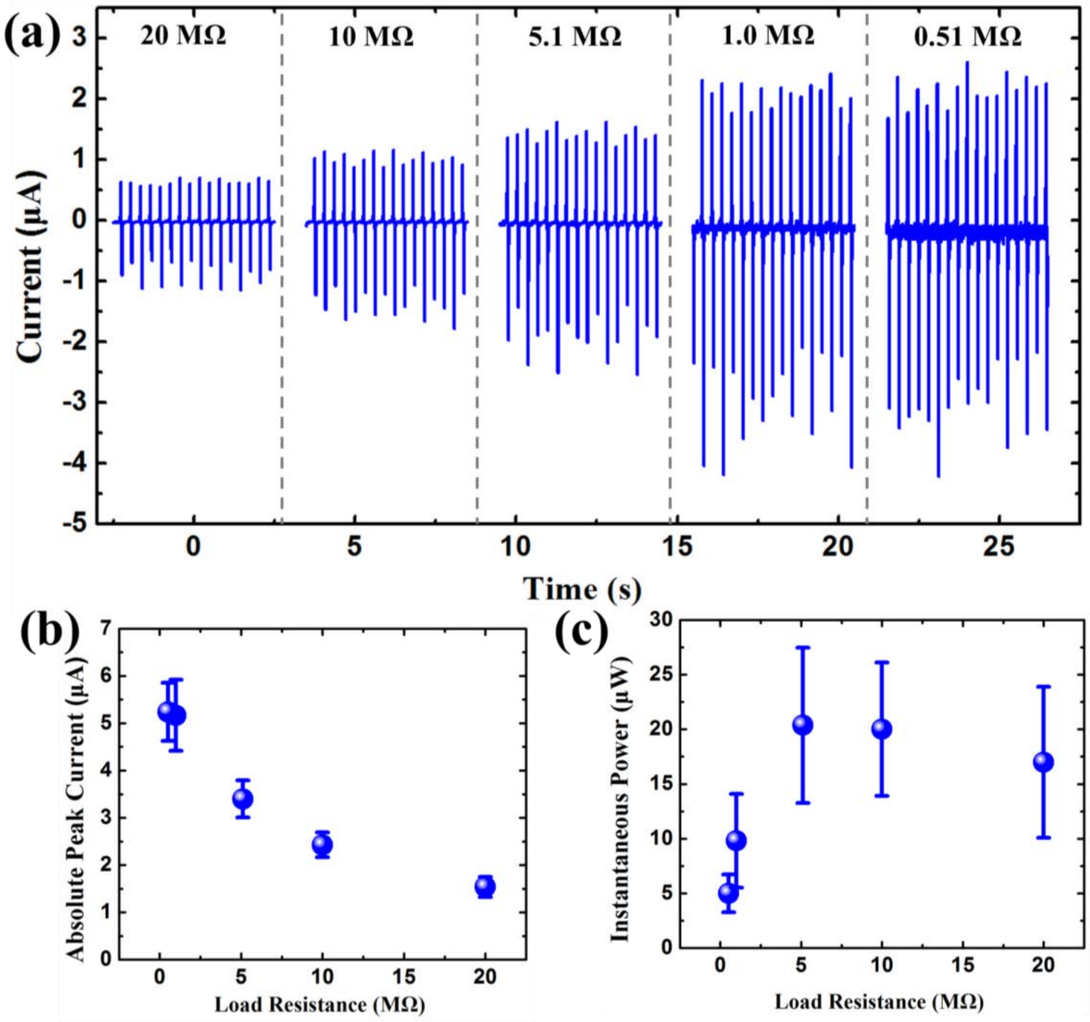

Figure 6. 20 Output performance of MLA-15 based TENG with different pure resistor as external load, (a) typical output current signals, (b) the dependence of average peak current on the load resistance, and (c) the dependence of instantaneous power on the load resistance

The load resistance was fixed at 5.1 MΩ to further investigate the influence of triggering conditions on the output performance of MLA-15 based TENG. For a quantitative evaluation without the influence of springs or elastic spacers, a modified free fall experiment device was developed for testing the output performance of TENG based on operation mode of vertical contact-separation mode of TENG. As shown in Fig. 6.21, it mainly consists of three parts: a freely movable falling weight, a fixed insulating stand, an external load, and a digital oscilloscope. Herein the pure resistor was used as external load and its resistance was fixed at 5.1 MΩ. A long stick of inverted "T"-shaped falling weight with the mass can be adjusted as required. An aluminum block with the size of 2.5 cm x 2.5 cm was adhered to the bottom surface of falling weight to play dual roles of top electrode and contact surface. Herein the total mass of falling weight with the adhered metal block was fixed at 400 g. A vertical cylinder was used to control the falling height of weight, which also can ensure the falling weight to impact the PDMS film vertically and freely. On the lower side, a conductive adhesive was adhered to the insulating stand for the immobilization of PDMS film. An oscilloscope was connected to the resistance load by the oscilloscope probes for real-timely monitoring the electric signals during the free falling process at ambient temperature of around 20 ºC and relative humidity of 65%. For the output performance test, the employed MLA-15 PDMS film was first impacted by a mechanical compression system to achieve the equilibrium surface charges, and then fixed on the insulation stand laminated with a conductive layer. The falling height was fixed at 1 cm, 3 cm and 5 cm, respectively. The falling test was repeated at least five times at each height.

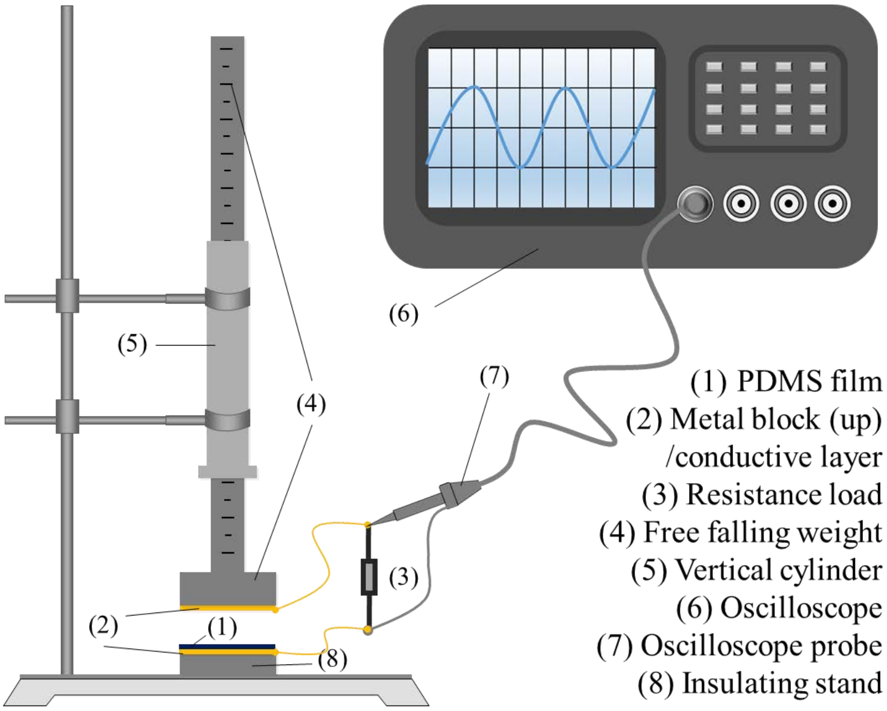

Figure 6. 21 Schematic of the modified free fall experiment for evaluating the output performance of TENGs

Different from the repetitive signals of TENGs generated by mechanical compression system before, the electrical signals triggered by the falling weight display an attenuated wavy curve. The typical output voltages of MLA-15 based TENG triggered by the falling weight at 1 cm, 3 cm and 5 cm are shown in Fig. 6.22a-c, respectively. The clearly attenuated peak signals well reflect the vibration attenuation process of the falling weight caused by rebounding. Basically, every collision can generate a pair of positive voltage peak and negative voltage peak. The peak voltages generated by the first collision were measured for the calculation of output voltage. The obtained voltages at 1 cm, 3 cm and 5 cm are 49.45 V, 79.50 V and 115.17 V, respectively. They were further plotted against the falling height, as shown in Fig. 6.22d. It shows that the output voltage generally possesses an increasing trend with the increase of falling height. This indicates that increasing the impact force can effectively promote the electric performance of PDMS film-based TENGs.

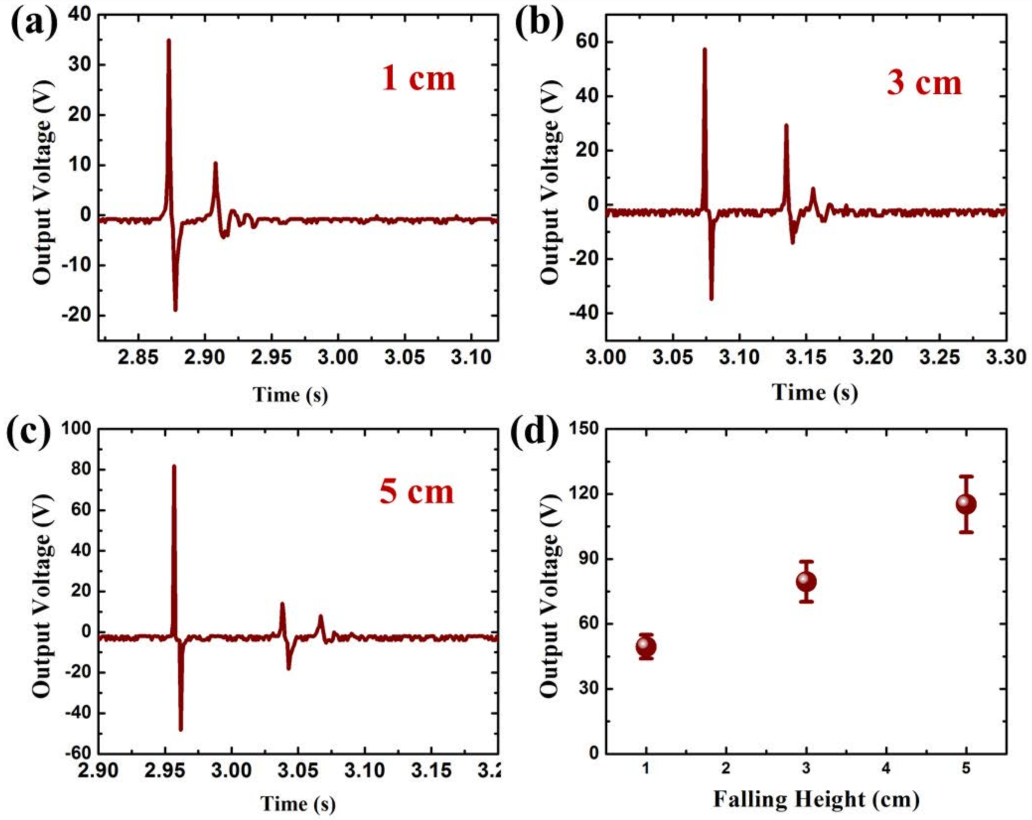

Figure 6. 22 Typical output voltage signals of MLA-15 based TENG triggered by the falling weight at different heights, (a) 1 cm, (b) 3 cm and (c) 5 cm, and (d) the dependence of output voltage on the falling height

6.4.2 HMLA-based TENGs

The electric performance of TENGs based on PDMS films with different HMLAs was evaluated by utilizing the similar strategies discussed above. A PDMS film was specifically prepared by using Cu/Ni-coated fabric as negative mold for control sample. Its surface microstructures show a positive fabric texture of the size identical with Cu/Ni-coated fabric, as revealed by SEM at different magnifications in Fig. 6.23. The difference of control film sample with HMLA film samples templated from F3C-BFAs is that there are no MLAs decorated on the fiber channels. Such PDMS film with only fabric texture was used for the assembly of fabric texture-based TENG, which was further employed as control sample for comparison.

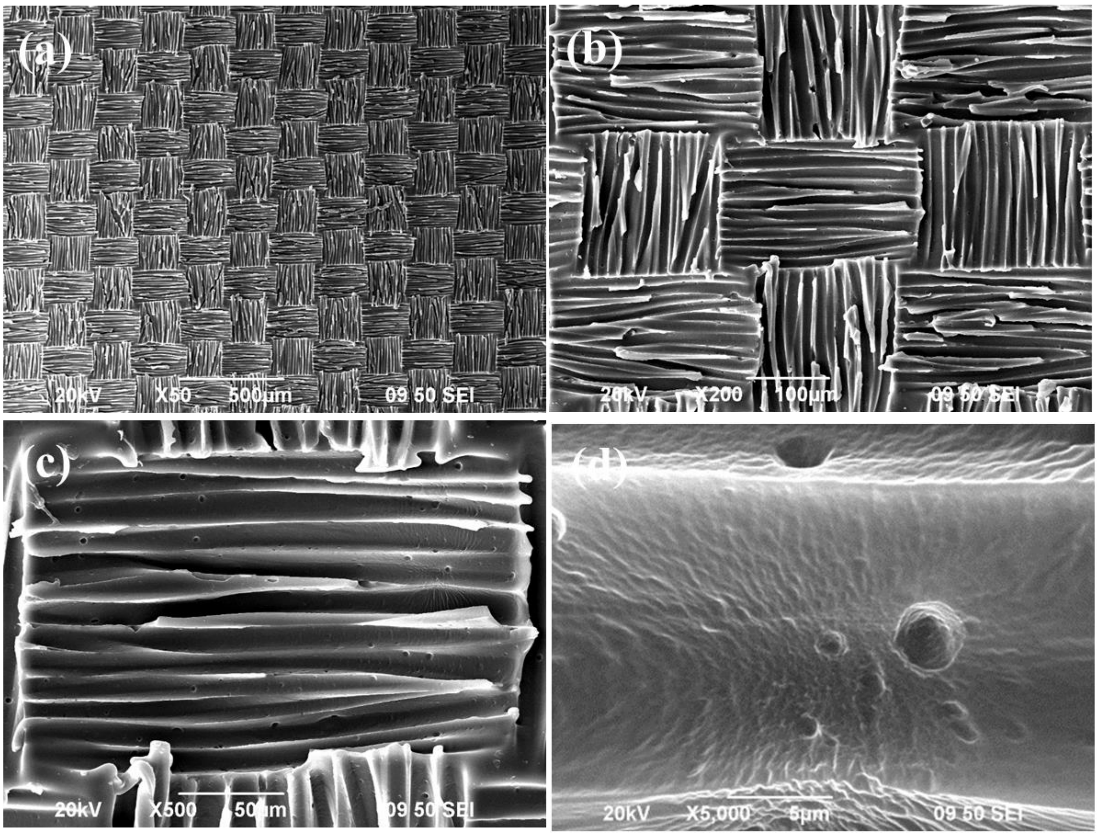

Figure 6. 23 SEM images at different magnifications of PDMS film with fabric texture templated from Cu/Ni-coated fabric

The typical V_{oc} pulse signals generated by TENGs based on PDMS films with fabric texture and different HMLAs are compared and shown in Fig. 6.24. It is obviously found that all HMLA based TENGs show larger peak voltages than fabric texture based TENG (approximately 5 V). The enhanced electric performance can be ascribed to the decoration of MLAs on the fabric surface, leading to an increase of effective contact area during the friction process. This contributes to producing more triboelectric charges for the generation of electricity. Among them, HMLA-60 based TENG possesses the best electric performance. The value of its peak voltage can be up to 30 V, which is much larger than those peak voltages produced by other HMLA-based TENGs and up to approximately six times larger than the peak voltage of fabric texture based TENG.

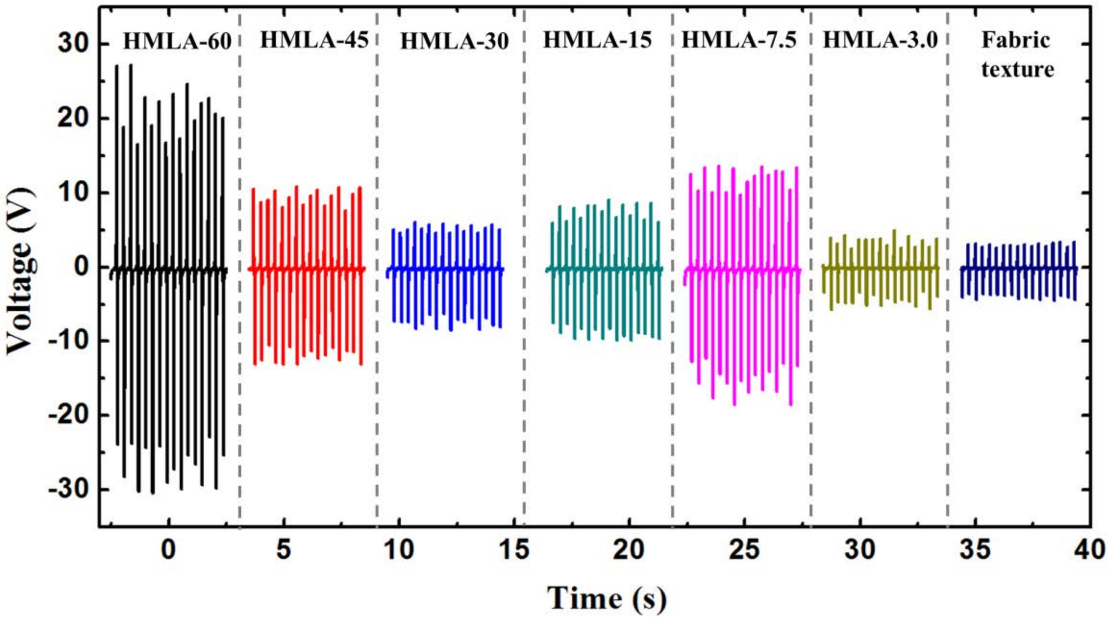

Figure 6. 24 Electric performance of TENGs based on PDMS films with different HMLAs and fabric texture

To find the matched external resistance, the output performance of HMLA-60 based TENG was further evaluated by connecting with different resistors as external load. The obtained typical current pulse signals are shown in Fig. 6.25a. The average peak current generally decreases with the increase of load resistance

(Fig. 6.25b), while the instantaneous power shows an increasing trend (Fig. 6.25c). At the load resistance of 20 MΩ, the average instantaneous power generated by HMLA-60 can be up to 34.70 μW.

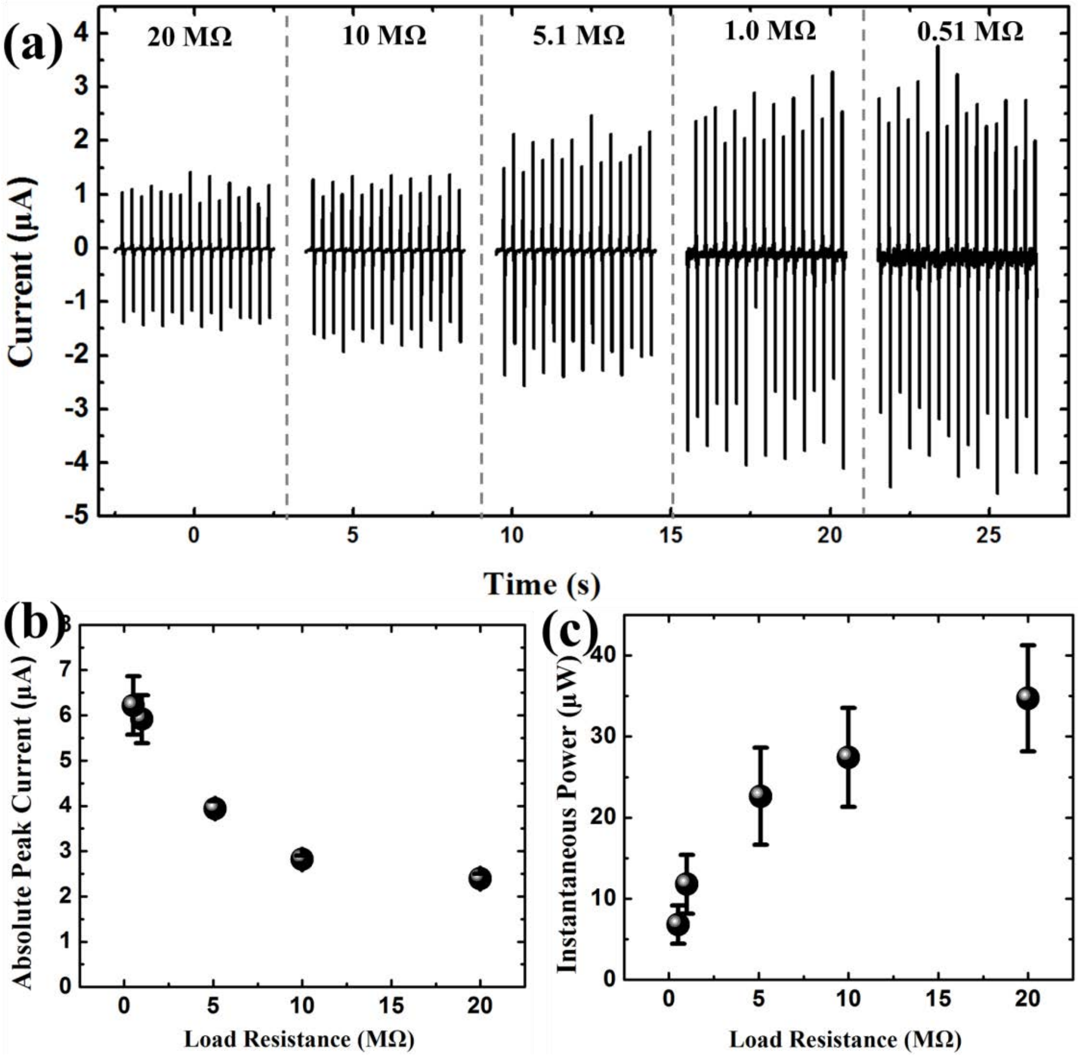

Figure 6. 25 Output performance of HMLA-60 based TENG with different pure resistor as external load, (a) typical output current signals, (b) the dependence of average peak current on the load resistance, and (c) the dependence of instantaneous power on the load resistance

The influence of impact force on the output performance of HMLA-60 based TENG was also further investigated by fixing the load resistance at 20 MΩ. The typical output voltages triggered by the falling weight at 1 cm, 3 cm and 5 cm are shown in Fig. 6.26a-c, respectively. Their average peak voltages are 59.93 V, 87.24 V and 98.74 V, respectively, showing an increasing trend with increase of falling height (Fig. 6.26d). This further demonstrates that the output performance of PDMS film-based TENGs can be effectively promoted by increasing the strength of external impact.

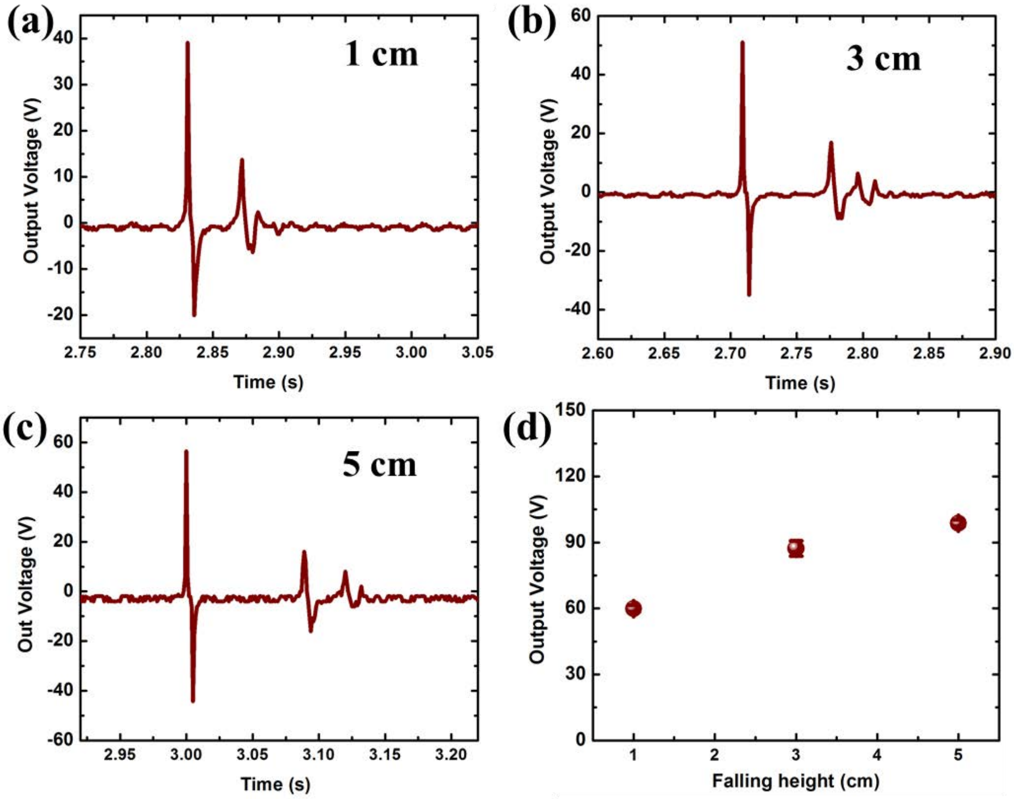

Figure 6. 26 Typical output voltage signals of HMLA-60 based TENG triggered by the falling weight at different heights, (a) 1 cm, (b) 3 cm and (c) 5 cm, and (d) the dependence of output voltage on the falling height

6.4.3 Electric performance comparison of MLA-based TENG and HMLA-based TENG

To compare the electric performance of MLA-15 based TENG and HMLA-60 based TENG under different impact strengthes, their output voltages at the matched external load resistance were used for the calculation of instantaneous power by the following equation.

$$P = {U_{peak}}^2 / R \tag{6.2}$$

Where P, R, U_{peak} represent the instantaneous power, external resistance, and the maximum peak voltage generated by the falling weight, respectively.

The calculated results are summarized in Fig. 6.27. The average instantaneous powers of MLA-15 based TENG triggered by the falling weight at 1 cm, 3 cm and 5 cm can be up to 175. 29 μW, 371.72 μW and 987.77 μW, while the corresponding values for HMLA-60 based TENG only are only 74.64 μW, 137.80 μW and 154.12 μW, respectively. These results indicate that, under the same triggering conditions, MLA-15 based TENG can possess a much better performance for converting mechanical energy into electricity than HMLA-60 based TENG.

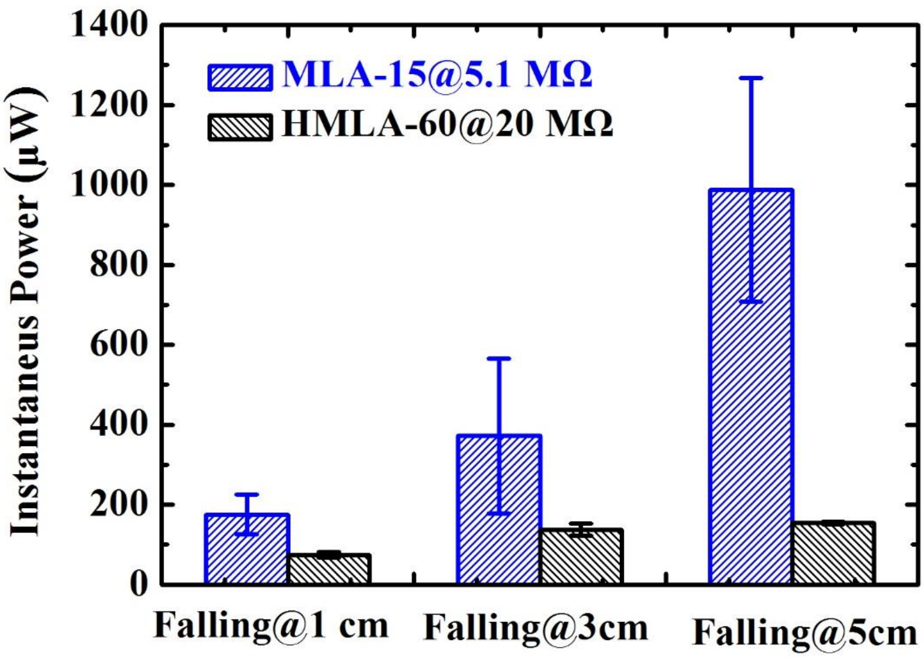

Figure 6. 27 Electric performance of MAL-15 based TENG with the matched load resistance of 5.1 MΩ and HMLA-60 based TENG with the matched load resistance of 20 MΩ under different height of falling weight

The various performances of TENGs above can be ascribed to the use of dielectric PDMS films with different surface microstructures as frictional surfaces. Generally, the TENG's performance is mainly determined by the triboelectric charges generated on the surfaces of dielectric materials *via* contact electrification. This is a complex process of combining bond cleavage, chemical changes and material transfer, which is influenced by many variables, such as surface morphology, material types, and triggering conditions. For the TENG based on the PDMS film with flat surface, its generation of triboelectric charges is mainly dependent on the elastic deformation of the whole film. While for TENGs based on PDMS films with MLAs and HMLAs, triboelectric charges can be generated by the elastic deformation of both numerous isolated microlenses, fabric texture-like regions and the whole film. When the same impact force was applied on PDMS film-based TENGs, isolated microlenses and other microstructures deform more easily and seriously than the whole film. This contributes to the production of more triboelectric charges under the same contact area, which leads to a higher triboelectric charge density. Therefore, when patterned and planar PDMS film-based TENGs are both at full contact state, the former will have better electric performance than the latter under the same triggering conditions.

However, there are no obvious rules found between the performance improvement of TENGs and the surface microstructures of PDMS films. One of the reasons can be ascribed to the different thickness of MLA region that changes reversely with the size variation. The decrease of MLA size generally accompanies with the increasing thickness of MLA region (which is comprised of three-dimensionally stacked micro lens). The decrease of MLA size may increase the number density of micro lens, thereby increasing the specific surface area for larger contact area to produce triboelectric charges. And the multiple layers of MLA region with smaller surface lens size tend to deform more easily under the impact of external force. However, some vacant space among sparsely stacked lenses may be left, which results in the decrease of effective contact area for contact electrification. This phenomenon is particularly serious for HMLA-based TENGs due to the larger height difference of fabric texture-like microstructures. Therefore, HMLA-based TENGs generally show less improved electric performance than MLA-based TENGs under specific triggering conditions.

6.5 Applications of PDMS film-based TENGs for harvesting mechanical energy generated by body motion

MLA-15 based TENG was further packaged for harvesting the mechanical energy generated by human body motion, such as finger tapping, hand clapping and walking. Fig. 6.28a shows the final product of MLA-15 based TENG with the size of 6 cm x 6 cm x 0.8 cm after packaging. Its inner structures are shown in Fig. 6.28b and c respectively. Al sheet was replaced by flexible conductive Cu/Ni-coated fabric. And a commercial PU sponge was used as elastic spacer. The packed MLA-15 based TENG is freestanding, bendable, lightweight (less than 10 g), and portable, which can be either placed on desk for harvesting finger tapping energy, held for harvesting the hand clapping energy, or built inside shoe sole for harvesting the mechanical energy generated by walking.

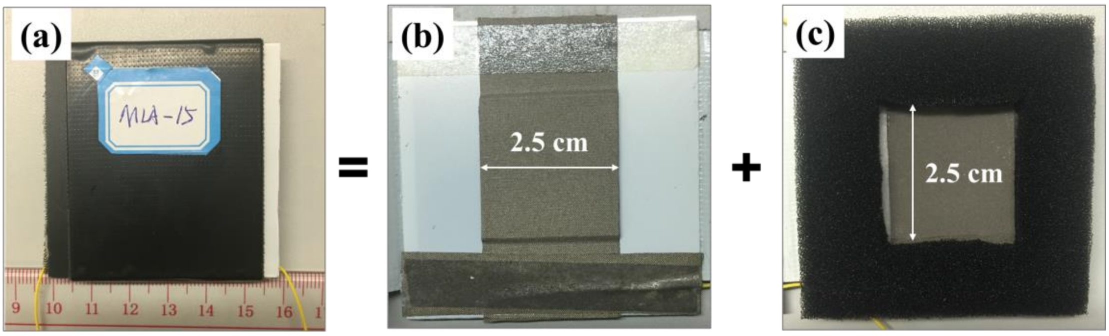

Figure 6. 28 Digital photographs of (a) the final MLA-15 based TENG after packaging, and (b) and (c) its inner structures

The MLA-15 based TENG possesses a high sensitivity to the very small force caused by the finger, and can also make an immediate response to the finger tapping. Fig. 6.29a shows the repetitive and sharp output voltage signals generated at the load resistance of 5.1 MΩ by the rapid finger tapping with a frequency of approximately 4.0 Hz. Because the external load was pure resistance, the electric energy was equal to the Joule heating energy. Therefore, its generated electric energy (E) can be calculated based on time-integral of the output voltages with the following equation

$$E = Q = \int_{t_1}^{t_2} \frac{U^2}{R} dt \tag{6.3}$$

where E is the electric energy generated by TENG, Q is the Joule heating energy, U is the output voltage, and R is the load resistance.

Fig. 29b shows a pair of positive voltage peak and negative voltage peak triggered by a finger tap. Its maximum peak voltage can be up to about 7.6 V. The total electric energy generated by this light tap is about 0.078 μJ.

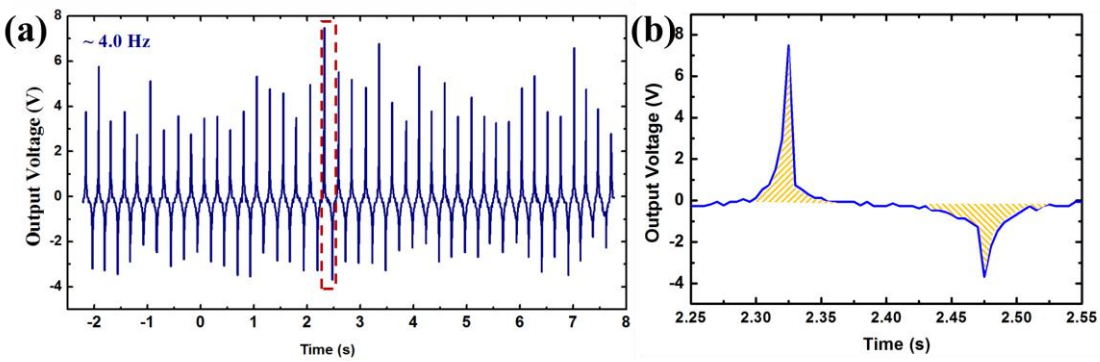

Figure 6. 29 (a) The electric performance of MLA-15 based TENG by rapid tapping with a finger, (b) a voltage pulse output produced by one finger tap

The output voltages of TENG generated by hand clapping at different frequencies are shown in Fig. 6.30a. It shows that the generated peak voltages generally possess an increasing trend with the increase of clapping frequency. At 5.5 Hz, the maximum peak voltage is up to 146.1 V (Fig. 6.30b). Even when the TENG was clapped with hand at a normal frequency (about 1.2 Hz), a maximum peak voltage of 93.6 V can be obtained (Fig. 6.30c). And the electric energy generated by one clap is 9.12 μJ at 5.5 Hz and 4.16 μJ at 1.2 Hz, respectively.

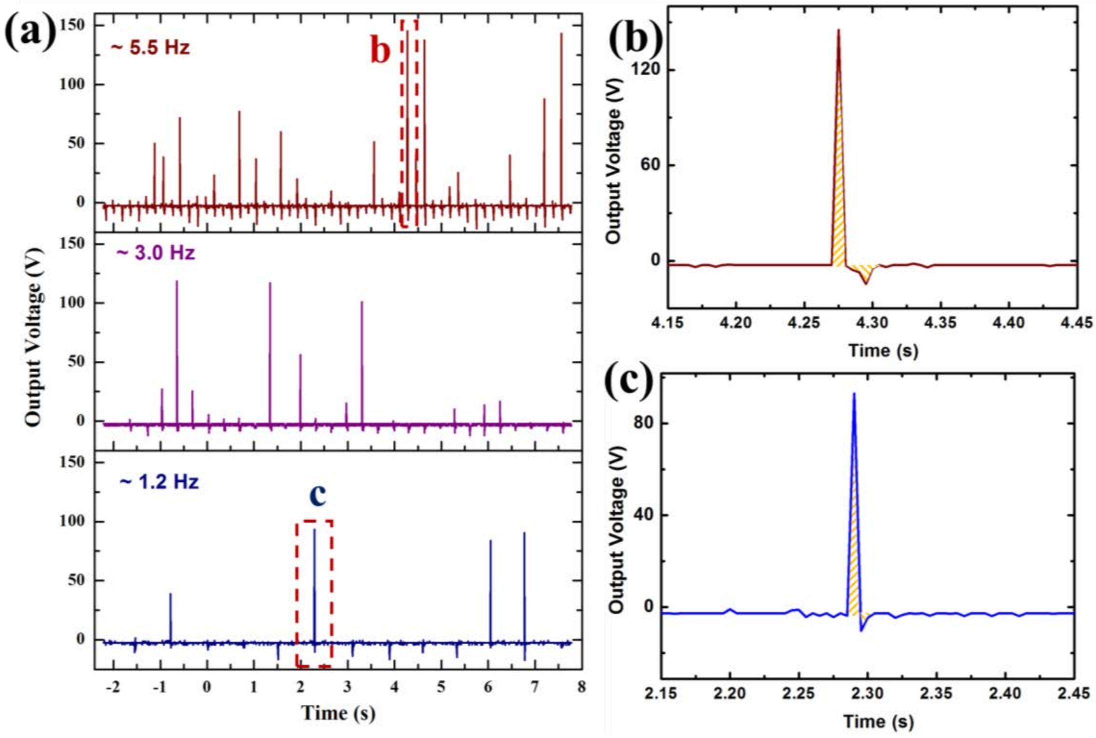

Figure 6. 30 (a) The electric performance of MLA-15 based TENG by handclapping at different frequencies, (b) a voltage pulse output produced by normal handclapping (~5.5 Hz) and (c) a voltage pulse output produced by rapid handclapping (~1.2 Hz) for the calculation of electric energy

The MLA-15 based TENG was also built under the shoe sole for harvesting the mechanical energy produced by a 60 Kg adult. The output voltages generated by human foot with the frequency from 0.5 Hz to 2.5 Hz were shown in Fig. 6.31a. It indicates that the output voltages generally show an increasing trend with the increase of pace frequency. The maximum peak voltages at 0.5 Hz (strolling, Fig. 6.31d), 1.5 Hz (normal walking, Fig. 6.31c), and 2.5 Hz (jogging, Fig. 6.31b) can be up to 4.9 V, 4.5 V and 60.4 V, respectively. The corresponding generated electric energies by one pace are 0.10 μJ, 0.29 μJ, and 1.93 μJ, respectively.

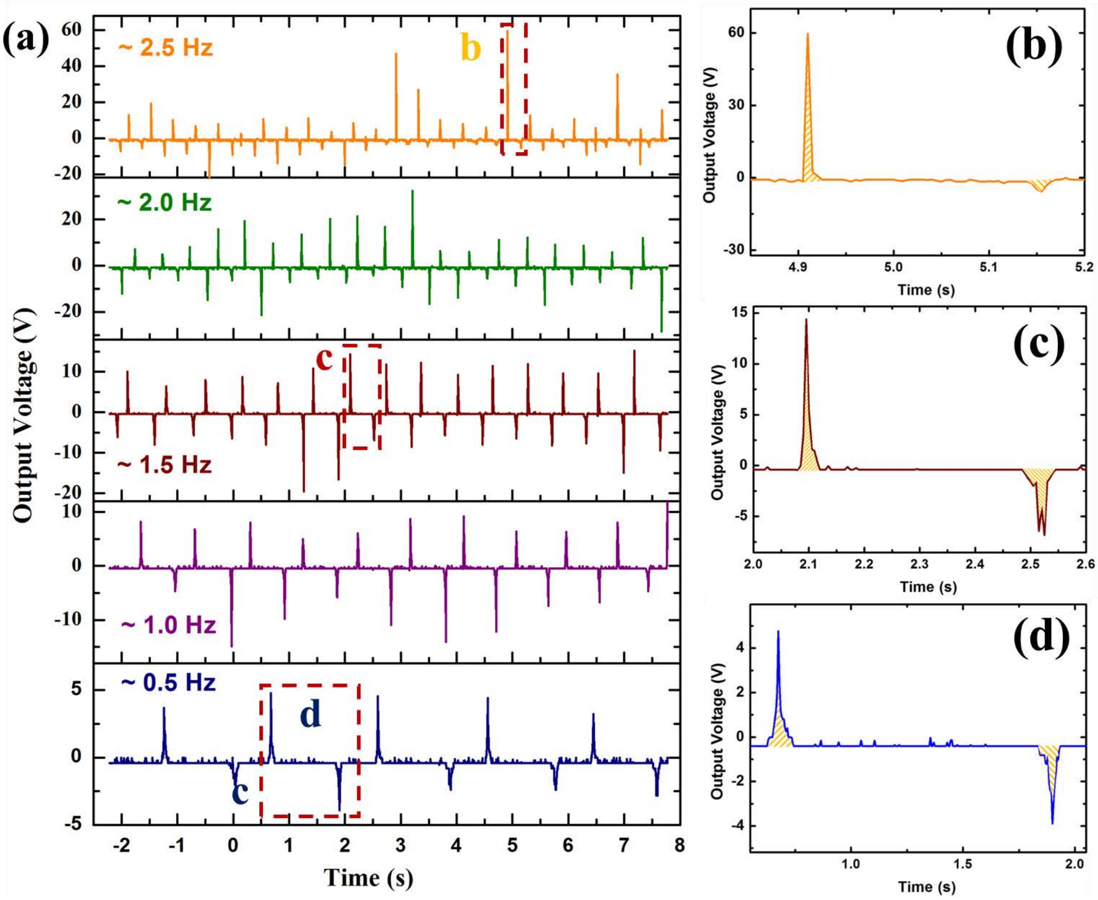

Figure 6. 31 (a) The electric performance of MLA-15 based TENG triggered by human foot at different frequencies, (b) a voltage pulse output produced by jogging (~2.5 Hz) and (c) a voltage pulse output produced by walking (~1.5 Hz), and (d) a voltage pulse output produced by strolling (~0.5 Hz)

6.6 Summary

In summary, a series of PDMS films with positive MLAs and HMLAs have been prepared by using BFA and F3C-BFA as negative molds for the assembly of vertical contact-separation based TENGs. Compared with planar PDMS film-based TENG, all MLA-based TENGs have an obviously enhanced electric performance, while all HMLA-based TENGs possess better capacity in harvesting mechanical energy than the fabric texture-based TENG. Among them, MLA-15 based TENG shows the most excellent performance on converting the mechanical energy into electricity under different triggering conditions. Such PDMS film-based TENGs were further successfully used to harvest the mechanical energy generated by different human body motions, including the finger tapping, hand clapping and walking with a frequency ranging from 0.5 Hz to 5.5 Hz.

This study shows the promising applications of MLAs and HMLAs derived from BFAs in TENGs for converting the mechanical energy generated by human body motions into electricity, which can potentially drive vast types of portable electronics and sensors for different purposes, such as health monitoring and medical care.

CHAPTER 7 Conclusions and Suggestions for Future Research

7.1 Conclusions

Fabrication of porous materials with controllable components and structures on desired substrates has long been a significant science subject because of its infinite potential of merging the structural, material and substrate properties for different applications with enhanced performance and economical cost. It is also always a thriving research area owing to the continuously emerging advanced materials, novel structures and new demands. This study has conducted a systematical research on the unique one-step self-assembly strategy of using water droplet arrays (or BFs) as soft templates for the fabrication of polymer films with controllable microstructures and materials on planar, nonplanar and flexible fabric substrates for high value applications in energy harvesting and wearable technology. Main significant conclusions have been drawn as follows.

1. The BF principle of water has been extended to non-aqueous liquid and more complex binary aqueous/non-aqueous liquids for controllable fabrication of polymeric microstructures involving hexagonally ordered BFAs, symmetrical microspheres and asymmetrical microspherical caps. Through the systematic and comparative study, the complex mechanisms behind the BF technique have been thoroughly elucidated from the initial spreading of solution film on substrate, the formation and spreading of nonsolvent BFs on solution film, the physical gelation of polymer-rich phase to the final

formation of polymer microstructures by complete removal of liquids.

2. A robust asphalt-assisted BF strategy has been developed for general fabrication of highly ordered and noncracking BFA films with easily obtained polymers, such as commercial PS, SBS, PEO and PC, on various substrates including glass, silicon, copper, copper grid, fabric, irregular particle, and even water surface under more easily accessible experimental conditions. This technique is also suitable for the incorporation of functional nanoparticles, such as TiO_2 NPs, Ag NWs, and Cu NWs with little influence on the regularity of pore arrays. When TiO_2-incorportated BFA films on suitable substrates were employed for photocatalytic degradation of pollutants in air and water, their corresponding degradation efficiencies are greatly increased by 67.7% and 153.5% in comparison to TiO_2 incorporated solid films, respectively.
3. A novel kind of textile composites possessing the porous microstructures of customized materials and maintaining the unique texture features and inherent properties of fabrics has been developed by systematical investigation of the formation of 3C-BFAs on nonplanar substrates with a novel silicon-containing graft copolymer PDMS-*g*-PAs. Moreover, taking advantages of the high silicon-containing character of PDMS-*g*-PAs, its BFA films are also successfully used as single-source precursor for the formation of tough honeycomb microstuctured ceramics by a hybrid strategy combing the plasma modification and in situ pyrolysis technique.

4. PDMS films with controllable MLAs and HMLAs prepared by using BFA and F3C-BFA as negative molds have been first applied for the assembly of vertical contact-separation based TENGs to convert mechanical energy into electricity. All MLA and HMLA-based TENGs display an obviously enhanced electric performance. Particularly MLA-15 based TENG HMLA-60 based TENG with an enhanced electric performance have been achieved. Moreover, the PDMS film-based TENGs were used to harvest the mechanical energy generated by different human body motions, such as the finger tapping, hand clapping and walking with a frequency ranging from 0.5 Hz to 5.5 Hz.

7.2 Limitations of the study and suggestions for future research

The achievements of this study have been summarized as above. The potential challenges and limitations arising from this study will be described in this section together with the recommendations for future work.

1. Performance test and evaluation of fabric-based 3D conformal porous microstructures

This study puts forward the concept of 3D conformal porous microstructured fabric (3C-PMF) and successfully demonstrates its feasibility of production by the BF technique. It has been demonstrated as good template for direct fabrication of hierarchical patterned films featured with both fabric textures and MLAs. Through the suitable introduction of functional materials and choice of fabric substrates, such kind of 3C-PMFs is also believed to have more promising applications in the fields of biology, energy and wearable technology. Therefore, more film-forming materials and textile substrates should be exploited for the development of new applications. In prior to practical applications, further more detailed investigations should also be carried out for the the establishment of an integrated testing system for the measurement of various properties of 3C-PMFs, such as flexibility, abrasion/fatigue resistance, porosity, and gas/water permeability.

2. The role of surface microstructures on the electric performance of TENGs

Although TENGs based on PDMS films with different MLAs and HMLs have been achieved with enhanced electric performance under certain triggering conditions, no obvious relationships can be found between the surface microstructures and TENGs' performance. More studies should be conducted to find the exact role of surface microstructures on the performance enhancement of TENGs under different triggering conditions. In addition, TENGs based on others working modes such as contact-sliding mode should also be developed for HMLAs to harvest the mechanical energy generated by body motion in future. These recommended studies will contribute to finding the optimal microstructures and triggering methods to produce effective friction for producing more triboelectric charges with less applied force (or work) for higher electric performance.

3. Further development of BF techniques and applications of BFAs

Although the used water is green and nontoxic and only film-forming material is left after the complete evaporation, it is noticed that the employed organic solvent during the BF process is toxic and massive. Therefore, an integrated BF devices containing condensing unit should be further developed for the recyclable use of solvent. Moreover, more different applications should be exploited for BFAs based on the used film-forming materials and incorporated functional nanoparticles

The binary BF technique provides a physical, mild, nondestructive and nontoxic strategy for one-step assembly of microspherical caps with adjustable morphology, which should have promising applications in catalyst and drug carriers. Further investigation of the BF techniques under other mixed nonsolvent vapors may open a new route for straightforward creation of more complex and novel polymeric microstructures.

REFERENCES

(1) Webb, H. K.; Crawford, R. J.; Ivanova, E. P. Wettability of natural superhydrophobic surfaces. *Adv Colloid Interfac* **2014,** *210*, 58.

(2) Cutkosky, M. R.; Kim, S. Design and fabrication of multi-material structures for bioinspired robots. *Philos T R Soc A* **2009,** *367* (1894), 1799.

(3) Cho, W. K.; Choi, I. S. Fabrication of hairy polymeric films inspired by geckos: Wetting and high adhesion properties. *Advanced Functional Materials* **2008,** *18* (7), 1089.

(4) Munch, E.; Launey, M. E.; Alsem, D. H.; Saiz, E.; Tomsia, A. P.; Ritchie, R. O. Tough, Bio-Inspired Hybrid Materials. *Science* **2008,** *322* (5907), 1516.

(5) Dushkina, N.; Lakhtakia, A. Structural Colors. *Engineered Biomimicry* **2013**, DOI:10.1016/B978-0-12-415995-2.00011-8 10.1016/B978-0-12-415995-2.00011-8, 267.

(6) Bhushan, B. Biomimetics: lessons from nature--an overview. *Philos Trans A Math Phys Eng Sci* **2009,** *367* (1893), 1445.

(7) Zhang, A. J.; Bai, H.; Li, L. Breath Figure: A Nature-Inspired Preparation Method for Ordered Porous Films. *Chem Rev* **2015,** *115* (18), 9801.

(8) Bunz, U. H. F. Breath Figures as a Dynamic Templating Method for Polymers and Nanomaterials. *Advanced materials* **2006,** *18* (8), 973.

(9) Wan, L. S.; Zhu, L. W.; Ou, Y.; Xu, Z. K. Multiple interfaces in self-assembled breath figures. *Chem Commun (Camb)* **2014,** *50* (31), 4024.

(10) Hernández-Guerrero, M.; Stenzel, M. H. Honeycomb structured polymer films via breath figures. *Polym. Chem.* **2012,** *3* (3), 563.

(11) Bai, H.; Du, C.; Zhang, A. J.; Li, L. Breath Figure Arrays: Unconventional Fabrications, Functionalizations, and Applications. *Angew Chem Int Edit* **2013,** *52* (47), 12240.

(12) Xue, L.; Zhang, J.; Han, Y. Phase separation induced ordered patterns in thin polymer blend films. *Progress in Polymer Science* **2012,** *37* (4), 564.

(13) Ma, H.; Hao, J. Ordered patterns and structures via interfacial self-assembly: superlattices, honeycomb structures and coffee rings. *Chem Soc Rev* **2011,** *40* (11), 5457.

(14) Escalé, P.; Rubatat, L.; Billon, L.; Save, M. Recent advances in honeycomb-structured porous polymer films prepared via breath figures. *European Polymer Journal* **2012,** *48* (6), 1001.

(15) Dou, Y. Y.; Jin, M. L.; Zhou, G. F.; Shui, L. L. Breath Figure Method for Construction of Honeycomb Films. *Membranes* **2015,** *5* (3), 399.

(16) Wang, Z. L. Triboelectric nanogenerators as new energy technology and self-powered sensors - Principles, problems and perspectives. *Faraday Discuss* **2014,** *176*, 447.

(17) Wang, Z. L. Triboelectric Nanogenerators as New Energy Technology for Self-Powered Systems and as Active Mechanical and Chemical Sensors. *Acs Nano* **2013,** *7* (11), 9533.

(18) Zhang, X. S.; Han, M. D.; Meng, B.; Zhang, H. X. High performance

triboelectric nanogenerators based on large-scale mass-fabrication technologies. *Nano Energy* **2015,** *11*, 304.

(19) Wang, Z. L.; Chen, J.; Lin, L. Progress in triboelectric nanogenerators as a new energy technology and self-powered sensors. *Energ Environ Sci* **2015,** *8* (8), 2250.

(20) Wu, D.; Xu, F.; Sun, B.; Fu, R.; He, H.; Matyjaszewski, K. Design and preparation of porous polymers. *Chem Rev* **2012,** *112* (7), 3959.

(21) Yaghi, O. M.; O'Keeffe, M.; Ockwig, N. W.; Chae, H. K.; Eddaoudi, M.; Kim, J. Reticular synthesis and the design of new materials. *Nature* **2003,** *423* (6941), 705.

(22) Wight, A.; Davis, M. Design and preparation of organic-inorganic hybrid catalysts. *Chem Rev* **2002,** *102* (10), 3589.

(23) Rowsell, J. L.; Yaghi, O. M. Metal–organic frameworks: a new class of porous materials. *Micropor Mesopor Mat* **2004,** *73* (1), 3.

(24) Davis, M. E. Ordered porous materials for emerging applications. *Nature* **2002,** *417* (6891), 813.

(25) Eddaoudi, M.; Kim, J.; Rosi, N.; Vodak, D.; Wachter, J.; O'Keeffe, M.; Yaghi, O. M. Systematic design of pore size and functionality in isoreticular MOFs and their application in methane storage. *Science* **2002,** *295* (5554), 469.

(26) Zhu, C.; Du, D.; Eychmüller, A.; Lin, Y. Engineering ordered and nonordered porous noble metal nanostructures: synthesis, assembly, and

their applications in electrochemistry. *Chem Rev* **2015,** *115* (16), 8896.

(27) Jia, L.; Cai, W. Micro/nanostructured ordered porous films and their structurally induced control of the gas sensing performances. *Advanced Functional Materials* **2010,** *20* (21), 3765.

(28) Dai, F.; Zai, J.; Yi, R.; Gordin, M. L.; Sohn, H.; Chen, S.; Wang, D. Bottom-up synthesis of high surface area mesoporous crystalline silicon and evaluation of its hydrogen evolution performance. *Nature communications* **2014,** *5*.

(29) De Volder, M. F.; Tawfick, S. H.; Baughman, R. H.; Hart, A. J. Carbon nanotubes: present and future commercial applications. *Science* **2013,** *339* (6119), 535.

(30) Novoselov, K. S.; Fal, V.; Colombo, L.; Gellert, P.; Schwab, M.; Kim, K. A roadmap for graphene. *Nature* **2012,** *490* (7419), 192.

(31) Butler, S. Z.; Hollen, S. M.; Cao, L.; Cui, Y.; Gupta, J. A.; Gutierrez, H. R.; Heinz, T. F.; Hong, S. S.; Huang, J.; Ismach, A. F. Progress, challenges, and opportunities in two-dimensional materials beyond graphene. *ACS nano* **2013,** *7* (4), 2898.

(32) Xu, M.; Liang, T.; Shi, M.; Chen, H. Graphene-like two-dimensional materials. *Chem Rev* **2013,** *113* (5), 3766.

(33) Wypych, G. *Handbook of polymers*; ChemTec Pub., 2012.

(34) Malhotra, B. D. *Handbook of polymers in electronics*; iSmithers Rapra Publishing, 2001.

(35) Matyjaszewski, K.; Tsarevsky, N. V. Nanostructured functional materials prepared by atom transfer radical polymerization. *Nat Chem* **2009,** *1* (4), 276.

(36) Matyjaszewski, K. Atom Transfer Radical Polymerization (ATRP): Current Status and Future Perspectives. *Macromolecules* **2012,** *45* (10), 4015.

(37) Moreau, W. M. *Semiconductor lithography: principles, practices, and materials*; Springer Science & Business Media, 2012.

(38) Shenton, M.; Stevens, G. Surface modification of polymer surfaces: atmospheric plasma versus vacuum plasma treatments. *Journal of Physics D: Applied Physics* **2001,** *34* (18), 2761.

(39) Boyd, I. W. *Laser processing of thin films and microstructures: oxidation, deposition and etching of insulators*; Springer Science & Business Media, 2013.

(40) Pierin, G.; Grotta, C.; Colombo, P.; Mattevi, C. Direct Ink Writing of micrometric SiOC ceramic structures using a preceramic polymer. *Journal of the European Ceramic Society* **2016,** *36* (7), 1589.

(41) Seidel, S.; Gupta, M. Systematic study of the growth and morphology of vapor deposited porous polymer membranes. *Journal of Vacuum Science & Technology A* **2014,** *32* (4).

(42) Hermes, S.; Schroder, F.; Amirjalayer, S.; Schmid, R.; Fischer, R. A. Loading of porous metal-organic open frameworks with organometallic

CVD precursors: inclusion compounds of the type LnM (a)@MOF-5. *J Mater Chem* **2006,** *16* (25), 2464.

(43) Tsivintzelis, I.; Sanxaridou, G.; Pavlidou, E.; Panayiotou, C. Foaming of polymers with supercritical fluids: A thermodynamic investigation. *The Journal of Supercritical Fluids* **2016,** *110*, 240.

(44) Lancelle-Beltran, E.; Prene, P.; Boscher, C.; Belleville, P.; Buvat, P.; Lambert, S.; Guillet, F.; Boissiere, C.; Grosso, D.; Sanchez, C. Nanostructured hybrid solar cells based on self-assembled mesoporous titania thin films. *Chem Mater* **2006,** *18* (26), 6152.

(45) Eckel, Z. C.; Zhou, C.; Martin, J. H.; Jacobsen, A. J.; Carter, W. B.; Schaedler, T. A. Additive manufacturing of polymer-derived ceramics. *Science* **2016,** *351* (6268), 58.

(46) Chi, M.-H.; Chang, C.-W.; Ko, H.-W.; Su, C.-H.; Lee, C.-W.; Peng, C.-H.; Chen, J.-T. Solvent-Induced Dewetting on Curved Substrates: Fabrication of Porous Polymer Nanotubes by Anodic Aluminum Oxide Templates. *Macromolecules* **2015,** *48* (17), 6241.

(47) Luo, Y.; Li, B.; Wang, W.; Wu, K.; Tan, B. Hypercrosslinked aromatic heterocyclic microporous polymers: a new class of highly selective CO2 capturing materials. *Advanced materials* **2012,** *24* (42), 5703.

(48) Sai, H.; Tan, K. W.; Hur, K.; Asenath-Smith, E.; Hovden, R.; Jiang, Y.; Riccio, M.; Muller, D. A.; Elser, V.; Estroff, L. A. Hierarchical porous polymer scaffolds from block copolymers. *Science* **2013,** *341* (6145), 530.

(49) Jiang, J.-X.; Li, Y.; Wu, X.; Xiao, J.; Adams, D. J.; Cooper, A. I. Conjugated microporous polymers with rose bengal dye for highly efficient heterogeneous organo-photocatalysis. *Macromolecules* **2013,** *46* (22), 8779.

(50) Jiang, J.-X.; Cooper, A. I. In *Functional Metal-Organic Frameworks: Gas Storage, Separation and Catalysis*; Springer, 2009.

(51) McKeown, N. B.; Budd, P. M. Exploitation of intrinsic microporosity in polymer-based materials. *Macromolecules* **2010,** *43* (12), 5163.

(52) Gong, J.; Zhang, A.; Bai, H.; Zhang, Q.; Du, C.; Li, L.; Hong, Y.; Li, J. Formation of nanoscale networks: selectively swelling amphiphilic block copolymers with CO2-expanded liquids. *Nanoscale* **2013,** *5* (3), 1195.

(53) Li, L.; Nemoto, T.; Sugiyama, K.; Yokoyama, H. CO2Foaming in Thin Films of Block Copolymer Containing Fluorinated Blocks. *Macromolecules* **2006,** *39* (14), 4746.

(54) Li, L.; Yokoyama, H. Nanoscale silica capsules ordered on a substrate: oxidation of nanocellular thin films of poly(styrene-b-dimethylsiloxane). *Angew Chem Int Ed Engl* **2006,** *45* (38), 6338.

(55) Yokoyama, H.; Li, L.; Dutriez, C.; Iwakura, Y.; Sugiyama, K.; Masunaga, H.; Sasaki, S.; Okuda, H. Horizontally and Vertically Aligned Polymeric Nanosheets: CO2-Induced Morphological Changes of Block Copolymer Thin Films. *Macromolecules* **2008,** *41* (22), 8626.

(56) Mai, Y.; Eisenberg, A. Self-assembly of block copolymers. *Chem Soc Rev*

2012, *41* (18), 5969.

(57) Hsueh, H.-Y.; Yao, C.-T.; Ho, R.-M. Well-ordered nanohybrids and nanoporous materials from gyroid block copolymer templates. *Chem Soc Rev* **2015,** *44* (7), 1974.

(58) Stein, A.; Wilson, B. E.; Rudisill, S. G. Design and functionality of colloidal-crystal-templated materials—chemical applications of inverse opals. *Chem Soc Rev* **2013,** *42* (7), 2763.

(59) Mijangos, C.; Hernández, R.; Martín, J. A review on the progress of polymer nanostructures with modulated morphologies and properties, using nanoporous AAO templates. *Progress in Polymer Science* **2016,** *54*, 148.

(60) He, H.; Zhong, M.; Konkolewicz, D.; Yacatto, K.; Rappold, T.; Sugar, G.; David, N. E.; Gelb, J.; Kotwal, N.; Merkle, A. Three-Dimensionally Ordered Macroporous Polymeric Materials by Colloidal Crystal Templating for Reversible CO2 Capture. *Advanced Functional Materials* **2013,** *23* (37), 4720.

(61) Fan, F.-R.; Lin, L.; Zhu, G.; Wu, W.; Zhang, R.; Wang, Z. L. Transparent triboelectric nanogenerators and self-powered pressure sensors based on micropatterned plastic films. *Nano letters* **2012,** *12* (6), 3109.

(62) Aitken, J. Breath Figures. *Proceedings of the Royal Society of Edinburgh* **1893,** *20*, 94.

(63) Rayleigh, L. Breath Figures. *Nature* **1911,** *86* (2169), 416.

(64) Aitken, J. Breath Figures. *Nature* **1911,** *86* (2172), 516.

(65) Rayleigh, L. Breath Figures. *Nature* **1912,** *90* (2251), 436.

(66) Aitken, J. Breath Figures. *Nature* **1913,** *90* (2258), 619.

(67) George, C. Breath Figures. *Nature* **1911,** *87* (2175), 10.

(68) Giltay, J. W. Breath Figures. *Nature* **1911,** *86* (2174), 585.

(69) Spurr, R. T.; Butlin, J. G. Breath Figures. *Nature* **1957,** (4571), 1187.

(70) Beysens, D.; Knobler, C. M. Growth of breath figures. *Phys Rev Lett* **1986,** *57* (12), 1433.

(71) Steyer, A.; Guenoun, P.; Beysens, D.; Knobler, C. M. Two-dimensional ordering during droplet growth on a liquid surface. *Physical Review B* **1990,** *42* (1), 1086.

(72) Beysens, D.; Steyer, A.; Guenoun, P.; Fritter, D.; Knobler, C. M. How does dew form? *Phase Transitions* **1991,** *31* (1-4), 219.

(73) Fritter, D.; Knobler, C. M.; Beysens, D. A. Experiments and simulation of the growth of droplets on a surface (breath figures). *Physical Review A* **1991,** *43* (6), 2858.

(74) Steyer, A.; Guenoun, P.; Beysens, D.; Knobler, C. M. Growth of droplets on a substrate by diffusion and coalescence. *Physical Review A* **1991,** *44* (12), 8271.

(75) Beysens, D. The formation of dew. *Atmospheric Research* **1995,** *39*, 215.

(76) Briscoe, B. J.; Galvin, K. P. Breath Figures. *Journal of Physics D: Applied Physics* **1990,** *23*, 1265.

(77) Briscoe, B. J.; Galvin, K. P. The evolution of a 2D constrained growth system of droplets-breath figures. *Journal of Physics D: Applied Physics* **1990**.

(78) Briscoe, B. J.; Galvin, K. P. An experimental study of the growth of breath figures. *Colloids and Surfaces* **1991,** *56*, 263.

(79) Briscoe, B. J.; Galvin, K. P. Growth with coalescence during condensation. *Physical Review A* **1991,** *43* (4), 1906.

(80) Family, F.; Meakin, P. Scaling of the droplet-size distribution in vapor-deposited thin films. *Phys Rev Lett* **1988,** *61* (4), 428.

(81) Family, F.; Meakin, P. Kinetics of droplet growth processes: Simulations, theory, and experiments. *Physical Review A* **1989,** *40* (7), 3836.

(82) Gupta, N. D.; Ghosh, S. A report on the wilson cloud chamber and its applications in physics. *Reviews of Modern Physics* **1946,** *18* (2), 225.

(83) Nepomnyashchy, A. A.; Golovin, A. A.; Tikhomirova, A. E.; Volpert, V. A. Nucleation and growth of droplets at a liquid-gas interface. *Phys Rev E* **2006,** *74* (2).

(84) Sigsbee, R. In *Nucleation*; Dekker New York, 1969.

(85) Rose, J. W. Dropwise condensation theory and experiment: a review. *P I Mech Eng a-J Pow* **2002,** *216* (A2), 115.

(86) Leach, R. N.; Stevens, F.; Langford, S. C.; Dickinson, J. T. Dropwise condensation: Experiments and simulations of nucleation and growth of water drops in a cooling system. *Langmuir* **2006,** *22* (21), 8864.

(87) Torresin, D.; Tiwari, M. K.; Del Col, D.; Poulikakos, D. Flow Condensation on Copper-Based Nanotextured Superhydrophobic Surfaces. *Langmuir* **2013,** *29* (2), 840.

(88) Hou, Y. M.; Yu, M.; Chen, X. M.; Wang, Z. K.; Yao, S. H. Recurrent Filmwise and Dropwise Condensation on a Beetle Mimetic Surface. *Acs Nano* **2015,** *9* (1), 71.

(89) Zhao, H.; Beysens, D. From droplet growth to film growth on a heterogeneous surface: condensation associated with a wettability gradient. *Langmuir* **1995,** *11* (2), 627.

(90) Knobler, C.; Beysens, D. Growth of breath figures on fluid surfaces. *EPL (Europhysics Letters)* **1988,** *6* (8), 707.

(91) Steyer, A.; Guenoun, P.; Beysens, D. Hexatic and fat-fractal structures for water droplets condensing on oil. *Phys Rev E* **1993,** *48* (1), 428.

(92) Pitois, O.; Francois, B. Crystallization of condensation droplets on a liquid surface. *Colloid Polym Sci* **1999,** *277* (6), 574.

(93) Yang, H. R.; Zhu, H. J.; Hendrix, M. M. R. M.; Lousberg, N. J. H. G. M.; de With, G.; Esteves, A. C. C.; Xin, J. H. Temperature-Triggered Collection and Release of Water from Fogs by a Sponge-Like Cotton Fabric. *Advanced materials* **2013,** *25* (8), 1150.

(94) Howarter, J. A.; Youngblood, J. P. Self-cleaning and anti-fog surfaces via stimuli-responsive polymer brushes. *Advanced materials* **2007,** *19* (22), 3838.

(95) Faustini, M.; Nicole, L.; Boissiere, C.; Innocenzi, P.; Sanchez, C.; Grosso, D. Hydrophobic, Antireflective, Self-Cleaning, and Antifogging Sol-Gel Coatings: An Example of Multifunctional Nanostructured Materials for Photovoltaic Cells. *Chem Mater* **2010,** *22* (15), 4406.

(96) Chevallier, P.; Turgeon, S.; Sarra-Bournet, C.; Turcotte, R.; Laroche, G. Characterization of Multilayer Anti-Fog Coatings. *ACS applied materials & interfaces* **2011,** *3* (3), 750.

(97) Chen, Y.; Zhang, Y. B.; Shi, L.; Li, J.; Xin, Y.; Yang, T. T.; Guo, Z. G. Transparent superhydrophobic/superhydrophilic coatings for self-cleaning and anti-fogging. *Appl Phys Lett* **2012,** *101* (3).

(98) Brown, P. S.; Atkinson, O.; Badyal, J. P. S. Ultrafast Oleophobic-Hydrophilic Switching Surfaces for Antifogging, Self-Cleaning, and Oil Water Separation. *ACS applied materials & interfaces* **2014,** *6* (10), 7504.

(99) Ragesh, P.; Ganesh, V. A.; Naira, S. V.; Nair, A. S. A review on 'self-cleaning and multifunctional materials'. *J Mater Chem A* **2014,** *2* (36), 14773.

(100) Widawski, G.; Rawiso, M.; Francois, B. Self-Organized Honeycomb Morphology of Star-Polymer Polystyrene Films. *Nature* **1994,** *369* (6479), 387.

(101) Francois, B.; Pitois, O.; Francois, J. Polymer films with a self-organized honeycomb morphology. *Advanced materials* **1995,** *7* (12), 1041.

(102) Francois, B.; Ederle, Y.; Mathis, C. Honeycomb membranes made from C-

60(PS)(6). *Synthetic Met* **1999,** *103* (1-3), 2362.

(103) Pitois, O.; Francois, B. Formation of ordered micro-porous membranes. *Eur Phys J B* **1999,** *8* (2), 225.

(104) Maruyama, N.; Koito, T.; Nishida, J.; Sawadaishi, T.; Cieren, X.; Ijiro, K.; Karthaus, O.; Shimomura, M. Mesoscopic patterns of molecular aggregates on solid substrates. *Thin solid films* **1998,** *327*, 854.

(105) Shimomura, M.; Koito, T.; Maruyama, N.; Arai, K.; Nishida, J.; Grasjo, L.; Karthaus, O.; Ijiro, K. Photonic and Electronic Applications of Mesoscopic Polymer Assemblies. *Molecular Crystals and Liquid Crystals Science and Technology Section a-Molecular Crystals and Liquid Crystals* **1998,** *322*, 305.

(106) Srinivasarao, M.; Collings, D.; Philips, A.; Patel, S. Three-dimensionally ordered array of air bubbles in a polymer film. *Science* **2001,** *292* (5514), 79.

(107) Li, X. Y.; Zhao, Q. L.; Xu, T. T.; Huang, J.; Wei, L. H.; Ma, Z. Highly ordered microporous polystyrene-b-poly(acrylic acid) films: Study on the influencing factors in their fabrication via a static breath-figure method. *European Polymer Journal* **2014,** *50*, 135.

(108) Chiu, Y.-C.; Kuo, C.-C.; Lin, C.-J.; Chen, W.-C. Highly ordered luminescent microporous films prepared from crystalline conjugated rod-coil diblock copolymers of PF-b-PSA and their superhydrophobic characteristics. *Soft Matter* **2011,** *7* (19), 9350.

(109) Zhu, L.-W.; Wan, L.-S.; Jin, J.; Xu, Z.-K. Honeycomb Porous Films Prepared from Porphyrin-Cored Star Polymers: Submicrometer Pores Induced by Transition of Monolayer into Multilayer Structures. *The Journal of Physical Chemistry C* **2013,** *117* (12), 6185.

(110) Wu, B.-H.; Zhu, L.-W.; Ou, Y.; Tang, W.; Wan, L.-S.; Xu, Z.-K. Systematic investigation on the formation of honeycomb-patterned porous films from amphiphilic block copolymers. *The Journal of Physical Chemistry C* **2015,** *119* (4), 1971.

(111) Silberberg, M. S.; Duran, R.; Haas, C. G.; Norman, A. D. *Chemistry: The molecular nature of matter and change*; McGraw-Hill New York, 2006.

(112) de Boer, B.; Stalmach, U.; Nijland, H.; Hadziioannou, G. Microporous honeycomb-structured films of semiconducting block copolymers and their use as patterned templates. *Advanced materials* **2000,** *12* (21), 1581.

(113) Battenbo, H.; Cobley, R. J.; Wilks, S. P. A quantitative study of the formation of breath figure templated polymer materials. *Soft Matter* **2011,** *7* (22), 10864.

(114) Cai, Y.; Zhang Newby, B.-m. Marangoni flow-induced self-assembly of hexagonal and stripelike nanoparticle patterns. *J Am Chem Soc* **2008,** *130* (19), 6076.

(115) Cai, Y.; Zhang Newby, B.-m. Porous polymer films templated by Marangoni flow-induced water droplet arrays. *Langmuir* **2009,** *25* (13), 7638.

(116) Sharma, V.; Song, L.; Jones, R. L.; Barrow, M. S.; Williams, P. R.; Srinivasarao, M. Effect of solvent choice on breath-figure-templated assembly of? holey? polymer films. *EPL (Europhysics Letters)* **2010,** *91* (3), 38001.

(117) Kuo, C.-T.; Lin, Y.-S.; Liu, T.-K.; Liu, H.-C.; Hung, W.-C.; Jiang, I.-M.; Tsai, M.-S.; Hsu, C.-C.; Wu, C.-Y. Dynamics of single-layer polymer breath figures. *Opt Express* **2010,** *18* (17), 18464.

(118) Barrow, M.; Jones, R.; Park, J.; Srinivasarao, M.; Williams, P.; Wright, C. Physical characterisation of microporous and nanoporous polymer films by atomic force microscopy, scanning electron microscopy and high speed video microphotography. *Journal of Spectroscopy* **2004,** *18* (4), 577.

(119) Li, J.; Li, Y.; Chan, C. Y.; Kwok, R. T.; Li, H.; Zrazhevskiy, P.; Gao, X.; Sun, J. Z.; Qin, A.; Tang, B. Z. An Aggregation-Induced-Emission Platform for Direct Visualization of Interfacial Dynamic Self-Assembly. *Angewandte Chemie International Edition* **2014,** *53* (49), 13518.

(120) Schatz, M. F.; Neitzel, G. P. Experiments on thermocapillary instabilities. *Annual review of fluid mechanics* **2001,** *33* (1), 93.

(121) Dell'Aversana, P.; Tontodonato, V.; Carotenuto, L. Suppression of coalescence and of wetting: The shape of the interstitial film. *Physics of Fluids (1994-present)* **1997,** *9* (9), 2475.

(122) Dell'Aversana, P.; Banavar, J. R.; Koplik, J. Suppression of coalescence by shear and temperature gradients. *Physics of Fluids (1994-present)* **1996,** *8*

(1), 15.

(123) Huang, T.; Xu, Z.; Kang, Q.; Cai, T.; Zhang, P.; Shen, D. Investigation on kinetic processes of fabrication of honeycomb-patterned polystyrene film and adsorption of surfactant by quartz crystal microbalance in impedance analysis method. *Colloids and Surfaces A: Physicochemical and Engineering Aspects* **2014,** *453*, 21.

(124) Guillen, G. R.; Pan, Y.; Li, M.; Hoek, E. M. V. Preparation and Characterization of Membranes Formed by Nonsolvent Induced Phase Separation: A Review. *Industrial & Engineering Chemistry Research* **2011,** *50* (7), 3798.

(125) Colborne, R. Precipitation of polymer solutions. *J Polym Sci* **1955,** *18* (87), 55.

(126) Li, Z. G.; Ma, X. Y.; Zang, D. Y.; Shang, B. R.; Qiang, X.; Hong, Q.; Guan, X. H. Morphology and wettability control of honeycomb porous films of amphiphilic fluorinated pentablock copolymers via breath figure method. *Rsc Advances* **2014,** *4* (91), 49655.

(127) Dong, R.; Ma, H.; Yan, J.; Fang, Y.; Hao, J. Tunable Morphology of 2D Honeycomb-Patterned Films and the Hydrophobicity of a Ferrocenyl-Based Oligomer. *Chemistry–A European Journal* **2011,** *17* (27), 7674.

(128) Billon, L.; Manguian, M.; Pellerin, V.; Joubert, M.; Eterradossi, O.; Garay, H. Tailoring highly ordered honeycomb films based on ionomer macromolecules by the bottom-up approach. *Macromolecules* **2008,** *42* (1),

345.

(129) Ma, H.; Tian, Y.; Wang, X. In situ optical microscopy observation of the growth and rearrangement behavior of surface holes in the breath figure process. *Polymer* **2011,** *52* (2), 489.

(130) Wong, K. H.; Hernández-Guerrero, M.; Granville, A. M.; Davis, T. P.; Barner-Kowollik, C.; Stenzel, M. H. Water-assisted formation of honeycomb structured porous films. *Journal of Porous Materials* **2006,** *13* (3-4), 213.

(131) Li, L.; Zhong, Y. W.; Li, J.; Chen, C. K.; Zhang, A. J.; Xu, J.; Ma, Z. Thermally stable and solvent resistant honeycomb structured polystyrene films via photochemical cross-linking. *J Mater Chem* **2009,** *19* (39), 7222.

(132) Ding, J. Y.; Gong, J. L.; Bai, H.; Li, L.; Zhong, Y. W.; Ma, Z.; Svrcek, V. Constructing honeycomb micropatterns on nonplanar substrates with high glass transition temperature polymers. *J Colloid Interf Sci* **2012,** *380*, 99.

(133) Park, M. S.; Joo, W.; Kim, J. K. Porous structures of polymer films prepared by spin coating with mixed solvents under humid condition. *Langmuir* **2006,** *22* (10), 4594.

(134) Park, M. S.; Kim, J. K. Breath figure patterns prepared by spin coating in a dry environment. *Langmuir* **2004,** *20* (13), 5347.

(135) Munoz-Bonilla, A.; Ibarboure, E.; Papon, E.; Rodriguez-Hernandez, J. Self-organized hierarchical structures in polymer surfaces: self-assembled nanostructures within breath figures. *Langmuir* **2009,** *25* (11), 6493.

(136) Scriven, L. MRS proceedings, 1988; p 717.

(137) Mansouri, J.; Yapit, E.; Chen, V. Polysulfone filtration membranes with isoporous structures prepared by a combination of dip-coating and breath figure approach. *J Membrane Sci* **2013,** *444*, 237.

(138) Zhu, L. W.; Ou, Y.; Wan, L. S.; Xu, Z. K. Polystyrenes with hydrophilic end groups: synthesis, characterization, and effects on the self-assembly of breath figure arrays. *J Phys Chem B* **2014,** *118* (3), 845.

(139) Zhang, S. S.; Cui, K.; Huang, J.; Zhao, Q. L.; Cao, S. K.; Ma, Z. Synthesis of diverse alpha,omega-telechelic polystyrenes with di- and tri-functionality via tandem or one-pot strategies combining aminolysis of RAFT-polystyrene and a thiol-ene "click" reaction. *Rsc Advances* **2015,** *5* (55), 44571.

(140) Zhu, L.-W.; Wu, B.-H.; Wan, L.-S.; Xu, Z.-K. Polystyrene with hydrophobic end groups: synthesis, kinetics, interfacial activity, and self-assemblies templated by breath figures. *Polym Chem-Uk* **2014,** *5* (14), 4311.

(141) Zhu, L. W.; Ou, Y.; Wan, L. S.; Xu, Z. K. Polystyrenes with Hydrophilic End Groups: Synthesis, Characterization, and Effects on the Self-Assembly of Breath Figure Arrays. *Journal of Physical Chemistry B* **2014,** *118* (3), 845.

(142) Samuel, A. Z.; Umapathy, S.; Ramakrishnan, S. Functionalized and postfunctionalizable porous polymeric films through evaporation-induced

phase separation using mixed solvents. *ACS applied materials & interfaces* **2011,** *3* (9), 3293.

(143) Liu, C.-X.; Lang, W.-Z.; Shi, B.-B.; Guo, Y.-J. Fabrication of ordered honeycomb porous polyvinyl chloride (PVC) films by breath figures method. *Mater Lett* **2013,** *107*, 53.

(144) Brown, P.; Talbot, E.; Wood, T.; Bain, C.; Badyal, J. Superhydrophobic hierarchical honeycomb surfaces. *Langmuir* **2012,** *28* (38), 13712.

(145) Shojaei-Zadeh, S.; Swanson, S. R.; Anna, S. L. Highly uniform micro-cavity arrays in flexible elastomer film. *Soft Matter* **2009,** *5* (4), 743.

(146) Lu, Y.; Ren, Y.; Wang, L.; Wang, X.; Li, C. Template synthesis of conducting polyaniline composites based on honeycomb ordered polycarbonate film. *Polymer* **2009,** *50* (9), 2035.

(147) Tian, Y.; Liu, S.; Ding, H.; Wang, L.; Liu, B.; Shi, Y. Formation of Honeycomb-Patterned Polyetherketone Cardo (PEK-C) Films in a Highly Humid Atmosphere. *Macromol Chem Phys* **2006,** *207* (21), 1998.

(148) Tian, Y.; Liu, S.; Ding, H.; Wang, L.; Liu, B.; Shi, Y. Formation of deformed honeycomb-patterned films from fluorinated polyimide. *Polymer* **2007,** *48* (8), 2338.

(149) Cong, H.; Wang, J.; Yu, B.; Tang, J. Preparation of a highly permeable ordered porous microfiltration membrane of brominated poly (phenylene oxide) on an ice substrate by the breath figure method. *Soft Matter* **2012,** *8* (34), 8835.

(150) Liu, Y.; Ma, H.; Tian, Y.; Xie, F.; Wang, X. Fabrication of Durable Honeycomb-Patterned Films of Poly (ether sulfone) s via Breath Figures. *Macromol Chem Phys* **2014,** *215* (15), 1446.

(151) Govor, L.; Bashmakov, I.; Kiebooms, R.; Dyakonov, V.; Parisi, J. Self-Organized Networks Based on Conjugated Polymers. *Advanced materials* **2001,** *13* (8), 588.

(152) Hill, J. P.; Lee, M. V.; Yu, X.-Y.; Okamoto, K.; Linford, M. R.; Ariga, K. Macroporous poly (aromatic amine): Synthesis and film fabrication. *Colloids and Surfaces A: Physicochemical and Engineering Aspects* **2010,** *354* (1), 156.

(153) Yu, C.; Zhai, J.; Gao, X.; Wan, M.; Jiang, L.; Li, T.; Li, Z. Water-assisted fabrication of polyaniline honeycomb structure film. *The Journal of Physical Chemistry B* **2004,** *108* (15), 4586.

(154) Yabu, H.; Akagi, K.; Shimomura, M. Micropatterning of liquid crystalline polyacetylene derivative by using self-organization processes. *Synthetic Met* **2009,** *159* (9), 762.

(155) Honarbakhsh, S.; Pourdeyhimi, B. Scaffolds for drug delivery, part I: electrospun porous poly (lactic acid) and poly (lactic acid)/poly (ethylene oxide) hybrid scaffolds. *Journal of materials science* **2011,** *46* (9), 2874.

(156) Wang, Z.; Zhao, C.; Pan, Z. Porous bead-on-string poly (lactic acid) fibrous membranes for air filtration. *J Colloid Interf Sci* **2015,** *441*, 121.

(157) Wu, X.; Wang, S. Regulating MC3T3-E1 cells on deformable poly (ε-

caprolactone) honeycomb films prepared using a surfactant-free breath figure method in a water-miscible solvent. *ACS applied materials & interfaces* **2012,** *4* (9), 4966.

(158) Huh, M.; Jung, M. H.; Park, Y. S.; Kang, T. B.; Nah, C.; Russell, R. A.; Holden, P. J.; Yun, S. I. Fabrication of honeycomb-structured porous films from poly (3-hydroxybutyrate) and poly (3-hydroxybutyrate-co-3-hydroxyvalerate) via the breath figures method. *Polymer Engineering & Science* **2012,** *52* (4), 920.

(159) Kim, W. J.; Basavaraja, C.; Thinh, P. Structural characterization and DC conductivity of honeycomb-patterned poly (ε-caprolactone)/gold nanoparticle-reduced graphite oxide composite films. *Mater Lett* **2013,** *90*, 14.

(160) Gurr, P. A.; Zhang, Z.; Hao, X. J.; Hughes, T. C.; Qiao, G. G. Highly Ordered Honeycomb Film Formation of Linear Polymers by the Breath Figure Technique. *Australian Journal of Chemistry* **2016,** *69* (10), 1130.

(161) Zhu, L. W.; Wu, B. H.; Wan, L. S.; Xu, Z. K. Polystyrene with hydrophobic end groups: synthesis, kinetics, interfacial activity, and self-assemblies templated by breath figures. *Polym Chem-Uk* **2014,** *5* (14), 4311.

(162) De Leon, A. S.; Malhotra, S.; Molina, M.; Haag, R.; Calderon, M.; Rodriguez-Hernandez, J.; Munoz-Bonilla, A. Dendritic amphiphiles as additives for honeycomb-like patterned surfaces by breath figures: Role of the molecular characteristics on the pore morphology. *Journal of Colloid*

and Interface Science **2015,** *440*, 263.

(163) Fukuhira, Y.; Yabu, H.; Ijiro, K.; Shimomura, M. Interfacial tension governs the formation of self-organized honeycomb-patterned polymer films. *Soft Matter* **2009,** *5* (10), 2037.

(164) Zhao, B.; Li, C.; Lu, Y.; Wang, X.; Liu, Z.; Zhang, J. Formation of ordered macroporous membranes from random copolymers by the breath figure method. *Polymer* **2005,** *46* (22), 9508.

(165) Honglawan, A.; Yang, S. Evaporative assembly of ordered microporous films and their hierarchical structures from amphiphilic random copolymers. *Soft Matter* **2012,** *8* (47), 11897.

(166) Zhang, Z.; Hao, X. J.; Gurr, P. A.; Blencowe, A.; Hughes, T. C.; Qiao, G. G. Honeycomb Films from Perfluoropolyether-Based Star and Micelle Architectures. *Australian Journal of Chemistry* **2012,** *65* (8), 1186.

(167) Qin, S.; Li, H.; Yuan, W. Z.; Zhang, Y. M. Fabrication of polymeric honeycomb microporous films: breath figures strategy and stabilization of water droplets by fluorinated diblock copolymer micelles. *Journal of Materials Science* **2012,** *47* (19), 6862.

(168) Li, L.; Li, J.; Zhong, Y.; Chen, C.; Ben, Y.; Gong, J.; Ma, Z. Formation of ceramic microstructures: honeycomb patterned polymer films as structure-directing agent. *J Mater Chem* **2010,** *20* (26), 5446.

(169) Li, J.; Zhao, Q.-L.; Chen, J.-Z.; Li, L.; Huang, J.; Ma, Z.; Zhong, Y.-W. Highly ordered microporous films containing a polyolefin segment

fabricated by the breath-figure method using well-defined polymethylene-b-polystyrene copolymers. *Polym Chem-Uk* **2010,** *1* (2), 164.

(170) Takekoh, R.; Russell, T. P. Multi-Length Scale Porous Polymers. *Advanced Functional Materials* **2014,** *24* (10), 1483.

(171) Ghannam, L.; Manguian, M.; François, J.; Billon, L. A versatile route to functional biomimetic coatings: ionomers for honeycomb-like structures. *Soft Matter* **2007,** *3* (12), 1492.

(172) Zhang, C.; Wang, X.; Min, K.; Lee, D.; Wei, C.; Schulhauser, H.; Gao, H. Developing porous honeycomb films using miktoarm star copolymers and exploring their application in particle separation. *Macromolecular rapid communications* **2014,** *35* (2), 221.

(173) Wang, C.; Mao, Y.; Wang, D.; Qu, Q.; Yang, G.; Hu, X. Fabrication of highly ordered microporous thin films by PS-b-PAA self-assembly and investigation of their tunable surface properties. *J Mater Chem* **2008,** *18* (6), 683.

(174) Escalé, P.; Rubatat, L.; Derail, C.; Save, M.; Billon, L. pH Sensitive Hierarchically Self-Organized Bioinspired Films. *Macromolecular rapid communications* **2011,** *32* (14), 1072.

(175) Ou, Y.; Zhu, L.-W.; Xiao, W.-D.; Yang, H.-C.; Jiang, Q.-J.; Li, X.; Lu, J.-G.; Wan, L.-S.; Xu, Z.-K. Nonlithographic fabrication of nanostructured micropatterns via breath figures and solution growth. *The Journal of Physical Chemistry C* **2014,** *118* (8), 4403.

(176) Ke, B.-B.; Wan, L.-S.; Xu, Z.-K. Controllable construction of carbohydrate microarrays by site-directed grafting on self-organized porous films. *Langmuir* **2010,** *26* (11), 8946.

(177) Kim, J.; Lew, B.; Kim, W. S. Facile fabrication of super-hydrophobic nano-needle arrays via breath figures method. *Nanoscale research letters* **2011,** *6* (1), 1.

(178) Wong, K. H.; Davis, T. P.; Barner-Kowollik, C.; Stenzel, M. H. Honeycomb structured porous films from amphiphilic block copolymers prepared via RAFT polymerization. *Polymer* **2007,** *48* (17), 4950.

(179) Park, J. S.; Lee, S. H.; Han, T. H.; Kim, S. O. Hierarchically ordered polymer films by templated organization of aqueous droplets. *Advanced Functional Materials* **2007,** *17* (14), 2315.

(180) Wang, L.-P.; Li, Y.-C.; Chen, L.-F.; Ban, C.-L.; Li, G.; Ni, J.-J. Fabrication of honeycomb-patterned porous films from PS-b-PNIPAM amphiphilic diblock copolymers synthesized via RITP. *J Colloid Interf Sci* **2014,** *420*, 112.

(181) Cheng, C.; Tian, Y.; Shi, Y.; Tang, R.; Xi, F. Ordered Honeycomb-Structured Films from Dendronized PMA-b-PEO Rod-Coil Block Copolymers. *Macromolecular rapid communications* **2005,** *26* (15), 1266.

(182) Zou, J.; Chen, H.; Chunder, A.; Yu, Y.; Huo, Q.; Zhai, L. Preparation of a Superhydrophobic and Conductive Nanocomposite Coating from a Carbon-Nanotube-Conjugated Block Copolymer Dispersion. *Advanced*

materials **2008,** *20* (17), 3337.

(183) Bolognesi, A.; Galeotti, F.; Giovanella, U.; Bertini, F.; Yunus, S. Nanophase separation in polystyrene-polyfluorene block copolymers thin films prepared through the breath figure procedure. *Langmuir* **2009,** *25* (9), 5333.

(184) Valtola, L.; Karesoja, M.; Tenhu, H.; Ihalainen, P.; Sarfraz, J.; Peltonen, J.; Malinen, M.; Urtti, A.; Hietala, S. Breath figure templated semifluorinated block copolymers with tunable surface properties and binding capabilities. *J Appl Polym Sci* **2015,** *132* (1).

(185) Pilati, F.; Montecchi, M.; Fabbri, P.; Synytska, A.; Messori, M.; Toselli, M.; Grundke, K.; Pospiech, D. Design of surface properties of PET films: Effect of fluorinated block copolymers. *J Colloid Interf Sci* **2007,** *315* (1), 210.

(186) Gong, J.; Xu, B.; Tao, X.; Li, L. Honeycomb Microstructured Silicon Oxycarbide Sheets from Silicon-Containing Graft Copolymer Films. *Plasma Process Polym* **2014,** *11* (11), 1001.

(187) Stenzel, M. H.; Davis, T. P.; Fane, A. G. Honeycomb structured porous films prepared from carbohydrate based polymers synthesized via the RAFT process. *J Mater Chem* **2003,** *13* (9), 2090.

(188) Zhang, Z.; Hughes, T. C.; Gurr, P. A.; Blencowe, A.; Hao, X.; Qiao, G. G. Influence of polymer elasticity on the formation of non-cracking honeycomb films. *Advanced materials* **2012,** *24* (31), 4327.

(189) Connal, L. A.; Vestberg, R.; Hawker, C. J.; Qiao, G. G. Fabrication of Reversibly Crosslinkable, 3-Dimensionally Conformal Polymeric Microstructures. *Advanced Functional Materials* **2008,** *18* (20), 3315.

(190) Connal, L. A.; Qiao, G. G. Honeycomb coated particles: porous doughnuts, golf balls and hollow porous pockets. *Soft Matter* **2007,** *3* (7), 837.

(191) Connal, L. A.; Qiao, G. G. Preparation of Porous Poly(dimethylsiloxane)-Based Honeycomb Materials with Hierarchal Surface Features and Their Use as Soft-Lithography Templates. *Advanced materials* **2006,** *18* (22), 3024.

(192) Hernández-Guerrero, M.; Davis, T. P.; Barner-Kowollik, C.; Stenzel, M. H. Polystyrene comb polymers built on cellulose or poly (styrene-co-2-hydroxyethylmethacrylate) backbones as substrates for the preparation of structured honeycomb films. *European Polymer Journal* **2005,** *41* (10), 2264.

(193) Hu, R.; Lam, J. W.; Li, M.; Deng, H.; Li, J.; Tang, B. Z. Homopolycyclotrimerization of A4-type tetrayne: A new approach for the creation of a soluble hyperbranched poly (tetraphenylethene) with multifunctionalities. *Journal of Polymer Science Part A: Polymer Chemistry* **2013,** *51* (22), 4752.

(194) Dong, W.; Zhou, Y.; Yan, D.; Mai, Y.; He, L.; Jin, C. Honeycomb-structured microporous films made from hyperbranched polymers by the breath figure method. *Langmuir* **2008,** *25* (1), 173.

(195) Liu, C.; Gao, C.; Yan, D. Honeycomb-Patterned Photoluminescent Films Fabricated by Self-Assembly of Hyperbranched Polymers. *Angewandte Chemie International Edition* **2007,** *46* (22), 4128.

(196) Hernandez-Guerrero, M.; Stenzel, M. H. Honeycomb structured polymer films via breath figures. *Polym Chem-Uk* **2012,** *3* (3), 563.

(197) Min, E. H.; Ting, S. R. S.; Billon, L.; Stenzel, M. H. Thermo-Responsive Glycopolymer Chains Grafted onto Honeycomb Structured Porous Films via RAFT Polymerization as a Thermo-Dependent Switcher for Lectin Concanavalin A Conjugation. *J Polym Sci Pol Chem* **2010,** *48* (15), 3440.

(198) Hernandez-Guerrero, M.; Min, E.; Barner-Kowollik, C.; Muller, A. H. E.; Stenzel, M. H. Grafting thermoresponsive polymers onto honeycomb structured porous films using the RAFT process. *J Mater Chem* **2008,** *18* (39), 4718.

(199) Stenzel, M. H.; Barner-Kowollik, C.; Davis, T. P. Formation of honeycomb-structured, porous films via breath figures with different polymer architectures. *J Polym Sci Pol Chem* **2006,** *44* (8), 2363.

(200) Hernandez-Guerrero, M.; Davis, T. P.; Barner-Kowollik, C.; Stenzel, M. H. Polystyrene comb polymers built on cellulose or poly(styrene-co-2-hydroxyethylmethacrylate) backbones as substrates for the preparation of structured honeycomb films. *European Polymer Journal* **2005,** *41* (10), 2264.

(201) Stenzel-Rosenbaum, M. H.; Davis, T. P.; Fane, A. G.; Chen, V. Porous

Polymer Films and Honeycomb Structures Made by the Self-Organization of Well-Defined Macromolecular Structures Created by Living Radical Polymerization Techniques. *Angewandte Chemie International Edition* **2001,** *40* (18), 3428.

(202) Yin, S.; Goldovsky, Y.; Herzberg, M.; Liu, L.; Sun, H.; Zhang, Y.; Meng, F.; Cao, X.; Sun, D. D.; Chen, H. Functional Free-Standing Graphene Honeycomb Films. *Advanced Functional Materials* **2013,** *23* (23), 2972.

(203) Ma, H. M.; Gao, P. C.; Fan, D. W.; Du, B.; Hao, J. C.; Wei, Q. Assembly of graphene nanocomposites into honeycomb-structured macroporous films with enhanced hydrophobicity. *New Journal of Chemistry* **2013,** *37* (5), 1307.

(204) Bai, S.; Shen, X.; Zhu, G.; Xu, Z.; Liu, Y. Reversible phase transfer of graphene oxide and its use in the synthesis of graphene-based hybrid materials. *Carbon* **2011,** *49* (13), 4563.

(205) Lee, S. H.; Kim, H. W.; Hwang, J. O.; Lee, W. J.; Kwon, J.; Bielawski, C. W.; Ruoff, R. S.; Kim, S. O. Three-dimensional self-assembly of graphene oxide platelets into mechanically flexible macroporous carbon films. *Angew Chem Int Ed Engl* **2010,** *49* (52), 10084.

(206) Takamori, H.; Fujigaya, T.; Yamaguchi, Y.; Nakashima, N. Simple Preparation of Self-Organized Single-Walled Carbon Nanotubes with Honeycomb Structures. *Advanced materials* **2007,** *19* (18), 2535.

(207) Saito, Y.; Shimomura, M.; Yabu, H. Breath Figures of Nanoscale Bricks: A

Universal Method for Creating Hierarchic Porous Materials from Inorganic Nanoparticles Stabilized with Mussel-Inspired Copolymers. *Macromolecular rapid communications* **2014,** *35* (20), 1763.

(208) Zhang, L.; Si, H.-Y.; Zhang, H.-L. Highly ordered fluorescent rings by “breath figures” on patterned substrates using polymer-free CdSe quantum dots. *J Mater Chem* **2008,** *18* (23), 2660.

(209) Wong, K. H.; Davis, T. P.; Barner-Kowollik, C.; Stenzel, M. H. Gold-loaded organic/inorganic nanocomposite honeycomb membranes. *Australian journal of chemistry* **2006,** *59* (8), 539.

(210) Wan, L.-S.; Li, Q.-L.; Chen, P.-C.; Xu, Z.-K. Patterned biocatalytic films via one-step self-assembly. *Chem Commun* **2012,** *48* (37), 4417.

(211) Nair, B. P.; Pavithran, C. Micropatterned Surfaces through Moisture-Induced Phase-Separation of Polystyrene− Clay Nanocomposite Particles. *Langmuir* **2010,** *26* (15), 12948.

(212) Ma, H.; Hao, J. Evaporation-Induced Ordered Honeycomb Structures of Gold Nanoparticles at the Air/Water Interface. *Chemistry–A European Journal* **2010,** *16* (2), 655.

(213) Ma, H.; Fan, D.; Li, G.; Xia, X.; Guo, H.; Du, B.; Wei, Q. Honeycomb-structured porous films prepared from polymer nanocomposites of gold nanorods. *Journal of Inorganic and Organometallic Polymers and Materials* **2013,** *23* (3), 587.

(214) Gómez-Segura, J.; Kazakova, O.; Davies, J.; Josephs-Franks, P.; Veciana,

J.; Ruiz-Molina, D. Self-organization of Mn 12 single-molecule magnets into ring structures induced by breath-figures as templates. *Chem Commun* **2005,** (45), 5615.

(215) Cai, X.; Cheng, K.; Oey, C.; Djurišić, A.; Chan, W.; Xie, M.; Chui, P. Porous metallic films fabricated by self-assembly of gold nanoparticles. *Thin Solid Films* **2005,** *491* (1), 66.

(216) Wang, L.; Maruf, S. H.; Maniglio, D.; Ding, Y. Fabrication and characterizations of crosslinked porous polymer films with varying chemical compositions. *Polymer* **2012,** *53* (17), 3749.

(217) Li, X.; Wang, Y.; Zhang, L.; Tan, S.; Yu, X.; Zhao, N.; Chen, G.; Xu, J. Fabrication of honeycomb-patterned polyalkylcyanoacrylate films from monomer solution by breath figures method. *J Colloid Interf Sci* **2010,** *350* (1), 253.

(218) Karthaus, O.; Cieren, X.; Maruyama, N.; Shimomura, M. Mesoscopic 2-D ordering of inorganic/organic hybrid materials. *Materials Science and Engineering: C* **1999,** *10* (1), 103.

(219) Chen, J.; Yan, X.; Zhao, Q.; Li, L.; Huang, F. Adjustable supramolecular polymer microstructures fabricated by the breath figure method. *Polym. Chem.* **2012,** *3* (2), 458.

(220) Heng, L.; Qin, W.; Chen, S.; Hu, R.; Li, J.; Zhao, N.; Wang, S.; Tang, B. Z.; Jiang, L. Fabrication of small organic luminogens honeycomb-structured films with aggregation-induced emission features. *J Mater*

Chem **2012,** *22* (31), 15869.

(221) Daly, R.; Sader, J. E.; Boland, J. J. The dominant role of the solvent–water interface in water droplet templating of polymers. *Soft Matter* **2013,** *9* (33), 7960.

(222) Cheng, C. X.; Tian, Y.; Shi, Y. Q.; Tang, R. P.; Xi, F. Porous polymer films and honeycomb structures based on amphiphilic dendronized block copolymers. *Langmuir* **2005,** *21* (14), 6576.

(223) Wang, L.; Tian, Y.; Ding, H.; Liu, B. Formation of ordered macroporous films from fluorinated polyimide by water droplets templating. *European polymer journal* **2007,** *43* (3), 862.

(224) Wang, Y.; Liu, Y.; Li, G.; Hao, J. Porphyrin-based honeycomb films and their antibacterial activity. *Langmuir* **2014,** *30* (22), 6419.

(225) Xiong, X.; Lin, M.; Zou, W.; Liu, X. Kinetic control of preparing honeycomb patterned porous film by the method of breath figure. *Reactive and Functional Polymers* **2011,** *71* (9), 964.

(226) Thong, A. Z.; Lim, D. S. W.; Ahsan, A.; Goh, G. T. W.; Xu, J.; Chin, J. M. Non-close-packed pore arrays through one-step breath figure self-assembly and reversal. *Chem Sci* **2014,** *5* (4), 1375.

(227) Li, J.; Peng, J.; Huang, W.; Wu, Y.; Fu, J.; Cong, Y.; Xue, L.; Han, Y. Ordered honeycomb-structured gold nanoparticle films with changeable pore morphology: from circle to ellipse. *Langmuir* **2005,** *21* (5), 2017.

(228) Yabu, H.; Jia, R.; Matsuo, Y.; Ijiro, K.; Yamamoto, S.; Nishino, F.; Takaki,

T.; Kuwahara, M.; Shimomura, M. Preparation of Highly Oriented Nano-Pit Arrays by Thermal Shrinking of Honeycomb-Patterned Polymer Films. *Advanced materials* **2008,** *20* (21), 4200.

(229) Wang, W.; Du, C.; Wang, X. F.; He, X. H.; Lin, J. P.; Li, L.; Lin, S. L. Directional Photomanipulation of Breath Figure Arrays. *Angew Chem Int Edit* **2014,** *53* (45), 12116.

(230) Ding, J. Y.; Zhang, A. J.; Bai, H.; Li, L.; Li, J.; Ma, Z. Breath figure in non-aqueous vapor. *Soft Matter* **2013,** *9* (2), 506.

(231) Xiong, X.; Zou, W.; Yu, Z.; Duan, J.; Liu, X.; Fan, S.; Zhou, H. Microsphere Pattern Prepared by a "Reverse" Breath Figure Method. *Macromolecules* **2009,** *42* (23), 9351.

(232) Zhang, S. S.; Cao, S. K.; Wang, S.; Zhao, Q. L.; Chen, J. Z.; Cui, K.; Ma, Z. Synthesis of well-defined alpha-fluorinated alkyl ester, omega-carboxyltelechelic polystyrenes and fabrication of their hydrophobic highly ordered porous films and microspheres. *Rsc Advances* **2015,** *5* (111), 91140.

(233) Gao, J. P.; Wu, W.; Rong, L.; Mao, G. L.; Ning, Y. N.; Zhao, Q. L.; Huang, J.; Ma, Z. Well-defined monocarboxyl-terminated polystyrene with low molecular weight: A candidate for the fabrication of highly ordered microporous films and microspheres via eae static breath-figure process. *European Polymer Journal* **2014,** *59*, 171.

(234) Zhang, A. J.; Du, C.; Bai, H.; Wang, Y. G.; Wang, J. W.; Li, L. Formation

of Breath Figure Arrays in Methanol Vapor Assisted by Surface Active Agents. *ACS applied materials & interfaces* **2014,** *6* (11), 8921.

(235) Ferrari, E.; Fabbri, P.; Pilati, F. Solvent and substrate contributions to the formation of breath figure patterns in polystyrene films. *Langmuir* **2011,** *27* (5), 1874.

(236) Liu, W. Y.; Chen, Y.; Liu, Y. J.; Hao, X. H. Advanced Materials Research, 2012; p 138.

(237) Hanafiah, N. B. M.; Vetrichelvan, M.; Valiyaveettil, S. Morphological investigations of self-assembled films from a pyridine-incorporated poly (p-phenylene). *Journal of Porous Materials* **2006,** *13* (3-4), 315.

(238) Chang, C.-C.; Juang, T.-Y.; Ting, W.-H.; Lin, M.-S.; Yeh, C.-M.; Dai, S. A.; Suen, S.-Y.; Liu, Y.-L.; Jeng, R.-J. Using a breath-figure method to self-organize honeycomb-like polymeric films from dendritic side-chain polymers. *Mater Chem Phys* **2011,** *128* (1), 157.

(239) Thong, A. Z.; Lim, D. S. W.; Ahsan, A.; Goh, G. T. W.; Xu, J. W.; Chin, J. M. Non-close-packed pore arrays through one-step breath figure self-assembly and reversal. *Chem Sci* **2014,** *5* (4), 1375.

(240) Nishikawa, T.; Ookura, R.; Nishida, J.; Arai, K.; Hayashi, J.; Kurono, N.; Sawadaishi, T.; Hara, M.; Shimomura, M. Fabrication of honeycomb film of an amphiphilic copolymer at the air-water interface. *Langmuir* **2002,** *18* (15), 5734.

(241) Govor, L. V.; Parisi, J. Hopping charge transport in honeycomb carbon

network structures. *Z Naturforsch A* **2002,** *57* (9-10), 757.

(242) Li, Z. G.; Ma, X. Y.; Zang, D. Y.; Hong, Q.; Guan, X. H. Honeycomb porous films of pentablock copolymer on liquid substrates via breath figure method and their hydrophobic properties with static and dynamic behaviour. *Rsc Advances* **2015,** *5* (27), 21084.

(243) Wan, L. S.; Li, J. W.; Ke, B. B.; Xu, Z. K. Ordered microporous membranes templated by breath figures for size-selective separation. *J Am Chem Soc* **2012,** *134* (1), 95.

(244) Ma, H. M.; Cui, J. W.; Song, A. X.; Hao, J. C. Fabrication of freestanding honeycomb films with through-pore structures via air/water interfacial self-assembly. *Chem Commun* **2011,** *47* (4), 1154.

(245) Du, C.; Zhang, A. J.; Bai, H.; Li, L. Robust Microsieves with Excellent Solvent Resistance: Cross-Linkage of Perforated Polymer Films with Honeycomb Structure. *Acs Macro Lett* **2013,** *2* (1), 27.

(246) Connal, L. A.; Vestberg, R.; Gurr, P. A.; Hawker, C. J.; Qiao, G. G. Patterning on nonplanar substrates: flexible honeycomb films from a range of self-assembling star copolymers. *Langmuir* **2008,** *24* (2), 556.

(247) Li, L.; Zhong, Y. W.; Gong, J. L.; Li, J. A.; Chen, C. K.; Zeng, B. R.; Ma, Z. Constructing robust 3-dimensionally conformal micropatterns: vulcanization of honeycomb structured polymeric films. *Soft Matter* **2011,** *7* (2), 546.

(248) Chen, D. W.; Liang, F. B.; Feng, D. X.; Xian, M.; Zhang, H. B.; Liu, H. Z.;

Du, F. L. An efficient route from reproducible glucose to 5-hydroxymethylfurfural catalyzed by porous coordination polymer heterogeneous catalysts. *Chemical Engineering Journal* **2016,** *300*, 177.

(249) Arulraj, A. D.; Arunkumar, A.; Vijayan, M.; Viswanath, K. B.; Vasantha, V. S. A simple route to Develop Highly porous Nano Polypyrrole/Reduced Graphene Oxide Composite film for Selective Determination of Dopamine. *Electrochim Acta* **2016,** *206*, 77.

(250) Lin, R. B.; Liu, S. Y.; Ye, J. W.; Li, X. Y.; Zhang, J. P. Photoluminescent Metal-Organic Frameworks for Gas Sensing. *Advanced Science* **2016,** *3* (7).

(251) Liu, C.; Kim, J. S.; Kwon, Y. Comparative Investigation on Thermal Insulation of Polyurethane Composites Filled with Silica Aerogel and Hollow Silica Microsphere. *J Nanosci Nanotechno* **2016,** *16* (2), 1703.

(252) Li, W. J.; Liu, J.; Sun, Z. H.; Liu, T. F.; Lu, J.; Gao, S. Y.; He, C.; Cao, R.; Luo, J. H. Integration of metal-organic frameworks into an electrochemical dielectric thin film for electronic applications. *Nature communications* **2016,** *7*.

(253) Armstrong, E.; O'Dwyer, C. Artificial opal photonic crystals and inverse opal structures - fundamentals and applications from optics to energy storage. *J Mater Chem C* **2015,** *3* (24), 6109.

(254) Feoktistova, N.; Rose, J.; Prokopovic, V. Z.; Vikulina, A. S.; Skirtach, A.; Volodkin, D. Controlling the Vaterite CaCO3 Crystal Pores. Design of Tailor-Made Polymer Based Microcapsules by Hard Templating. *Langmuir*

2016, *32* (17), 4229.

(255) Taylor, R. G. D.; Bezzu, C. G.; Carta, M.; Msayib, K. J.; Walker, J.; Short, R.; Kariuki, B. M.; McKeown, N. B. The Synthesis of Organic Molecules of Intrinsic Microporosity Designed to Frustrate Efficient Molecular Packing. *Chemistry-a European Journal* **2016,** *22* (7), 2466.

(256) Yanagishita, T.; Hidaka, T.; Suzuki, M.; Masuda, H. Polymer lenses with antireflection structures prepared using anodic porous alumina molds. *Journal of Vacuum Science & Technology B* **2016,** *34* (2).

(257) Li, H.; Zhao, X. Y.; Wu, P. F.; Zhang, S. X.; Geng, B. Facile preparation of superhydrophobic and superoleophilic porous polymer membranes for oil/water separation from a polyarylester polydimethylsiloxane block copolymer. *Journal of Materials Science* **2016,** *51* (6), 3211.

(258) Lv, Y. Q.; Cao, Y.; Svec, F.; Tan, T. W. Porous polymer-based monolithic layers enabling pH triggered switching between superhydrophobic and superhydrophilic properties. *Chem Commun* **2014,** *50* (89), 13809.

(259) Xu, B.; Ding, Y. Y.; Qu, S. B.; Cai, Z. S. Superamphiphobic cotton fabrics with enhanced stability. *Appl Surf Sci* **2015,** *356*, 951.

(260) Pandey, P.; Chauhan, R. S. Membranes for gas separation. *Progress in Polymer Science* **2001,** *26* (6), 853.

(261) Tokarev, I.; Minko, S. Stimuli-Responsive Porous Hydrogels at Interfaces for Molecular Filtration, Separation, Controlled Release, and Gating in Capsules and Membranes. *Advanced materials* **2010,** *22* (31), 3446.

(262) Liu, D. S.; Ashcraft, J. N.; Mannarino, M. M.; Silberstein, M. N.; Argun, A. A.; Rutledge, G. C.; Boyce, M. C.; Hammond, P. T. Spray Layer-by-Layer Electrospun Composite Proton Exchange Membranes. *Advanced Functional Materials* **2013,** *23* (24), 3087.

(263) Yabu, H.; Shimomura, M. Simple fabrication of micro lens arrays. *Langmuir* **2005,** *21* (5), 1709.

(264) Ling, X. Y.; Acikgoz, C.; Phang, I. Y.; Hempenius, M. A.; Reinhoudt, D. N.; Vancso, G. J.; Huskens, J. 3D ordered nanostructures fabricated by nanosphere lithography using an organometallic etch mask. *Nanoscale* **2010,** *2* (8), 1455.

(265) Hagedon, M.; Heikenfeld, J. A hybrid of microreplication and mask-less photolithography for creating dual porosity and textured surface membranes. *J Micromech Microeng* **2013,** *23* (11).

(266) Sun, T. Y.; Xu, Z. M.; Zhao, W. N.; Wu, X. H.; Liu, S. S.; Zhang, Z.; Wang, S. B.; Liu, W.; Liu, S. Y.; Peng, J. Fabrication of the similar porous alumina silicon template for soft UV nanoimprint lithography. *Appl Surf Sci* **2013,** *276*, 363.

(267) Sirbuly, D. J.; Lowman, G. M.; Scott, B.; Stucky, G. D.; Buratto, S. K. Patterned microstructures of porous silicon by dry-removal soft lithography. *Advanced materials* **2003,** *15* (2), 149.

(268) Connal, L. A.; Qiao, G. G. Preparation of porous poly(dimethylsiloxane)-based honeycomb materials with hierarchal surface features and their use

as soft-lithography templates. *Advanced materials* **2006,** *18* (22), 3024.

(269) Garg, T.; Singh, O.; Arora, S.; Murthy, R. S. R. Scaffold: A Novel Carrier for Cell and Drug Delivery. *Critical Reviews in Therapeutic Drug Carrier Systems* **2012,** *29* (1), 1.

(270) Wei, S.; Zhang, Y. L.; Ding, H.; Liu, J. Y.; Sun, J.; He, Y. Y.; Li, Z. Q.; Xiao, F. S. Solvothermal fabrication of adsorptive polymer monolith with large nanopores towards biomolecules immobilization. *Colloid Surface A* **2011,** *380* (1-3), 29.

(271) Liu, G. Q.; Zhu, C. L.; Xu, J.; Xin, Y.; Yang, T. T.; Li, J.; Shi, L.; Guo, Z. G.; Liu, W. M. Thermo-responsive hollow silica microgels with controlled drug release properties. *Colloids and Surfaces B-Biointerfaces* **2013,** *111*, 7.

(272) Li, X. C.; Jiang, G. L.; He, G. H.; Zheng, W. J.; Tan, Y.; Xiao, W. Preparation of porous PPy-TiO2 composites: Improved visible light photoactivity and the mechanism. *Chemical Engineering Journal* **2014,** *236*, 480.

(273) Foo, M. L.; Matsuda, R.; Kitagawa, S. Functional Hybrid Porous Coordination Polymers. *Chem Mater* **2014,** *26* (1), 310.

(274) Murray, L. J.; Dinca, M.; Long, J. R. Hydrogen storage in metal-organic frameworks. *Chem Soc Rev* **2009,** *38* (5), 1294.

(275) Liu, J.; Thallapally, P. K.; McGrail, B. P.; Brown, D. R.; Liu, J. Progress in adsorption-based CO2 capture by metal-organic frameworks. *Chem Soc*

Rev **2012,** *41* (6), 2308.

(276) Wu, Z. Y.; Liang, H. W.; Chen, L. F.; Hu, B. C.; Yu, S. H. Bacterial Cellulose: A Robust Platform for Design of Three Dimensional Carbon-Based Functional Nanomaterials. *Accounts Chem Res* **2016,** *49* (1), 96.

(277) Guo, J. X.; Zhang, H. J.; Geng, H. Y.; Mi, X. Q.; Ding, G. J.; Jiao, Z. Efficient one-pot synthesis of peapod-like hollow carbon nanomaterials for utrahigh drug loading capacity. *J Colloid Interf Sci* **2015,** *437*, 90.

(278) Narisawa, M. Silicone Resin Applications for Ceramic Precursors and Composites. *Materials* **2010,** *3* (6), 3518.

(279) Kumar, B. V. M.; Kim, Y. W. Processing of polysiloxane-derived porous ceramics: a review. *Science and Technology of Advanced Materials* **2010,** *11* (4).

(280) Kroke, E.; Li, Y. L.; Konetschny, C.; Lecomte, E.; Fasel, C.; Riedel, R. Silazane derived ceramics and related materials. *Materials Science & Engineering R-Reports* **2000,** *26* (4-6), 97.

(281) Liu, C.; Li, F.; Ma, L. P.; Cheng, H. M. Advanced Materials for Energy Storage. *Advanced materials* **2010,** *22* (8), E28.

(282) Arico, A. S.; Bruce, P.; Scrosati, B.; Tarascon, J. M.; Van Schalkwijk, W. Nanostructured materials for advanced energy conversion and storage devices. *Nature Materials* **2005,** *4* (5), 366.

(283) Wang, C. C.; Li, J. R.; Lv, X. L.; Zhang, Y. Q.; Guo, G. S. Photocatalytic organic pollutants degradation in metal-organic frameworks. *Energ*

Environ Sci **2014,** *7* (9), 2831.

(284) Li, S. L.; Xu, Q. Metal-organic frameworks as platforms for clean energy. *Energ Environ Sci* **2013,** *6* (6), 1656.

(285) Dutta, S.; Bhaumik, A.; Wu, K. C. W. Hierarchically porous carbon derived from polymers and biomass: effect of interconnected pores on energy applications. *Energ Environ Sci* **2014,** *7* (11), 3574.

(286) Zhai, Y. P.; Dou, Y. Q.; Zhao, D. Y.; Fulvio, P. F.; Mayes, R. T.; Dai, S. Carbon Materials for Chemical Capacitive Energy Storage. *Advanced materials* **2011,** *23* (42), 4828.

(287) Linic, S.; Christopher, P.; Ingram, D. B. Plasmonic-metal nanostructures for efficient conversion of solar to chemical energy. *Nature Materials* **2011,** *10* (12), 911.

(288) Roscow, J. I.; Taylor, J.; Bowen, C. R. Manufacture and characterization of porous ferroelectrics for piezoelectric energy harvesting applications. *Ferroelectrics* **2016,** *498* (1), 40.

(289) Ghosh, S. K.; Sinha, T. K.; Mahanty, B.; Mandal, D. Self-poled Efficient Flexible "Ferroelectretic" Nanogenerator: A New Class of Piezoelectric Energy Harvester. *Energy Technology* **2015,** *3* (12), 1190.

(290) Suyal, G.; Seifert, A.; Setter, N. Pyroelectric nanoporous films: Synthesis and properties. *Appl Phys Lett* **2002,** *81* (6), 1059.

(291) Navid, A.; Lynch, C. S.; Pilon, L. Purified and porous poly(vinylidene fluoride-trifluoroethylene) thin films for pyroelectric infrared sensing and

energy harvesting. *Smart Materials & Structures* **2010,** *19* (5).

(292) Lang, S. B.; Muensit, S. Review of some lesser-known applications of piezoelectric and pyroelectric polymers. *Applied Physics a-Materials Science & Processing* **2006,** *85* (2), 125.

(293) Snook, G. A.; Kao, P.; Best, A. S. Conducting-polymer-based supercapacitor devices and electrodes. *Journal of Power Sources* **2011,** *196* (1), 1.

(294) Krebs, F. C. Fabrication and processing of polymer solar cells: a review of printing and coating techniques. *Solar energy materials and solar cells* **2009,** *93* (4), 394.

(295) Cheng, Y.-J.; Yang, S.-H.; Hsu, C.-S. Synthesis of conjugated polymers for organic solar cell applications. *Chem Rev* **2009,** *109* (11), 5868.

(296) Fukada, E. History and recent progress in piezoelectric polymers. *IEEE Transactions on ultrasonics, ferroelectrics, and frequency control* **2000,** *47* (6), 1277.

(297) Fan, F.-R.; Tian, Z.-Q.; Lin Wang, Z. Flexible triboelectric generator. *Nano Energy* **2012,** *1* (2), 328.

(298) Wang, S. H.; Lin, L.; Wang, Z. L. Triboelectric nanogenerators as self-powered active sensors. *Nano Energy* **2015,** *11*, 436.

(299) Fan, F.-R.; Tian, Z.-Q.; Wang, Z. L. Flexible triboelectric generator. *Nano Energy* **2012,** *1* (2), 328.

(300) Zhu, G.; Lin, Z. H.; Jing, Q.; Bai, P.; Pan, C.; Yang, Y.; Zhou, Y.; Wang, Z.

L. Toward large-scale energy harvesting by a nanoparticle-enhanced triboelectric nanogenerator. *Nano letters* **2013,** *13* (2), 847.

(301) Lee, K. Y.; Chun, J.; Lee, J. H.; Kim, K. N.; Kang, N. R.; Kim, J. Y.; Kim, M. H.; Shin, K. S.; Gupta, M. K.; Baik, J. M.et al. Hydrophobic sponge structure-based triboelectric nanogenerator. *Advanced materials* **2014,** *26* (29), 5037.

(302) Fan, F. R.; Lin, L.; Zhu, G.; Wu, W.; Zhang, R.; Wang, Z. L. Transparent triboelectric nanogenerators and self-powered pressure sensors based on micropatterned plastic films. *Nano letters* **2012,** *12* (6), 3109.

(303) Jeong, C. K.; Baek, K. M.; Niu, S.; Nam, T. W.; Hur, Y. H.; Park, D. Y.; Hwang, G. T.; Byun, M.; Wang, Z. L.; Jung, Y. S.et al. Topographically-designed triboelectric nanogenerator via block copolymer self-assembly. *Nano letters* **2014,** *14* (12), 7031.

(304) Kim, D.; Jeon, S. B.; Kim, J. Y.; Seol, M. L.; Kim, S. O.; Choi, Y. K. High-performance nanopattern triboelectric generator by block copolymer lithography. *Nano Energy* **2015,** *12*, 331.

(305) Zhu, G.; Zhou, Y. S.; Bai, P.; Meng, X. S.; Jing, Q. S.; Chen, J.; Wang, Z. L. A Shape-Adaptive Thin-Film-Based Approach for 50% High-Efficiency Energy Generation Through Micro-Grating Sliding Electrification. *Advanced materials* **2014,** *26* (23), 3788.

(306) Tang, W.; Jiang, T.; Fan, F. R.; Yu, A. F.; Zhang, C.; Cao, X.; Wang, Z. L. Liquid-Metal Electrode for High-Performance Triboelectric

Nanogenerator at an Instantaneous Energy Conversion Efficiency of 70.6%. *Advanced Functional Materials* **2015,** *25* (24), 3718.

(307) Xie, Y. N.; Wang, S. H.; Niu, S. M.; Lin, L.; Jing, Q. S.; Yang, J.; Wu, Z. Y.; Wang, Z. L. Grating-Structured Freestanding Triboelectric-Layer Nanogenerator for Harvesting Mechanical Energy at 85% Total Conversion Efficiency. *Advanced materials* **2014,** *26* (38), 6599.

(308) Zhu, G.; Bai, P.; Chen, J.; Wang, Z. L. Power-generating shoe insole based on triboelectric nanogenerators for self-powered consumer electronics. *Nano Energy* **2013,** *2* (5), 688.

(309) Zhou, T.; Zhang, C.; Han, C. B.; Fan, F. R.; Tang, W.; Wang, Z. L. Woven Structured Triboelectric Nanogenerator for Wearable Devices. *ACS applied materials & interfaces* **2014,** *6* (16), 14695.

(310) Wang, S.; Xie, Y.; Niu, S.; Lin, L.; Wang, Z. L. Freestanding triboelectric-layer-based nanogenerators for harvesting energy from a moving object or human motion in contact and non-contact modes. *Advanced materials* **2014,** *26* (18), 2818.

(311) Fuh, Y. K.; Chen, P. C.; Ho, H. C.; Huang, Z. M.; Li, S. C. All-direction energy harvester based on nano/micro fibers as flexible and stretchable sensors for human motion detection. *Rsc Advances* **2015,** *5* (83), 67787.

(312) Cheng, X. L.; Meng, B.; Zhang, X. S.; Han, M. D.; Su, Z. M.; Zhang, H. X. Wearable electrode-free triboelectric generator for harvesting biomechanical energy. *Nano Energy* **2015,** *12*, 19.

(313) Bai, P.; Zhu, G.; Lin, Z.-H.; Jing, Q.; Chen, J.; Zhang, G.; Ma, J.; Wang, Z. L. Integrated multilayered triboelectric nanogenerator for harvesting biomechanical energy from human motions. *Acs Nano* **2013,** *7* (4), 3713.

(314) Xie, Y. N.; Wang, S. H.; Lin, L.; Jing, Q. S.; Lin, Z. H.; Niu, S. M.; Wu, Z. Y.; Wang, Z. L. Rotary Triboelectric Nanogenerator Based on a Hybridized Mechanism for Harvesting Wind Energy. *Acs Nano* **2013,** *7* (8), 7119.

(315) Xie, Y. N.; Wang, S. H.; Niu, S. M.; Lin, L.; Jing, Q. S.; Su, Y. J.; Wu, Z. Y.; Wang, Z. L. Multi-layered disk triboelectric nanogenerator for harvesting hydropower. *Nano Energy* **2014,** *6*, 129.

(316) Liang, Q. J.; Yan, X. Q.; Gu, Y. S.; Zhang, K.; Liang, M. Y.; Lu, S. N.; Zheng, X.; Zhang, Y. Highly transparent triboelectric nanogenerator for harvesting water-related energy reinforced by antireflection coating. *Sci Rep-Uk* **2015,** *5*.

(317) Yang, Y.; Zhang, H. L.; Zhong, X. D.; Yi, F.; Yu, R. M.; Zhang, Y.; Wang, Z. L. Electret Film-Enhanced Triboelectric Nanogenerator Matrix for Self-Powered Instantaneous Tactile Imaging. *ACS applied materials & interfaces* **2014,** *6* (5), 3680.

(318) Lin, L.; Xie, Y. N.; Wang, S. H.; Wu, W. Z.; Niu, S. M.; Wen, X. N.; Wang, Z. L. Triboelectric Active Sensor Array for Self-Powered Static and Dynamic Pressure Detection and Tactile Imaging. *Acs Nano* **2013,** *7* (9), 8266.

(319) Yi, F.; Lin, L.; Niu, S. M.; Yang, J.; Wu, W. Z.; Wang, S. H.; Liao, Q. L.;

Zhang, Y.; Wang, Z. L. Self-Powered Trajectory, Velocity, and Acceleration Tracking of a Moving Object/Body using a Triboelectric Sensor. *Advanced Functional Materials* **2014,** *24* (47), 7488.

(320) Yang, Y.; Zhou, Y. S.; Zhang, H. L.; Liu, Y.; Lee, S. M.; Wang, Z. L. A Single-Electrode Based Triboelectric Nanogenerator as Self-Powered Tracking System. *Advanced materials* **2013,** *25* (45), 6594.

(321) Yang, Y.; Zhou, Y. S.; Zhang, H.; Liu, Y.; Lee, S.; Wang, Z. L. A single-electrode based triboelectric nanogenerator as self-powered tracking system. *Advanced materials* **2013,** *25* (45), 6594.

(322) Su, Y. J.; Zhu, G.; Yang, W. Q.; Yang, J.; Chen, J.; Jing, Q. S.; Wu, Z. M.; Jiang, Y. D.; Wang, Z. L. Triboelectric Sensor for Self-Powered Tracking of Object Motion inside Tubing. *Acs Nano* **2014,** *8* (4), 3843.

(323) Han, C. B.; Zhang, C.; Li, X. H.; Zhang, L. M.; Zhou, T.; Hu, W. G.; Wang, Z. L. Self-powered velocity and trajectory tracking sensor array made of planar triboelectric nanogenerator pixels. *Nano Energy* **2014,** *9*, 325.

(324) Chen, M. X.; Li, X. Y.; Lin, L.; Du, W. M.; Han, X.; Zhu, J.; Pan, C. F.; Wang, Z. L. Triboelectric Nanogenerators as a Self-Powered Motion Tracking System. *Advanced Functional Materials* **2014,** *24* (32), 5059.

(325) Zhu, G.; Pan, C.; Guo, W.; Chen, C. Y.; Zhou, Y.; Yu, R.; Wang, Z. L. Triboelectric-generator-driven pulse electrodeposition for micropatterning. *Nano letters* **2012,** *12* (9), 4960.

(326) Hwang, B. U.; Lee, J. H.; Trung, T. Q.; Roh, E.; Kim, D. I.; Kim, S. W.;

Lee, N. E. Transparent Stretchable Self-Powered Patchable Sensor Platform with Ultrasensitive Recognition of Human Activities. *Acs Nano* **2015,** *9* (9), 8801.

(327) Fan, F. R.; Lin, L.; Zhu, G.; Wu, W. Z.; Zhang, R.; Wang, Z. L. Transparent Triboelectric Nanogenerators and Self-Powered Pressure Sensors Based on Micropatterned Plastic Films. *Nano letters* **2012,** *12* (6), 3109.

(328) Lin, Z. H.; Zhu, G.; Zhou, Y. S.; Yang, Y.; Bai, P.; Chen, J.; Wang, Z. L. A Self-Powered Triboelectric Nanosensor for Mercury Ion Detection. *Angew Chem Int Edit* **2013,** *52* (19), 5065.

(329) Li, L.; Zhong, Y. W.; Li, J.; Gong, J. L.; Ben, Y.; Xu, J.; Chen, X. P.; Ma, Z. Breath figure lithography: A facile and versatile method for micropatterning. *J Colloid Interf Sci* **2010,** *342* (1), 192.

(330) Yao, B. J.; Zhu, Q. Z.; Yao, L. L.; Hao, J. C. Fabrication of honeycomb-structured poly(ethylene glycol)-block-poly(lactic acid) porous films and biomedical applications for cell growth. *Appl Surf Sci* **2015,** *332*, 287.

(331) Sato, K.; Hasebe, K.; Tanaka, M.; Takebayashi, M.; Nishikawa, K.; Shimomura, M.; Kawai, T.; Matsushita, M.; Todo, S. *Preparation of the honeycomb patterned porous film of biodegradable polymer for tissue engineering scaffolds*, 2003.

(332) Xu, W. Z.; Zhang, X. Y.; Kadla, J. F. Design of Functionalized Cellulosic Honeycomb Films: Site-Specific Biomolecule Modification via "Click Chemistry". *Biomacromolecules* **2012,** *13* (2), 350.

(333) Xu, W. Z.; Kadla, J. F. Honeycomb Films of Cellulose Azide: Molecular Structure and Formation of Porous Films. *Langmuir* **2013,** *29* (2), 727.

(334) Wan, L. S.; Li, Q. L.; Chen, P. C.; Xu, Z. K. Patterned biocatalytic films via one-step self-assembly. *Chem Commun (Camb)* **2012,** *48* (37), 4417.

(335) Ding, L.; Zhang, A. J.; Li, W. Q.; Bai, H.; Li, L. Multi-length scale porous polymer films from hypercrosslinked breath figure arrays. *J Colloid Interf Sci* **2016,** *461*, 179.

(336) Kurono, N.; Shimada, R.; Ishihara, T.; Shimomura, M. Fabrication and optical property of self-organized honeycomb-patterned films. *Molecular Crystals and Liquid Crystals* **2002,** *377* (1), 285.

(337) Miller, S.; Bao, Z. N. Fabrication of flexible pressure sensors with microstructured polydimethylsiloxane dielectrics using the breath figures method. *J Mater Res* **2015,** *30* (23), 3584.

(338) Zhou, W. X.; Chen, J.; Li, Y.; Wang, D. B.; Chen, J. Y.; Feng, X. M.; Huang, Z. D.; Liu, R. Q.; Lin, X. J.; Zhang, H. M.et al. Copper Mesh Templated by Breath-Figure Polymer Films as Flexible Transparent Electrodes for Organic Photovoltaic Devices. *ACS applied materials & interfaces* **2016,** *8* (17), 11122.

(339) ImageJ software. https://imagej.nih.gov/ij/.

(340) Adam, N.; Livingston, H. Contact angles and work of adhesion. **1958**.

(341) Haynes, W. M. *CRC handbook of chemistry and physics*; CRC press, 2014.

(342) Dobbs, H.; Bonn, D. Predicting wetting behavior from initial spreading

coefficients. *Langmuir* **2001,** *17* (15), 4674.

(343) Hansen, C. M. *Hansen solubility parameters: a user's handbook*; CRC press, 2007.

(344) Xu, S.; Li, M.; Mitov, Z.; Kumacheva, E. Surface textures induced by convection in thin films of polymeric and polymerizable fluids. *Progress in organic coatings* **2003,** *48* (2), 227.

(345) Ito, K. Silicone handbook. *Nikkankougyoushinbunsya, Tokyo* **1990**.

(346) Borah, D.; Shaw, M. T.; Holmes, J. D.; Morris, M. A. Sub-10 nm Feature Size PS-b-PDMS Block Copolymer Structures Fabricated by a Microwave-Assisted Solvothermal Process. *ACS applied materials & interfaces* **2013,** *5* (6), 2004.

(347) Mullins, O. C. The asphaltenes. *Annu Rev Anal Chem (Palo Alto Calif)* **2011,** *4*, 393.

(348) Binks, B.; Lumsdon, S. Pickering emulsions stabilized by monodisperse latex particles: effects of particle size. *Langmuir* **2001,** *17* (15), 4540.

(349) Pickering, S. U. CXCVI.—emulsions. *Journal of the Chemical Society, Transactions* **1907,** *91*, 2001.

(350) Hassan, M.; Mohammad, L. N.; Asadi, S.; Dylla, H.; Cooper, S. Sustainable Photocatalytic Asphalt Pavements for Mitigation of Nitrogen Oxide and Sulfur Dioxide Vehicle Emissions. *Journal of Materials in Civil Engineering* **2013,** *25* (3), 365.

(351) Konstantinou, I. K.; Albanis, T. A. TiO2-assisted photocatalytic

degradation of azo dyes in aqueous solution: kinetic and mechanistic investigations. *Applied Catalysis B: Environmental* **2004,** *49* (1), 1.

(352) Khataee, A. R.; Kasiri, M. B. Photocatalytic degradation of organic dyes in the presence of nanostructured titanium dioxide: Influence of the chemical structure of dyes. *Journal of Molecular Catalysis A: Chemical* **2010,** *328* (1-2), 8.

(353) Leng, Z.; Yu, H. Novel Method of Coating Titanium Dioxide on to Asphalt Mixture Based on the Breath Figure Process for Air-Purifying Purpose. *Journal of Materials in Civil Engineering* **2016,** *28* (5), 04015188.

(354) Agrios, A. G.; Pichat, P. State of the art and perspectives on materials and applications of photocatalysis over TiO 2. *Journal of Applied Electrochemistry* **2005,** *35* (7), 655.

(355) Chen, J.; Poon, C.-s. Photocatalytic construction and building materials: from fundamentals to applications. *Building and Environment* **2009,** *44* (9), 1899.

(356) Chen, M.; Liu, Y. NO x removal from vehicle emissions by functionality surface of asphalt road. *Journal of hazardous materials* **2010,** *174* (1), 375.

(357) Liu, Y.; Wang, X.; Qi, K.; Xin, J. H. Functionalization of cotton with carbon nanotubes. *J Mater Chem* **2008,** *18* (29), 3454.

(358) Tao, X. *Smart fibres, fabrics and clothing: fundamentals and applications*; Elsevier, 2001.

(359) Park, S.; Jayaraman, S. Smart textiles: Wearable electronic systems. *MRS*

bulletin **2003,** *28* (08), 585.

(360) Wei, Q. *Surface modification of textiles*; Elsevier, 2009.

(361) Smith, W. C. *Smart textile coatings and laminates*; Elsevier, 2010.

(362) Chao, C.-C.; Ho, R.-M.; Georgopanos, P.; Avgeropoulos, A.; Thomas, E. L. Silicon oxy carbide nanorings from polystyrene-b-polydimethylsiloxane diblock copolymer thin films. *Soft Matter* **2010,** *6* (15), 3582.

(363) Taylor, R.; Brandon, J.; Morrell, P. Microstructure, composition and property relationships of plasma-sprayed thermal barrier coatings. *Surface and Coatings technology* **1992,** *50* (2), 141.

(364) Müller, M.; Oehr, C. Comments on "an essay on contact angle measurements" by Strobel and Lyons. *Plasma Process Polym* **2011,** *8* (1), 19.

(365) Di Mundo, R.; Palumbo, F. Comments regarding 'an essay on contact angle measurements'. *Plasma Process Polym* **2011,** *8* (1), 14.